

**University College London**

# **A computational study of calcium carbonate**

Thesis submitted for the degree of Doctor of Philosophy (PhD) by

**Qi Wang**

Supervised by

Prof. Nora H. de Leeuw

University College London

Department of Chemistry

September 2011

## **Declaration**

I, Qi Wang, confirm that this is my own work and the use of all materials from other sources has been properly indicated in the thesis.

---

Qi Wang

September 2011

## Abstract

---

This thesis presents the results of computer simulation studies of impurity incorporation in calcite and the aggregation of calcite particles, using a combination of classical computational techniques based on interatomic potentials, namely molecular mechanics and molecular dynamics simulations.

Firstly, the atomistic simulation techniques have been employed to investigate the thermodynamics of mixing in calcite with seven divalent cationic impurities ( $\text{Mg}^{2+}$ ,  $\text{Ni}^{2+}$ ,  $\text{Co}^{2+}$ ,  $\text{Zn}^{2+}$ ,  $\text{Fe}^{2+}$ ,  $\text{Mn}^{2+}$  and  $\text{Cd}^{2+}$ ), based on the calculation of all inequivalent site occupancy configurations in  $2 \times 2 \times 1$  and  $3 \times 3 \times 1$  supercells of the calcite structure. In addition to the enthalpy of mixing, the configurational entropy and mixing free energy have also been calculated, providing an insight into the mixing behaviour as a function of the temperature for a series of carbonate solid solutions. The calculations have revealed that the solubility of the cationic impurities in calcite is largely related to the cationic coordination distance with oxygen.

Secondly, the aggregation process has been investigated implementing classical computational techniques, and especially the interaction of a calcite nanoparticle with the major calcite surfaces, where the adhesion energy and optimised geometries of a typical calcite nanoparticle on different surfaces in vacuum and aqueous environment have been calculated. The results show the orientation of a nanoparticle is a key factor that effects the interactions, besides the size and structure of the nanoparticle. The most stable aggregated configuration occurs when the lattices of the nanoparticle and the surface are perfectly aligned.

Finally, a number of symmetric calcite tilt grain boundaries have been constructed to act as models of two calcite nanoparticles, after collision has occurred but before growth has a chance to commence. Molecular dynamics simulations were then employed to study the stability of these tilt grain boundaries and the growth of a series of calcium carbonate units at the contact points in the pure and hydrated calcite tilt grain boundaries. The calculation have proved that the initial incorporation of a  $\text{CaCO}_3$  unit is preferential at the obtuse step in a grain boundary, and the growth velocity of the acute step is 1.3 to 2.1 times higher than that of the obtuse step, once the initial growth unit has been deposited on the steps. This study has evaluated the conditions required for the growth of new calcium carbonate materials in the calcite tilt grain boundaries.

## List of Publications

---

The work described in this thesis has been published in the following papers:

**Qi Wang**, Ricardo Grau-Crespo and Nora H. de Leeuw (2011) Mixing thermodynamics of the calcite-structured (Mn,Ca)CO<sub>3</sub> solid solution: A computer simulation study. *Journal of Physical Chemistry C*, accepted.

**Qi Wang** and Nora H. de Leeuw (2009) A computer simulation study of the thermodynamics of mixing in the (Mn,Ca)CO<sub>3</sub> solid solution. *Geochimica et Cosmochimica Acta*, Vol. 73: A1412.

**Qi Wang** and Nora H. de Leeuw (2008) A computer modelling study of CdCO<sub>3</sub>-CaCO<sub>3</sub> solid solutions. *Mineralogical Magazine*, Vol. 72: 525-529.

## Acknowledgement

---

First of all, I would like to thank my supervisor, Prof. Nora H. de Leeuw, for her distinguished guidance and generous support during the past four years. This thesis really wouldn't have been possible without her supervision.

Particular thanks should go to Dr. Zhimei Du and Dr. Ricardo Grau-Crespo, for their invaluable guidance and helpful discussion throughout this project. I would like to give my acknowledgement to the whole group, where I received lots of help and encouragements. A special thank you to Prof. Steve Parker, who gave me lots of kind help and guidance during my visit in Bath University.

I am grateful to the China Scholarship Council (CSC) for financial support and University College London for an Overseas Research Studentship. I also thank the EU-funded "Mineral Nucleation and Growth Kinetics (MIN-GRO) Marie-Curie Research and Training Network" for funding. I also acknowledge the use of the UCL *Legion* High Performance Computing Facility and associated support services in the completion of this project.

Finally, I sincerely thank my grandparents, parents and fiancé Dr. Qiyao Feng for showing concerns, giving loves and support to me during my four years PhD study in UCL. I would like to dedicate this thesis to them. Thank you very much.

# Table of Contents

---

<b>DECLARATION</b> .....	2
<b>ABSTRACT</b> .....	3
<b>LIST OF PUBLICATIONS</b> .....	5
<b>ACKNOWLEDGEMENT</b> .....	6
<b>TABLE OF CONTENTS</b> .....	7
<b>LIST OF FIGURES</b> .....	20
<b>LIST OF TABLES</b> .....	20
<b>LIST OF ABBREVIATIONS</b> .....	20
<b>Chapter 1 Introduction</b> .....	21
1.1 Calcium carbonate.....	22
1.2 Incorporation of impurities in calcium carbonate.....	24
1.2.1 Heavy metals in nature .....	26
1.2.2 Carbonate solid solutions.....	27
1.2.3 Experimental studies of carbonate solid solutions .....	29
1.2.4 Theoretical studies of carbonate solid solutions.....	31
1.3 The growth and dissolution of calcium carbonate.....	34
1.3.1 Nucleation and growth of calcium carbonate.....	34
1.3.2 Dissolution of calcite .....	37
1.4 Aggregation of calcite nanoparticles .....	38
1.5 Aims and overview of the thesis.....	41
<b>Chapter 2 Computational Methodology</b> .....	43
2.1 Molecular mechanics.....	44
2.1.1 Potential energy surface.....	44
2.1.2 Energy minimisation algorithm.....	45

## Table of Contents

---

2.1.3 Static lattice optimisation.....	48
2.1.4 Surface simulations.....	50
2.1.5 Construction of calcite nanoparticles .....	55
2.2 Molecular dynamics.....	56
2.2.1 Finite difference methods.....	57
2.2.2 Ensembles .....	60
2.2.3 Periodic boundary conditions.....	61
2.2.4 Running MD simulations .....	62
2.2.5 Analysis.....	65
<b>Chapter 3 Potential models.....</b>	<b>67</b>
3.1 The Born model of solids.....	68
3.2 The Ewald method.....	69
3.3 Electronic polarisability .....	70
3.4 Short range potential functions.....	72
3.4.1 Buckingham potential function .....	72
3.4.2 Morse potential function .....	73
3.4.3 Lennard-Jones potential function .....	74
3.4.4 Many body potential function .....	74
3.5 Potentials of carbonates and water.....	76
3.6 Derivation of potentials for Ni, Co, Zn and Mn carbonates .....	78
<b>Chapter 4 Mixing thermodynamics of calcite with divalent cation impurities..</b>	<b>82</b>
4.1 Introduction.....	83
4.2 Configurational statistics.....	85
4.3 Structure and configurational entropy.....	89
4.4 MnCO <sub>3</sub> -CaCO <sub>3</sub> solid solutions .....	94
4.5 CdCO <sub>3</sub> -CaCO <sub>3</sub> solid solutions .....	104
4.6 FeCO <sub>3</sub> -CaCO <sub>3</sub> solid solutions.....	109
4.7 Uptake of Zn <sup>2+</sup> and Co <sup>2+</sup> to calcite.....	113
4.8 Uptake of Mg <sup>2+</sup> and Ni <sup>2+</sup> to calcite .....	115

4.9 Chapter summary.....	119
<b>Chapter 5 Investigation of the interaction between calcite nanoparticle and calcite surfaces .....</b>	<b>121</b>
5.1 Introduction.....	122
5.2 Calcite surfaces .....	122
5.3 Calcite nanoparticle.....	129
5.4 Adhesion energy of a nanoparticle on the surface .....	130
5.5 Interaction between a nanoparticle <sub>104</sub> and calcite surfaces .....	132
5.5.1 Nanoparticle <sub>104</sub> and pure {10 $\bar{1}$ 4} surface .....	134
5.5.2 Nanoparticle <sub>104</sub> and hydrated {10 $\bar{1}$ 4} surface.....	136
5.5.3 The effect of the size of a nanoparticle <sub>104</sub> .....	141
5.5.4 Nanoparticle <sub>104</sub> and pure {0001} surface.....	142
5.5.5 Nanoparticle <sub>104</sub> and hydrated {0001} surface .....	146
5.5.6 Nanoparticle <sub>104</sub> and stepped surfaces .....	149
5.6 Interaction between a nanoparticle <sub>001</sub> and calcite surfaces .....	153
5.6.1 Nanoparticle <sub>001</sub> and pure {10 $\bar{1}$ 4} surface .....	155
5.6.2 Nanoparticle <sub>001</sub> and hydrated {10 $\bar{1}$ 4} surface.....	156
5.6.3 Nanoparticle <sub>001</sub> and pure {0001} surface.....	159
5.6.4 Nanoparticle <sub>001</sub> and hydrated {0001} surface .....	163
5.7 Chapter summary.....	164
<b>Chapter 6 The growth of calcium carbonate at tilt grain boundaries and stepped surfaces.....</b>	<b>166</b>
6.1 Introduction.....	167
6.2 Methods .....	169
6.3 Tilt grain boundaries of calcite .....	172
6.4 Single calcium carbonate unit in aqueous environment .....	179
6.5 The growth of calcium carbonate in pure grain boundaries .....	181
6.6 The growth of calcium carbonate in hydrated grain boundaries.....	186
6.7 Chapter summary.....	191

<b>Chapter 7 Conclusions and Future works</b> .....	193
7.1 Conclusions.....	194
7.1.1 The incorporation of cationic impurities in calcite.....	194
7.1.2 The adhesion of calcite nanoparticle on calcite surface .....	195
7.1.3 The growth of calcium carbonate units in tilt grain boundary .....	195
7.2 Future works.....	198
<b>BIBLIOGRAPHIC</b> .....	200

## List of Figures

- Figure 1.1:** Illustration of orthorhombic double cells of aragonite, (a) side view, and (b) top view, (Ca = green, O = red, C = grey). ..... 23
- Figure 1.2:** Hexagonal representation of a calcite unit cell, (a) side view, and (b) top view (Ca = green, O = red, C = grey). ..... 24
- Figure 1.3:** Illustration of  $\{10\bar{1}4\}$  and  $\{0001\}$  planes of calcite. The  $\{0001\}$  plane has two terminations, i.e. a  $\text{Ca}^{2+}$  termination and a  $\text{CO}_3^{2-}$  termination..... 25
- Figure 1.4:** Photographs of crystals of (a) manganocalcite ( $\text{Mn}_x\text{Ca}_{1-x}\text{CO}_3$ ) from Yunnan, China and (b) rhodochrosite ( $\text{MnCO}_3$ ) from Chihuahua, Mexico. .... 28
- Figure 1.5:** Growth morphology of calcite as a function of the  $\text{Ca}^{2+}/\text{CO}_3^{2-}$  ratio. (a) At low  $\text{Ca}^{2+}/\text{CO}_3^{2-}$  ratio, the obtuse steps do not advance. Both step orientations have a high kink density, as evidenced by their roughness. (b) At intermediate ratios, both obtuse and acute step orientations are straight and advance. (c) At high ratios, the obtuse step orientation continues to grow, whereas the acute step has become pinned and etch-pits are observed, (Stack and Grantham, 2010)..... 36
- Figure 1.6:** SEM images of micro-sized aggregated  $\text{CaCO}_3$  particles, (Collier *et al.*, 2000). ..... 39
- Figure 2.1:** Local minimum and global minimum on a potential energy surface..... 45
- Figure 2.2:** Side view of two types of surfaces as classified by Tasker. (a) Type I surface consisting of charge neutral layers, and (b) Type II surface consisting of positive and negative charged planes but with a charge neutral and non-dipolar repeat unit. The dashed line representatives the two dimensional periodicity..... 51
- Figure 2.3:** Stacking sequences showing (a) a Type III surface, consisting of alternating positive and negative ions giving rise to a dipolar repeat unit, and (b) a reconstructed Type III surface, where half the surface ions have been moved to the bottom of the surface in order to remove the net dipole. The dashed line representatives the two dimensional periodicity..... 52
- Figure 2.4:** The two region approach used in METADISE, (a) a crystal; (b) the complete crystal containing two blocks and (c) half a crystal, exposing a surface.. 53
- Figure 2.5:** (a) Calcite crystal growing from the aqueous solution (Didymus *et al.*, 1993) and (b) equilibrium morphology of calcite particle constructed by the Wulff construction method..... 56

- Figure 2.6:** A two-dimensional periodic system. Molecules can enter and leave each box across each of the four edges. In a three-dimensional system, molecules would be free to across any of the six cube faces (Allen & Tildesley, 1999)..... 62
- Figure 3.1:** Plots showing the variation in the long-range, short-range and total potential energies as a function of  $r_{ij}$  for a  $\text{Ca}^{2+}\text{-O}^{2-}$  ion pair..... 68
- Figure 3.2:** Schematic representation of the core-shell model: (a) no displacement, unpolarised. (b) displacement, polarised. The blue sphere, representing the core, has the charge  $Xe$ . The open grey sphere, representing the shell, has the charge of  $Ye$ . The core and shell are connected by a spring of force constant  $K$ , (Murphy, 2009). ..... 71
- Figure 3.3:** The three-body interaction in a carbonate group. .... 75
- Figure 3.4:** The four-body interaction of four atoms lying in two planes with a torsional angle  $\theta$ ..... 75
- Figure 4.1:** The structures of the most stable configurations for  $x = n/6$  ( $n = 1, 2, 3$ ). The lowest-energy structures for  $n = 4$  and  $5$  can be obtained from the ones with  $n = 2$  and  $1$ , respectively, if  $\text{Ca}^{2+}$  and impurity  $\text{Me}^{2+}$  positions are swapped. The  $n = 3$  case ( $x = 0.5$ ) corresponds to the ordered dolomite-type structure. (Ca = green, C = grey, O = red, Me = blue)..... 90
- Figure 4.2:** The lowest (black line) and highest (blue line) lattice energies of mixed systems for  $\text{Me}^{2+}$  composition  $x = 0.25$ , compared to the average lattice energy in the configurational space (red line). .... 91
- Figure 4.3:** Configurational spectrum of lattice energies corresponding to the composition of  $\text{Cd}_{0.25}\text{Ca}_{0.75}\text{CO}_3$  at 300 K, as calculated in a  $2 \times 2 \times 1$  supercell. .... 91
- Figure 4.4:** Variation of the configurational entropy corresponding to the composition of  $\text{Me}_{0.33}\text{Ca}_{0.67}\text{CO}_3$  at 300 K, as calculated in a  $2 \times 2 \times 1$  supercell. .... 93
- Figure 4.5:** Variation of the maximum configurational entropy (in the full disorder limit) with the supercell size. .... 93
- Figure 4.6:** Calculated and experimental mixing enthalpies for the Ca-rich  $\text{Mn}_x\text{Ca}_{1-x}\text{CO}_3$  solid solution. The empty squares in red colour correspond to calculations in the full disorder limit with the  $3 \times 3 \times 1$  supercell. .... 97
- Figure 4.7:** Calculated and experimental mixing enthalpies for the Mn-rich  $\text{Mn}_x\text{Ca}_{1-x}\text{CO}_3$  solid solution. The empty squares in red colour correspond to calculations in the full disorder limit with the  $3 \times 3 \times 1$  supercell. .... 98
- Figure 4.8:** The structure of kutnahorite, showing  $\text{Mn}^{2+}$  and  $\text{Ca}^{2+}$  occupy alternating interlayers. (Ca = green, Mn = purple, C = grey, O = red).....100
- Figure 4.9:** The variation of enthalpy of mixing with different number of  $\text{Mn}_{0.5}\text{Ca}_{0.5}\text{CO}_3$  configurations at 3000 K and infinitely high temperature.....101

<b>Figure 4.10:</b> The different in free energy $\Delta G$ between the disordered $\text{Mn}_{0.5}\text{Ca}_{0.5}\text{CO}_3$ and kutnahorite as a function of temperature. The negative $\Delta G$ indicates the disordered $\text{Mn}_{0.5}\text{Ca}_{0.5}\text{CO}_3$ is more stable than ordered kutnahorite at this temperature. .....	102
<b>Figure 4.11:</b> Calculated free energy of mixing with full range of $\text{Mn}^{2+}$ compositions at 900 K. ....	103
<b>Figure 4.12:</b> Variation of the lattice parameters of $\text{Mn}_x\text{Ca}_{1-x}\text{CO}_3$ as a function of composition, in comparison with experiment (Katsikopoulos <i>et al.</i> , 2009). ....	104
<b>Figure 4.13:</b> The variation of enthalpy of mixing with different number of inequivalent $\text{Cd}_{0.5}\text{Ca}_{0.5}\text{CO}_3$ configurations at 300 K and 1000 K. ....	106
<b>Figure 4.14:</b> Calculated mixing enthalpy and mixing free energy of the $\text{Cd}_x\text{Ca}_{1-x}\text{CO}_3$ system as a function of $\text{Cd}^{2+}$ composition, as calculated for a $2 \times 2 \times 1$ supercell. ....	107
<b>Figure 4.15:</b> Comparison between theoretical and experimental excess free energies $G^E$ findings for $\text{Cd}_x\text{Ca}_{1-x}\text{CO}_3$ at 300 K. ....	108
<b>Figure 4.16:</b> Calculated enthalpy of mixing in the $\text{Fe}_x\text{Ca}_{1-x}\text{CO}_3$ system. The solid lines show the enthalpy isotherms between 300 K and 1500 K with a step of 300 K. The dashed lines show the enthalpy at an infinitely high temperature. ....	110
<b>Figure 4.17:</b> Calculated free energy of mixing of the $\text{Fe}_x\text{Ca}_{1-x}\text{CO}_3$ system as a function of $\text{Fe}^{2+}$ compositions. ....	111
<b>Figure 4.18:</b> Comparison between theoretical excess Gibbs free energies $G^E$ for the $\text{Fe}_x\text{Ca}_{1-x}\text{CO}_3$ solid solutions at 823 K. ....	112
<b>Figure 4.19:</b> Calculated free energy of mixing with full range of $\text{Co}^{2+}$ or $\text{Zn}^{2+}$ compositions; (a) $\text{Co}_x\text{Ca}_{1-x}\text{CO}_3$ , (b) $\text{Zn}_x\text{Ca}_{1-x}\text{CO}_3$ . ....	114
<b>Figure 4.20:</b> Calculated free energy of mixing of the binary $(\text{Mg,Ca})\text{CO}_3$ system as a function of $\text{Mg}^{2+}$ composition, (a) calcite-dolomite, (b) dolomite-magnetite. ....	118
<b>Figure 4.21:</b> Calculated free energy of mixing of the binary systems as a function of $\text{Ni}^{2+}$ composition. (a) $\text{CaCO}_3\text{-Ca}_{0.5}\text{Ni}_{0.5}\text{CO}_3$ , (b) $\text{Ca}_{0.5}\text{Ni}_{0.5}\text{CO}_3\text{-NiCO}_3$ . ....	119
<b>Figure 5.1:</b> Top view and side view of pure planar surfaces, (a) $\{10\bar{1}4\}$ surface, (b) $\text{CO}_3^{2-}$ terminated $\{0001\}$ surface and (c) $\text{Ca}^{2+}$ terminated $\{0001\}$ surface. (Ca = green, C = grey, O = red). ....	124
<b>Figure 5.2:</b> Side view of pure stepped surfaces, (a) acute $\{3\ 1\ \bar{4}\ 8\}$ surface and (b) obtuse $\{3\ \bar{1}\ \bar{2}\ 16\}$ surface. (Ca = green, C = grey, O = red). ....	125
<b>Figure 5.3:</b> Top view and side view of hydrated planar surfaces with monolayer of water, (a) $\{10\bar{1}4\}$ surface, (b) $\text{CO}_3^{2-}$ terminated $\{0001\}$ surface and (c) $\text{Ca}^{2+}$ terminated $\{0001\}$ surface. (Ca = green, C = grey, O = red, H = white, $\text{O}_{\text{water}}$ = blue). ....	127

<b>Figure 5.4:</b> Side view of hydrated stepped surfaces with monolayer of water, (a) acute $\{3\ 1\ \bar{4}\ 8\}$ surface and (b) obtuse $\{3\ \bar{1}\ \bar{2}\ 16\}$ surface (Ca = green, C = grey, O = red, H = white, $O_{\text{water}}$ = blue).....	128
<b>Figure 5.5:</b> Morphology of $\text{CaCO}_3$ nanoparticle, showing (a) $\{10\bar{1}4\}$ surface (b) $\{0001\}$ - $\text{Ca}^{2+}$ surface and (c) $\{0001\}$ - $\text{CO}_3^{2-}$ surface. ....	130
<b>Figure 5.6:</b> Examples of a calcite nanoparticle <sub>104</sub> on the top plane of planar $\{10\bar{1}4\}$ surface. (Ca = green, C = grey, O = red).....	131
<b>Figure 5.7:</b> The variation of unrelaxed adhesion energies with distance between pure $\{10\bar{1}4\}$ surface and a calcite nanoparticle <sub>104</sub> in vacuum. Results for some orientations have been omitted for clarity. ....	134
<b>Figure 5.8:</b> 3-D and 2-D adhesion energy contour of the nanoparticle <sub>104</sub> on the pure $\{10\bar{1}4\}$ surface with a rotation of (a) and (b) $\theta = 0^\circ$ , (c) and (d) $\theta = 180^\circ$ . (Ca = green, C = grey, O = red). ....	135
<b>Figure 5.9:</b> Adhesion energy as a function of the distance between the monolayer hydrated $\{10\bar{1}4\}$ surface and a nanoparticle <sub>104</sub> . Results for some orientations have been omitted for clarity. ....	136
<b>Figure 5.10:</b> Adhesion energy as a function of the orientation of a nanoparticle <sub>104</sub> on pure (black triangle) and hydrated (red circle) $\{10\bar{1}4\}$ surface. ....	137
<b>Figure 5.11:</b> 3-D and 2-D adhesion energy contours of the nanoparticle <sub>104</sub> on the hydrated $\{10\bar{1}4\}$ surface with a rotation of $\theta = 0^\circ$ . (Ca = green, C = grey, H = white, O = red, $O_{\text{water}}$ = blue). ....	138
<b>Figure 5.12:</b> Side view of the unrelaxed interfacial system of the monolayer hydrated $\{10\bar{1}4\}$ surface/calcite nanoparticle <sub>104</sub> at a rotation of $0^\circ$ . (Ca = green, C = grey, O = red, $O_{\text{water}}$ = blue, H = white).....	139
<b>Figure 5.13:</b> Adhesion energy as a function of the distance between the hydrated $\{10\bar{1}4\}$ surface with multilayer water and the nanoparticle <sub>104</sub> at a rotation of $0^\circ$ . ...	140
<b>Figure 5.14:</b> The twist pathway of a nanoparticle <sub>104</sub> through the multilayer water, where $P_i$ ( $i = 1, 2, 3$ and $4$ ) is the position of local energy minimum. ....	140
<b>Figure 5.15:</b> Unrelaxed adhesion energies as a function of the orientations of the nanoparticle <sub>104</sub> for the pure (triangle) and monolayer hydrated (circle) $\{10\bar{1}4\}$ interfacial systems, ( $d = 1.0$ nm: black line, $d = 1.3$ nm: red line). ....	141
<b>Figure 5.16:</b> Adhesion energy as a function of the distance between the pure $\{0001\}$ surface and a nanoparticle <sub>104</sub> . Results for some orientations have been omitted for clarity.....	143
<b>Figure 5.17:</b> Adhesion energy as a function of the orientation of a nanoparticle <sub>104</sub> on pure $\{0001\}$ surfaces.....	144

<b>Figure 5.18:</b> 2-D adhesion energy contour of the nanoparticle <sub>104</sub> on the pure {0001} surface with a rotation of $\theta = 0^\circ$ , (a) CO <sub>3</sub> <sup>2-</sup> termination and (b) Ca <sup>2+</sup> termination. ..145	145
<b>Figure 5.19:</b> Side view of the top plane of (a) {0001}-CO <sub>3</sub> <sup>2-</sup> surface, (b) {0001}-Ca <sup>2+</sup> surface and (c) {10 $\bar{1}$ 4} surface, (Ca = green, C = grey, O = red).....146	146
<b>Figure 5.20:</b> Adhesion energy as a function of the distance between the monolayer hydrated {0001} surface and a nanoparticle <sub>104</sub> . Results for some orientations have been omitted for clarity. ....147	147
<b>Figure 5.21:</b> Adhesion energy as a function of the distance between the multilayer hydrated {0001} surface and the nanoparticle <sub>104</sub> at a rotation of $0^\circ$ .....147	147
<b>Figure 5.22:</b> The twist pathway of a nanoparticle <sub>104</sub> through the multilayer water, where $P_i$ is the position of local energy minimum, (a) {0001}-CO <sub>3</sub> <sup>2-</sup> surface, from $P_1$ to $P_4$ ; (b) {0001}-Ca <sup>2+</sup> surface, from $P_1$ to $P_3$ .....148	148
<b>Figure 5.23:</b> Side view of the unrelaxed interfacial systems of a nanoparticle <sub>104</sub> on the pure stepped surface, (a) acute stepped {3 1 $\bar{4}$ 8} surface and (b) obtuse stepped {3 $\bar{1}$ $\bar{2}$ 16} surface, where the nanoparticle is at a rotation of $0^\circ$ with respect to the terraces of the stepped surfaces (Ca = green, O = red, C = grey).....150	150
<b>Figure 5.24:</b> The variation of adhesion energy as the nanoparticle <sub>104</sub> moving along the step wall of pure {3 1 $\bar{4}$ 8} surface (black line) and planar {10 $\bar{1}$ 4} surfaces (red line). ....151	151
<b>Figure 5.25:</b> Adhesion energy as a function of the height between a nanoparticle <sub>104</sub> and the hydrated planar and stepped surfaces. ....152	152
<b>Figure 5.26:</b> Adhesion energy as a function of the distance between the pure {10 $\bar{1}$ 4} surface and a nanoparticle <sub>001</sub> . Results for some orientations have been omitted for clarity due to the periodic reiteration. ....156	156
<b>Figure 5.27:</b> Side view of the most stable interfacial configurations of the pure {10 $\bar{1}$ 4} surface with a calcite nanoparticle <sub>001</sub> . (a) nanoparticle <sub>001</sub> -Ca and (b) nanoparticle <sub>001</sub> -CO <sub>3</sub> , (Ca = green; C = grey; O = red).....157	157
<b>Figure 5.28:</b> Adhesion energy as a function of the distance between the hydrated {10 $\bar{1}$ 4} surface and nanoparticle <sub>001</sub> . Results for other orientations have been omitted for clarity. ....158	158
<b>Figure 5.29:</b> Side view of the most stable interfacial configuration of the hydrated {10 $\bar{1}$ 4} surface with a nanoparticle <sub>001</sub> -CO <sub>3</sub> (a $0^\circ$ rotation), where the blue dashes lines show the hydrogen bonds, (Ca = green, C = grey, O = red, O <sub>water</sub> = blue, H = white). ....159	159
<b>Figure 5.30:</b> Adhesion energy as a function of the distance between a nanoparticle <sub>001</sub> and pure {0001} surface. Results for other orientations have been omitted for clarity. ....160	160

- Figure 5.31:** Side view of the most stable interfacial configurations of the pure {0001} surface with a nanoparticle<sub>001-Ca</sub>. (a) Ca<sup>2+</sup> termination and (b) CO<sub>3</sub><sup>2-</sup> termination, (Ca = green; C = grey; O = red).....161
- Figure 5.32:** Adhesion energy as a function of the orientation of the nanoparticle<sub>001</sub> on pure {0001} surfaces. A nanoparticle<sub>001-Ca</sub> on the {0001}-CO<sub>3</sub><sup>2-</sup> surface (red line and circle) and {0001}-Ca<sup>2+</sup> surface (black line and triangle); a nanoparticle<sub>001-CO3</sub> on the {0001}-CO<sub>3</sub><sup>2-</sup> surface (green line and circle) and {0001}-Ca<sup>2+</sup> surface (blue line and triangle).....162
- Figure 5.33:** Adhesion energy as a function of the orientation of the nanoparticle<sub>001</sub> on hydrated {0001} surface: {0001}-CO<sub>3</sub><sup>2-</sup> surface (circle) and {0001}-Ca<sup>2+</sup> surface (triangle).....163
- Figure 6.1:** Side views of the unrelaxed calcite tilt grain boundaries: (a) A-grain boundary and (b) O-grain boundary. The surface area of each {10 $\bar{1}$ 4} terrace between the steps is 620.9 Å<sup>2</sup>. (Ca = green, C = gray, O = red).....170
- Figure 6.2:** Side view of relaxed calcite grain boundaries: (a) A-grain boundary and (b) O-grain boundary. The surface area of the {10 $\bar{1}$ 4} terrace is 1241.8 Å<sup>2</sup>. (Ca = green, C = gray, O = red).....173
- Figure 6.3:** Snapshot of hydrated grain boundaries after 250 ps MD simulations, where four distinct Ca<sup>2+</sup> sites are labelled in the interfacial regions. The Ca<sup>2+</sup> in the acute step of the joints are labelled Ca<sub>a,j</sub>; the Ca<sup>2+</sup> in the obtuse step of the joints are labelled Ca<sub>o,j</sub>; the Ca<sup>2+</sup> at the step of original stepped surface are labelled Ca<sub>c</sub>, and Ca<sub>t</sub> stands for the Ca<sup>2+</sup> in the middle of the terraces. (a) A-grain boundary and (b) O-grain boundary. (Ca = green, O = red, C = grey, O<sub>water</sub> = red, H = white). .....176
- Figure 6.4:** Radial distribution functions (RDF) for the local environment in the water at structurally different Ca<sup>2+</sup> surface sites. (a) A-grain boundary and (b) O-grain boundary. ....178
- Figure 6.5:** Representative snapshot from the MD simulations taken at 10 ps. (Ca = green; C = grey; O = red; H = white).....180
- Figure 6.6:** Radial distribution functions (RDF) of the Ca<sup>2+</sup>-O<sub>carbonate</sub> and Ca<sup>2+</sup>-O<sub>water</sub>. ....181
- Figure 6.7:** Initial structures of the O-grain boundary with single CaCO<sub>3</sub> unit in vacuum. The CaCO<sub>3</sub> unit was added at four different positions (P-I, I = 1, 2, 3 and 4) in the channel void, respectively.....183
- Figure 6.8:** Schematic diagram of the incorporation of the first and second CaCO<sub>3</sub> units along the step in the grain boundary. (Ca = green, C = black, O = red).....183
- Figure 6.9:** The growth energies of addition of successive CaCO<sub>3</sub> units at the steps of the joints (Position-1 and Position-2) in the A-grain boundary and O-grain boundary in vacuum. ....185

**Figure 6.10:** Bar charts of the average growth energies per  $\text{CaCO}_3$  unit released upon the growth of a full  $\text{CaCO}_3$  row in the A-grain boundary and O-grain boundary. ...186

**Figure 6.11:** The energies of addition of successive  $\text{CaCO}_3$  units at the steps of the joints (Position-1 and Position-2) in the A-grain boundary and O-grain boundary under aqueous conditions. ....189

**Figure 6.12:** Bar charts of the average growth energies per  $\text{CaCO}_3$  unit released upon the growth of a full  $\text{CaCO}_3$  row at the hydrated A-grain boundary and O-grain boundary systems.....190

## List of Tables

---

<b>Table 3.1</b> Potential parameters used in this thesis (short-range cutoff 20 Å). .....	77
<b>Table 3.2</b> Interionic Buckingham potentials obtained from fits to NiCO <sub>3</sub> , CoCO <sub>3</sub> , MnCO <sub>3</sub> and ZnCO <sub>3</sub> structures and enthalpies of reaction 3.14.....	80
<b>Table 3.3</b> Calculated and experimental properties of NiCO <sub>3</sub> , CoCO <sub>3</sub> , ZnCO <sub>3</sub> , MnCO <sub>3</sub> and CaCO <sub>3</sub> .....	81
<b>Table 4.1</b> Total number of configurations ( <i>W</i> ) and number of symmetrically inequivalent configurations ( <i>M</i> ) for each composition Me <sub><i>x</i></sub> Ca <sub>1-<i>x</i></sub> CO <sub>3</sub> in 2 × 2 × 1 and 3 × 3 × 1 supercells (A and B stand for either Ca or impurity). .....	88
<b>Table 4.2</b> Some data on rhombohedral carbonates.....	120
<b>Table 5.1</b> Surface energies of pure calcite surfaces (Jm <sup>-2</sup> ) .....	123
<b>Table 5.2</b> Surface energies of hydrated calcite surfaces (Jm <sup>-2</sup> ).....	126
<b>Table 5.3</b> Unrelaxed adhesion energies of a calcite nanoparticle <sub>104</sub> on the calcite planar surfaces in vacuum and aqueous solution.....	133
<b>Table 5.4</b> Relaxed adhesion energies of a calcite nanoparticle <sub>104</sub> on the calcite planar surfaces in vacuum and aqueous solution. ....	133
<b>Table 5.5:</b> The lowest unrelaxed adhesion energy of a nanoparticle <sub>104</sub> to the planar {10 $\bar{1}$ 4} and stepped {3 1 $\bar{4}$ 8}, {3 $\bar{1}$ $\bar{2}$ 16} surfaces. ....	150
<b>Table 5.6</b> Unrelaxed adhesion energies of a calcite nanoparticle <sub>001-Ca</sub> on the calcite planar surfaces in vacuum and aqueous solution.....	154
<b>Table 5.7</b> Unrelaxed adhesion energies of a calcite nanoparticle <sub>001-CO3</sub> on the calcite planar surfaces in vacuum and aqueous solution.....	155
<b>Table 6.1</b> Boundary and cleavage energies of the non-hydrated grain boundaries..	174
<b>Table 6.2</b> Boundary and hydration energies of the hydrated grain boundaries.....	175
<b>Table 6.3</b> Local environment of Ca <sup>2+</sup> ions at structurally different positions in the hydrated grain boundaries. The distance listed here are from RDF results. ....	177
<b>Table 6.4</b> Average configurational energies for the CaCO <sub>3</sub> unit in vacuum and water, and liquid water following simulations at 300 K for 0.2 ns. ....	180
<b>Table 6.5</b> Growth energies of incorporation of CaCO <sub>3</sub> units at various growth sites	

on the two non-hydrated grain boundaries ( $\text{kJmol}^{-1}$ ).....184

**Table 6.6** Growth energies of incorporation of  $\text{CaCO}_3$  units at various growth sites in the hydrated A-grain boundary and O-grain boundary, as calculated by equation 6.6 ( $\text{kJmol}^{-1}$ ). .....187

**Table 6.7** Growth energies of incorporation of  $\text{CaCO}_3$  units at various growth sites in the hydrated A-grain boundary and O-grain boundary, as calculated by equation 6.7 ( $\text{kJmol}^{-1}$ ). .....188

## List of Abbreviations

---

AFM	Atomic Force Microscopy
BCCF	The British Calcium Carbonates Federation
BFGS	Broyden Fletcher Goldfarb Shanno
DFT	Density Functional Theory
GULP	General Utility Lattice Program
IMANA	The Industrial Minerals Association North America
LEED	Low Energy Electron Diffraction
MC	Monte Carlo
MD	Molecular Dynamics
MM	Molecular Mechanics
NPT	Constant Number, Pressure and Temperature
NST	Constant Number, Pressure and Temperature
NVE	Constant Number, Volume and Energy
NVT	Constant Number, Volume and Temperature
PBC	Periodic Boundary Condition
PES	Potential Energy Surface
RDF	Radial Distribution Function
SEM	Scanning Electron Microscopy
SOD	Site Occupancy Disorder
TEM	Transmission Electron Microscopy
XPS	X-ray Photoelectron Spectroscopy
XRD	X-Ray Diffraction
WAXS	Wide Angle X-ray Scattering

# 1

## Introduction

---

Calcium carbonate is one of the most abundant minerals in our environment. It has been studied for more than a century because of its important role in geochemical, biological and industrial processes. This chapter gives a brief description of two important topics: the incorporation of cationic impurities in calcium carbonate and the growth and dissolution of calcium carbonate, where both experimental studies and computer modelling investigations are included. It also introduces the objectives of this thesis and provides an overview of the subsequent chapters.

## 1.1 Calcium carbonate

Calcium carbonate ( $\text{CaCO}_3$ ) is one of the most abundant materials found in sedimentary rock in all parts of the Earth surface.  $\text{CaCO}_3$  makes up 4% of the earth's crust and forms the rock types like limestone and chalk. Limestone makes up about 10% of all sedimentary rocks and is composed largely of the minerals calcite and aragonite (different crystal forms of  $\text{CaCO}_3$ ). Chalk is a white sedimentary rock, a form of limestone composed of the mineral calcite (Frye, 1981; Deer *et al.*, 1992).  $\text{CaCO}_3$  is also an important component in biological systems, such as shells of marine organisms, pearls and egg shells (Beruto and Giordani, 1993).

$\text{CaCO}_3$  has been the subject of extensive and varied research because of its fundamental applications in industrial, pharmaceutical and environmental fields.  $\text{CaCO}_3$  is a common raw substance in the construction industry, both as a building material (e.g. marble) and as an ingredient of cement. Because of its antacid properties,  $\text{CaCO}_3$  is also used to neutralize acidic conditions in both water and soil in industrial fields (BCCF, 2007; IMANA, 2010).  $\text{CaCO}_3$  is widely used as fillers in paper, rubber, plastics and paints to improve relevant mechanical properties of industrial materials (Zuiderduin *et al.*, 2003; Rocha *et al.*, 2005). It is also used as a carbon isotope counter in marine carbonates, with a view to assessing the relationship between carbon-induced emission and climate change (Romanek *et al.*, 1992). As a dietary supplement,  $\text{CaCO}_3$  is an inexpensive calcium source or gastric antacid in the pharmaceutical industry (Lieberman *et al.*, 1990; Gabriely *et al.*, 2008). Furthermore,  $\text{CaCO}_3$  has been shown to chemically interact with various solvated heavy ions, such as  $\text{Fe}^{2+}$ ,  $\text{Cd}^{2+}$  and  $\text{Mn}^{2+}$  (Stipp and Hochella, 1991; Stipp, 1998; Park *et al.*, 1996), and some organic molecules when exposed to aqueous solutions (Lebron and Suarez, 1998; Hoch *et al.*, 2000). Hence  $\text{CaCO}_3$  can be applied in water

treatment because of its strong surface interaction with heavy metals in the environment.

$\text{CaCO}_3$  exists in nature as several polymorphs: amorphous calcium carbonate, ikaite ( $\text{CaCO}_3 \cdot 6\text{H}_2\text{O}$ ), vaterite, aragonite and calcite. Both amorphous  $\text{CaCO}_3$  and ikaite are metastable in the environment and change easily to the more stable polymorph calcite (Deer *et al.*, 1992; Chang *et al.*, 1996). Vaterite ( $\mu\text{-CaCO}_3$ ) is also a metastable phase of  $\text{CaCO}_3$  at ambient conditions at the surface of the Earth. Once vaterite is exposed to water, it converts to aragonite or calcite (Palache *et al.*, 1951).

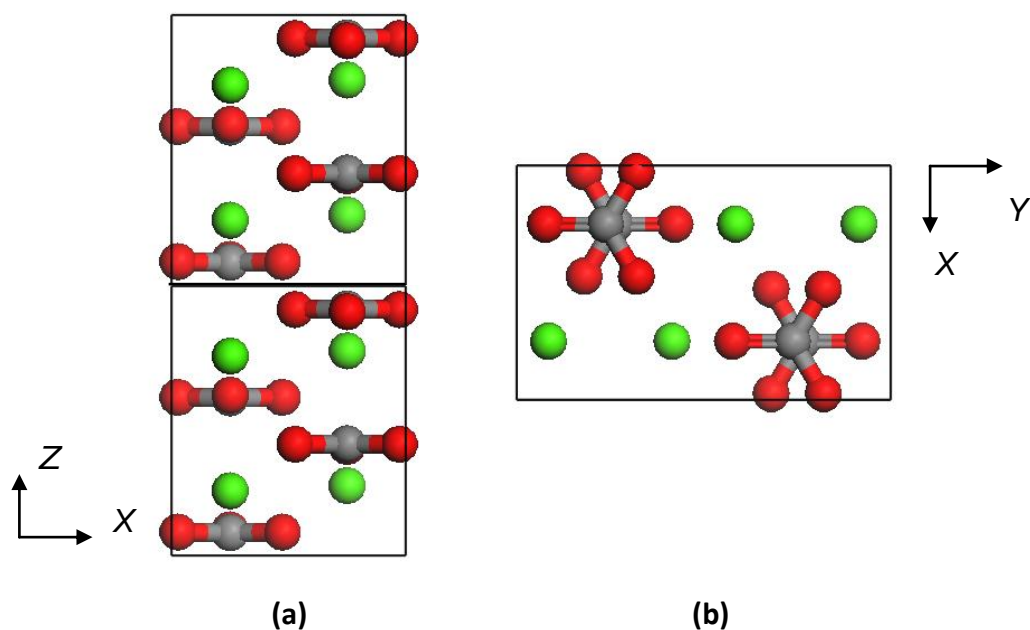


**Figure 1.1:** Illustration of orthorhombic double cells of aragonite, (a) side view, and (b) top view, (Ca = green, O = red, C = grey).

Aragonite is one of the two common, naturally occurring polymorphs of  $\text{CaCO}_3$ . It is formed by biological and physical processes, including precipitation from marine and freshwater environments. In particular, aragonite is the major constituent of coral reefs, shells, pearls and other biominerals, where it grows preferentially at ambient conditions due to the effect of organic templates (Morse and Mackenzie,

1990). Aragonite is thermodynamically unstable at standard temperature and pressure, and tends to alter to calcite over geologic time (Chang *et al.*, 1996). Aragonite has an orthorhombic crystal structure with space group  $Pm\bar{c}n$ . The experimental structure found by Dickens and Bowen (1971) is  $a = 4.960 \text{ \AA}$ ,  $b = 7.964 \text{ \AA}$ , and  $c = 5.738 \text{ \AA}$  and  $\alpha = \beta = \gamma = 90^\circ$ ; containing four  $\text{CaCO}_3$  (Figure 1.1).

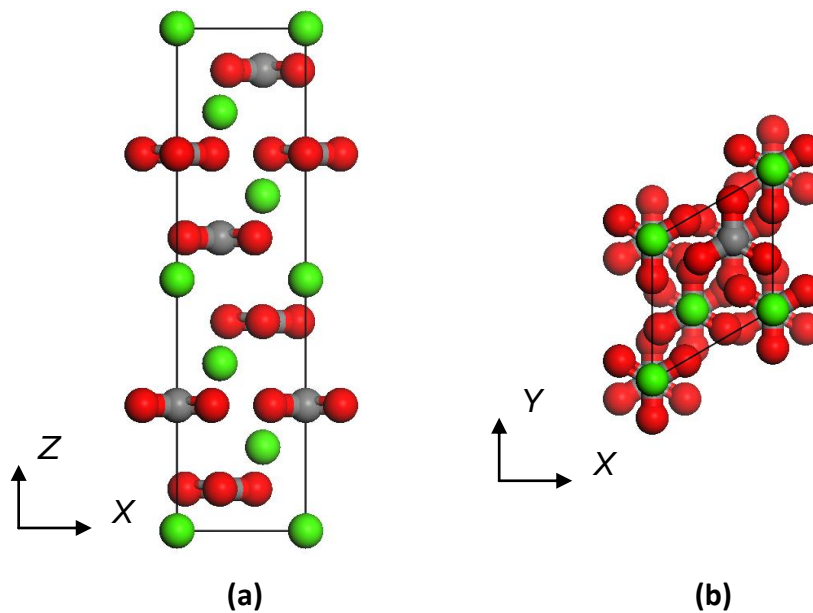


**Figure 1.2:** Hexagonal representation of a calcite unit cell, (a) side view, and (b) top view (Ca = green, O = red, C = grey).

Calcite is the most common and stable form of  $\text{CaCO}_3$  in the environment. It is stable at atmospheric pressure and temperature and only decomposes at 973 K, becoming calcium oxide (Kuriyavar *et al.*, 2000). The rhombohedral crystal structure of calcite was firstly determined using X-ray diffraction (XRD) by Bragg in 1914. The rhombohedral crystal structure can be defined using hexagonal axes and calcite surface are usually referred to using hexagonal indices, where four Miller indices are used instead of three and this convention is followed in this thesis. The hexagonal unit cell of calcite has  $a = b = 4.990 \text{ \AA}$ ,  $c = 17.061 \text{ \AA}$ , and  $\alpha = \beta = 90^\circ$ ,  $\gamma = 120^\circ$  (Deer *et al.*, 1992), shown in Figure 1.2. The  $\text{CO}_3^{2-}$  groups in calcite are arranged

differently to the corresponding groups in aragonite. Unlike in aragonite, the  $\text{CO}_3^{2-}$  groups do not lie in two layers that point in opposite directions. Instead they lie in a single plane pointing in the same direction, showing alternating layering of planar  $\text{CO}_3^{2-}$  groups and  $\text{Ca}^{2+}$  ions. Each oxygen atom in  $\text{CO}_3^{2-}$  group is surrounded by two  $\text{Ca}^{2+}$  ions in the calcite and three in aragonite (Bragg, 1924).

The  $\text{Ca}^{2+}$  and  $\text{CO}_3^{2-}$  ions in calcite are held together through ionic bonding and it is easy to cleave the crystal, as an external force can cause a plane of atoms to shift into a position where ions with the same charge are next to each other, causing repulsive and cleavage (Frye, 1981; Lardge, 2009). Figure 1.3 illustrated a series of possible cleavage planes. The  $\{10\bar{1}4\}$  plane contains both  $\text{Ca}^{2+}$  and  $\text{CO}_3^{2-}$  ions, making it charge neutral. It also has a higher density of ions compared to other possible neutral planes, leading to its stability (de Leeuw and Parker, 1997; 1998). The  $\{0001\}$  plane is terminated by either  $\text{Ca}^{2+}$  or  $\text{CO}_3^{2-}$  groups, leading to a positively or negatively charged surface respectively.

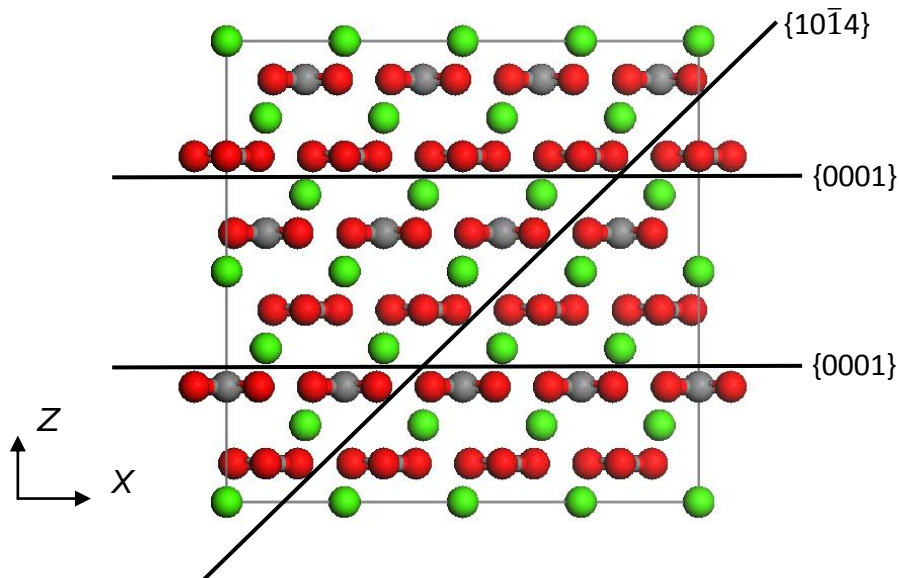


**Figure 1.3:** Illustration of  $\{10\bar{1}4\}$  and  $\{0001\}$  planes of calcite. The  $\{0001\}$  plane has two terminations, i.e. a  $\text{Ca}^{2+}$  termination and a  $\text{CO}_3^{2-}$  termination.

## 1.2 Incorporation of impurities in calcium carbonate

### 1.2.1 Heavy metals in nature

The incorporation of impurities into calcite in natural water is of interest to a variety of geochemistry and environmental applications. Some heavy metals, such as Cd, Mn, Cu, Pb and Ni, are toxic to human health when they are present in high concentrations in water (Nriagu, 1980, 1981; Alloway, 1995; Järup, 2003). In the natural aquatic environment, the toxic metals usually come from soil and rocks through weathering and microbial activity. Some heavy metals are also produced by human activities from industrial and agricultural wastes, which then contaminate the groundwater.

Calcite is an abundant carbonate mineral in sedimentary terrains, since the dissolution and precipitation of calcite occurs quickly relative to most natural flow rates. Calcite is not a closed system under standard conditions; it can absorb ions originating from fluid inclusions when groundwater is in contact with calcite during their flow paths in sedimentary terrains (Stipp *et al.*, 1998). Therefore calcite is usually used as a perfect sorbent to decrease the concentration of heavy metals in the groundwater.

During this process, calcite can take up the dissolved ions via a dissolution-recrystallization process to form stable carbonate phases. Some divalent cations, such as  $Mg^{2+}$ ,  $Ni^{2+}$ ,  $Fe^{2+}$ ,  $Co^{2+}$ ,  $Zn^{2+}$ ,  $Cd^{2+}$  and  $Mn^{2+}$ , are smaller than  $Ca^{2+}$  and hence are energetically favoured to become part of the rhombohedral (calcite) polymorph, while bigger cations such as  $Sr^{2+}$ ,  $Pb^{2+}$  and  $Ba^{2+}$  are included in the orthorhombic (aragonite) polymorph. The explanation for this behaviour concerns the coordination numbers of  $Ca^{2+}$ . The coordination numbers of  $Ca^{2+}$  in calcite and

aragonite are six and nine, respectively. This would lead us to expect that the calcite arrangement (less dense packing of atoms) would be preferred where the ionic radius is fairly small, and that the aragonite arrangement (more densely packed atoms) would be preferred where the ionic radius is fairly large. The maximum solubility of heavy metals in  $\text{CaCO}_3$  is mostly controlled by their reaction with relevant sorbent. Understanding this incorporation process of heavy metals that occurs in nature could greatly reduce the environmental pollution.

### 1.2.2 Carbonate solid solutions

The incorporation of impurity ions in calcite has been found to be a process of sorption, which is the change of mass of a chemical in the solid phase as a result of mass transfer between fluid and solid. It includes three steps: (i) true adsorption on the surface; (ii) absorption or diffusion into the bulk, and (iii) surface precipitation to form an adherent phase that may consist of chemical species derived from both the aqueous solution and dissolution of the solid (Prieto *et al.*, 2003). Studies of the sorption rate of dissolved metals with calcite have consistently observed a rapid initial removal from the solution followed by a much slower uptake. The fast initial removal is frequently interpreted as being the result of chemisorption, whereas the following slow uptake is assumed to present surface precipitation or coprecipitation.

A solid solution occurs when the impurity ions partition into calcite and substitute  $\text{Ca}^{2+}$  in the lattice during deposition, forming a single crystal phase. Such solid solution partitioning is favoured in many geologic environments both at the high temperatures and ambient temperatures. For example, a  $\text{MnCO}_3$ - $\text{CaCO}_3$  solid solution is formed when  $\text{Mn}^{2+}$  ( $r = 0.83 \text{ \AA}$ ) substitutes  $\text{Ca}^{2+}$  ( $r = 1.00 \text{ \AA}$ ) in calcite. This solid solution can be presented as  $\text{Mn}_x\text{Ca}_{1-x}\text{CO}_3$ , where  $x$  is the fraction of metal

ion sites occupied by  $\text{Mn}^{2+}$ . The natural  $(\text{Mn,Ca})\text{CO}_3$  solid solution, namely manganocalcite, is widely distributed around the world. Its colour becomes redder with a higher proportion of manganese, as illustrated in Figure 1.4.

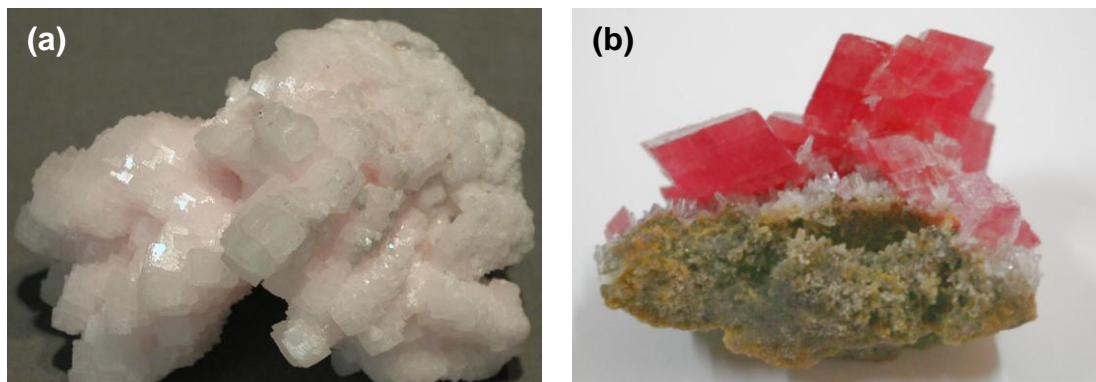


**Figure 1.4:** Photographs of crystals of (a) manganocalcite ( $\text{Mn}_x\text{Ca}_{1-x}\text{CO}_3$ ) from Yunnan, China and (b) rhodochrosite ( $\text{MnCO}_3$ ) from Chihuahua, Mexico.

Although some divalent cations can fully substitute for  $\text{Ca}^{2+}$  in calcite to retain the equivalent rhombohedral structure, only magnesite ( $\text{MgCO}_3$ ), rhodochrosite ( $\text{MnCO}_3$ ), siderite ( $\text{FeCO}_3$ ) and dolomite ( $\text{Ca}_{0.5}\text{Mg}_{0.5}\text{CO}_3$ ) typically occur in nature. Their structure is also comprised of alternating metal cation layers and planar  $\text{CO}_3^{2-}$  group layers normal to the  $c$ -axis. Some rhombohedral carbonates can occur with significant solid solutions in nature, but pure end members are only produced synthetically. For example, the transition metal carbonates  $\text{CdCO}_3$ ,  $\text{ZnCO}_3$ ,  $\text{CoCO}_3$ , and  $\text{NiCO}_3$ . Divalent cations with ionic radius larger than  $\text{Ca}^{2+}$  usually prefer the orthorhombic structure, for example the naturally occurring compounds strontianite ( $\text{SrCO}_3$ ) and witherite ( $\text{BaCO}_3$ ). The solubility of cationic impurities in calcite is generally controlled by the thermodynamics and reaction kinetics of the incorporation of the impurities into calcite (Zachara *et al.*, 1991; Stipp *et al.*, 1998). Experimental and computational techniques are being developed to gain a full understanding of the incorporation of cationic impurities into calcite.

### 1.2.3 Experimental studies of carbonate solid solutions

A large number of publications have been concerned with carbonate solid solutions. In most experiments, mechanical mixtures of specific carbonates and pure calcite are used. The synthesized intermediate samples are then characterized by various experimental techniques, such as X-ray photoelectron spectroscopy (XPS) (Stipp *et al.*, 1992), X-ray diffraction (XRD) (Capobianco and Navrotsky, 1987; Fenter *et al.*, 2000; Lee *et al.*, 2002; Katsikopoulos *et al.*, 2009), Low energy electron diffraction (LEED) (Stipp *et al.*, 1992) and atomic force microscopy (AFM) (Hausner *et al.*, 2006; Stack and Grantham, 2010), in an attempt to determine the composition, structure and *in situ* surface analysis. XPS uses X-rays of known wavelength to eject the electrons from the core and valence levels of atoms in the near surface of a solid. An element in a monolayer on the surface may be visible whereas the same amount of materials somewhere in the near-surface may not (Stipp *et al.*, 1992). The X-ray diffraction techniques can detect clear ordering patterns in mixed compounds; however, they are not well suited to assess the level of disorder in poorly ordered samples. LEED patterns can be used to determine atomic order in the top-most layers in a solid and have been used to determine the size and shape of the surface (for more details, see Hochella *et al.*, 1990). Although the technique of AFM can provide spectacular imagery of equilibrium and growing surfaces of calcite in the presence or absence of different impurities, AFM is limited in that it does not provide compositional information, does not see below the surface, and has relatively poor atomic scale resolution (Chiarello *et al.*, 1997). On the other hand, *in situ* measurement synchrotron X-ray scattering can give exact information of the structure at the atomic scale, microtopography and composition of single crystal mineral-water interfaces (Gratz *et al.*, 1993; Chiarello *et al.*, 1997; Teng *et al.*, 1998; Brown *et al.*, 1999).

In spite of the rapid development of the experimental techniques, the thermodynamic properties of the carbonate solid solutions from experiments are still difficult to determine, because it usually involves a three-phase system: a carbonate solid, a solution and CO<sub>2</sub> gas (Rock *et al.*, 1994; McBeath *et al.*, 1998). Several aspects must be considered in advance of any interpretation of the experimental results: (i) the complete series precipitated at ambient temperatures do not prove complete miscibility. Under some conditions, the slow rate of solid state diffusion and the presence of high activation energy barriers may kinetically impede the precipitated solids from unmixing (Katsikopoulos *et al.*, 2009); (ii) the presence or absence of compositional and structural heterogeneities must be clarified; (iii) unmixing and ordering are not necessarily incompatible. Some solid solutions tend to both order and unmix in the same system, and the two processes cannot be regarded as mutually exclusive (Carpenter, 1980; Putnis, 1992). When cooling such kinds of solid solutions, both exsolution and ordering are possible and the final structure is determined by the relative kinetics of the two processes under the cooling conditions. For example, the dolomite-type intermediate Cd<sub>0.5</sub>Mg<sub>0.5</sub>CO<sub>3</sub> solid solution is thermodynamically stable with the negative enthalpy of formation. Meanwhile, the enthalpy of mixing is positive (Katsikopoulos *et al.*, 2009).

The factors controlling cations sorption and adsorption selectivity on calcite are not fully understood, because individual investigators have studied single metal sorbates. Comparisons between these studies are difficult because of the use of different calcite sorbates, electrolyte solutions, and experimental procedures, all of which can exert a strong influence on the reactions responsible (adsorption, diffusion and precipitation) for cation sorption to calcite. Thus, trends have not been established between sorption behaviours, sorbate properties, and the solution composition that could be used to determine the sorption mechanism and the

chemical basis for surface selectivity. The development of computational theory, such as the distribution coefficient model (Tesoriero, 1996) and its application to this problem was an important milestone. These methods provided a scheme for predicting carbonate assembly, but since this model does not explicitly characterize the microscopic growth unit, predicting how inhibitors interfere with the terraces, ledges and kinks is not purely intuitive.

#### **1.2.4 Theoretical studies of carbonate solid solutions**

Knowledge of the thermodynamic properties of cationic impurities in carbonate minerals are necessary to evaluate order and disorder relations, deformation and crystal growth, but slow transport rates and decomposition of carbonate phases at high temperatures limit further experimental investigations. The application of computer modelling in the geological and materials sciences can demonstrate the mechanisms on an atomistic scale and extend the capability to evaluate materials properties to the regime, where direct experimental measurements are difficult or impossible to perform. Computer simulations do not replace the role of experimental measurements, but provide a solid framework for evaluating mechanisms and properties under conditions which are not accessible to the experiments.

The computational simulations can roughly be divided into two techniques. Firstly, atomistic simulations based on the description of interatomic forces by pair potential functions, the accuracy of which dictates the quality of the simulation results (Voter, 1996). These methods are often used for materials, for which at least some experimental properties, such as lattice structure, elastic constants and bulk modulus, are already known. Secondly, density functional theory (DFT), which is a quantum mechanical modelling method used in physics and chemistry to investigate

the electronic structure of many-body systems. With this method, the properties of a many-electron system can be determined by using the wave functions. DFT is one of the most popular and versatile methods in condensed-matter physics and computational chemistry (Vitek, 1996).

Although the developing quantum mechanical calculation methods in recent years can provide highly accurate results of the electronic structure of a many-body system; in some cases, the details of electronic structure are less important than the long-time phase space behavior of large molecule systems, e.g. the thermodynamic and kinetic properties, which can be modelled successfully by atomistic simulations while avoiding quantum mechanical calculations entirely.

Atomistic simulation techniques are widely used to investigate the complex minerals at atomic level and can be extended to include the full range of impurity proportions to evaluate thermodynamic properties at some temperatures. Many computational investigations have been carried out on calcite bulk and surfaces. Parker *et al.* (1993) used an atomistic model for calcite to study surface precipitation and dissolution processes. De Leeuw *et al.* (1999, 2000 and 2002) have completed a series of simulation studies of calcite surfaces based on the carbonate potential of Pavese *et al.* (1996). Noteworthy in this work is the incorporation of an adsorbed water layer onto the calcite surfaces, leading a more realistic model of the calcite surfaces. The dominant  $\{1\ 0\ \bar{1}\ 4\}$  cleavage surface of calcite remains the most stable surface in both vacuum and aqueous environment. Various theoretical investigations of the structures and physical properties of calcite-like carbonates have also been published (Catti and Pavese, 1997; Cygan, 2000; Dove *et al.*, 1992; Fidler *et al.*, 2000; Austen, 2005). Their works focused on parameterization for a series of carbonates; extensive testing of both rigid ion and shell models of the lattice; and calculating properties, such as elastic and optical properties. These studies on

calcite-like carbonates demonstrate the importance of atomic simulations in providing a theoretical description of complex surface processes for carbonates, and how the theoretical models assist the experimentalist in evaluating competing models to understand mechanisms and explain experimental observations.

Nowadays the approaches to model the solid solutions rely on the assumption that the thermodynamics effects of mixing and ordering can be predicted by investigating the enthalpy of sufficiently supercell structures with differently arranged exchangeable atoms. To reflect the properties of an infinite large system, the supercell should be adequately large, bringing a huge number of possible configurations. It is difficult to perform a direct study of the complete configurations for a large supercell even if interatomic potential methods are employed. Several approaches have been developed to treat these large numbers of configurations. For example, the thermodynamics of the (Mn,Ca)CO<sub>3</sub> system (and also of the tertiary system including Mg besides Ca and Mn) have been discussed in recent papers by Vinograd *et al.* (2009 and 2010), where a simplified pair-wise interaction model is employed to perform Monte Carlo (MC) simulations in a very large supercell (12 × 12 × 3) of the structure, allowing full convergence of the calculations with respect to cell size. Another different approach, which reduces the number of site occupancy configurations to be calculated when modelling site disorder in solids, by taking advantage of the crystal symmetry of the lattice (Grau-Crespo *et al.*, 2007), has been applied in this thesis. Within this approach, only a series of inequivalent configurations are to be considered to model the cationic disorder in binary carbonate solid solutions. Although this approach cannot afford a large supercell size, but instead allows us to obtain explicitly the energy of each configuration, using a physically meaningful interaction model and including relaxation effects. Details of this approach are described in Chapter 4.

## 1.3 The growth and dissolution of calcium carbonate

When the concentration of  $\text{CaCO}_3$  in natural water exceeds the saturation level, precipitation/crystallisation of  $\text{CaCO}_3$  occurs. The growth and dissolution of  $\text{CaCO}_3$  from supersaturated solutions have been studied for many years, as it represents an important role in geochemical, biological and industrial fields. The organisms control the growth of  $\text{CaCO}_3$  crystals for strengthening their structures and functionality (Belcher *et al.*, 1996; Meldrum, 2003). For many technological applications a precise control over the particle size, morphology and specific surface area during precipitation and dissolution would be highly desirable (Aschauer *et al.*, 2010).

### 1.3.1 Nucleation and growth of calcium carbonate

In contrast with many other crystals, the rate of formation of  $\text{CaCO}_3$  in solution is fast and increases with temperature. A considerable number of experimental and computational studies have investigated the nucleation of  $\text{CaCO}_3$  in different solutions and found this nucleation is far more complicated than the classical nucleation theory (Coelfen and Mann, 2003; Rieger *et al.*, 2007), which assumes there is an activation barrier to form an initial crystalline nucleus followed by a step-by-step addition of further atoms (Mullin, 1992). Recent experimental works (Gebauer *et al.*, 2008; Pouget *et al.*, 2009) have suggested that the nucleation pathway of  $\text{CaCO}_3$  depends on the  $\text{Ca}^{2+}/\text{CO}_3^{2-}$  supersaturation.

Many experimental studies have found that small clusters of  $\text{CaCO}_3$  play a role in the pre-nucleation of calcite in highly supersaturated  $\text{Ca}^{2+}/\text{CO}_3^{2-}$  solutions. For example, Ogino *et al.* (1987) have shown that amorphous  $\text{CaCO}_3$  particles precipitate rapidly but convert to a mixture of all three dehydrated phases in the order of a few

minutes before being converted eventually to crystalline calcite. Subsequent investigations have shown that the amorphous particles, which are formed firstly, are strongly hydrated (Rieger *et al.*, 1997; Bolze *et al.*, 2002). Recently, investigations using TEM, SEM, and *in situ* WAXS (Rieger *et al.*, 1997; Wolf, 2008) have examined the growth of CaCO<sub>3</sub> in highly supersaturated solutions. Again, an initial amorphous, hydrated precursor phase is observed, which quickly converts to a mixture of both calcite and vaterite particles. One possible explanation is that the amorphous CaCO<sub>3</sub> particle has a lower surface energy than calcite nanoparticle, and hence a much lower nucleation barrier (Kerisit *et al.*, 2005).

The study of CaCO<sub>3</sub> precipitation from solution and growth by computer simulation is hampered because simulations of large numbers of atoms over long time-scales are required. Recently, two important developments have allowed simulation techniques to be applied to the study of nucleation and growth of CaCO<sub>3</sub>. The first is the process from experimental techniques in understanding the relationship between the CaCO<sub>3</sub> structure and its morphology, which can provide high quality results to compare with simulations. The second development is the considerable increase in the computational resources which make the modelling of complex systems possible, especially in the investigation of the material structures and the thermodynamic properties of complex phases. For example, a simulation (Martin *et al.*, 2006) starting from small nanoparticles ( $d = 1.6$  nm, 18 CaCO<sub>3</sub> units) of amorphous CaCO<sub>3</sub> in water has shown that these nanoparticles agglomerate to form larger amorphous particles. A recent study (Lamoureux *et al.*, 2008) used metadynamics to explore the conformational space available to an amorphous CaCO<sub>3</sub> nanoparticle containing 75 CaCO<sub>3</sub> units. Molecular dynamics (MD) simulations of CaCO<sub>3</sub> precipitation in water by Tribello *et al.* (2009) support that the first step in the mineralisation is the homogeneous nucleation of amorphous particles, which present

a transient precursor phase of more stable crystalline polymorphs like calcite.

On the contrary, at lower  $\text{Ca}^{2+}/\text{CO}_3^{2-}$  supersaturation, the diffusion controlled growth of amorphous  $\text{CaCO}_3$  particles is slowed and there is sufficient time for the small clusters to rearrange to a structure that more resemble calcite. Recent experiments have observed calcite crystals very early in the reaction mixture at low supersaturation (Gebauer *et al.*, 2008; Pouget *et al.*, 2009).



**Figure 1.5:** Growth morphology of calcite as a function of the  $\text{Ca}^{2+}/\text{CO}_3^{2-}$  ratio. (a) At low  $\text{Ca}^{2+}/\text{CO}_3^{2-}$  ratio, the obtuse steps do not advance. Both step orientations have a high kink density, as evidenced by their roughness. (b) At intermediate ratios, both obtuse and acute step orientations are straight and advance. (c) At high ratios, the obtuse step orientation continues to grow, whereas the acute step has become pinned and etch-pits are observed, (Stack and Grantham, 2010).

When the calcite nanoparticles are stable in solution, the growth of  $\text{CaCO}_3$  is found to occur through steps (Gratz *et al.*, 1993) and dislocations (Hiller *et al.*, 1993), often in monolayer from the step as observed by Liang *et al.* (1996) in their AFM study of the calcite  $\{1\ 0\ \bar{1}\ 4\}$  surface under aqueous conditions. Gratz *et al.* (1993) studied calcite growth at two monomolecular steps by *in situ* AFM techniques and found the growth velocity of calcite at the obtuse step is 1.5 - 2.25 times of that at the acute step depending on the supersaturation. A theoretical study of calcite growth by

de Leeuw *et al.* (2002) also established that the activation energy required to create the first kink site at the acute step is 1.5 times of that at the obtuse step. Furthermore, the growth rates of monolayer steps on the  $\{1\ 0\ \bar{1}\ 4\}$  plane have been measured as a function of the aqueous  $\text{Ca}^{2+}/\text{CO}_3^{2-}$  ratio by Stack and Grantham (2010). They found that the response of obtuse and acute steps to the  $\text{Ca}^{2+}/\text{CO}_3^{2-}$  ratio is variable, and the growth rates will be a maximum at a  $\text{Ca}^{2+}/\text{CO}_3^{2-}$  ratio of 1:1. The growth of  $\text{CaCO}_3$  becomes kinetically inhibited and dissolution features are observed at high ratios. AFM images of this process are shown in Figure 1.5.

### 1.3.2 Dissolution of calcite

The dissolution of calcite has been the subject of various experimental and computational modelling studies. The understanding of this process would shed light on a system, where calcite is an unwanted nuisance. For example, limescale, which has a main component of calcite, precipitates out from the hot water in heating devices. Hard water contains calcium bicarbonate ( $\text{Ca}(\text{HCO}_3)_2$ ) and similar salts.  $\text{Ca}(\text{HCO}_3)_2$  is soluble in water, but the soluble bicarbonate converts to poorly-soluble carbonate at temperatures above 70 °C, leading to deposit of calcite in places where water is heated. Accruing limescale can impair heat transfer and damage the heating element. Limescale can also be found on old pipes where hard water has been continually running through and has deposited calcite. This can build up and reduce water flow, eventually block the water pipes.

Experimental studies have examined the dissolution of calcite under aqueous environment using AFM techniques (Stipp *et al.*, 1994; Liang and Baer, 1997). Shallow pits were observed during the initial dissolution stage with a depth of 3 or 6 Å, the approximate depth of one or two layers of calcite. Observation of the deep pits

clearly indicated the presence of two different types of steps, namely acute and obtuse steps, which retreated at different velocities, with the obtuse step retreating 2.3 times faster than the acute step.

The dissolution process of calcite has also been investigated by MD simulations. It is found that the energy barrier to dissolution at both steps and for both ions were considerably less than for dissolving the ions directly from a flat surface. Dissolving a  $\text{CO}_3^{2-}$  group from a step was found to be more energetically favourable than a  $\text{Ca}^{2+}$  ion (Kerisit and Parker, 2004; Spagnoli *et al.*, 2006).

Another study of MD simulations by de Leeuw *et al.* (1999) also looked at the dissolution of  $\text{CaCO}_3$  units from the acute stepped  $\{3\ 1\ \bar{4}\ 8\}$  surface and obtuse stepped  $\{3\ \bar{1}\ \bar{2}\ 16\}$  surface. The results showed that the formation of the double kinks on the obtuse step cost less energy than dissolution from the acute step, probably due to the lower stability of the obtuse surface. This simulation also suggested that formation of the kink sites on the dissolving edge of the obtuse step of calcite is the rate determining step and this edge is predicted to dissolve preferentially, which is in agreement with experimental findings of calcite dissolution under aqueous conditions.

## 1.4 Aggregation of calcite nanoparticles

Calcite particles on the micro-scale (i.e. nanoparticles) have gained increasing attention due to their fundamental role in calcite crystal growth, where the controlled growth of calcite can lead to the formation of materials with different morphologies (Colfen, 2003; Domingo, 2004).

The aggregation of calcite nanoparticles, which is a common phenomenon in the

synthesis, has primarily been studied experimentally by electron microscopy and kinetic analysis, for example scanning electron microscopy (SEM) and transmission electron microscopy (TEM), as shown in Figure 1.6 (Söhnel and Mullin, 1982; Tohda *et al.* 1994; Collier *et al.* 2000). When investigating the alignment between calcite particles in crystalline aggregates at low ionic solution using SEM and TEM, Collier *et al.* (2000) found that about 40% of the samples are in perfect alignment. They proposed that the alignment is induced by an ability of the crystallites to re-align into a more favourable energy state before they are fixed into place. Liew *et al.* (2003) confirmed that the rate of aggregation between crystals in a supersaturated solution depended on the rate of collision, as well as the probability of that collision surviving, which suggested that the probability depends on the strength of the newly formed neck between the crystals and the hydrodynamic force acting to pull them apart. Other authors (Rieger *et al.* 2007; Wolf *et al.* 2008) have pointed out that the adhesion of small clusters of  $\text{CaCO}_3$  onto the large surface plays a key role in the initial stages of  $\text{CaCO}_3$  growth. However, quantitative information on the driving forces that leads to the aggregation of nanoparticles is sparse.

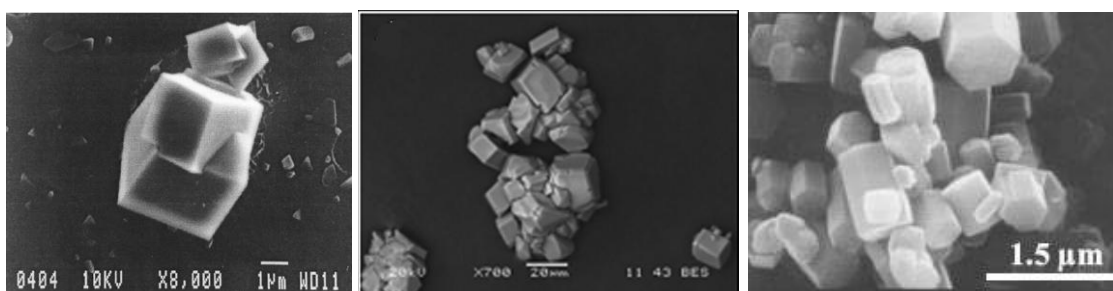


**Figure 1.6:** SEM images of micro-sized aggregated  $\text{CaCO}_3$  particles, (Collier *et al.*, 2000).

Computational studies have been used extensively to study nanoparticles in a wide variety of situations, including modelling the stability, crystal nucleation and the interaction with water (Sayle *et al.*, 2004; Kerist *et al.*, 2005; Feng *et al.*, 2006).

The structures and stabilities of a single nanoparticle (e.g. ZnS or TiO<sub>2</sub> nanoparticle), are dependent upon environment conditions (Zhang and Banfield, 2004; Koparde and Cummings, 2005). Huang *et al.* (2004) were one of the first to show that the MD simulations can be used to describe aggregation of nanoparticles and predict experimentally observed phase driven by aggregation. Kerisit *et al.* (2005) used MD simulations to study the stability of calcite nanoparticles of different sizes, both in vacuum and aqueous environment. Their work revealed that the water molecules in the first hydration layer complete the coordination shell of the surface ions, preserving structural order even in the smallest of the nanoparticles ( $d = 1.0$  nm). Close to the particle surface, the structure of the water itself shows features similar to those on planar  $\{10\bar{1}4\}$  surfaces, although the molecules are far less tightly bound. Spagnoli *et al.* (2008) carried out MD simulations to calculate the free energy change of aggregation of MgO and calcite nanoparticles. Their calculations indicated that there was a free energy barrier to aggregation and the aggregation can occur as the result of fluctuations in orientation where different orientations may drive the crystal growth via oriented aggregation.

Even though much progress have been made toward a fundamental understanding of the aggregation process of calcite nanoparticles, many important questions remain, including the mechanisms of aggregation of nanoparticles, which is where computer modelling at the atomic level will be able to provide detailed information.

## 1.5 Aims and overview of the thesis

In view of the importance of  $\text{CaCO}_3$  in geochemical, biological and industrial processes, a range of computer simulation techniques have been employed to perform a comprehensive and quantitative study of  $\text{CaCO}_3$ , where the focus is split into two parts, namely the cationic impurity incorporation in calcite and the aggregation of calcite nanoparticles. The main objectives of the thesis are as follow:

(i) To provide thermodynamic and structural details of the complete solid solutions of calcite with a series of divalent cations.

(ii) To establish the key factors that affect the interaction of a  $\text{CaCO}_3$  nanoparticle and major calcite surfaces at the atomic level.

(iii) To gain insight into the structure and stability of the calcite tilt grain boundaries and further explore the growth of newly-formed joints during the aggregation process of calcite particles.

Chapter 2 will introduce the computational methods used in this thesis to explore the calcium carbonate system. Both molecular mechanics and molecular dynamics will be discussed in this section. Chapter 3 will present a summary of the potential model functions and parameters used in this study, including a new set of potential parameters for some divalent cations, which were derived with existing calcite potential model.

In Chapter 4 atomistic simulation techniques have been applied to investigate the mixing thermodynamics of calcite with a series of divalent cations, where results are compared to available experimental data. In Chapter 5, molecular mechanics simulations of the interaction between calcite nanoparticles and calcite surfaces will

be discussed. The adhesion energy and optimized geometries of the nanoparticle on major surfaces in vacuum and aqueous environment will be investigated. Chapter 6 will introduce molecular dynamic simulations performed on calcite tilt grain boundaries. The growth of a series of  $\text{CaCO}_3$  units at contact points between two colliding nanoparticles in aqueous environment is explored.

Finally, Chapter 7 will summarise the findings of this study and draw conclusions about impurity incorporation in calcite and the aggregation of calcite nanoparticles, based on the results presented in this thesis.

# 2

## Computational Methodology

---

Molecular mechanics is one common method applied in computational simulations, calculating the potential energy of any arrangement of atoms or molecules in the material system by a potential function or force field. Molecular dynamics is another specialised discipline of computer simulations based on classic Newton's law of motion, allowing insight into the molecular motion on an atomic scale. This chapter gives a brief description of these computational methodologies used in this thesis and the analysis of the results of these simulations. Finally, some key components of the simulation codes applied in this thesis are also presented.

## 2.1 Molecular mechanics

Molecular mechanics (MM) was first used in the 1970s to describe the application of classical mechanics to model small molecules or large material assemblies with more than thousands of atoms. In MM each atom is treated as a single ball, assigned a radius, polarisability and a constant charge. Bonded interactions are treated as “springs” with an equilibrium distance equal to the experimental or calculated bond length (Andrews, 1930). The potential energy of the system is then made up of the electrostatic interactions and the short range interactions, such as the Van der Waals attractions and repulsions. These interactions are calculated using force fields, which are described in Chapter 3. One representative application of MM is energy minimisation, where the force field is used as an optimisation criterion and the local minimum is searched by an appropriate algorithm.

### 2.1.1 Potential energy surface

The potential energy of some molecules or large material assembly is a complicated and multi-dimensional function of the atomic coordinates. Changes of the potential energy of a system with the coordinates can be represented as movement on a curve or multidimensional surface, which is called a potential energy surface (PES). The visualization of a two dimensional PES would be like a landscape, where  $X$  and  $Y$  directions are equivalent to two geometrical parameters of the system and  $Z$ , the height of the land, would be the energy associated with a given value of variables. Especially interesting points on the PES in MM are the stationary points, where the first derivative of the energy with respect to the atomic coordinates is zero. A minimum point will be one type of stationary points. The minimum with the

lowest energy on the whole PES is the global energy minimum, whereas other minima with higher energies are local energy minima (Figure 2.1). At the global energy minimum, the arrangement of the atoms corresponds to the stable state of the system and any movement away from a minimum gives a configuration with a higher energy, while the local minima may represent metastable phases.

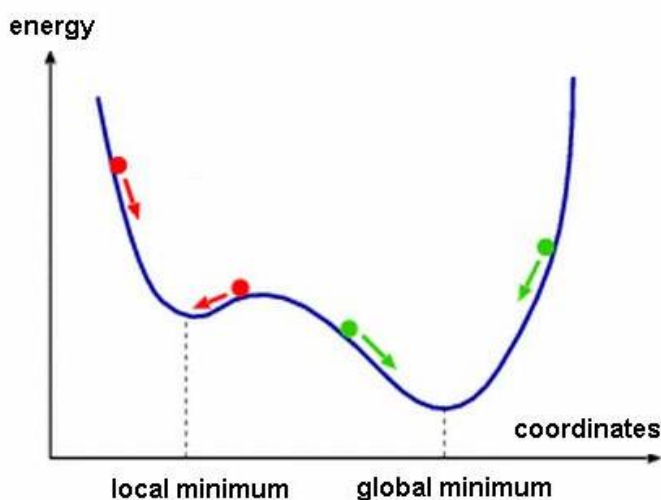


**Figure 2.1:** Local minimum and global minimum on a potential energy surface.

### 2.1.2 Energy minimisation algorithm

Energy minimisation, which is also called energy optimisation, is simply used to find the local energy minimum of a system by iteratively adjusting the coordinates of the atoms in the system. Starting from a non-equilibrium configuration, energy minimisation employs the mathematical procedure of optimisation to move atoms so as to reduce the net forces (the gradients of potential energy) on the atoms until they become zero and the second derivatives are positive:

$$\frac{\partial U}{\partial r} = 0; \quad \frac{\partial^2 U}{\partial r^2} > 0. \quad (2.1)$$

where  $U$  is the internal energy of a system and  $r$  is the coordinate of the system (the

Cartesian or internal coordinates). The term zero force is used since the first derivative of the internal energy with respect to distance is force. If the internal energy of a system with coordinates  $r$ , is  $U(r)$ , then the internal energy at a new set of coordinates  $r + dr$ , is:

$$U(r + dr) = U(r) + \frac{\partial U}{\partial r} dr + \frac{1}{2} \frac{\partial^2 U}{\partial r^2} (dr)^2 + \dots \quad (2.2)$$

The first derivative can be collectively written as the gradient vector  $\mathbf{g}$  and the second derivative matrix is referred to as the Hessian matrix  $H$ .

Derivatives are useful in energy minimisation as they provide information about the shape of the PES and significantly enhance the efficiency with where the minimum is located. The direction of the gradient vector  $\mathbf{g}$  indicates where the energy minimum lies and the magnitude indicates the steepness of the local slope. The second derivative indicates the curvature of the function, predicting where the function will change direction. The gradient-based algorithms are the most popular methods for energy minimisation, and they can be classified according to the highest-order derivative used. For example, first-order algorithms use the first derivative and second-order algorithms use both first and second derivatives.

To find an energy minimum by first-order algorithms, the gradient vector  $\mathbf{g}$  is used to determine the direction of movement and a line search is used to determine the magnitude of the step length. In Steepest-Descent algorithm, this process is then repeated until convergence. However, a disadvantage of this method is that many small steps may be performed when proceeding down a long narrow valley. The Steepest-Decent algorithm is forced to make a right angled turn at each point, even though that might not be the best route to the energy minimum. Conjugate-Gradients algorithm is far more efficient, where subsequent steps are made orthogonal to the

previous search vectors. For a quadratic energy surface, this will converge to the minimum in a number of steps equal to the number of variables.

If we use the second-order algorithms, for example Newton-Raphson algorithm, then the displacement vector  $\Delta r$ , from the current position to the minimum is given by the equation:

$$\Delta r = -H^{-1}g \quad (2.3)$$

For a realistic energy surface, equation 2.3 becomes increasingly approximate when the starting position is far away from the minimum and there is the possibility that we achieve some other stationary point, such as a transition state. Consequently, the expression is modified to be:

$$\Delta r = -\lambda H^{-1}g \quad (2.4)$$

where  $\lambda$  is a scalar quantity determined by performing a line search along the search direction to find the one-dimensional minimum and the procedure becomes iterative again, as per conjugate gradients. The key step of Newton-Raphson algorithm is the inversion of the Hessian matrix  $H$  in large system, which may vary slowly from one step to the next. It is therefore wasteful and undesirable to invert this matrix in every step of the optimisation. This can be avoided by using the Quasi-Newton method, where the Hessian matrix  $H$  does not need to be computed and is updated by analyzing successive gradient vectors instead. One of the most widely employed Quasi-Newton methods is the BFGS method (suggested independently by Broyden, Fletcher, Goldfarb and Shanno in 1970). The Hessian matrix  $H$  is initialized by performing an exact inversion of the second derivatives and is then subsequently updated for a number of cycles.

The most appropriate algorithm or combination of algorithms for a given problem depends on the size of the system, number of variables and the memory requirement. Most minimisation algorithms can go downhill or uphill on the PES and locate the minimum or maximum, respectively, that is near to the starting point, which is likely to be a local energy minimum, thus we require a means of generating different starting points to locate more than one local minimum. In this thesis, a combination of Conjugate-Gradients and Newton-Raphson algorithms is used during the energy minimisation.

### 2.1.3 Static lattice optimisation

The static lattice energy of a crystal,  $U_L$ , is defined as the energy released when different gaseous ions making up the crystal are brought to their lattice positions. The lattice energy may also be defined as the energy required to completely separate one mole of a solid ionic compound into gaseous ionic constituents. The lattice energy of the simulated crystal will be at a minimum when the ionic distances exactly match the observed crystal structure. In practice the lattice is always relaxed until it reaches a minimum energy configuration, even though there may be some error from the observed structure. In a constant pressure minimisation, the lattice is minimised with respect to both atomic coordinates and the bulk strains acting upon the cell dimensions.

The system can be minimised by iteratively adjusting the atomic coordinates until the forces on the atoms are zero in equation 2.1. The lattice energy of the new set of coordinates  $\mathbf{r}'$  is related to the old coordinates  $\mathbf{r}$  by the second-order expansion: (Catlow and Macrodt, 1982)

$$U_L(\mathbf{r}') = U_L(\mathbf{r}) + \mathbf{g}^T \boldsymbol{\delta} + \frac{1}{2} (\boldsymbol{\delta}^T \cdot \mathbf{H} \cdot \boldsymbol{\delta}) \quad (2.5)$$

where  $\mathbf{g}^T$  is the transpose of the vector  $\mathbf{g}$  and  $\delta$  is a generalized strain vector with  $3N$  orthogonal displacement components  $d\mathbf{r}$  and six bulk strain components  $d\boldsymbol{\varepsilon}$ . The vector  $\mathbf{g}$  corresponds to the first derivative of the lattice energy with respect to the atomic displacements and bulk strains, and vector  $H$  is the Hessian matrix:

$$\mathbf{g} = \left( \frac{\partial U_L}{\partial \mathbf{r}}, \frac{\partial U_L}{\partial \boldsymbol{\varepsilon}} \right), \quad (2.6)$$

$$H = \begin{pmatrix} \frac{\partial^2 U_L}{\partial \mathbf{r}^2} & \frac{\partial^2 U_L}{\partial \mathbf{r} \partial \boldsymbol{\varepsilon}} \\ \frac{\partial^2 U_L}{\partial \boldsymbol{\varepsilon} \partial \mathbf{r}} & \frac{\partial^2 U_L}{\partial \boldsymbol{\varepsilon}^2} \end{pmatrix}. \quad (2.7)$$

The new coordinates  $\mathbf{r}'$  are related to the original coordinates  $\mathbf{r}$  by:

$$\mathbf{r}' = \Delta\boldsymbol{\varepsilon}(\mathbf{r} + d\mathbf{r}) \quad (2.8)$$

where  $\Delta\boldsymbol{\varepsilon}$  is the Voight matrix representation of the vector  $d\boldsymbol{\varepsilon}$ :

$$\Delta\boldsymbol{\varepsilon} = \begin{pmatrix} d\varepsilon_1 & \frac{1}{2}d\varepsilon_6 & \frac{1}{2}d\varepsilon_5 \\ \frac{1}{2}d\varepsilon_6 & d\varepsilon_2 & \frac{1}{2}d\varepsilon_4 \\ \frac{1}{2}d\varepsilon_5 & \frac{1}{2}d\varepsilon_4 & d\varepsilon_3 \end{pmatrix} \quad (2.9)$$

When minimising under constant pressure, the bulk strain must also be minimised by relaxing the cell vectors. The bulk strains are defined such that they transform each vector  $\mathbf{r}$  in the lattice to  $\mathbf{r}'$ , where

$$\mathbf{r}' = (\mathbf{I} + \boldsymbol{\varepsilon}) \cdot \mathbf{r} \quad (2.10)$$

where  $\mathbf{I}$  is known as the identity matrix and  $\boldsymbol{\varepsilon}$  is the strain matrix discussed previously. The strains are calculated assuming Hooke's Law, with a constant of

proportionality given by the elastic constant tensor. New positions and lattice vectors can then be calculated.

The computer code GULP (The General Utility Lattice Program) (Gale, 1997) was used in this thesis to optimise the lattice structures of calcite-type carbonates and obtain the bulk properties, such as lattice energy, elastic constants, bulk modulus and lattice vectors. All the optimisations were performed under constant pressure by the Conjugate-Gradients and Newton-Raphson algorithms. The optimised lattice structure was then used in the calculation of the thermodynamics of pure and doped carbonates.

#### **2.1.4 Surface simulations**

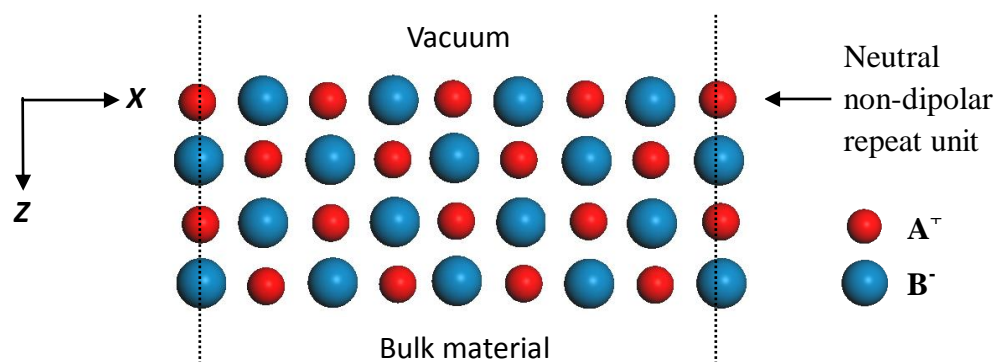
All surface simulations in this thesis have been carried out using the computer code METADISE (Minimum Energy Techniques Applied to Defects, Interfaces and Surface Energies) (Watson *et al.*, 1996), which is designed to model dislocations, interfaces and surfaces. Following the approach of Tasker (1979), the simulation model consists of a series of planes parallel to the surface and periodic in two dimensions. Tasker identified three different types of surfaces:

(I) Type I surface (Figure 2.2.a) comprises a stack of uncharged planes, where cations and anions are in stoichiometric ratio.

(II) Type II surface (Figure 2.2.b) comprises a stack of charged planes, but the repeat unit is charge-neutral and there is no net dipole perpendicular to the surface;

(III) Type III surface (Figure 2.3) consists of a stack of charged planes where the repeat unit has a dipole moment perpendicular to the surface.

(a) Type- I



(b) Type- II

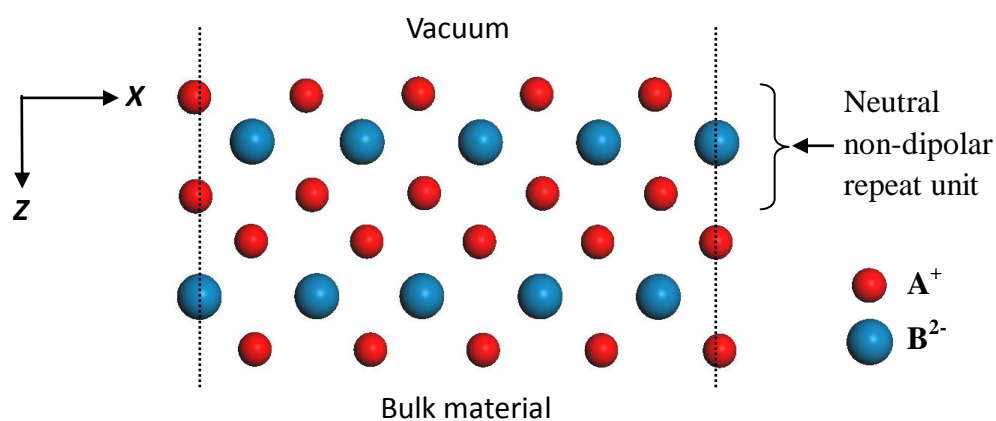


**Figure 2.2:** Side view of two types of surfaces as classified by Tasker. (a) Type I surface consisting of charge neutral layers, and (b) Type II surface consisting of positive and negative charged planes but with a charge neutral and non-dipolar repeat unit. The dashed line representatives the two dimensional periodicity.

When a dipole moment perpendicular to the surface is present (Type III surface), the surface energy diverges and is infinite (Bertaut, 1958). In this case, the surface needs to be reconstructed to remove the dipole, which is often achieved by removing half the ions from the surface layer at the top of the repeat unit and transferring them to the bottom (Figure 2.3). Following this method, the surface is partly vacant, either in cations or anions, and then the surface energy can be calculated.

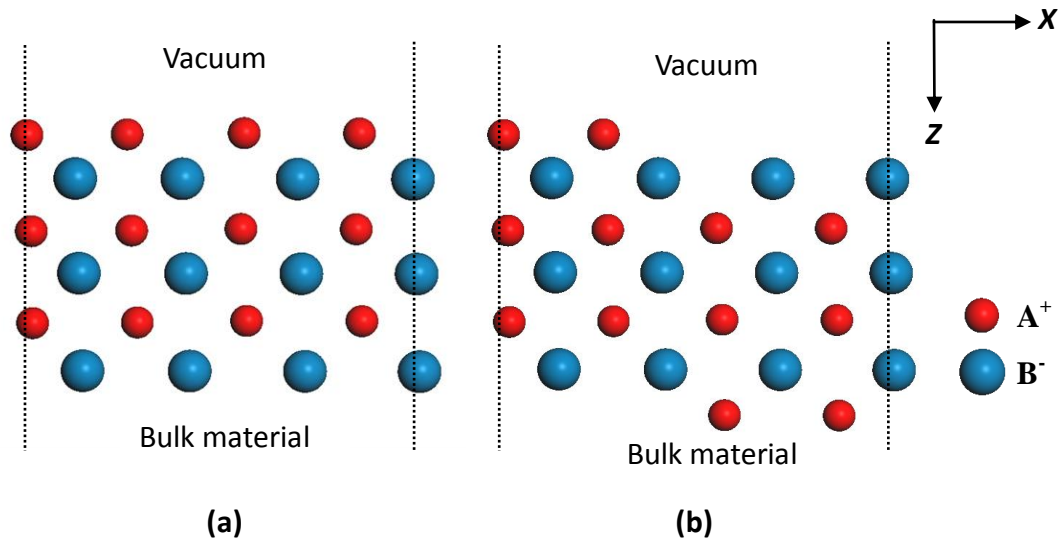


**Figure 2.3:** Stacking sequences showing (a) a Type III surface, consisting of alternating positive and negative ions giving rise to a dipolar repeat unit, and (b) a reconstructed Type III surface, where half the surface ions have been moved to the bottom of the surface in order to remove the net dipole. The dashed line represents the two dimensional periodicity.

When generating the surfaces, the crystal is divided into two blocks each comprising two regions, region I and region II, as shown in Figure 2.4. Region I contains those atoms near the surface, which are allowed to relax to their mechanical equilibrium, while region II contains those atoms further away, which represent the rest of the crystal and are kept fixed at their bulk equilibrium position. Inclusion of region II is necessary to ensure that the potential energies of atoms in region I are modelled correctly. Both region I and region II need to be sufficiently large for the potential energy to converge. The bulk of the crystal is modelled by the two blocks together while the surface is represented by a single block with the top of region I as the free surface. Interfaces such as stacking faults and grain boundaries can be studied by fitting two surface blocks together in different orientations.



adsorbing water one-by-one onto the surface with the most energetically favourable configuration used as the input for the adsorption of further water. Many experiments and computer simulations have indicated that water molecules organize into very ordered layers at the mineral-water interface. For example, Ghose *et al.* (2010) reported crystal truncation rod results of the hydrated goethite surface, showing the presence of adsorbed water layers above the surface. Spagnoli *et al.* (2011) studied MgO nanoparticles in a box of water using MD simulations, which indicated that water above the {100} faces mimics the flat surfaces of the nanoparticle and produces highly structured, ordered layers of water that extend to approximately 8 Å above the surface. Similar behaviour was also identified at MgO (de Leeuw and Parker, 1998) and  $\alpha$ -quartz surfaces (Du and de Leeuw, 2006), thus it is expected to be a general effect at ionic surfaces. The adsorbed water layers are shown to affect the structure and energy of the underlying surface, and this study therefore has considered several adsorbed water layers above the calcite surface (up to 8 Å above the surface). A full monolayer coverage, is meant that no more adsorbents can be adsorbed onto the surface without the formation of a second layer or adsorption becoming endothermic. The surface energy of the hydrated surface is defined by:

$$\gamma_{hydrated} = \frac{U_{hydrated} - nU_{water} - U_{bulk}}{A} \quad (2.12)$$

where  $U_{hydrated}$  is the energy of the surface with adsorbed water,  $U_{water}$  is the energy of a water molecule and  $n$  is the number of water molecules adsorbed to the surface. The energy of a water molecule is made up of two parts; its internal energy, which is the energy of an isolated gaseous molecule; and its solvation energy, which is the energy required to remove the molecule from its hydration shell in the aqueous solution.

### 2.1.5 Construction of CaCO<sub>3</sub> nanoparticles

The program METADISE was also used to construct the CaCO<sub>3</sub> nanoparticles from the relaxed bulk structure of calcite. The approach involves the use of Wulff construction methodology (1901), based on the surface energies of different two dimensional surfaces. For a crystal consisting of a given number of atoms, the equilibrium shape is that which minimizes the surface energy. In the three dimensional Wulff construction, for a spherical coordinate system, a vector is drawn parallel to the normal of the surface, with its length proportional to the surface energy. At the end point of the vectors, tangent planes are drawn. If repeated for all surfaces, the tangents limit the equilibrium shape. If a particular surface has a higher surface energy, it will grow faster resulting in a small area or complete disappearance from the final shape, while the face with the lower surface energy grows more slowly, resulting in a large surface area, which hence will be expressed in the polyhedron. This method of predicting calcite morphologies on the basis of thermodynamic factors has been very successful when compared with experimentally obtained calcite shapes, where the equilibrium morphology of pure calcite expresses the dominant  $\{10\bar{1}4\}$  surface, as shown in Figure 2.5.

The morphology is then used to carve out the structure from bulk calcite, thus generating an initial structure for a nanoparticle. However, if the origin of the nanoparticle is at the crystallographic origin, where an ion is at the corner of the crystal lattice, the outer surfaces of the nanoparticle would have an overall net charge which may result in the energy of the nanoparticle diverging during the structure optimisation. In order to create a charge-neutral particle, a suitable centre of the particle is selected by a scanning technique, where the points on a grid are defined at 0.1 Å intervals along each of the Cartesian axes. The different origins are tested

which generate different configurations. Native origin is assumed to adapt the lowest configurational energy and the charge of the crystal. This method has been applied successfully in simulations of calcite (Kerisit *et al.*, 2005; Cooke and Elliott, 2007) and MgO (Spagnoli *et al.*, 2011) particles.

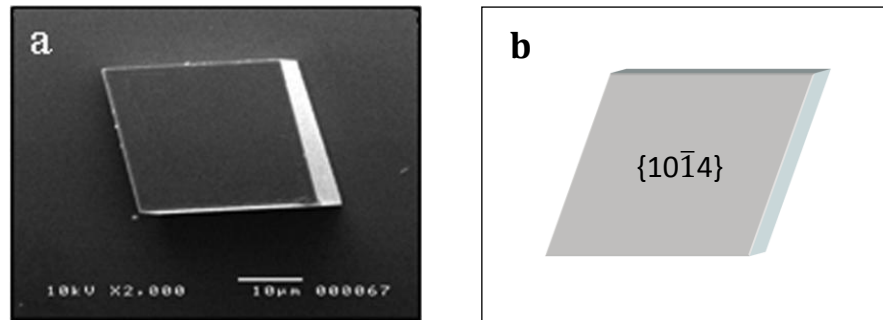


**Figure 2.5:** (a) Calcite crystal growing from the aqueous solution (Didymus *et al.*, 1993) and (b) equilibrium morphology of calcite particle constructed by the Wulff construction method.

## 2.2 Molecular dynamics

Molecular dynamics (MD) is an approach to simulate time-dependent behaviour of molecular systems. All forms of molecular dynamics simulations are based on the behaviour of the molecular systems according to Newton's law of motion, where the force applied to an atom in the system is proportional to its acceleration, or variation in speed over time.

$$m_i \frac{\partial^2 \mathbf{r}_i}{\partial t^2} = F_i(\mathbf{r}_1, \mathbf{r}_2, \dots, \mathbf{r}_N) \quad (2.13)$$

where  $m_i$  is the mass of an atom in the system,  $r_i$  is the position of this atom at time  $t$ ; and  $F_i$  is the force acting on it, from a potential energy  $U$  created by their interaction with all other atoms in the system in an instant of time  $\Delta t$ .

$$F_i = \nabla_i U(r_1, r_2, \dots, r_N) \quad (2.14)$$

Under the influence of continuous interactions, the motions of all particles are coupled together, giving rise to a many-body problem that cannot be solved analytically. The equations of motion are then solved in a finite difference approximation at successive time steps ( $\Delta t$ ), where the velocities and positions of the atoms are calculated at each time step and used for successive interactions.

### 2.2.1 Finite difference methods

There are many algorithms for integrating the equation of motion using finite difference methods, several of which are commonly used in MD calculations. All algorithms assume that the positions and dynamical properties, such as velocities and accelerations, can be approximated as Taylor expansion series:

$$r(t + \Delta t) = r(t) + \Delta t v(t) + \frac{1}{2} \Delta t^2 a(t) + \frac{1}{6} \Delta t^3 b(t) + \frac{1}{24} \Delta t^4 c(t) + \dots \quad (2.15)$$

$$v(t + \Delta t) = v(t) + \Delta t a(t) + \frac{1}{2} \Delta t^2 b(t) + \frac{1}{6} \Delta t^3 c(t) + \dots \quad (2.16)$$

$$a(t + \Delta t) = a(t) + \Delta t b(t) + \frac{1}{2} \Delta t^2 c(t) + \dots \quad (2.17)$$

$$b(t + \Delta t) = b(t) + \Delta t c(t) + \dots \quad (2.18)$$

Where  $r$  and  $v$  are the positions and velocities respectively,  $a$  is the acceleration and  $b$  is the third derivative of the position with respect to time. The Verlet algorithm (Verlet, 1967) is one of the most widely used method for integrating the equations of motion, which uses the positions  $r(t)$  and accelerations  $a(t)$  at time  $t$ , and the position from the previous step,  $r(t-\Delta t)$ , to predict the new position at  $t+\Delta t$ ,  $r(t+\Delta t)$ . The idea for this integration algorithm is based on a third order Taylor expansion series of the

position:

$$r(t + \Delta t) = r(t) + v(t)\Delta t + \frac{1}{2}a(t)\Delta t^2 + \frac{1}{6}b(t)\Delta t^3 + O(\Delta t^4); \quad (2.19)$$

$$r(t - \Delta t) = r(t) - v(t)\Delta t + \frac{1}{2}a(t)\Delta t^2 - \frac{1}{6}b(t)\Delta t^3 + O(\Delta t^4). \quad (2.20)$$

where  $O(\Delta t^4)$  is the error associated with the truncation of the expression at the third order. Then the addition of equation 2.19 and 2.20 gives:

$$r(t + \Delta t) = 2r(t) - r(t - \Delta t) + \Delta t^2 a(t) + O(\Delta t^4) \quad (2.21)$$

and the velocities can be calculated from the previous and new positions by:

$$v(t) = [r(t + \Delta t) - r(t - \Delta t)] / 2\Delta t \quad (2.22)$$

However, this equation is subject to errors in  $\Delta t^2$ , and this may lead to a loss of precision in the calculation of the velocities compared with the position. Several variations on the Verlet algorithm have been developed, one of which is the Leap-Frog algorithm (Hockney, 1970), which uses the following algorithm:

$$r(t + \Delta t) = r(t) + \Delta t v(t + \frac{1}{2}\Delta t), \quad (2.23)$$

$$v(t + \frac{1}{2}\Delta t) = v(t - \frac{1}{2}\Delta t) + \Delta t a(t). \quad (2.24)$$

where the velocities  $v(t + \Delta t/2)$  are calculated firstly from the velocities at time  $(t - \Delta t/2)$  and the accelerations at time  $t$ . The positions  $r(t + \Delta t)$  are then deduced from the velocities just calculated, together with the positions at time  $r(t)$  using equation 2.23. The velocities at time  $t$  can be calculated as the average of the velocities at  $(t + \Delta t/2)$  and  $(t - \Delta t/2)$ .

Two advantages of the Leap-Frog algorithm over the Verlet algorithm are that

the Leap-Frog algorithm includes the velocity and it does not need the calculation of the differences of large numbers. However, it is not possible to calculate the kinetic energy contribution to the total energy at the same time as the positions are defined, because the positions and velocities are not synchronised.

An alternative Verlet algorithm that does store positions, velocities and accelerations at the same time, which minimises rounding errors, has also been proposed (Swope et al., 1982). This Velocity-Verlet algorithm has the form:

$$r(t + \Delta t) = r(t) + \Delta t v(t) + \frac{1}{2} \Delta t^2 a(t), \quad (2.25)$$

$$v(t + \frac{1}{2} \Delta t) = v(t) + \frac{1}{2} \Delta t [a(t) + a(t + \Delta t)]. \quad (2.26)$$

This algorithm has three stages. In the first stage it requires values of position  $r$ , velocity  $v$  and acceleration  $a$  at time  $t$  and  $(t + \Delta t)$ . The first stage is to advance the velocities to  $(t + \Delta t/2)$  by integration of the force and then to advance the positions to a full step  $(t + \Delta t)$  using the new half-step velocities. Alternative algorithms are the Beeman algorithm and the Predictor-Corrector method, which are more complex and time consuming than Verlet algorithm (Sadus, 2002).

The choice of the time step in MD simulation is also important. Choosing it too small will waste computer time. Using a too large time step leads to a bad integration of the equation of motion and no conservation of the total energy, and the molecular vibrations need to be sampled at small enough intervals to ensure that they are sampled properly. The magnitude of the time step is therefore limited by the maximum frequency,  $\gamma_{\max}$  of the vibrations between the component particles and must be smaller than  $\gamma_{\max}$  in order to sample the fastest vibrational motion during the simulation.

### 2.2.2 Ensembles

The concept of ensemble was first introduced by J. Willard Gibbs in 1878. A statistical ensemble is a finite collection of all possible systems which have different microscopic states but identical thermodynamic state. The simplest ensemble is the micro-canonical (NVE) ensemble, in which the number of particles ( $N$ ), volume ( $V$ ) and the energy ( $E$ ) are all kept constant, although the pressure and temperature are allowed to fluctuate. Further ensembles can be generated by modifying the equations of motion.

The canonical ensemble (NVT) keeps constant the number of particles, the volume and the temperature by regulating the temperature with an external heat bath. The energy and pressure are allowed to fluctuate. The temperature of the heat bath is set to the desired internal temperature and the system is regulated by a thermostat. The NVT ensemble is appropriate choice when isolated nanoparticle is modelled in vacuum without periodic boundary conditions. If pressure is not a significant factor, the NVT ensemble provides the advantage of less perturbation of the trajectory, due to the absence of coupling to a pressure bath.

In a model with variable cell size, maintaining a constant pressure (NPT) requires the addition of a barostat coupled to the thermostat. In a similar method to the addition of a thermostat, the equations of motion are modified further to include a friction coefficient that regulates the pressure of the system against a constant set pressure.

NST ensemble is an extension of the constant pressure (NPT) ensemble. In addition to the hydrostatic pressure, which is applied isotropically, NST ensemble allow us to control the  $xx$ ,  $yy$ ,  $zz$ ,  $xy$ ,  $yz$  and  $xz$  components of the stress tensor. This

ensemble is particularly useful if the study of stress-strain relationship in polymeric or metallic materials.

### 2.2.3 Periodic boundary conditions

The size of any simulated system is generally limited by the available storage of the host computer (e.g.  $10 \leq N \leq 10,000$  atoms) and execution speed of the program, because each atom can interact with other atoms, causing the time required to evaluate the forces on the atoms to be proportional to  $N^2$ . No matter how large the system is, its number of atoms  $N$  would be negligible compared with the number of atoms contained in a macroscopic piece of matter, and the ratio between the number of surface atoms and the total number of atoms would be much larger than in reality, causing surface effect to be much more important than it should be. Furthermore, the force evaluation loop remains the principal factor limiting the size of the system that can be simulated.

When modelling an isolated molecular system containing a small number of atoms, clearly an appreciable fraction of atoms would lie close to the periphery of the system, and significant surface effects would be evident. A solution to this problem is to use periodic boundary conditions (PBC). When using PBC, particles are enclosed in a box, and this box is replicated to infinity by rigid translation in all the three Cartesian directions, completely filling the space and forming an infinite macro-lattice. In other words, if one of the atoms is located at position  $\mathbf{r}$  in the box, it is assumed that this atom really represents an infinite set of atoms located at  $(\mathbf{r} + l\mathbf{a} + m\mathbf{b} + n\mathbf{c})$ , where  $l, m, n$  are integer numbers and  $\mathbf{a}, \mathbf{b}, \mathbf{c}$  are cell vectors. A two-dimensional version of such a periodic system is shown in Figure 2.6. As a particle moves through a boundary, all its corresponding images move across their

corresponding boundaries in exactly the same way. The central box simply forms a convenient coordinate system for measuring locations of the  $N$  molecules. However, when simulating an isolated nanoparticle in vacuum, where no periodic boundary conditions are applied, direct summation of the Coulomb pair interaction is adequate and the real space cutoff is chosen in order to incorporate all pairs of atoms within the simulation box.

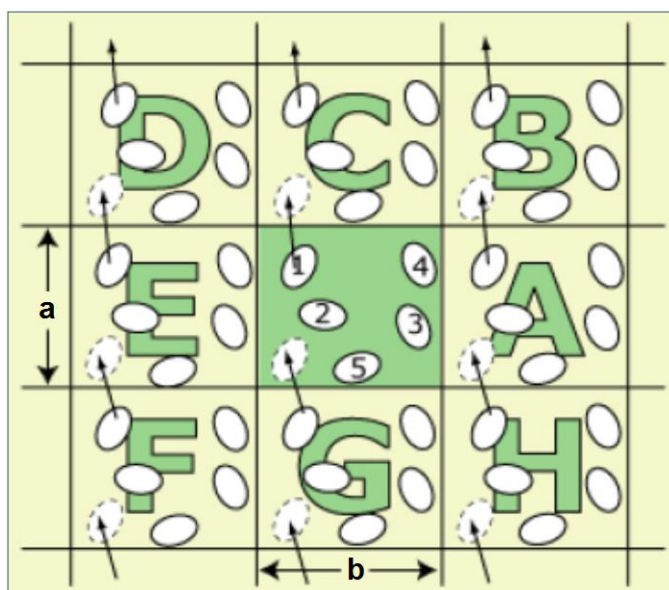


**Figure 2.6:** A two dimensional periodic system. Molecules can enter and leave each box across each of the four edges. In a three dimensional system, molecules would be free to across any of the six cube faces (Allen and Tildesley, 1999).

#### 2.2.4 Running MD simulations

The first step in a MD simulation is to establish an initial configuration of the system. It is advisable to do an energy minimization of the structure. This removes any strong repulsive or attractive forces that may exist, which might otherwise lead to local structural distortion and result in an unstable simulation. Initial velocities at a low temperature are assigned to each atom of the system and are often adjusted so

that the total momentum of the system is zero, thus avoiding unnecessary displacement of the whole system.

Having setup the system and assigned the initial velocities, the simulation can commence. At each step the force on each atom must be calculated by differentiating the potential functions. Newton's equations of motion are integrated to propagate the system in time. Periodically, new velocities are assigned at a slightly higher temperature and the simulation is allowed to continue. The initialization step is terminated when the temperature stabilizes (the energy of the system is constant) and no longer needs renormalization for this purpose because it has reached steady state.

The next step is to carry out the simulations in a given virtual time, which contains a significant number of time steps  $\Delta t$ . In this process the positions and velocities of the atoms in selected steps are recorded and stored. Generally, the MD simulations are performed under conditions of constant number of atoms, temperature and volume, but its trajectory can be modified to sample other ensembles. Even in a constant NVE simulation it is usually desirable to perform a simulation at a particular temperature and it is common practice during the equilibration phase to adjust the temperature to the desired values.

When the system has achieved equilibrium, then the production phase can commence. At the start of the production phase all counters are set to zero and the system is allowed to evolve. In a micro-canonical ensemble (NVE) no velocity scaling is performed during the simulation and the temperature becomes a calculated property of the system. Various properties are routinely calculated and stored during the production phase for subsequent analysis and processing. Careful monitoring of these properties during the simulations can show whether the system is well behaved or not. It may be necessary to restart a simulation if problems are encountered. It is

also usual to store the positions, forces and velocities at regular intervals, from which other properties depending on these quantities can be determined at the end of the simulation.

There are many available computer codes to run MD simulations depending on the potentials used and the target applications. One of them is the DL\_POLY code (Smith and Forester, 1996), which is designed to facilitate MD simulations of macromolecules, polymers, ionic systems and solutions on a distributed memory parallel computer. DL\_POLY allows almost any functional form of interatomic potential to be used in the MD simulations. For the two-body terms, the standard harmonic term is available as well as the Buckingham, Morse and Lennard-Jones potential functions. It is also relatively easy to adapt forcefields from other libraries to DL\_POLY. The details of above interatomic potential functions will be discussed in Chapter 3.

The integration algorithms in DL\_POLY are based on the Verlet Leap-Frog scheme discussed above, and the Nosé-Hoover algorithm is used for the thermostat, as it can generate trajectories in both NVT and NPT ensembles, thus keeping the simulations consistent. The thermostat parameters are set at 0.1 ps and the barostat relaxation time is set at 0.5 ps. The simulations performed for this thesis are initially performed using NVE and NVT ensembles to equilibrate the systems for a period, and followed by both equilibration and the final data production run at NPT or NST for another period of some time. A time step of 0.1 fs is applied to maintain the stability of the simulations. The production phase produces a range of properties at each time step, including structure, temperature, volume and energies. The energies reported in the MD simulations in this thesis are the average configurational energies obtained over each production phase, whereas the structures shown in the figures are usually snapshots.

### 2.2.5 Analysis

The simplest way to analysis the results of the MD simulations is to visualise the trajectory and animate the time evolution of the system. It is possible to observe the growth and dissolution of crystals and phase transitions. Furthermore, a variety of other properties can be calculated from the MD simulations, including thermodynamic properties, radial distribution functions and diffusion coefficients.

The internal calculations in the simulation keep tracking of a number of thermodynamic properties from which the instantaneous and ensemble average values may be extracted. The total instantaneous potential energy for a time step is calculated as the sum of the values from the evaluation of the interatomic potential functions. Additionally, the instantaneous kinetic energy, at a time  $t$ , can be calculated from the velocities of atoms in the system as

$$U_k(t) = \frac{1}{2} \sum_i^N m_i v_i^2(t) \quad (2.27)$$

where  $v_i(t)$  is the velocity of an atom with the mass  $m_i$ . This equation gives the instantaneous kinetic energy and so the total energy is the sum of the potential and kinetic energies. All of these quantities may be averaged over the length of the simulation to give the ensemble averages or plotted with respect to time to observe changes in the system.

The instantaneous temperature of the system is related to the kinetic energy of the atoms. There is a contribution to  $U_k$  of  $k_B T/2$  for each degree of freedom in the system, so for any time step the temperature becomes

$$T = \frac{\sum_i^N m_i v_i^2(t)}{k_B f} \quad (2.28)$$

$k_B$  is the Boltzmann constant and  $f$  is the number of degrees of freedom. A complete system is described by a maximum of  $3N$  independent Cartesian coordinate degrees of freedom (as an aside, each of these may be treated entirely independently in calculations, enabling the calculations to be vectorised to increase speed). Constraints and boundaries imposed on the system will reduce the number of degrees of freedom.

The radial distribution function (RDF),  $g(r)$ , is a useful measure of the surroundings of an atom. For each atom type the distances to other atoms are sorted into shells.

$$g(r) = \frac{n(r)}{\rho(r)} \times \frac{1}{4\pi r^2 \Delta r} \quad (2.31)$$

where  $n(r)$  is the occupancy of a shell of width  $\Delta r$  at a radius  $r$  from the atom. The factor of the mean atom density  $\rho(r)$ , ensures that the distribution is normalized. Values are averaged from all atoms in the sample and over each time step. For a fixed ideal lattice,  $g(r)$  will be zero except at neighbour separation distances. At increased finite temperatures the atomic vibrations cause movement away from these ideal positions and the peaks in the function broaden.

# 3

## Potential models

---

An interatomic potential model refers to a collection of parameters of mathematical functions used to describe the interatomic interactions of a system. An accurate potential model is essential to obtain reliable results. This chapter presents a summary of the interatomic potential functions and parameters used in this thesis. In addition, a new set of potential parameters for divalent cations  $\text{Co}^{2+}$ ,  $\text{Zn}^{2+}$ ,  $\text{Mn}^{2+}$  and  $\text{Ni}^{2+}$  were derived with the existing calcite potential model. Details of the derivation of these parameters are also presented in this chapter.

### 3.1 The Born model of solids

The atomic simulations in this thesis are based on the Born model of solids (Born and Huang, 1954), which assumes that the interactions between the ions in the system are a combination of long-range electrostatic forces and short-range forces, including both the repulsions and the Van der Waals attractions between neighbouring electron clouds. The potential energy of the system is the sum of the interactions between all ions, and can be described by the equation:

$$U(r_{ij}) = \sum_{ij} \frac{q_i q_j}{4\pi\epsilon_0 r_{ij}} + \sum_{ij} \Phi_{ij}(r_{ij}) \quad (3.1)$$

The left term of equation 3.1 is the long-range electrostatic interactions between the ions, where  $q_i$  and  $q_j$  are the charges of the ions  $i$  and  $j$  respectively,  $r_{ij}$  is the distance between ions  $i$  and  $j$ , and  $\epsilon_0$  is the permittivity of free space. The right term represents the short-range forces, which are described below and include primarily two-body interactions. For example, the variation of the interaction of Ca-O in modelling of the  $\text{CaCO}_3$  is shown in Figure 3.1.

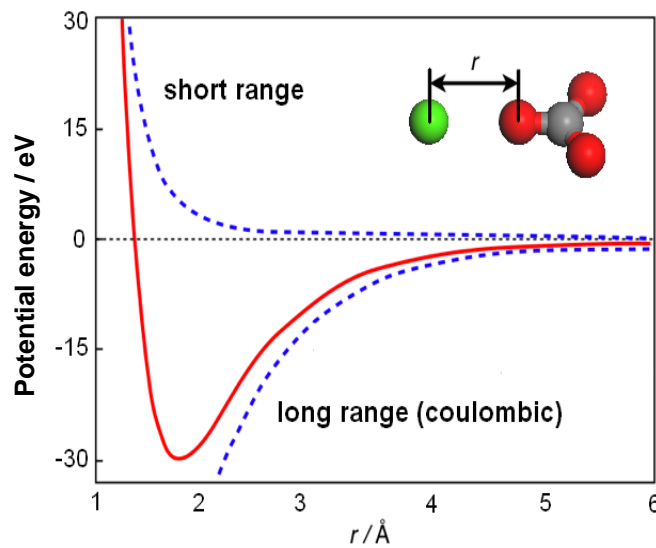


**Figure 3.1:** Plots showing the variation in the long-range, short-range and total potential energies as a function of  $r_{ij}$  for a  $\text{Ca}^{2+}\text{-O}^{2-}$  ion pair.

Other contributions are also considered, such as bond bending terms to convey the directionality of certain bonds in the crystal, for instance in the modelling of the covalent bonds in the carbonate group of  $\text{CaCO}_3$ , and four-body interactions such as dihedral terms.

### 3.2 The Ewald method

The internal energy equation of the Born model seems deceptively simple. However, the long-range electrostatic part of the potential energy is too slow to converge as a function of  $r_{ij}$  in real-space. This problem has been solved by using the Ewald summation method (Ewald, 1921), which replaces the summation of potential energies in real space with an equivalent summation in Fourier space. The advantage of this approach is the rapid convergence of the Fourier space summation compared to its real-space equivalent when the real-space interactions are long-range. Because it is maximally efficient to decompose the interaction potential into a short-range component summed in real space and a long-range component summed in Fourier space.

Each point charge in the system is viewed as being surrounded by a Gaussian charge distribution of equal magnitude and *opposite* sign, with charge density:

$$\rho_i(r_i) = \frac{q_i \alpha^3}{\pi^{3/2}} \exp(-\alpha^2 r_i^2) \quad (3.2)$$

where  $\alpha$  is a positive parameter that determines the width of the distribution, and  $r_i$  is the position relative to the centre of distribution. This introduced charge distribution screens the interaction between neighbouring point-charges, effectively limiting them to a short range. Consequently, the sum over all charges and their images in real space converges rapidly, which is now given by:

$$U_{sr} = \frac{1}{2} \sum_{ij} q_i q_j \frac{\text{erfc}(\alpha r_{ij})}{r_{ij}} \quad (3.3)$$

where  $\text{erfc}(x)$  is defined as the complimentary error function:

$$\text{erfc}(x) = 1 - \text{erf}(x) = 1 - \frac{2}{\pi^{1/2}} \int_0^x \exp(-u^2) du \quad (3.4)$$

A second Gaussian charge distribution of the same sign and magnitude as the original distribution is added in order to maintain the neutrality of charges. This time the sum is performed in the Fourier space to solve the resulting Poisson's equation.

$$U_{fr} = \frac{1}{2\pi V} \sum_{i,j} q_i q_j \sum_{m \neq 0} \frac{\exp[-(\pi m / \alpha)^2 + 2\pi m \cdot (r_i - r_j)]}{m^2} \quad (3.5)$$

where  $m$  are the reciprocal vectors and  $V$  is the volume of the unit cell of the crystal. A correction self-term needs to be subtracted in order to cancel out the interaction of each of the introduced artificial counter-charges with itself. Finally, the total electrostatic energy per unit cell can then be calculated as:

$$\Phi_{ij} = U_{sr} + U_{fr} - \frac{\alpha}{\pi^{1/2}} \sum_i q_i^2 \quad (3.6)$$

### 3.3 Electronic polarisability

One simple way to include the electronic polarisability of the atoms is to use the core-shell model (Dick and Overhauser, 1958), where the polarisable ion is represented by a massless shell connected to a core containing all the mass. The total charge of the ion is the sum of the charges of the core and shell. The position of the core represents the position of the ion in the crystal lattice and the position of the shell shows the electronic polarisability of the atom. The core and shell are connected by a harmonic spring, as shown in Figure 3.2. The spring constant  $K$  and the charge

of the shell  $Ye$  then determine the polarisability of the ion as follows:

$$\alpha_p = \frac{Ye^2}{4\pi\epsilon_0 K} \quad (3.7)$$

Both  $K$  and  $Ye$  can be fitted empirically to reproduce experimental properties, such as dielectric and elastic constants. The short-range forces are assumed to act between the shells while the Coulombic forces act between all shells and cores, except between the core and shell of the same ion. The core-shell model has been successful in modelling various properties and it has been used in all static energy minimisation calculations in this thesis to describe the polarisability of the oxygen in the  $\text{CO}_3^{2-}$  group and water.

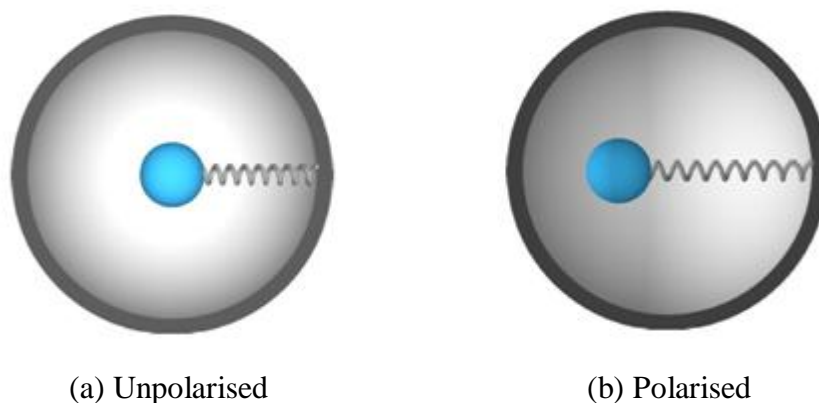


**Figure 3.2:** Schematic representation of the core-shell model: (a) no displacement, unpolarised. (b) displacement, polarised. The blue sphere, representing the core, has the charge  $Xe$ . The open grey sphere, representing the shell, has the charge of  $Ye$ . The core and shell are connected by a spring of force constant  $K$ , (Murphy, 2009).

The core-shell model of electronic polarisability employed in MD simulations is slightly different, because the massless shells do not obey the normal dynamic laws. In DL\_POLY, a small mass is assigned to the shell following the approach introduced by Mitchell and Fincham (1993). For example, the oxygen shell in this thesis is given a mass of 0.2 a.u., which is small enough, compared to the mass of hydrogen atom

(1.0 a.u.), in order to minimise energy exchange between the vibrations of oxygen core and shell and the oxygen and hydrogen vibrations. Due to the use of a shell model, a time step of 0.1 fs is applied to maintain the stability of the simulations.

### 3.4 Short-range potential functions

The two-body potential functions act between neighbouring charge clouds, the shells of the polarisable anions and the cores in the case of cations. They come in a number of analytical forms, all describing the potential energy as a function of interionic separation. These potential functions act without taking into account directionality of any bonds. Three-body potential function acts between three ions and is used when covalent bonds are present in the system. The terms define angles and dihedrals between the ions and as such convey directionality to the bonds. The short-range potential functions used in this thesis are described below.

#### 3.4.1 Buckingham potential function

The Buckingham potential (Buckingham, 1938) is one of the most widely used functions for the interaction of two bodies which are not directly bonded.

$$\Phi_{ij}(r_{ij}) = A_{ij} \exp\left(-\frac{r_{ij}}{\rho_{ij}}\right) - \frac{C_{ij}}{r_{ij}^6} \quad (3.8)$$

where  $A_{ij}$ ,  $\rho_{ij}$  and  $C_{ij}$  are the parameters to describe the interaction between two atoms  $i$  and  $j$  and  $r_{ij}$  is the interatomic distance.  $A_{ij}$  and  $\rho_{ij}$  are related to the number of electrons and the electron density respectively. The first term of the function describes the short-range repulsive interaction between the atoms, which originates from the Pauli Exclusion Principle (1925), while the second represents the attractive Van der Waals forces. Since the exponential term converges to a constant as the

distance  $r_{ij}$  approaches to zero, while the second term diverges, it runs the risk of an un-physical “Buckingham catastrophe”, when used in simulations of charged systems. This occurs when the electrostatic attraction artificially overcomes the repulsive barrier (White, 1997). Minimizing the energy of a structure which accidentally has a very short distance between two atoms will thus result in “nuclear fusion”. Special precautions have to be taken to avoid this problem (Jensen, 2007). Occasionally, the second term of the Buckingham potential used in this thesis is omitted altogether and the  $A_{ij}$  parameter is adjusted to take into account both the long-range attractive forces and short-range repulsions.

### 3.4.2 Morse potential function

The Morse potential (Morse, 1929) is used for modelling covalent bonds and capable of modelling anharmonicity. As such interatomic distances away from the equilibrium bond distance can be simulated reliably with this potential function, for example the carbon-oxygen bond in the  $\text{CO}_3^{2-}$  group.

$$\Phi_{ij}(r_{ij}) = D_{ij}(1 - e^{-\alpha(r_{ij} - r_0)})^2 \quad (3.9)$$

where  $D_{ij}$  is the depth of the potential well, i.e. the thermodynamic dissociation energy of the bond,  $r_0$  is the equilibrium bond length, and  $\alpha$  is a constant controlling the “width” of the potential. The form of the Morse potential function ensures that at infinite separation of the two atoms the potential energy is zero while the potential energy is at a minimum at the equilibrium bond distance. Sometimes the Morse potential is used with subtraction of the Coulombic interaction and as such it is the only potential function describing a bond between two nearest neighbours. Interactions between second and further nearest neighbours can be described by Coulombic interactions and another short-range potential function.

### 3.4.3 Lennard-Jones potential function

The Lennard-Jones potential (Lennard-Jones, 1924), of which the commonest form is also referred to as the 6-12 potential, is one of the most widely used potential functions to approximate the interaction between a pair of atoms. It has the following simplified form:

$$\Phi_{ij}(r_{ij}) = \frac{A}{r_{ij}^{12}} - \frac{B}{r_{ij}^6} \quad (3.10)$$

with  $A = 4\epsilon\sigma^{12}$  and  $B = 4\epsilon\sigma^6$ , where  $\epsilon$  is the depth of the potential well and  $\sigma$  is the finite distance where the inter-particle potential is zero. The repulsive part is dependent on  $r^{-12}$  and thus acts at close range, while the attractive part is proportional to  $r^{-6}$  and becomes dominant at longer range. The parameters can be fitted to reproduce experimental data or accurate quantum chemistry calculations. Due to its computational simplicity, the Lennard-Jones potential is used extensively in computer simulations even though more accurate potentials exist. For example, it is often used for modelling oxygen-oxygen interactions in water potential models, such as the SCP and TIP5P models (Jorgensen *et al.*, 1983; Rick, 2004).

### 3.4.4 Many body potential function

The three-body harmonic potential is used to describe the partial covalency in the  $\text{CO}_3^{2-}$  group and maintain the bond angle between two carbon-oxygen bonds.

$$\Phi_{ijk}(\theta_{ijk}) = \frac{1}{2} k_{ijk} (\theta_{ijk} - \theta_0)^2 \quad (3.11)$$

where  $k_{ijk}$  is the force constant and  $(\theta_{ijk} - \theta_0)$  is the deviation from the equilibrium angle  $\theta_0$ . The function acts between a central ion  $i$  and two ions  $j$  and  $k$  bonded to  $i$  making the bond angle  $\theta_{ijk}$  (see Figure 3.3).

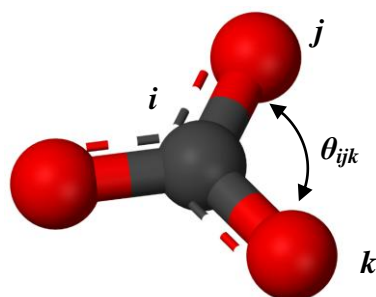


**Figure 3.3:** The three-body interaction in a carbonate group.

The four-body out of plane potential is applied to planar arrangements of three bonds or torsional angles (Figure 3.4). The four-body potential function for the  $\text{CO}_3^{2-}$  group is described as follows by Pavese *et al.* (1996).

$$\Phi_{ijkl} = k_{ijkl} [1 - s \cos(N\theta)] \quad (3.12)$$

where  $k_{ijkl}$  is the force constant,  $s$  is  $\pm 1$  and  $N$  is an integer which gives the periodicity of the torsion, which is 2 in the case of the planar  $\text{CO}_3^{2-}$  group. The above functional form means that the energy has a minimum value when  $\theta$  is 0 or  $\pi$  radians and all atoms lie in the same plane in the  $\text{CO}_3^{2-}$  group.

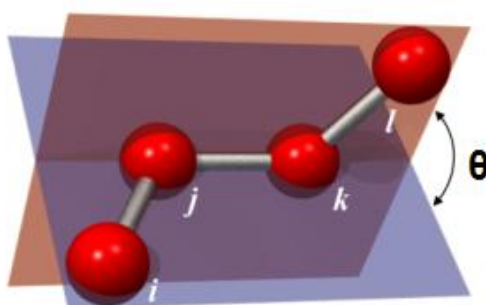


**Figure 3.4:** The four-body interaction of four atoms lying in two planes with a torsional angle  $\theta$ .

### 3.5 Potentials of carbonates and water

The potential parameters of calcite used in this thesis are from Pavese *et al.* (1996), who derived them empirically in a study of the thermal dependence of structural and elastic properties of calcite. The oxygen-oxygen and calcium-oxygen interactions are modelled by a Buckingham potential. The covalency within the  $\text{CO}_3^{2-}$  group is modelled by a Morse potential plus a three-body potential and a torsional potential function to restrain the planar  $\text{CO}_3^{2-}$  group from folding. Although Pavese *et al.*'s potential model was fitted to bulk structure; it has been applied successfully to the accurate representations of calcite surfaces (de Leeuw and Parker, 1998, 2000, 2001). The potential parameters used for  $\text{CdCO}_3$ ,  $\text{MgCO}_3$  and  $\text{FeCO}_3$  were derived by de Leeuw (2002), which were fitted to reproduce the unit cell volumes of relative carbonates with respect to calcite, as well as relative energies of formation of these carbonates, using on the same potential parameters of  $\text{CO}_3^{2-}$  group.

The water potential model is that of de Leeuw and Parker (1998) with the added hydrogen-bonding modification of Kerisit and Parker (2004). For the interactions between water and calcite, the potential parameters come from de Leeuw *et al.* (1999). The potential parameters used in the thesis are summarised in Table 3.1.

**Table 3.1** Potential parameters used in this thesis (short-range cutoff 20 Å). (Parameters for CaCO<sub>3</sub> are from Pavese *et al.*, 1996; Parameters for Mg, Fe, Cd are from de Leeuw, 2002; parameters for water are from de Leeuw and Parker, 1998 and Kerisit and Parker, 2004).

ions	Charge		core-shell Interaction / eVÅ <sup>-2</sup>
	core	shell	
Ca, Mg, Fe, Cd	+2		
C	+1.135		
H	+0.400		
O	+0.587	-1.632	507.4
O <sub>water</sub>	+1.250	-2.050	209.449602
Buckingham Potential			
Ion pair	A / eV	$\rho / \text{Å}$	C / eVÅ <sup>6</sup>
Ca-O	1550.0	0.297	0.0
Mg-O	1092.2	0.27926	0.0
Fe-O	14600.0	0.2055	0.0
Cd-O	747097.4	0.1549	0.0
Ca-O <sub>water</sub>	1186.6	0.297	0.0
H-O	396.3	0.23	0.0
H-O <sub>water</sub>	396.3	0.25	10.0
O-O	16732.0	0.213	3.47
O-O <sub>water</sub>	12533.6	0.213	12.09
Lennard-Jones Potential			
	A / eVÅ <sup>12</sup>		B / eVÅ <sup>6</sup>
O <sub>water</sub> -O <sub>water</sub>	39344.98		42.15
Morse Potential			
	D / eV	$\alpha / \text{Å}^{-1}$	R <sub>0</sub> / Å
C-O <sub>core</sub>	4.71	3.8	1.18
H-O <sub>water-shell</sub>	6.203713	2.22003	0.92376
Three Body Potential			
	k / eVrad <sup>-2</sup>		$\Theta_0$
O <sub>core</sub> -C-O <sub>core</sub>	1.69000		120.0
H-O <sub>water-shell</sub> -H	4.19978		108.69
Four Body Potential			
	k / eVrad <sup>-2</sup>		$\Theta_0$
C-O <sub>core</sub> -O <sub>core</sub> -O <sub>core</sub>	0.11290		180.0

### 3.6 Derivation of potentials for Ni, Co, Zn and Mn carbonates

There are two ways to derive the potential parameters for the short-range potential functions. One is a non-empirical method which is based on *ab initio* calculations to obtain the data for the parameterization, such as the equilibrium geometry and the energy surface corresponding to a particular structural distortion. The other is an empirical method which determines the parameters of the pair potential functions to reproduce specific experimental properties, such as crystallographic data, unit cell dimensions and elastic constants. The empirical method often produces a series of values, which can repeat the lattice parameters for a given structure. However, it is much more desirable and accurate to consult as many observable properties as possible.

The potential parameters for  $\text{NiCO}_3$ ,  $\text{CoCO}_3$ ,  $\text{ZnCO}_3$  and  $\text{MnCO}_3$  in this thesis were derived using GULP (Gale, 1997) by a penalty minimisation scheme. In this scheme, the total penalty of a system is the sum of the deviations of calculated properties, such as atomic positions or elastic parameters, from measured values weighted according to accuracy. During fitting, the parameters of the interatomic potentials are adjusted so as to minimize the penalty value of the system until it has converged. The following options were used when fitting the potential parameters in GULP. (i) Constant pressure and relaxed fitting algorithm where both cores and shells of ions are allowed to move within the cell during fitting. (ii) Newton-Raphson algorithm was applied during energy optimisation. (iii) Parameters were generally fitted one at a time, except where a material had a well-defined structure and known elastic constants.

The primitive rhombohedral cell was used in the simulation of the bulk structure of calcite-type carbonates, although lattice parameters are reported here in hexagonal

coordinates as the two representations are mathematically equivalent. The potential parameters for  $\text{NiCO}_3$ ,  $\text{CoCO}_3$ ,  $\text{ZnCO}_3$  and  $\text{MnCO}_3$  were derived by GULP to be compatible with the potential model of calcite by Pavese *et al.*, where the calculated hexagonal unit cell volume is  $348.3 \text{ \AA}^3$  ( $a = 4.797 \text{ \AA}$ ,  $c = 17.482 \text{ \AA}$ ,  $\alpha = 90^\circ$  and  $\gamma = 120^\circ$ ). During fitting, the potentials were required to retain the relative hexagonal unit cell volumes in the experimental ratio:

$$V_{Ca} : V_{Mn} : V_{Co} : V_{Zn} : V_{Ni} = 1.34 : 1.12 : 1.02 : 1.02 : 1 \quad (3.13)$$

The only degree of freedom allowed in fitting the potentials was in the cation-oxygen Buckingham potential. Due to the non-directional nature of the metal cation as described by the Buckingham potential of equation 3.8, there is no explicit term that addresses the d-electrons of the transition metal cations. The transition metal cations are represented as spherical rigid ions with no electronic polarization, as in  $\text{Ca}^{2+}$ , and therefore magnetic effects are ignored. Fortunately, magnetism is unlikely to affect the issues, such as the enthalpy and free energy of mixing, which are interested in exploring in this thesis.

In order to obtain the reliable enthalpies for cation substitutions, the relative enthalpies of formation are required to be sensible. Therefore the enthalpy of the following reaction is required to be reproduced accurately:



where  $Me$  is Ni, Co, Zn or Mn. The potential parameters were therefore derived such that the calculated enthalpies of reaction 3.14 agree to within 2.2% of the experimental enthalpies. In this calculation the vibrational effects (both zero-point and heat capacity) were included in the enthalpies, although they contribute very little to the reaction enthalpy, for example, only 1.3 kJ/mol (0.5%) of the reaction

enthalpy for  $\text{MnCO}_3$ . Table 3.2 provides the optimized interatomic potential parameters of these four carbonates obtained through this process, and a comparison of calculated and experimental parameters for the various carbonates is listed in Table 3.3.

**Table 3.2** Interionic Buckingham potentials obtained from fits to  $\text{NiCO}_3$ ,  $\text{CoCO}_3$ ,  $\text{MnCO}_3$  and  $\text{ZnCO}_3$  structures and enthalpies of reaction 3.14.

Ion pair	$A / \text{eV}$	$\rho / \text{\AA}$	$C / \text{eV}\text{\AA}^6$
Ni-O	1103.38	0.26661	0.0
Co-O	1561.50	0.26740	0.0
Mn-O	1704.60	0.27400	0.0
Zn-O	1506.62	0.26903	0.0

No interatomic potential model is perfect, and usually the description of some properties can only be improved at the expense of worsening the description of others. For example, the parameters of Buckingham potential for  $\text{Co}^{2+}$  and  $\text{Zn}^{2+}$  introduced in this thesis are less well reproduced the experimental bulk modulus, and the calculated bulk modulus of  $\text{ZnCO}_3$  is bigger than that of  $\text{CoCO}_3$ , which is contradict with experiments. However, both the ratio of the cell parameters and calculated enthalpies of reaction 3.14 are reproduced very well, therefore these parameters should provide an adequate description of the incorporation of single kind of cationic impurity in calcite.

**Table 3.3** Calculated and experimental properties of NiCO<sub>3</sub>, CoCO<sub>3</sub>, ZnCO<sub>3</sub>, MnCO<sub>3</sub> and CaCO<sub>3</sub>. (Experimental lattice parameters are from Deer *et al.*, 1992; bulk modulus are from Zhang and Reeder, 1999; the enthalpies of formation of carbonates are from Lide, 2000).

Carbonates		Volume /Å <sup>3</sup>	a / Å	c / Å	c/a	Bulk modulus / GPa	$\Delta H_{\text{Eq-3.14}}$ / kJmol <sup>-1</sup>
CaCO <sub>3</sub>	experiment	367.8	4.99	17.06	3.42	76.1	/
	literature	348.3	4.80	17.48	3.64	80.4	/
ZnCO <sub>3</sub>	experiment	281.01	4.67	14.88	3.19	123	462.5
	this work	264.42	4.46	15.35	3.44	216	454.4
CoCO <sub>3</sub>	experiment	281.22	4.67	14.89	3.18	124	426.7
	this work	269.07	4.48	15.48	3.46	213	416.3
MnCO <sub>3</sub>	experiment	307.89	4.78	15.56	3.26	126	279.3
	this work	285.24	4.55	15.91	3.49	135	275.2
NiCO <sub>3</sub>	experiment	274.65	4.64	14.73	3.17	131	440.2
	this work	236.25	4.33	14.55	3.36	150	432.9

# 4

## Mixing thermodynamics of calcite with divalent cation impurities

---

In this chapter atomistic simulation techniques have been employed to investigate the thermodynamics of mixing calcite with divalent cation impurities  $Me^{2+}$  ( $Cd^{2+}$ ,  $Mn^{2+}$ ,  $Fe^{2+}$ ,  $Co^{2+}$ ,  $Zn^{2+}$ ,  $Mg^{2+}$  and  $Ni^{2+}$ ), based on the calculation of all inequivalent site occupancy configurations in relevant supercells of calcite structure. The simulations predict that the miscibility of calcite and other carbonates is largely related to the cationic coordination distance with oxygen. Detailed comparisons of the simulations with available experimental results are also provided in this chapter.

## 4.1 Introduction

Metal cations, such as  $\text{Cd}^{2+}$ ,  $\text{Mn}^{2+}$ ,  $\text{Zn}^{2+}$ ,  $\text{Fe}^{2+}$ ,  $\text{Co}^{2+}$ ,  $\text{Ni}^{2+}$  and  $\text{Mg}^{2+}$ , are commonly present in calcite, which can take up the impurity cations via a dissolution recrystallisation process. The solubility and migration of divalent cations in calcite is largely limited by the phase equilibrium of two carbonates, many of which form calcite-type solid solutions. For example, studies by Tesoriero and Pankow (1996) showed that in the presence of calcite, precipitation of  $\text{Cd}^{2+}$  as a carbonate solid solution will always occur, even when  $\text{Cd}^{2+}$  is present at trace levels, due to the strong tendency of this cation to partition into calcite. It is therefore very useful to investigate the thermodynamics of these extensive solid solutions to gain insight into the flux of divalent cations in aquifers and soil.

Although the mixed carbonate solid solutions have been widely studied using experimental techniques, such as solution calorimetry, seemingly contradictory results are still reported in the literature, particularly with respect to the range of the miscibility at different temperatures and the thermodynamics of the mixing properties at intermediate compositions, since the slow kinetic rate at high temperatures and pressure limits further progress in experiments. One of the most straightforward theoretical models for predicting the thermodynamics of binary carbonate solid solutions is the electrostatic model from Lippmann (1980). However, some assumptions in this model limit its power of prediction. For example, Lippmann's model assumes all calcite-type carbonates should have the same Madelung constant.

As an effective complementary technique to experiment, computer modelling can be used to study complex mineral structures and processes at the atomic level,

including the formation of solid solutions, where it is possible to access the thermodynamic properties without the effect of unknown kinetic factors. Interatomic potential models, in particular, have been used extensively to simulate the structures and properties of rhombohedral carbonates (Cygan, 2000; de Leeuw and Parker, 1996, 1997; Austen, 2005). These studies have demonstrated the suitability of molecular simulations in providing a theoretical description of complex bulk and surface processes in carbonates, and how the theoretical models assist experiment in the evaluation and interpretation of experimental observations.

For a carbonate solid solution, the number of possible configurations for each composition increases rapidly with the size of the simulation supercell, leading to concomitant computational cost. Several approaches have been developed to treat these large numbers of configurations. For example, the thermodynamics of the binary (Mn,Ca)CO<sub>3</sub> system and tertiary (Mg,Mn,Ca)CO<sub>3</sub> system have been discussed in recent papers by Vinograd *et al.* (2009 and 2010), where a simplified pair-wise interaction model is employed to perform Monte Carlo simulations in a very large supercell of the structure, allowing full convergence of the calculations with respect to cell size. An alternative approach, which has been adopted in this study, is to reduce the complete set of configurations to the symmetrically inequivalent configurations by taking advantage of the crystal symmetry of calcite. This method keeps an accurate description of the interatomic interactions and relaxation effects explicitly in the simulations, based on the calculation of all inequivalent site occupancy configurations in a smaller supercell of the calcite structure. It also makes possible to calculate effective properties, beyond the energy, based on configurational averages (for example, effective cell parameters as a function of composition), and to evaluate easily the contribution of vibrational effects.

In this chapter atomistic simulation techniques have been applied to investigate the thermodynamic properties of the entire compositional range of a series of binary carbonate solid solutions  $(\text{Me,Ca})\text{CO}_3$  ( $\text{Me} = \text{Cd}^{2+}, \text{Mn}^{2+}, \text{Zn}^{2+}, \text{Fe}^{2+}, \text{Co}^{2+}, \text{Ni}^{2+}, \text{Mg}^{2+}$ ), following the above approach. In addition to the enthalpy of mixing, the calculation of the configurational entropy and free energy has also been included; therefore it is possible to study the mixing behaviour as a function of temperatures for these binary carbonate solid solutions. The results were then compared with experimental measurements from calorimetric methods.

## 4.2 Configurational statistics

The distribution of cationic impurities in the hexagonal calcite lattice was investigated utilizing the SOD (Site Occupancy Disorder) program (Grau-Crespo, 2007), which generates the complete configurational space for each composition of one supercell and then extracts the symmetrically inequivalent configurations by considering the symmetry operators of the parent structure. Typically this procedure significantly reduces the number of configurations to be calculated in the GULP code (Gale, 1997). Once the configurational spectrum is obtained, it is possible to derive configurational entropies and enthalpies, based on the assumption that the extent of the occurrence of one particular configuration in the disordered solid can be described by a Boltzmann-like probability which is calculated, assuming zero external pressure and ignoring vibrational contributions, from the energy  $U_m$  of the configuration (the minimum energy of the optimised structure at constant pressure), and its degeneracy  $\Omega_m$  (the number of times that the configuration is repeated in the complete configurational space):

$$P_m = \frac{\Omega_m}{Z} \exp(-U_m / k_B T) \quad (4.1)$$

where  $m = 1, \dots, M$  ( $M$  is the number of inequivalent configurations),  $k_B = 8.6173 \times 10^{-5} \text{ eVK}^{-1}$  is the Boltzmann's constant, and  $Z$  is the configurational partition function.

$$Z = \sum_{m=1}^M \Omega_m \exp(-U_m / k_B T) \quad (4.2)$$

In this study, the enthalpy of each configuration is simply its lattice energy, as any external pressure has not been considered in the calculations, and the vibrational contributions to the enthalpy have been ignored, which were shown in a previous study on  $(\text{Fe,Cr})_2\text{O}_3$  solid solution to be negligible (Benny *et al.*, 2009). Then the enthalpy per formula  $H$  at each composition is calculated as an average in the configurational space:

$$H = \frac{1}{N} \sum_{m=1}^M P_m H_m = \frac{1}{N} \sum_{m=1}^M P_m U_m \quad (4.3)$$

where  $N$  is the number of formula units in the supercell, while the configurational free energy  $G$  and the entropy  $S$  can be obtained from the partition function  $Z$ :

$$G = -\frac{1}{N} k_B T \ln Z ; \quad (4.4)$$

$$S = \frac{H - G}{T} = -\frac{1}{N} k_B \sum_{m=1}^M P_m \ln \frac{P_m}{\Omega_m} . \quad (4.5)$$

It is worth noting that the calculated enthalpies of the disordered systems tend to converge very rapidly with the size of the simulation cell, although the convergence of entropies is much slower (Todorov, 2004). Therefore, the calculations, which are based on relatively small supercells, can provide precise enthalpies, while the calculated entropies are only used to qualitatively access the degree of disorder in the solid solutions. The degree of convergence of the entropies with the size of the supercell is discussed below based on the difference between the full-disorder

entropy for the given supercell:

$$S_{\max}(x, N) = \frac{1}{N} k_B \ln \frac{N!}{[Nx]![N(1-x)]!}. \quad (4.6)$$

and the exact full-disorder result:

$$S_{\text{ideal}}(x) = \lim_{N \rightarrow \infty} S_{\max}(x, N) = -k_B [x \ln x + (1-x) \ln(1-x)]. \quad (4.7)$$

Any property  $A_m$  defined for each configuration  $m$  can be averaged over the configurational ensemble as:

$$A = \sum_{m=1}^M P_m A_m \quad (4.8)$$

But the interpretation of this average should be done carefully. When the averaging of system properties is performed in the reduced space of inequivalent configurations, each configuration  $m$  represents a set of  $\Omega_m$  equivalent configurations, and therefore the property  $A_m$  must be the same for all configurations in that set. For example, if  $\mathbf{a}_m$  and  $\mathbf{b}_m$  are the equilibrium cell vectors for each inequivalent configuration  $m$ , the average value of the cell parameters  $\mathbf{a}$  corresponding to the disordered crystal cannot be calculated as the direct average of the  $|\mathbf{a}_m|$  values, as this result could be different from the direct average of the  $|\mathbf{b}_m|$  values, breaking the rotational symmetry of the hexagonal cell. Therefore we have calculated the cell parameter  $\mathbf{a}$  by equation:

$$a = \left( \sum_{m=1}^M P_m |\mathbf{a}_m \times \mathbf{b}_m| \right)^{\frac{1}{2}} \quad (4.9)$$

Since the absolute value of the vector product  $\mathbf{a}_m \times \mathbf{b}_m$  is invariant within a set of equivalent configurations. The cell parameter  $\mathbf{c}$  was obtained directly by configurational averaging of the  $|\mathbf{c}_m|$  values.

In order to interpret the thermodynamic properties of the binary solid solutions in an appropriate way, the size of the simulation cell in the calculations must be clarified. The cation substitutions in  $2 \times 2 \times 1$  and  $3 \times 3 \times 1$  supercells have been considered, which contain 24 and 54 cation sites respectively. The extension along the  $x/y$ -axes is studied, as  $a < c$  in the unit cell and the interactions of cations in neighbouring cells thus could have more effect in  $x/y$ -axes. The total number of configurations and symmetrically inequivalent configurations for two supercells are listed in Table 4.1, where  $x$  is the molar fraction of the impurity cations in the solid solutions.

**Table 4.1** Total number of configurations ( $W$ ) and number of symmetrically inequivalent configurations ( $M$ ) for each composition  $\text{Me}_x\text{Ca}_{1-x}\text{CO}_3$  in  $2 \times 2 \times 1$  and  $3 \times 3 \times 1$  supercells (A and B stand for either Ca or impurity).

Cell composition	$x$ or $1-x$	$W$	$M$
$\text{A}_{24}(\text{CO}_3)_{24}$	0	1	1
$\text{A}_{23}\text{B}(\text{CO}_3)_{24}$	0.042	24	1
$\text{A}_{22}\text{B}_2(\text{CO}_3)_{24}$	0.083	276	7
$\text{A}_{21}\text{B}_3(\text{CO}_3)_{24}$	0.125	2024	20
$\text{A}_{20}\text{B}_4(\text{CO}_3)_{24}$	0.167	10626	102
$\text{A}_{19}\text{B}_5(\text{CO}_3)_{24}$	0.208	42504	317
$\text{A}_{18}\text{B}_6(\text{CO}_3)_{24}$	0.250	134596	1033
$\text{A}_{17}\text{B}_7(\text{CO}_3)_{24}$	0.292	346104	2467
$\text{A}_{16}\text{B}_8(\text{CO}_3)_{24}$	0.333	735471	5330
$\text{A}_{53}\text{B}(\text{CO}_3)_{54}$	0.019	54	1
$\text{A}_{52}\text{B}_2(\text{CO}_3)_{54}$	0.037	1431	11
$\text{A}_{51}\text{B}_3(\text{CO}_3)_{54}$	0.056	24804	86
$\text{A}_{50}\text{B}_4(\text{CO}_3)_{54}$	0.074	316251	1051

For the  $2 \times 2 \times 1$  supercell, the full spectrum of configurations was not calculated for  $\text{Me}^{2+}$  composition  $0.333 < x < 0.667$  due to the still prohibitive computational cost. For example, for the intermediate composition  $x = 0.5$ , it leads to a total of almost three million configurations, which is computationally too expensive to calculate directly. Instead, a random sampling method was employed and the convergence of the calculated properties with respect to the sample size was checked. The  $3 \times 3 \times 1$  supercell was only employed at low concentrations to test the convergence of enthalpies with respect to cell size.

### 4.3 Structure and configurational entropy

Firstly, the equilibrium geometries and energies of the divalent cation substituted configurations in a  $2 \times 2 \times 1$  supercell of the calcite structure were calculated using the methods above. As calcite and other rhombohedral carbonate minerals are iso-structural, the introduction of impurity cations in either material does not significantly affect the structure beyond local relaxations.

In order to understand the driving force towards the cationic ordering in the calcite-type structure, the most stable (lowest energy) configuration has been identified. Figure 4.1 shows the lowest-energy configurations for  $x = 0.167$ ,  $x = 0.333$  and  $x = 0.5$ . A clear pattern emerges here: cationic dopants prefer to concentrate on the same layer perpendicular to the hexagonal cell main axis (c-axis), and at the same time, these full impurity layers prefer to be as far as possible from each other. These ordered patterns are consistent with a simple interaction model where  $\text{Mn}^{2+}$ - $\text{Mn}^{2+}$  interactions are favourable within (0001) planes but unfavourable between planes, as suggested recently by Katsikopoulos et al. (2009) based on empirical evidence. This tendency is quite strong and remains valid for all

compositions in the solid solutions, as will be discussed below.

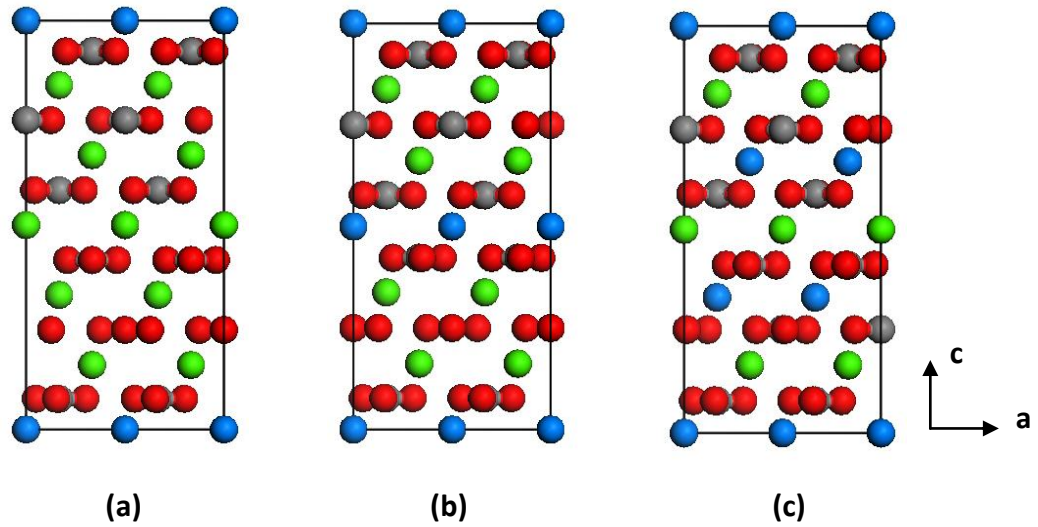


**Figure 4.1:** The structures of the most stable configurations for  $x = n/6$  ( $n = 1, 2, 3$ ). The lowest-energy structures for  $n = 4$  and 5 can be obtained from the ones with  $n = 2$  and 1, respectively, if  $\text{Ca}^{2+}$  and impurity  $\text{Me}^{2+}$  positions are swapped. The  $n = 3$  case ( $x = 0.5$ ) corresponds to the ordered dolomite-type structure. (Ca = green, C = grey, O = red, Me = blue).

Figure 4.2 shows the calculated lattice energy  $U_m$  of the mixed systems for Me composition  $x = 0.25$ , where the black line is the lowest lattice energy, the blue line is the highest lattice energy, and the red line is the average in the complete configurational space for this composition. A simple inspection of the results shows that the difference between the lowest and highest lattice energies  $U_m$  generally declines with increasing Me-O coordination distance, namely  $\Delta U_{\text{Ni}} > \Delta U_{\text{Mg}} > \Delta U_{\text{Zn}} > \Delta U_{\text{Co}} > \Delta U_{\text{Fe}} > \Delta U_{\text{Mn}} > \Delta U_{\text{Cd}}$ . For the mixed carbonate system containing either  $\text{Ni}^{2+}$ ,  $\text{Mg}^{2+}$ ,  $\text{Zn}^{2+}$ ,  $\text{Co}^{2+}$  or  $\text{Fe}^{2+}$ , the average lattice energy approximately equals the lowest lattice energy; therefore a large degree of cation ordering should be expected in these systems, at least when temperature is not included in the calculations.

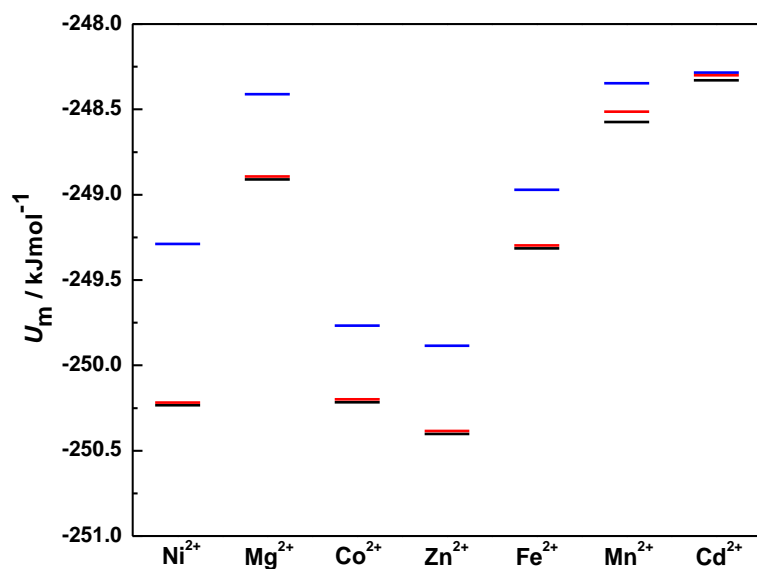


**Figure 4.2:** The lowest (black line) and highest (blue line) lattice energies of mixed systems for  $\text{Me}^{2+}$  composition  $x = 0.25$ , compared to the average lattice energy in the configurational space (red line).

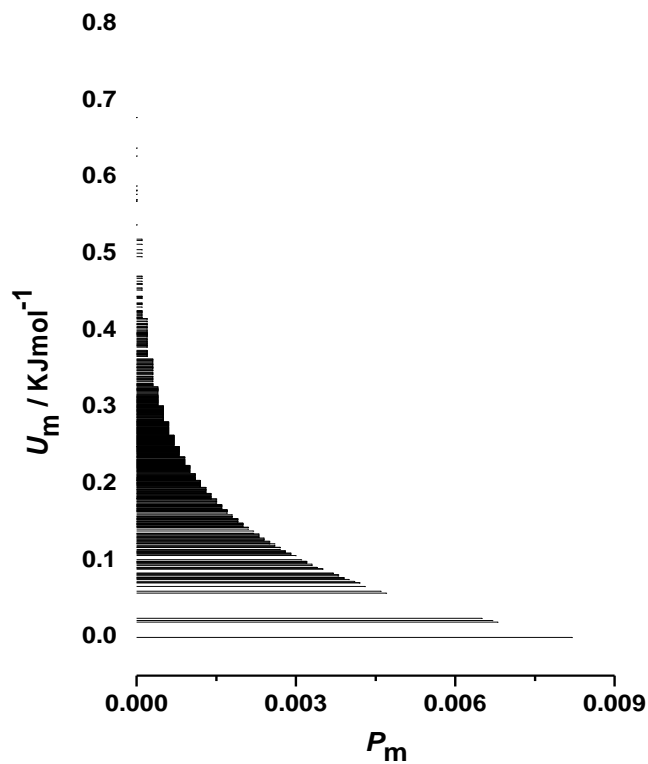


**Figure 4.3:** Configurational spectrum of lattice energies corresponding to the composition of  $\text{Cd}_{0.25}\text{Ca}_{0.75}\text{CO}_3$  at 300 K, as calculated in a  $2 \times 2 \times 1$  supercell.

On the contrary, there should be a certain degree of cationic ordering in the cases of  $\text{Mn}^{2+}$  or  $\text{Cd}^{2+}$ . The spectrum of configurations corresponding to  $\text{Cd}^{2+}$  composition  $x = 0.25$  at 300 K is shown in Figure 4.3, where the zero-level (ground state) is defined as the lattice energy of the most stable configuration. The number of configurations with more homogeneous  $\text{Cd}^{2+}$  distribution is larger than those with cation ordering, and the entropic effect is much stronger than the weak stabilization yielded by the interaction between the impurities. Thus a great deal of cation disorder should be present in the  $\text{Cd}^{2+}$  distribution at moderate temperatures.

The configurational entropy provides a quantitative measure of the degree of cation ordering in the mixed systems. As the impurity cation composition  $x = 0.042$  corresponds to one  $\text{Me}^{2+}$  substitution of any of the 24 equivalent  $\text{Ca}^{2+}$  in a  $2 \times 2 \times 1$  supercell, all 24 configurations are therefore equivalent and the configurational entropy remains at its maximum value,  $S_{max}$ , for this supercell with an increase in temperature. For other impurity compositions, where there are a number of possible inequivalent distributions of the cations, the configurational entropy is not constant and gradually approaches the maximum value at high temperatures. Figure 4.4 shows the variation of the configurational entropy of the solid solutions with temperatures at  $\text{Me}^{2+}$  composition  $x = 0.333$ . For  $\text{Cd}^{2+}$ , the entropy curve quickly reaches 96% of its maximum value at 300 K, and 98% at 700 K, which means the solid solution is almost ideally disordered even at relatively low temperatures of around 300 K. For  $\text{Mn}^{2+}$ , the configurational entropy reaches 16% of its maximum value at 300 K, and 74% at 1000 K, indicating that some level of ordering can be present at low temperatures (<1000 K), if there is full configurational equilibrium. For other cations,  $\text{Ni}^{2+}$ ,  $\text{Mg}^{2+}$ ,  $\text{Zn}^{2+}$ ,  $\text{Co}^{2+}$  and  $\text{Fe}^{2+}$ , the configurational entropy deviates from its maximum value even at relevant high temperature (e.g. ~1900 K), which means that a great deal of cation ordering should be expected in these solid solutions.

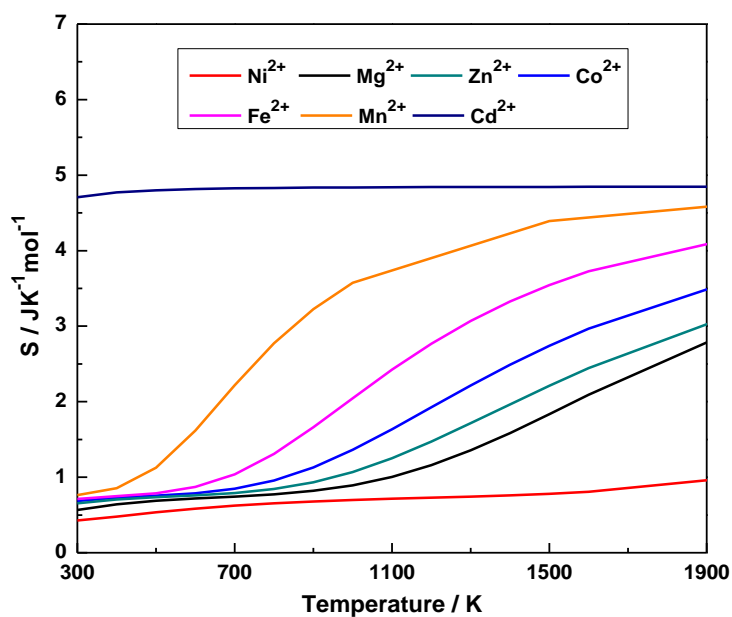


**Figure 4.4:** Variation of the configurational entropy corresponding to the composition of  $\text{Me}_{0.33}\text{Ca}_{0.67}\text{CO}_3$  at 300 K, as calculated in a  $2 \times 2 \times 1$  supercell.

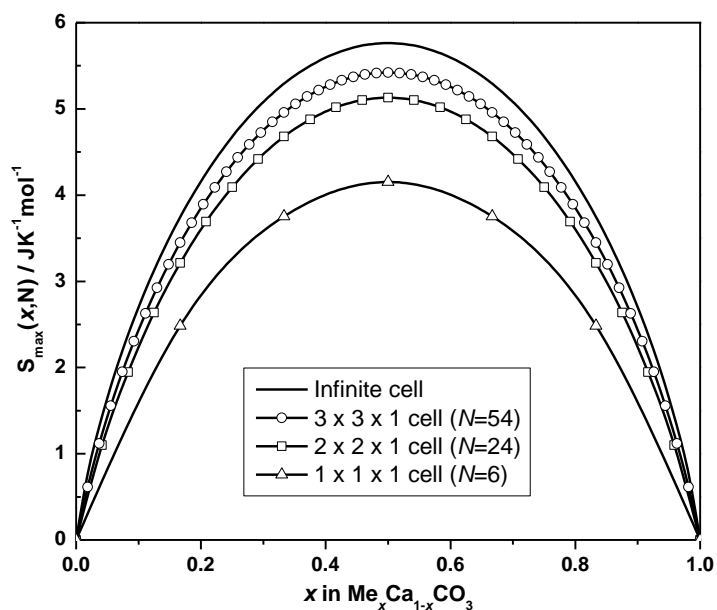


**Figure 4.5:** Variation of the maximum configurational entropy (in the full disorder limit) with the supercell size.

It is important to note here that the absolute entropy values are not well converged with respect to the supercell size  $2 \times 2 \times 1$  for  $N = 24$ . To illustrate this

point, the variation of the maximum entropy  $S_{max}$  for different cell sizes in comparison with the exact results in the full disorder limit, for which an analytical expression exists (equation 4.7), is shown in Figure 4.5. For the  $2 \times 2 \times 1$  supercell ( $N = 24$ ) the high temperature limit is in significant error (e.g. by 12% for  $x = 0.25$ ). Although the calculated configurational entropies are not fully converged, they are still useful to assess the level of order to be expected in the systems.

## 4.4 $\text{MnCO}_3\text{-CaCO}_3$ solid solutions

Manganese carbonate ( $\text{MnCO}_3$ ) occurs naturally as the mineral rhodochrosite, which is iso-structural with calcite. The significant difference in ionic radius between  $\text{Ca}^{2+}$  (1.00 Å) and  $\text{Mn}^{2+}$  (0.83 Å) for six-fold coordination suggests that a fully disordered solution is unlikely to occur in the mixed carbonate. The variation of the configurational entropy of the  $(\text{Mn,Ca})\text{CO}_3$  system with temperature also indicates that a random distribution of  $\text{Mn}^{2+}$  can only be present in calcite at high temperatures, as we have discussed before.

Although  $(\text{Mn,Ca})\text{CO}_3$  solid solutions have been widely studied using experimental techniques, seemingly contradictory results are still reported in the literature, particularly in respect of the range of the miscibility gap at different temperatures and the thermodynamics of the mixing properties at intermediate compositions. Several researchers have proposed the existence of a wide miscibility gap in the  $\text{Mn}_x\text{Ca}_{1-x}\text{CO}_3$  solid solution. For example, Goldsmith and Graf (1957) reported the existence of a miscibility gap for  $0.6 < x < 0.75$  at ambient temperatures, and suggested that complete miscibility only occurs above 823 K. De Capitani and Peters (1981) studied the solvus in the  $(\text{Mn,Ca})\text{CO}_3$  system and found that the critical point lies at 813 K with a miscibility gap for  $0.5 < x < 0.9$  at 623 K. In contrast, other

studies that have analyzed samples of natural and synthetic origin, have found that the miscibility gap covers most of the  $Mn^{2+}$  compositional range at room temperature (Winter *et al.*, 1981; Pedersen, 1982; McBeath *et al.*, 1998).

The intermediate composition  $Mn_{0.5}Ca_{0.5}CO_3$  and the stability of the ordered phase with this composition (kutnahorite) at different temperatures also leave a number of unanswered questions. For example, Capobianco and Navrotsky (1987) reported a positive free energy of mixing for the  $Mn_{0.5}Ca_{0.5}CO_3$  system at high temperature. Similarly, Katsikopoulos *et al.* (2009) also determined from calorimetric measurements a positive enthalpy of mixing for the  $Mn_{0.5}Ca_{0.5}CO_3$  system at 298 K, although McBeath and co-workers (1998) measured a negative value at 298 K. Furthermore, whereas the ordered kutnahorite structure has been found in previous work, Katsikopoulos *et al.* (2009) indicated that it is not likely to precipitate at ambient temperatures, and the X-ray diffraction experiments do not show the clear superstructure reflections typical of kutnahorite ordering. They argue that these incompatible results are probably due to kinetic factors, such as precipitation rate and phase equilibrium at high supersaturation, which are difficult to control in experiments.

In order to study the thermodynamic stabilities of the solid solutions, including the contribution from the configurational entropy, it is useful to evaluate the enthalpy of mixing and free energy of mixing as a function of composition at a range of temperatures:

$$\Delta H_{mix} = H[Mn_xCa_{1-x}CO_3] - (1-x)\frac{1}{N}U[CaCO_3] - x\frac{1}{N}U[MnCO_3] \quad (4.10)$$

$$\Delta G_{mix} = G[Mn_xCa_{1-x}CO_3] - (1-x)\frac{1}{N}U[CaCO_3] - x\frac{1}{N}U[MnCO_3] \quad (4.11)$$

where  $H[Mn_xCa_{1-x}CO_3]$  is the enthalpy per formula unit of the solid solution,

$G[\text{Ca}_{1-x}\text{Mn}_x\text{CO}_3]$  is the free energy per formula unit of the mixed system, and  $U[\text{CaCO}_3]$  and  $U[\text{MnCO}_3]$  are the lattice energies of the pure calcite and rhodochrosite, as there are no configurational entropy contributions to the free energy of the pure carbonate systems.

The negligible errors associated with using the internal energies  $U$  (instead of the proper enthalpies  $H$ , which include both zero-point and heat capacity contributions) have been found. For example, for  $\text{Mn}_{1/24}\text{Ca}_{23/24}\text{CO}_3$  at 298 K, the enthalpy of mixing changes from  $\Delta H_{mix} = 0.707 \text{ kJmol}^{-1}$  to  $0.699 \text{ kJmol}^{-1}$  when vibrational contributions are considered, which is change of  $\sim 1\%$  only. This is not surprising, as vibrational contributions to mixing enthalpies tend to be very small (Benny *et al.*, 2009; Ruiz-Hernandez *et al.*, 2010). This simplification is a significant advantage to the simulation, as the free energy minimisation costs much more computational time and requires a separate set of energy minimisation at each temperature. Conversely, the same set of configuration energies can be used for the statistics at any temperature if the vibrational contribution is ignored.

At first the fully disordered  $\text{Mn}_x\text{Ca}_{1-x}\text{CO}_3$  system for compositions  $x < 0.33$  was investigated. All the equilibrium geometries and energies of the Ca-rich configurations were calculated, and the average energy was taken in the high temperature limit ( $T \rightarrow \infty$ ), i.e., configurations were only weighted by their degeneracies, regardless of their energies. Figure 4.6 shows the enthalpies of mixing  $\Delta H_{mix}$  as a function of  $\text{Mn}^{2+}$  composition, together with experimental findings by other authors. The calculated  $\Delta H_{mix}$  of the fully disordered system is clearly positive, which is also seen in experiments. The consideration of a larger simulation cell ( $3 \times 3 \times 1$ , red empty squares in Figure 4.6), does not seem to alter significantly the values of the mixing enthalpy. However, the theoretical values seem to be too high

when compared with the calorimetric measurements by Katsikopoulos *et al.* (2009) and Capobianco & Navrotsky (1987).

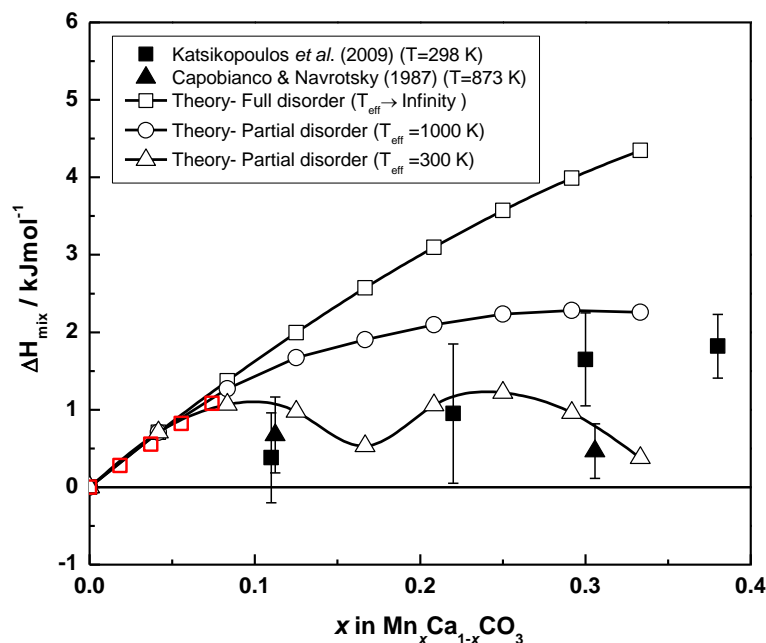


**Figure 4.6:** Calculated and experimental mixing enthalpies for the Ca-rich  $\text{Mn}_x\text{Ca}_{1-x}\text{CO}_3$  solid solution. The empty squares in red colour correspond to calculations in the full disorder limit with the  $3 \times 3 \times 1$  supercell.

This discrepancy can arise from systematic errors in either the simulations or the experiments. However, it is also possible to explain this discrepancy by considering that there may be some degree of ordering in the experimental samples, which reduces their mixing enthalpies with respect to the full disorder limit. It is notable that although Katsikopoulos *et al.* (2009) were able to rule out kutnahorite type (see Figure 4.1c) of ordering in their samples, based on the absence of superstructure reflections in the X-ray diffraction (XRD) patterns, diffraction techniques are not well suited to assess the level of disorder in poorly ordered samples, say, in comparison with the ideal disorder limit. Therefore, the suggestion of imperfect disorder in the samples does not conflict with the available experimental information. Figure 4.6 also illustrates the enthalpies of mixing for the calcium-rich mixed system

considering full equilibration at 300 K and 1000 K. The theoretical values of  $\Delta H_{mix}$  of the partially ordered systems are lower as a result of higher weighting of the lower-energy configurations. In this case, the theoretical prediction agrees much better with the experimental results, especially when considering the wide error bars of the experimental data points.

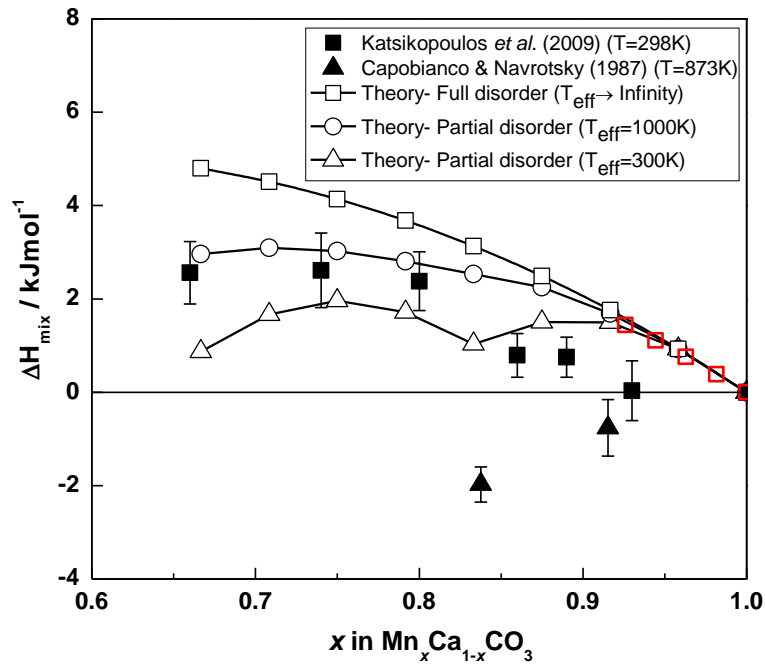


**Figure 4.7:** Calculated and experimental mixing enthalpies for the Mn-rich  $\text{Mn}_x\text{Ca}_{1-x}\text{CO}_3$  solid solution. The empty squares in red colour correspond to calculations in the full disorder limit with the  $3 \times 3 \times 1$  supercell.

Similar trends of mixing enthalpies were also found in the case of Ca-substituted rhodochrosite, i.e.  $\text{Mn}_x\text{Ca}_{1-x}\text{CO}_3$  solid solutions with high concentrations of  $\text{Mn}^{2+}$ . Figure 4.7 shows the enthalpies of mixing as a function of  $\text{Mn}^{2+}$  composition ( $x > 0.66$ ), again compared with experiments. As for the Ca-rich compositions, the consideration of a larger  $3 \times 3 \times 1$  supercell does not change significantly the values of the mixing enthalpies. The  $\Delta H_{mix}$  for the incorporation of  $\text{Ca}^{2+}$  in rhodochrosite is somewhat higher than for  $\text{Mn}^{2+}$  impurities in calcite, i.e. it is energetically more

expensive to substitute  $\text{Ca}^{2+}$  into rhodochrosite than  $\text{Mn}^{2+}$  into calcite, due to the larger ionic radius of  $\text{Ca}^{2+}$  compared to  $\text{Mn}^{2+}$ . It is generally found that smaller cations can substitute more easily in positions normally occupied by larger cations, which causes less elastic strain in the lattice than the opposite scenario (McLean, 1957; de Leeuw and Parker, 2000). Similar to the incorporation of  $\text{Mn}^{2+}$  in calcite, the positive values of the calculated  $\Delta H_{mix}$  in the fully disordered  $(\text{Mn,Ca})\text{CO}_3$  systems are somewhat higher than the experimental measurements. Again when partial cation ordering is considered in the systems, the enthalpy of mixing decreases and becomes closer to the experimental measurements by Katsikopoulos *et al.* (2009). It is interesting to note that earlier experiments by Capobianco & Navrotsky (1987) had reported negative values of  $\Delta H_{mix}$  for these Mn-rich compositions. Our calculated mixing enthalpies, as well as those obtained in the simulations by Vinograd *et al.* (2010), are positive for these compositions, in agreement with the most recent experiments. As pointed out by Katsikopoulos *et al.* (2009), it seems likely that these measurements were performed on samples with significant level of ordering.

The structure, cation ordering behaviour and stability in  $\text{Mn}_{0.5}\text{Ca}_{0.5}\text{CO}_3$  at different temperatures have also been investigated. The fully ordered  $\text{Mn}_{0.5}\text{Ca}_{0.5}\text{CO}_3$  structure has been detected in the natural mineral kutnahorite (Fron del, 1955), which exhibits dolomite-type cation ordering, where  $\text{Mn}^{2+}$  and  $\text{Ca}^{2+}$  layers alternate with layers of  $\text{CO}_3^{2-}$  groups along the crystallographic c-axis, as displayed in Figure 4.8. When simulating the cation disorder in a  $2 \times 2 \times 1$  supercell, this composition ( $x = 0.5$ ) leads to a total of almost three million configurations, which are computationally too expensive to calculate directly. Therefore, a random sampling method has been employed to generate a series of groups, where the number of configurations increases in successive groups from 1,000 to 10,000. The enthalpy of mixing  $\Delta H_{mix}$

based on the equilibrium geometries and energies of all the configurations in each group were then calculated. The results show that the configurational spectrum is very dense, with many configurations having very similar energies. However, in all cases, the lowest energy arrangement of cations corresponds to the dolomite-like kutnahorite structure. The least stable configuration found in the random sampling had lattice energy of  $56 \text{ kJmol}^{-1}$  ( $2.3 \text{ kJmol}^{-1}$  per formula unit) higher than the ordered kutnahorite structure.

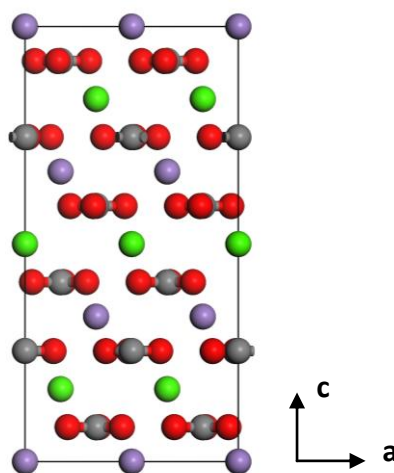


**Figure 4.8:** The structure of kutnahorite, showing  $\text{Mn}^{2+}$  and  $\text{Ca}^{2+}$  occupy alternating interlayers. (Ca = green, Mn = purple, C = grey, O = red).

In order to test the convergence of the results with respect to the configuration sample size, it has been checked that the calculated mixing enthalpy at high temperature does not depend on the inclusion of the kutnahorite configuration in the sample (Figure 4.9). In the limit of full disorder ( $T \rightarrow \infty$ ), the exclusion of the kutnahorite configuration does not make any difference on the average enthalpy even for relatively small sample sizes (*e.g.* 1,000 configurations). However, if equilibration at a finite temperature (*e.g.* 3000 K) is allowed, much more configurations are required to produce a robust result. For  $\sim 10,000$  configurations, the average is practically independent of the presence of the kutnahorite

configuration. Therefore, a sample of this size can be assumed to provide a good representation of the energy distribution in the full configurational spectrum at this temperature.

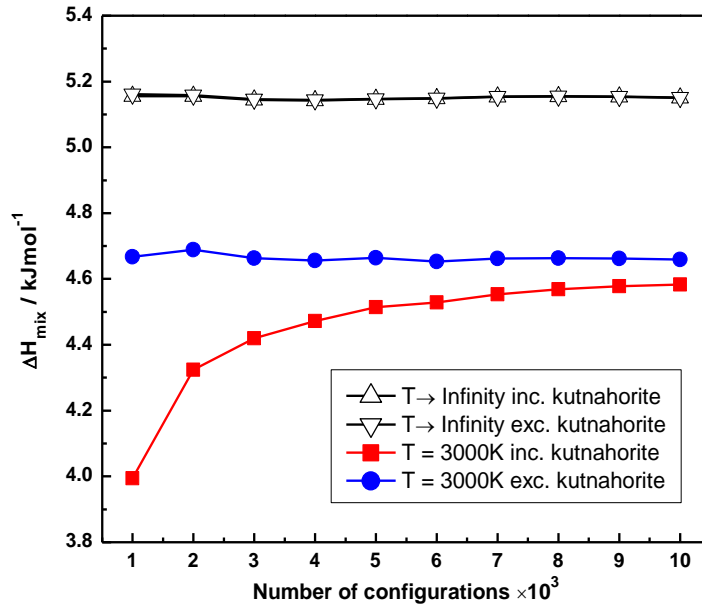


**Figure 4.9:** The variation of enthalpy of mixing with different number of  $\text{Mn}_{0.5}\text{Ca}_{0.5}\text{CO}_3$  configurations at 3000 K and infinitely high temperature.

Figure 4.9 also shows that there is a significant difference in the average enthalpy between the fully disordered solid solution, where all the configurations enter with the same weight, and one with some level of ordering, where the lowest-energy configurations have increased weights. The temperature of 3000 K in this case does not represent a real thermal effect, but it is introduced to show the increasing presence of lower-energy cation arrangements, which is possible even in a sample that is not in configurational equilibrium. As in the cases of Ca-rich and Mn-rich solid solutions, the assumption of such a moderate degree of cation ordering leads to better agreement of the calculations with experimental results. The transition temperature of kutnahorite to disordered  $\text{Mn}_{0.5}\text{Ca}_{0.5}\text{CO}_3$  has been evaluated, by computing the free energy difference between the disordered and ordered phases:

$$\Delta G = H_{disordered} - TS_{disordered} - H_{kutnahorite} \quad (4.12)$$

where  $H_{disordered}$  is the enthalpy of the disordered  $Mn_{0.5}Ca_{0.5}CO_3$  solid solution,  $H_{kutnahorite}$  is the enthalpy of the ordered kutnahorite phase and  $S_{ideal}$  is the ideal entropy of the  $Mn_{0.5}Ca_{0.5}CO_3$  system, which is calculated theoretically:

$$S_{ideal} = -k_B[x \ln x + (1-x) \ln(1-x)] = k_B \ln 2 = 5.763 \times 10^{-3} kJmol^{-1}K^{-1} \quad (4.13)$$

The enthalpy of the disordered  $Mn_{0.5}Ca_{0.5}CO_3$  solid solution was evaluated in equation 4.12 both in the limit of full disorder and in the case of some incipient ordering, corresponding to the 3000 K calculation explained above.

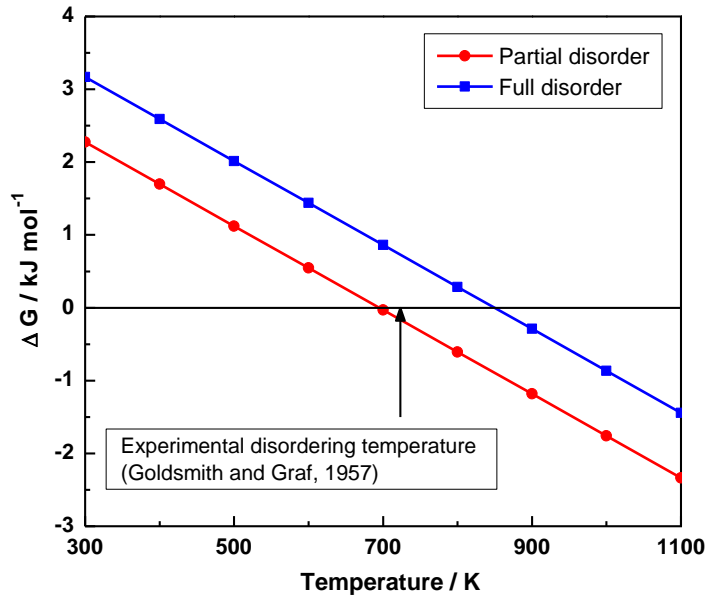


**Figure 4.10:** The different in free energy  $\Delta G$  between the disordered  $Mn_{0.5}Ca_{0.5}CO_3$  and kutnahorite as a function of temperature. The negative  $\Delta G$  indicates the disordered  $Mn_{0.5}Ca_{0.5}CO_3$  is more stable than ordered kutnahorite at this temperature.

Figure 4.10 illustrates that the disordered phase is predicted to become stable at 849 K if the full disorder enthalpy is used. However, allowing for some degree of ordering in the solid solution reduces the transition temperature to 695 K, which is in

better agreement with the experimental disordering temperature of kutnahorite (723 K) given by Goldsmith and Graf (1957). Thus, again, agreement between theory and experiment is better if it is assumed that *disordered* solid solutions are not really fully disordered but contain some small bias towards lower energy configurations.

Due to the positive enthalpy of mixing of the (Mn,Ca)CO<sub>3</sub> solid solution, the system can only form a full disordered phase at high temperature (e.g. 849 K). Therefore, the free energy of mixing  $\Delta G_{mix}$  was then calculated using equation 4.11 to study the thermodynamic stability of the disordered (Mn,Ca)CO<sub>3</sub> solid solution, including the contribution from the configurational entropy. In order to compare with experiment, where the mixed system is thought to be disordered, the free energy of the system  $G[\text{Mn}_x\text{Ca}_{1-x}\text{CO}_3]$  at the relevant temperature was estimated from the enthalpy of the fully disordered system and the ideal entropy.

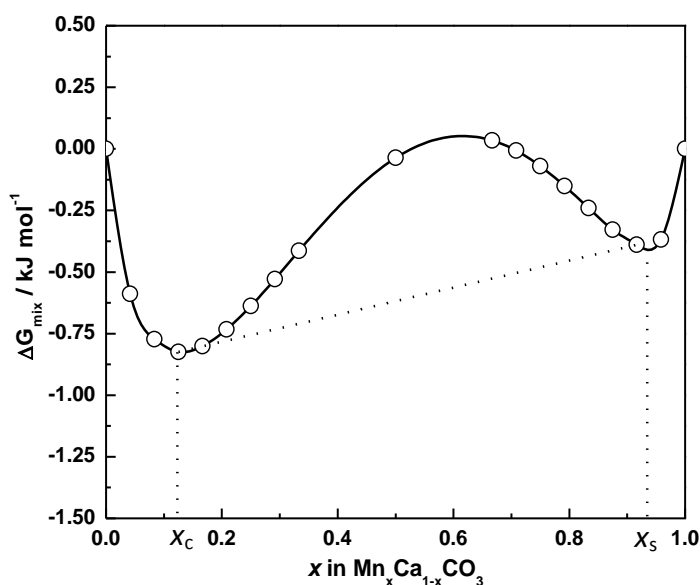


**Figure 4.11:** Calculated free energy of mixing with full range of Mn<sup>2+</sup> compositions at 900 K.

Figure 4.11 displays the calculated free energy of mixing  $\Delta G_{mix}$  at 900 K. The  $\Delta G_{mix}$  is negative for the whole Mn<sup>2+</sup> composition at 900 K with the curve exhibiting

two local minima at  $x_c = 0.12$  and  $x_s = 0.92$ , which indicates the formation of a metastable solid solution with respect to separation into a Ca-rich and Mn-rich phase in the range of  $0.12 < x < 0.92$ . This miscibility gap is similar to the reports by Katsikopoulos *et al.* (2009), where a miscibility gap in disordered  $(\text{Mn,Ca})\text{CO}_3$  solid solution was found for a  $\text{Mn}^{2+}$  composition of  $0.13 < x < 0.98$ .

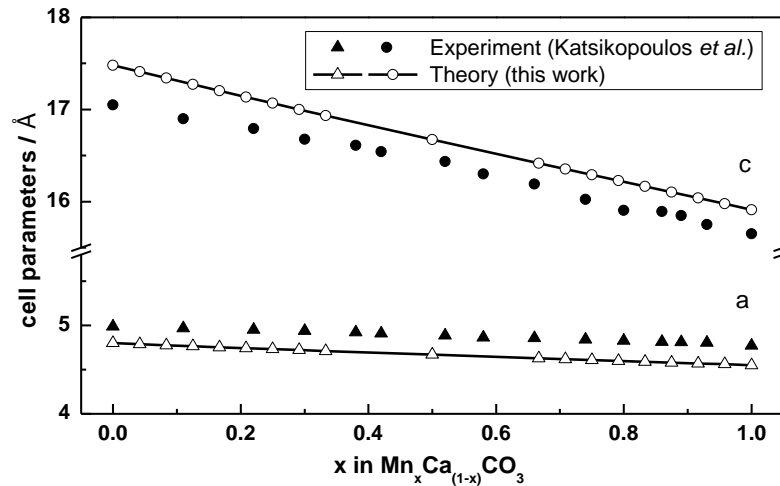


**Figure 4.12:** Variation of the lattice parameters of  $\text{Mn}_x\text{Ca}_{1-x}\text{CO}_3$  as a function of composition, in comparison with experiment (Katsikopoulos *et al.*, 2009).

The average lattice parameters of the fully disordered  $\text{Mn}_x\text{Ca}_{1-x}\text{CO}_3$  systems were calculated through equation 4.9. The variation of the lattice parameters  $a$  (where  $a = b$ ) and  $c$  with  $\text{Mn}^{2+}$  composition is plotted in Figure 4.12, which shows that both lattice parameters decrease with increasing  $\text{Mn}^{2+}$  substitution, as expected from the smaller ionic radius of  $\text{Mn}^{2+}$  compared to  $\text{Ca}^{2+}$ , and in agreement with experiments. The small deviation from the linear Vegard's law reported in the paper by Katsikopoulos *et al.* (2009) for intermediate compositions was not obtained in the calculations in the full disorder limit, suggesting that the non-linear behaviour is most likely associated with a deviation from perfect disorder in the experimental samples, consistent with the discussion above.

## 4.5 CdCO<sub>3</sub>-CaCO<sub>3</sub> solid solutions

Otavite (CdCO<sub>3</sub>) is a rare mineral in nature as Cd is usually a trace element in other minerals, and it is iso-structural with calcite. The ionic radii of Ca<sup>2+</sup> and Cd<sup>2+</sup> in octahedral coordination to oxygen are 1.00 Å and 0.97 Å (Shannon and Prewitt, 1969). Therefore, a complete miscibility in (Cd,Ca)CO<sub>3</sub> solid solution could be conjectured due to the similarity in ionic radii of two metals.

The Cd<sub>x</sub>Ca<sub>1-x</sub>CO<sub>3</sub> systems have been studied in various experiments, which have showed high values of the distribution coefficient of Cd<sup>2+</sup> in calcite. The relatively rapid initial uptake of Cd<sup>2+</sup> at the calcite surface has been interpreted as chemisorption, and the long-term uptake by calcite occurs via surface precipitation of (Cd,Ca)CO<sub>3</sub> solid solutions. Most sorption experiments have been carried out with extremely low concentrations of Cd<sup>2+</sup> and in the presence of complexing ligands to avoid saturation with respect to pure otavite. However, a study by Tesoriero and Pankow (1996) has shown that if calcite is present, precipitation of Cd<sup>2+</sup> as a carbonate solid solution will always occur, even when Cd<sup>2+</sup> is present at trace levels, due to the strong tendency of this ion to partition into calcite.

To estimate the thermodynamic properties of (Cd,Ca)CO<sub>3</sub> solid solutions, Königsberger *et al.* (1991) overcame partial disequilibrium by achieving states that successively approximate equilibrium and they concluded that the mixing in the (Cd,Ca)CO<sub>3</sub> solid solution was ideal. Stipp *et al.* (1992) also report nearly ideal mixing between an otavite layer grown epitaxially over calcite. However, Davis *et al.* (1987) and Rock *et al.* (1994) suspected that the mixing was non-ideal on the basis of the discrepancies between the measured distribution coefficient and the distribution coefficient predicted from ideal mixing, although the discrepancies are sensitive to uncertainties in the estimates of the free energy of formation,  $\Delta G_f[\text{CdCO}_{3(s)}]$ .

Firstly, we have investigated the structure, cation ordering behaviour and stability of the intermediate composition,  $\text{Cd}_{0.5}\text{Ca}_{0.5}\text{CO}_3$ , at different temperatures. The random sampling method was also employed here to generate a series of groups, where the number of inequivalent configurations increases in successive groups from 1,000 to 10,000. The enthalpy of mixing  $\Delta H_{mix}$  based on the equilibrium geometries and energies of all the configurations were calculated in each group. The results showed that the fully ordered  $\text{Cd}_{0.5}\text{Ca}_{0.5}\text{CO}_3$  structure exhibits dolomite-type cation ordering. Additionally, the configurational spectrum of  $\text{Cd}_{0.5}\text{Ca}_{0.5}\text{CO}_3$  in the  $2 \times 2 \times 1$  supercell is very dense, with many configurations having very similar energies.

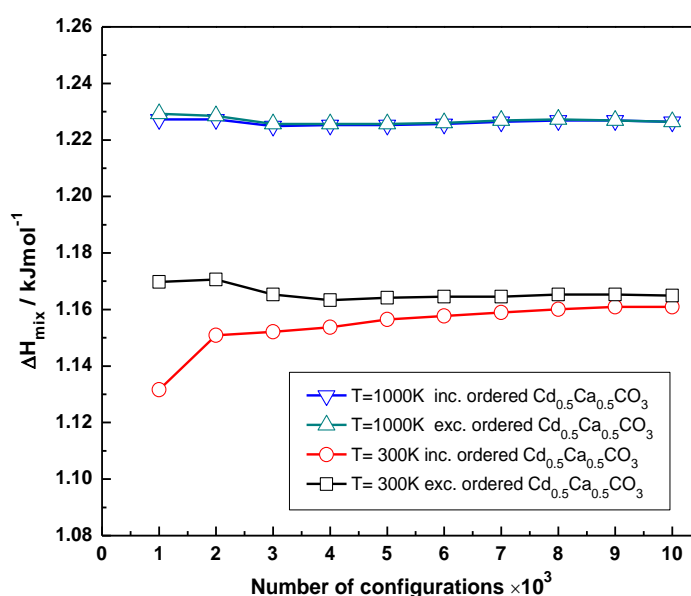


**Figure 4.13:** The variation of enthalpy of mixing with different number of inequivalent  $\text{Cd}_{0.5}\text{Ca}_{0.5}\text{CO}_3$  configurations at 300 K and 1000 K.

Figure 4.13 shows the convergence of enthalpy of mixing,  $\Delta H_{mix}$ , with respect to the configuration sample size, which indicates that the calculated mixing enthalpy at high temperature (e.g.  $\sim 1000$  K) does not depend on the inclusion of the ordered dolomite-type configuration in the sample. The mixing enthalpy is practically dependent on the sample size and the presence of the ordered configuration at 300 K.

Although the enthalpy of mixing starts to converge when the number of configurations is larger than 5,000, a sample size of  $\sim 10,000$  configurations can provide a more precise representation of the energy distribution in the full configurational spectrum at this temperature (300 K).

The calculated enthalpy of mixing of the  $\text{CdCO}_3\text{-CaCO}_3$  solid solution is small and positive, as it is shown in Figure 4.14. Therefore the mixing is a slightly exothermic process. The thermodynamic stability of the solid solutions is given by the free energy of mixing, which is calculated by equation 4.11. The mixing free energies are negative at all temperatures of interest, indicating the formation of stable solid solutions and  $\text{Cd}^{2+}$  is soluble in calcite throughout the fully composition range in calcite under moderate conditions. The calculated results agree with previous experimental findings, which proved the  $\text{CaCO}_3\text{-CdCO}_3$  solid solutions are thermodynamic stable under moderate conditions (Königsberger *et al.*, 1991; Stipp *et al.*, 1992).

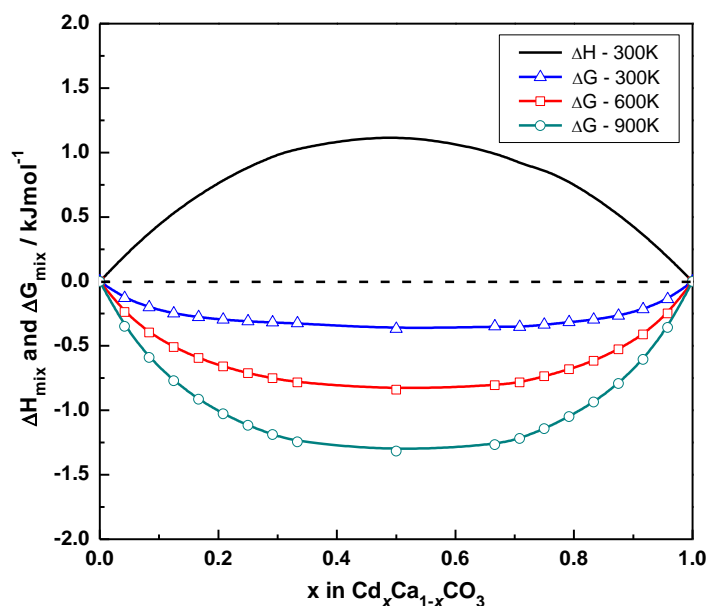


**Figure 4.14:** Calculated mixing enthalpy and mixing free energy of the  $\text{Cd}_x\text{Ca}_{1-x}\text{CO}_3$  system as a function of  $\text{Cd}^{2+}$  composition, as calculated for a  $2 \times 2 \times 1$  supercell.

Besides the free energy of mixing  $\Delta G_{mix}$ , it is common to report the excess free energy  $G^E$  of the solid solution, defined as:

$$G^E = \Delta G_{mix} - \Delta G_{mix}^{ideal} \quad (4.14)$$

$\Delta G_{mix}^{ideal}$  is the free energy of mixing in an ideal solid solution, where the only contribution comes from the ideal entropy corresponding to a fully disordered solid.

$$\Delta G_{mix}^{ideal} = k_B T [x \ln x + (1-x) \ln(1-x)] \quad (4.15)$$

The excess free energy  $G^E$  therefore contains all the non-ideal contributions to the mixing free energy: an enthalpy part ( $\Delta H_{mix}$ ) and an entropy part, which contains both the deviation of the configurational entropy from ideality and a contribution from the vibrational entropy of mixing.

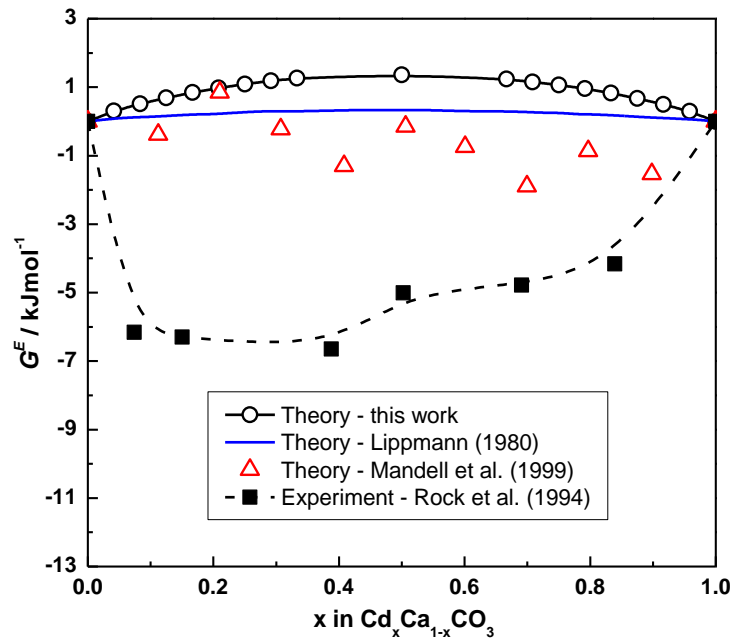


**Figure 4.15:** Comparison between theoretical and experimental excess free energies  $G^E$  findings for  $\text{Cd}_x\text{Ca}_{1-x}\text{CO}_3$  at 300 K.

Figure 4.15 shows a comparison of the calculated excess free energy  $G^E$  for  $\text{Cd}_x\text{Ca}_{1-x}\text{CO}_3$  at 300 K with the theoretical  $G^E$  prediction of Lippmann's electrostatic

model (1980), Mandell *et al.*'s (1999) lattice energy model and Rock *et al.*'s (1994) experimental findings, which are based on electrochemical cell-voltage measurement. The positive excess free energy indicates the mixing in  $\text{CdCO}_3\text{-CaCO}_3$  solid solution is non-ideal. The calculated theoretical values are not far from the  $G^E$  results by Lippmann (1980). The experimental results by Rock *et al.*, on the other hand, contrast significantly with the theoretical results. The difference of excess free energy between theoretical calculation and experimental measurement is expected because the magnitude of the estimated  $G^E$  is sensitive to the choice of free energy of formation of  $\text{CdCO}_3$ , which is uncertain in the experiments.

## 4.6 $\text{FeCO}_3\text{-CaCO}_3$ solid solutions

Siderite ( $\text{FeCO}_3$ ) is commonly found in hydrothermal veins and at shallow burial depths in sedimentary rocks. It also has the calcite-type structure, but as the ionic radius of  $\text{Fe}^{2+}$  (0.75Å) is only three quarters of that of  $\text{Ca}^{2+}$  in six-fold coordination, there should be obvious effect on the local structure of calcite. The variation of the configurational entropy of the  $(\text{Fe,Ca})\text{CO}_3$  system with temperature also indicates that some degree of cation ordering should be expected in the  $\text{FeCO}_3\text{-CaCO}_3$  solid solutions (see Figure 4.4).

The intermediate composition  $\text{Fe}_{0.5}\text{Ca}_{0.5}\text{CO}_3$  has never been detected in the natural environment. The enthalpy of mixing  $\Delta H_{mix}$  was calculated in successive groups from 1000 to 10,000 configurations by the random sampling method. The lowest energy arrangement of cations corresponds to the dolomite-type structure, and its lattice energy is  $110 \text{ kJmol}^{-1}$  ( $4.6 \text{ kJmol}^{-1}$  per formula unit) lower than the least stable configuration found in the random sampling. Although the number of configurations with more homogeneous  $\text{Fe}^{2+}$  distributions is larger than the ordered

dolomite-type structure, this entropic effect is weaker than the stabilization provided by the interaction in ordered dolomite-type structure. The calculated enthalpy of mixing  $\Delta H_{mix}$  does not depend on the sample size below 1500 K. Therefore, only 1000 configurations including ordered dolomite-type structure are assumed to be representative of the energy distribution in the configurational spectrum below 1500K.

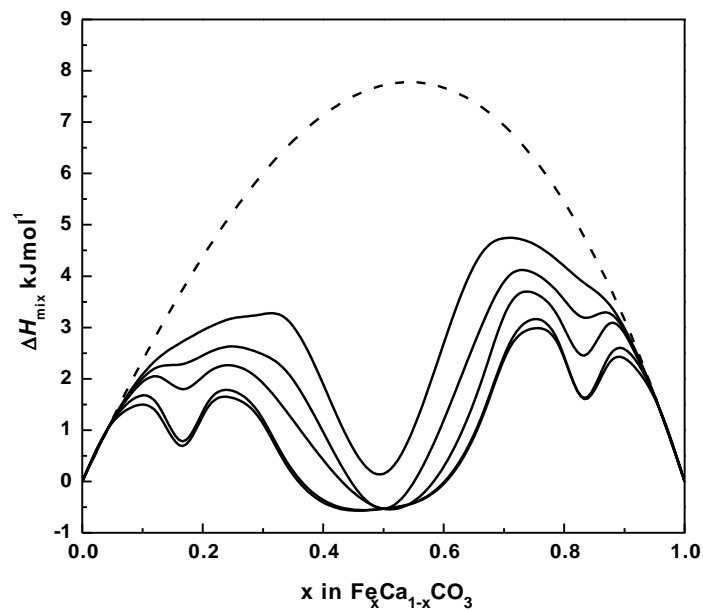


**Figure 4.16:** Calculated enthalpy of mixing in the  $\text{Fe}_x\text{Ca}_{1-x}\text{CO}_3$  system. The solid lines show the enthalpy isotherms between 300 K and 1500 K with a step of 300 K. The dashed lines show the enthalpy at an infinitely high temperature.

Figure 4.16 shows the enthalpies of mixing as a function of  $\text{Fe}^{2+}$  composition, as calculated in a  $2 \times 2 \times 1$  supercell. The calculated  $\Delta H_{mix}$  for the incorporation of  $\text{Ca}^{2+}$  in siderite is slightly higher than for  $\text{Fe}^{2+}$  in calcite, i.e. it is energetically more expensive to substitute  $\text{Ca}^{2+}$  into siderite than  $\text{Fe}^{2+}$  into calcite, due to the larger ionic radius of  $\text{Ca}^{2+}$  compared to  $\text{Fe}^{2+}$ . The  $\Delta H_{mix}$  of the mixed system is positive, indicating that the formation of the  $(\text{Fe,Ca})\text{CO}_3$  solid solution from pure calcite and siderite is endothermic except in the intermediate range of compositions. For the

intermediate compositions, the  $\Delta H_{mix}$  curves overlap each other below 1200 K as a result of higher weighting of the lower-energy configuration (dolomite-type structure). These results do not completely coincide with the native enthalpy of mixing of the mixed systems at low temperatures, as other mixed layered ordering structure like the dolomite-type structure, may also be present in the whole configurational spectrum.

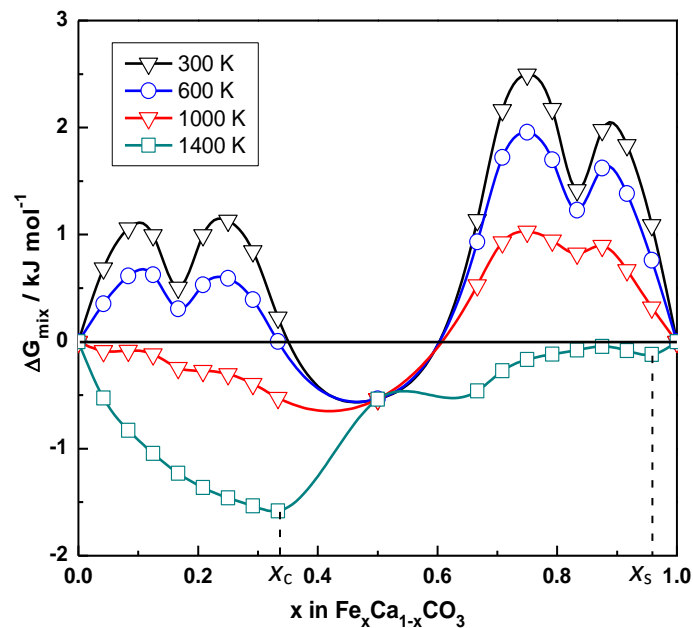


**Figure 4.17:** Calculated free energy of mixing of the  $\text{Fe}_x\text{Ca}_{1-x}\text{CO}_3$  system as a function of  $\text{Fe}^{2+}$  compositions.

The thermodynamic stability of  $(\text{Fe},\text{Ca})\text{CO}_3$  solid solution is given by the free energy of mixing calculated by equation 4.11 between 300 K and 1400 K, as illustrated in Figure 4.17. The maximum solubility of Fe in calcite is very close to  $x = 0.4$  at 1000 K. The free energy of mixing is negative for full Fe compositions above 1400 K, and there are two minima at  $x_c = 0.33$  and  $x_s = 0.96$ , which define a miscibility gap between calcite and siderite. The solid with composition between  $x_c < x < x_s$  is thermodynamically metastable with respect to a mechanical mixture of

phases with composition  $x_c$  and  $x_s$ . The prediction of a miscibility range in the  $\text{Fe}_x\text{Ca}_{1-x}\text{CO}_3$  solid solutions is in agreement with experimental studies. Goldsmith (1959) reported that the lower limit of the miscibility gap is 0.37 at 973 K, whereas Rosenberg (1963) predicted the miscibility gap between  $0.17 < x < 0.85$  at 823 K. It is noteworthy that the intermediate compositions are metastable and could not precipitate below 1400 K, which also confirmed the experimental findings. The dolomite-type  $\text{Fe}_{0.5}\text{Ca}_{0.5}\text{CO}_3$  has never been reported as a natural mineral and it is not a stable phase in the temperature range from 573 K to 823 K.

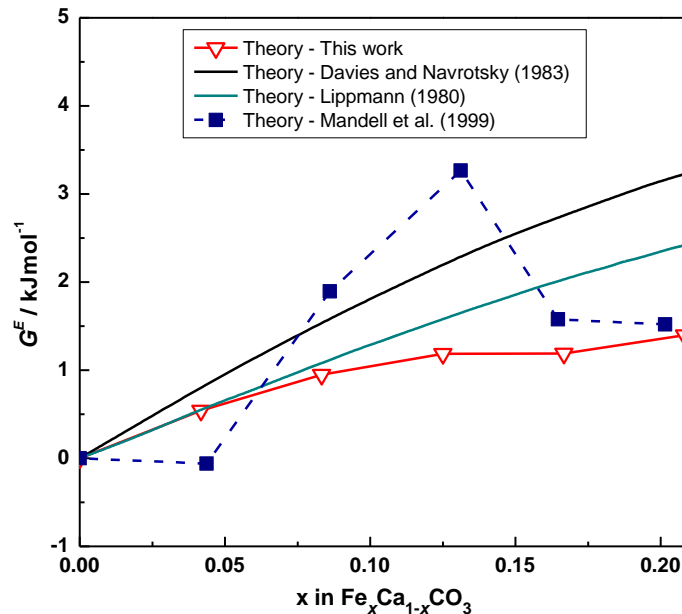


**Figure 4.18:** Comparison between theoretical excess Gibbs free energies  $G^E$  for the  $\text{Fe}_x\text{Ca}_{1-x}\text{CO}_3$  solid solutions at 823 K.

The results of excess free energy  $G^E$  for the  $\text{Fe}_x\text{Ca}_{1-x}\text{CO}_3$  system are displayed in Figure 4.18, together with theoretical finding by other authors. The positive excess free energy indicates the mixing in the  $\text{Fe}_x\text{Ca}_{1-x}\text{CO}_3$  solid solution is non-ideal. Davies and Navrotsky (1983) obtained positive  $G^E$  for the  $\text{Fe}_x\text{Ca}_{1-x}\text{CO}_3$  system from 573 K to 1073 K using a sub-regular solution model containing empirically

thermodynamic interaction parameters. Mandell *et al.* (1999) used an extending lattice energy calculation model to investigate the pure carbonate minerals and also predicted positive excess free energy at 823 K. The theoretical excess energies addressed in this work are consistent with these theoretical results by other authors.

## 4.7 Uptake of $\text{Zn}^{2+}$ and $\text{Co}^{2+}$ to calcite

The ionic radii and coordination distances to oxygen of  $\text{Zn}^{2+}$  and  $\text{Co}^{2+}$  in six-fold coordination are very similar. Smithsonite ( $\text{ZnCO}_3$ ) is commonly found in the natural environment, whereas cobalt calcite ( $\text{CoCO}_3$ ) is rare in nature. Smithsonite can form limited solid solutions with rhodochrosite and siderite. However, substitution of  $\text{Co}^{2+}$  in the structure of the common rhombohedral carbonates is not observed to any significant extent in nature, unlike the commonly observed substitutions of  $\text{Zn}^{2+}$ .

Various studies have used kinetic-spectroscopic techniques to investigate the interaction of  $\text{Zn}^{2+}$  with calcite. All experimental findings have shown a strong adsorbing behaviour of  $\text{Zn}^{2+}$  on the calcite surface, which can be described best by a Langmuir model (Zachara *et al.*, 1988; Temmam *et al.*, 2000; El-Korashy, 2003). For example, a spectroscopy study of synthetic and natural calcite samples containing traces of  $\text{Zn}^{2+}$  by Reeder *et al.* (1999) confirmed the substitution of  $\text{Zn}^{2+}$  for  $\text{Ca}^{2+}$  in octahedral coordination occurs via exchange with  $\text{Ca}^{2+}$  in a surface-adsorbed layer. The presence of large amounts of  $\text{Zn}^{2+}$  in a  $\text{Ca}^{2+}/\text{CO}_3^{2-}$ -bearing fluid reduces the growth rate of calcite, hinders the crystallisation of calcite and favours the formation of hydrozincite or aragonite (Glasner *et al.*, 1980; Meyer, 1984; Wada *et al.*, 1995). Freij *et al.* (2004) used AFM and batch sorption experiments to study the interaction of  $\text{Zn}^{2+}$  with calcite  $\{1\ 0\ \bar{1}\ 4\}$  surfaces during growth and dissolution. Their results showed that the growth of calcite in the presence of  $\text{Zn}^{2+}$  occurs by two-dimensional

nucleation, the growth rate decreasing with the development of each subsequent layer. All these studies provided significant information on the strong interaction of  $\text{Zn}^{2+}$  with calcite under different conditions, using various techniques. However, none dealt with the thermodynamic properties of the  $(\text{Zn,Ca})\text{CO}_3$  solid solutions at the atomic level, which are needed to understand the mechanism of adsorption and substitution.

At first the mixing enthalpies  $\Delta H_{\text{mix}}$  of intermediate composition  $\text{Zn}_{0.5}\text{Ca}_{0.5}\text{CO}_3$  and  $\text{Co}_{0.5}\text{Ca}_{0.5}\text{CO}_3$  in a  $2 \times 2 \times 1$  supercell have been calculated, based on the random sampling method. Because of the strong stabilization provided by the interaction in the ordered dolomite-type structure, the mixing enthalpies  $\Delta H_{\text{mix}}$  of both systems do not change with increasing sample size below 1500 K, which are similar to that of the  $(\text{Fe,Ca})\text{CO}_3$  system. Again, only the ordered dolomite-type configuration has been used in the calculation of the mixing free energy rather than the average of the whole configuration spectrum of  $\text{Zn}_{0.5}\text{Ca}_{0.5}\text{CO}_3$  and  $\text{Co}_{0.5}\text{Ca}_{0.5}\text{CO}_3$  below 1500 K.

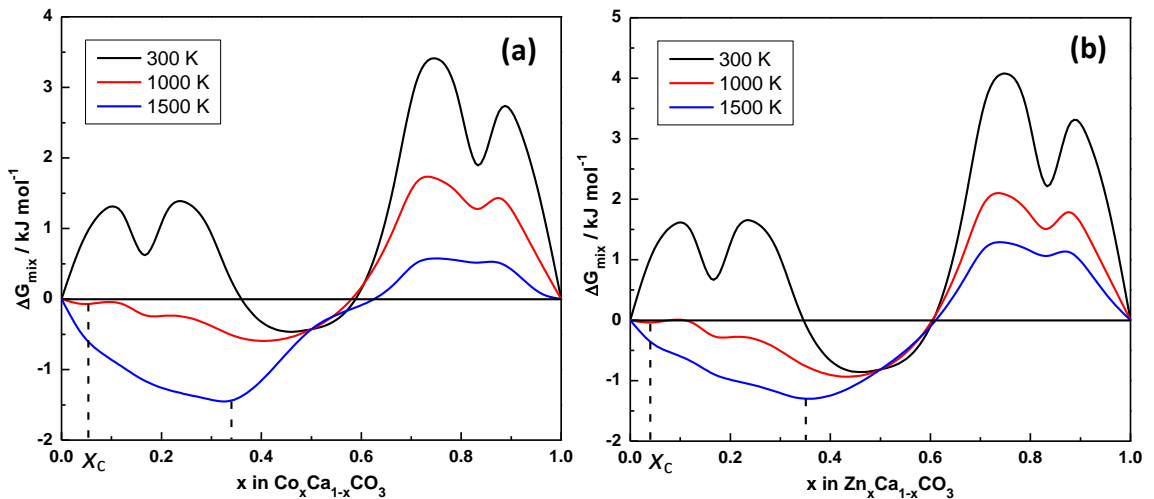


**Figure 4.19:** Calculated free energy of mixing with full range of  $\text{Co}^{2+}$  or  $\text{Zn}^{2+}$  compositions; (a)  $\text{Co}_x\text{Ca}_{1-x}\text{CO}_3$ , (b)  $\text{Zn}_x\text{Ca}_{1-x}\text{CO}_3$ .

The mixing free energy of the  $\text{Zn}_x\text{Ca}_{1-x}\text{CO}_3$  and  $\text{Co}_x\text{Ca}_{1-x}\text{CO}_3$  systems are calculated by equation 4.11 between 300 K and 1500 K, respectively. For the  $\text{Co}_x\text{Ca}_{1-x}\text{CO}_3$  system (see Figure 4.19a),  $\text{CoCO}_3$  is soluble in calcite below the  $\text{Co}^{2+}$  composition  $x = 0.06$  at 1000 K, and the solubility is close to  $x = 0.34$  at 1500 K. The solubility of  $\text{ZnCO}_3$  in calcite (see Figure 4.19b) is  $x < 0.04$  at 1000 K and  $x < 0.35$  at 1500 K, which is similar to that of  $\text{CoCO}_3$ . The free energy of mixing  $\Delta G_{mix}$  for  $\text{Co}^{2+}$  or  $\text{Zn}^{2+}$  is positive for the compositions  $x > 0.6$  indicating  $\text{Ca}^{2+}$  can be soluble in neither  $\text{CoCO}_3$  nor  $\text{ZnCO}_3$  below 1500 K.

The calculated miscibility range is not far from the experimental findings. Goldsmith and Northrop (1965) reported that the limit of the miscibility of  $\text{Co}_x\text{Ca}_{1-x}\text{CO}_3$  is  $x = 0.04$  at 873 K and  $x = 0.15$  at 1073 K. Limited coprecipitation of  $\text{Zn}^{2+}$  with  $\text{CaCO}_3$  has also been observed between 300 K and 523 K (Crocket and Winchester, 1966; Tsusue and Holland, 1966). Furthermore, although the free energies of mixing of the intermediate composition  $\text{Co}_{0.5}\text{Ca}_{0.5}\text{CO}_3$  and  $\text{Zn}_{0.5}\text{Ca}_{0.5}\text{CO}_3$  are negative, these mixed systems are metastable and tend to change into a Ca-rich phase below 1500 K, which also confirms that the dolomite-type  $\text{Co}_{0.5}\text{Ca}_{0.5}\text{CO}_3$  or  $\text{Zn}_{0.5}\text{Ca}_{0.5}\text{CO}_3$  does not exist in synthesis or nature (Goldsmith and Northrop, 1965).

## 4.8 Uptake of $\text{Mg}^{2+}$ and $\text{Ni}^{2+}$ to calcite

The ionic radii of  $\text{Mg}^{2+}$  (0.65 Å) and  $\text{Ni}^{2+}$  (0.72 Å) are much smaller than  $\text{Ca}^{2+}$  (1.00 Å). Former studies indicate that it is energetically favourable for  $\text{Mg}^{2+}$  to substitute  $\text{Ca}^{2+}$  in calcite due to the smaller ionic radius (Fork, 1974; Davis *et al.*, 2000). Magnesite ( $\text{MgCO}_3$ ) and dolomite ( $\text{MgCa}(\text{CO}_3)_2$ ) typically occur in nature, but nickel carbonate ( $\text{NiCO}_3$ ) has never been known as a mineral. Comparing with one of the best studied carbonate system  $(\text{Mg,Ca})\text{CO}_3$ , the  $(\text{Ni,Ca})\text{CO}_3$  system is still

less researched by experiment due to the decomposition of carbonates.

The (Mg,Ca)CO<sub>3</sub> system is one of the best studied metal calcite systems. Magnesium is considered as an important modifier of CaCO<sub>3</sub> growth and morphologies in aqueous solution. Although the presence of Mg<sup>2+</sup> in CaCO<sub>3</sub> is studied increasingly, the physical basis by which Mg<sup>2+</sup> modifies calcite growth has yet to be discerned. Bulk studies have suggested that the growth of calcite is inhibited through either step-blocking by Mg<sup>2+</sup> adsorption and slow dehydration (Lippman, 1960; Gutjahr *et al.*, 1996) or enhanced mineral solubility associated with lattice strain caused by the incorporated Mg<sup>2+</sup> (Fork, 1974; Berner, 1975). Davis *et al.* (2000) used AFM to resolve the mechanism of calcite inhibition by Mg<sup>2+</sup> at the molecular scale and determine the thermodynamic and kinetic controls of Mg<sup>2+</sup> on calcite formation. Their experiments demonstrated that Mg<sup>2+</sup> inhibits calcite growth by incorporation into the calcite lattice. The resultant increase in the mineral solubility forms the underlying physical basis for the reduced calcite growth rates observed in the presence of Mg<sup>2+</sup>. Hence a further understanding of the (Mg,Ca)CO<sub>3</sub> solid solution requires an accurate assessment as to how Mg<sup>2+</sup> modifies the calcite growth via solubility.

The structure and cationic ordering behaviour for the intermediate composition of dolomite (Mg<sub>0.5</sub>Ca<sub>0.5</sub>CO<sub>3</sub>) and Ni<sub>0.5</sub>Ca<sub>0.5</sub>CO<sub>3</sub> were initially investigated at different temperatures based on the random sampling method. The lowest energy arrangement of cations in the whole configurational spectrum corresponds to the dolomite-type structure. The least stable configuration found in the random sampling had a lattice energy of 148.5 kJmol<sup>-1</sup> (6.2 kJmol<sup>-1</sup> per formula unit) higher than the ordered dolomite structure. The lattice energy of dolomite-type Ni<sub>0.5</sub>Ca<sub>0.5</sub>CO<sub>3</sub> is 279.5 kJmol<sup>-1</sup> (11.6 kJmol<sup>-1</sup> per formula unit) lower than that of the least stable configuration. The stabilization provided by the interaction within the ordered

dolomite structure is so strong that there will be no configurational entropy contributions to the free energy of mixing  $\Delta G_{mix}$  of the intermediate compositions below 1500 K. Therefore, the lattice energy of the dolomite-type configuration can be assumed to be equal to the average enthalpy of intermediate compositions  $Mg_{0.5}Ca_{0.5}CO_3$  and  $Ni_{0.5}Ca_{0.5}CO_3$  below 1500 K.

The solubility of  $Mg^{2+}$  in calcite was then evaluated by calculating the free energy of mixing  $\Delta G_{mix}$  between calcite and ordered dolomite phase (equation 4.16,  $0 < x < 0.5$ ), or between dolomite and magnetite (equation 4.17,  $0.5 < x < 1$ ) as a function of  $Mg^{2+}$  compositions at a range of temperatures:

$$\Delta G_{mix}^1 = G[Mg_xCa_{1-x}CO_3] - (1-2x)U[CaCO_3] - 2xU[Mg_{0.5}Ca_{0.5}CO_3] \quad (4.16)$$

$$\Delta G_{mix}^2 = G[Mg_xCa_{1-x}CO_3] - (2x-1)U[MgCO_3] - (2-2x)U[Mg_{0.5}Ca_{0.5}CO_3] \quad (4.17)$$

where  $G[Mg_xCa_{1-x}CO_3]$  is the free energy of the mixed system, and  $U[Mg_{0.5}Ca_{0.5}CO_3]$  is the lattice energy of the pure dolomite, as there is no configurational entropy contributions to the free energy of the stable dolomite.

Figure 4.20 displays the calculated free energy of mixing  $\Delta G_{mix}$  in the binary systems of calcite-dolomite and dolomite-magnetite from 500 K to 1500 K. The solubility of  $Mg^{2+}$  in calcite is up to  $x = 0.04$  at 1000 K. The  $\Delta G_{mix}$  is negative for the  $Mg^{2+}$  composition  $0 < x < 0.33$  at 1500 K, which suggests magnesian calcite and dolomite can form stable solid solutions at this temperature, where the  $Mg^{2+}$  compositions in the stable phase is at least up to 0.33. This miscibility between magnesian calcite and dolomite agrees with the experiments by Goldsmith and Heard (1961), where the top of the solvus outlining the two-phase field is at  $Mg^{2+}$  composition  $x = 0.43$  at 1348 K, and above the solvus a single-phase region extends from calcite to dolomite. Conversely, the miscibility gap between dolomite and

magnesite is considerably wider and the solubility of  $\text{Ca}^{2+}$  in magnesite is up to 0.04 at 1500 K.

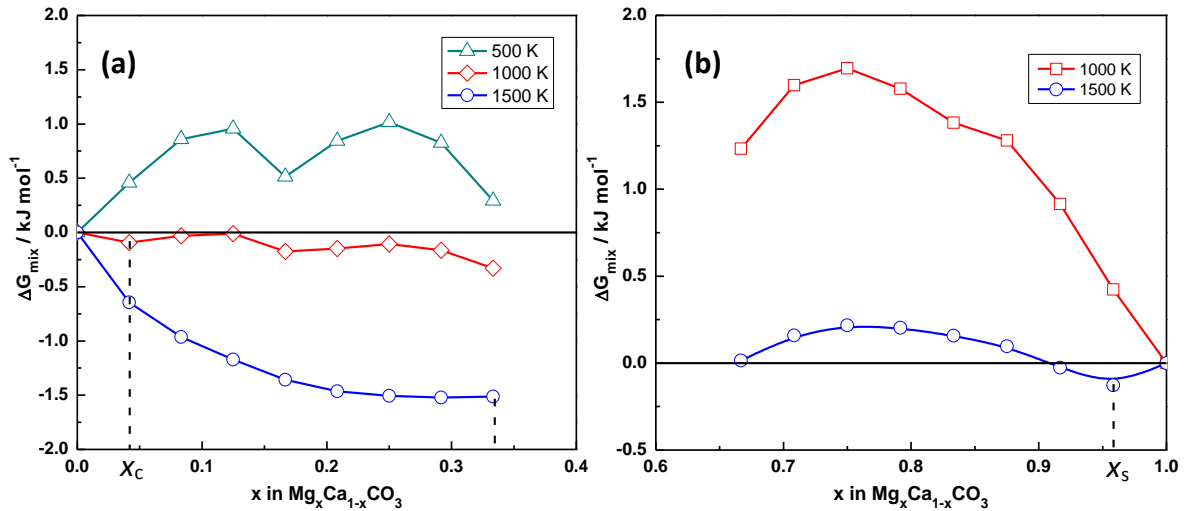


**Figure 4.20:** Calculated free energy of mixing of the binary  $(\text{Mg,Ca})\text{CO}_3$  system as a function of  $\text{Mg}^{2+}$  composition, (a) calcite-dolomite, (b) dolomite-magnesite.

Subsequently, the solid solubility in  $(\text{Ni,Ca})\text{CO}_3$  solid solutions has been evaluated by calculating the free energy of mixing  $\Delta G_{\text{mix}}$  between calcite, ordered dolomite-type  $\text{Ni}_{0.5}\text{Ca}_{0.5}\text{CO}_3$  and  $\text{NiCO}_3$ . The dolomite-type  $\text{Ni}_{0.5}\text{Ca}_{0.5}\text{CO}_3$  was assumed to be a stable phase below 1500 K in this calculation, although it does not exist in nature. The calculated free energy of mixing  $\Delta G_{\text{mix}}$  in the binary systems of  $\text{CaCO}_3 - \text{Ni}_{0.5}\text{Ca}_{0.5}\text{CO}_3$  and  $\text{Ni}_{0.5}\text{Ca}_{0.5}\text{CO}_3 - \text{NiCO}_3$  from 500 K to 1500 K are showed in Figure 4.21. A simple inspection of the results shows that in both cases the free energies of mixing are positive from 500 K to 1500 K. As such there can be neither  $\text{Ni}^{2+}$  substitution in calcite nor  $\text{Ca}^{2+}$  substitution in  $\text{NiCO}_3$  even at high temperatures (e.g.  $\sim 1500$  K). Furthermore, the dolomite-type structure  $\text{Ni}_{0.5}\text{Ca}_{0.5}\text{CO}_3$  is not stable due to the limit substitution of  $\text{Ni}^{2+}$  in calcite and vice versa.

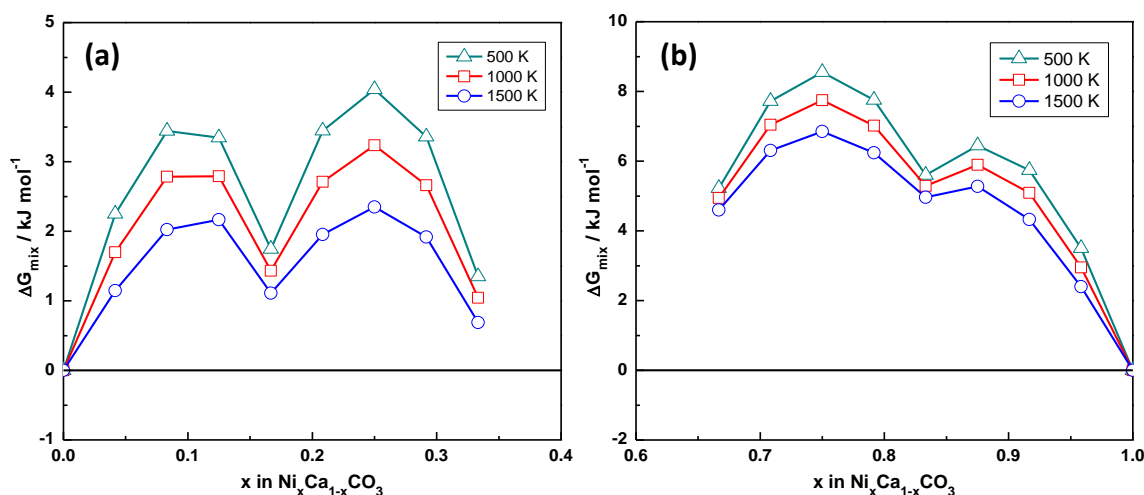


**Figure 4.21:** Calculated free energy of mixing of the binary systems as a function of  $\text{Ni}^{2+}$  composition. (a)  $\text{CaCO}_3\text{-Ca}_{0.5}\text{Ni}_{0.5}\text{CO}_3$ , (b)  $\text{Ca}_{0.5}\text{Ni}_{0.5}\text{CO}_3\text{-NiCO}_3$

## 4.9 Chapter summary

The mixing thermodynamics of binary  $\text{CaCO}_3\text{-MeCO}_3$  solid solutions ( $\text{Me} = \text{Mg}, \text{Ni}, \text{Co}, \text{Zn}, \text{Fe}, \text{Mn}$  and  $\text{Cd}$ ) in the whole range of  $\text{Me}^{2+}$  compositions have been investigated by atomistic simulation techniques. The ionic radius, coordination distance and solubility of divalent cations in calcite are summarised in Table 4.2.

The calculations show that  $\text{CdCO}_3$  and  $\text{CaCO}_3$  form a continuous stable solid solution in the whole  $\text{Cd}^{2+}$  compositions at moderate temperatures. While there is a miscibility gap at  $\text{Mn}^{2+}$  composition  $0.12 < x < 0.92$  in the  $(\text{Mn},\text{Ca})\text{CO}_3$  system, which contains a small degree of cationic ordering rather than the expected completely random distribution. A higher abundance of cation ordering is present in the  $(\text{Fe},\text{Ca})\text{CO}_3$ ,  $(\text{Co},\text{Ca})\text{CO}_3$ ,  $(\text{Zn},\text{Ca})\text{CO}_3$ ,  $(\text{Mg},\text{Ca})\text{CO}_3$  and  $(\text{Ni},\text{Ca})\text{CO}_3$  systems, and the solubility of these cations in calcite is thus very limited. All investigated carbonate systems show higher solubility of the smaller ions in calcite than that of  $\text{Ca}^{2+}$  in the other end-member carbonates. The dolomite-type compounds

$\text{Me}_{0.5}\text{Ca}_{0.5}\text{CO}_3$ , are not observed to form with  $\text{Cd}^{2+}$ ,  $\text{Fe}^{2+}$ ,  $\text{Co}^{2+}$ ,  $\text{Zn}^{2+}$  and  $\text{Ni}^{2+}$ . For  $\text{Mn}^{2+}$ , the ordered kutnahorite is metastable and behaves disorder above 695 K. According to the calculations, the solubility of impurity cations in calcite, which is in good agreement with available experimental results, is largely related to the cationic coordination distance with oxygen. Ionic radius is clearly not the controlling factor in these binary carbonate solid solutions.

**Table 4.2** Some data on rhombohedral carbonates.

Cations	Radius / Å	Me-O / Å	Solubility in calcite (calculation)	Solubility in calcite (experiment)	Dolomite type structure
$\text{Ca}^{2+}$	1.00	2.40	complete (300 K)	complete (298 K)	/
$\text{Cd}^{2+}$	0.97	2.26	complete (300 K)	complete (298 K)	No
$\text{Mn}^{2+}$	0.83	2.16	$x < 0.12$ (900 K)	$x < 0.13$ (298 K)	Yes
$\text{Fe}^{2+}$	0.75	2.12	$x < 0.4$ (1000 K)	$x < 0.35$ (1023 K)	No
$\text{Co}^{2+}$	0.72	2.10	$x < 0.06$ (1000 K)	$x < 0.13$ (1023 K)	No
$\text{Zn}^{2+}$	0.75	2.09	$x < 0.04$ (1000 K)	$x < 0.2$ (1023 K)	No
$\text{Mg}^{2+}$	0.65	2.08	$x < 0.04$ (1000 K)	$x < 0.12$ (1023 K)	Yes
$\text{Ni}^{2+}$	0.72	1.99	no	$x < 0.05$ (1023 K)	No

# 5

## **Investigation of the interaction between calcite nanoparticle and calcite surfaces**

---

When two calcite particles collide in the solution, the interaction between the particles holds them together for a short while before they are separated by the fluid shear force. If the interaction is strong, or the particles are growing quickly, the particles will remain bound together to form an aggregate. In this chapter atomic simulation techniques have been applied to establish the key factors that affect the interaction between a calcite nanoparticle and some major calcite surfaces. Both planar and stepped surfaces in vacuum and aqueous environment have been considered. This study provides quantitative information for experimental studies of the aggregation of calcite nanoparticles during the crystal growth process.

## 5.1 Introduction

Recently, the growth of calcite has been studied extensively both in experiments (Dobson *et al.* 2005; Wasylenki *et al.* 2005) and computational modelling (de Leeuw *et al.* 1999; de Leeuw 2002), and calcite particles on the micro-scale (*i.e.* nanoparticles) have gained increasing attention due to their fundamental role in calcite crystal growth, where the aggregation of nanoparticles can lead to the formation of crystals with different morphologies (Colfen, 2003; Domingo, 2004). Aggregation of calcite particles could arise from a combination of many effects: solid-state properties, growth habit and crystallization conditions, such as solution supersaturation and flow rate. However, it is still not fully understood how we can achieve control over this process.

The aggregation between a small nanoparticle and a larger nanoparticle can be approximated as the adhesion of a small nanoparticle onto a substrate, namely a large surface. In this chapter the epitaxial matching of calcite nanoparticles to a number of common calcite surfaces has been investigated by using computer modelling at the atomic level. By separately modelling calcite nanoparticle with different morphology and substrate, it is possible to comment on the effect of lattice matching on the adhesion energy and explain experimental findings during the calcite crystal aggregation process.

## 5.2 Calcite surfaces

The rhombohedral structure of calcite, which has a space group  $R\bar{3}c$ , hexagonal lattice vectors  $a = b = 4.990 \text{ \AA}$ ,  $c = 17.061 \text{ \AA}$  (Deer *et al.*, 1992), was used as the starting bulk structure. The computer code METADISE (Watson *et al.*, 1996) was

then employed to optimise the bulk structure and resulting structure was used to create the planar and stepped surfaces. Two planar surfaces  $\{1\ 0\ \bar{1}\ 4\}$ ,  $\{0001\}$  and two stepped surfaces  $\{3\ 1\ \bar{4}\ 8\}$ ,  $\{3\ \bar{1}\ \bar{2}\ 16\}$  are considered in this study. A series of simulations were carried out to determine the optimised structures and surface energies of the cleaved surfaces in vacuum. The results are listed in Table 5.1.

**Table 5.1** Surface energies of pure calcite surfaces ( $\text{Jm}^{-2}$ )

surface	unrelaxed surface	relaxed surface
$\{1\ 0\ \bar{1}\ 4\}$	0.64	0.57
$\{0001\}$ - $\text{CO}_3^{2-}$	1.59	0.98
$\{0001\}$ - $\text{Ca}^{2+}$	2.39	0.99
$\{3\ 1\ \bar{4}\ 8\}$	1.15	0.88
$\{3\ \bar{1}\ \bar{2}\ 16\}$	0.91	0.72

The  $\{1\ 0\ \bar{1}\ 4\}$  surface is the most stable surface of calcite and dominates its observed morphology. It consists of layers of calcium, carbon and one oxygen atom in a plane with the other two oxygen atoms above and below this plane, as shown in Figure 5.1a. It has a higher density of ions compared with other possible charge neutral planes, leading to its low surface energy and stability. The  $\{0001\}$  surface is a common twinning plane, which according to Pastero's statistical work (2004) occurs to almost 17% in natural calcite samples. The  $\{0001\}$  surface contains alternating planes of  $\text{Ca}^{2+}$  and  $\text{CO}_3^{2-}$  groups, which produces a dipole moment perpendicular to the surface. Polar surfaces are unstable by themselves and will either reconstruct to neutralize the dipole moment or adsorb ions to remove the dipole moment. In this study, the dipole moment is removed by moving half the ions from the top layer of the surface to the bottom, creating surface vacancies in the process. As a result two  $\{0001\}$  surfaces with different terminations have been created, namely a  $\text{CO}_3^{2-}$

terminated surface (Figure 5.1b) and a  $\text{Ca}^{2+}$  terminated surface (Figure 5.1c).

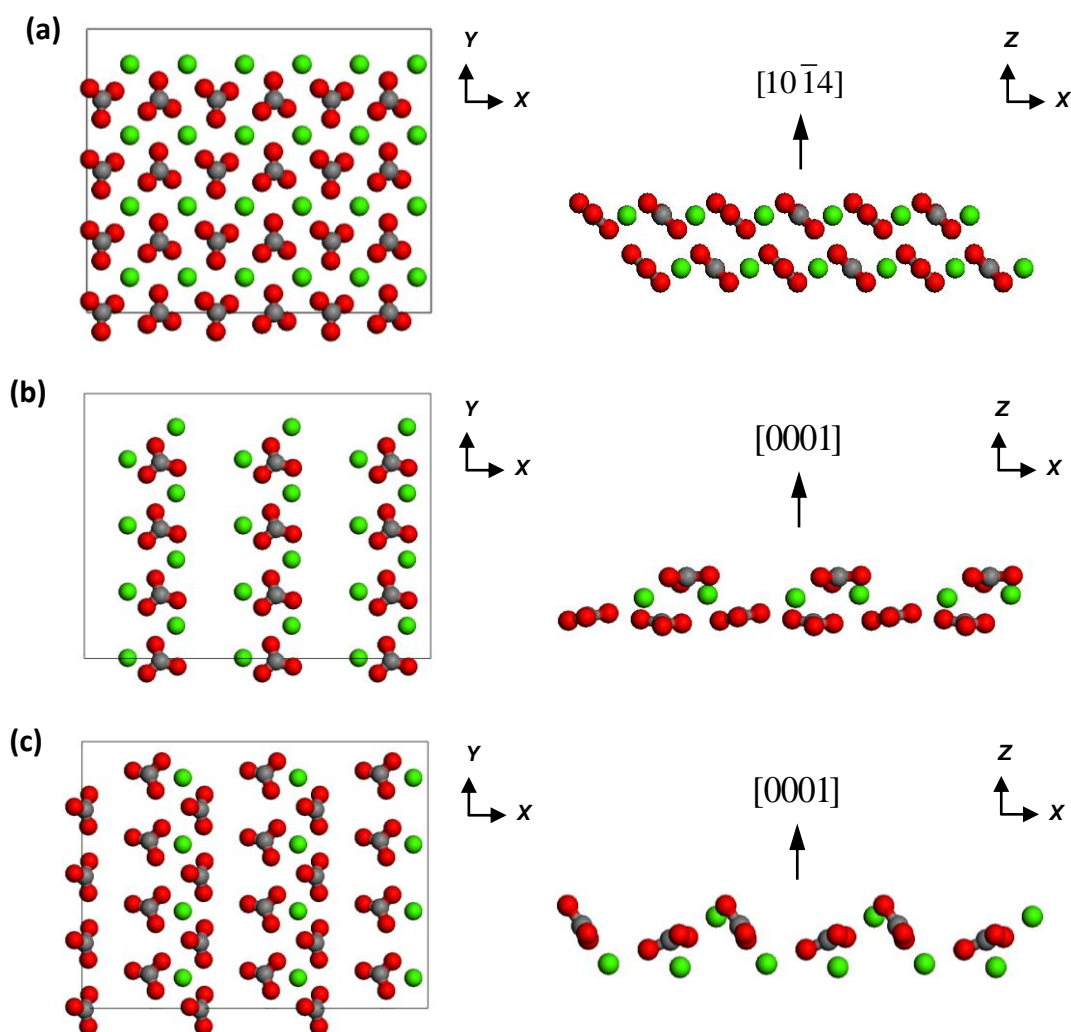


**Figure 5.1:** Top view and side views of pure planar surfaces, (a)  $\{10\bar{1}4\}$  surface, (b)  $\text{CO}_3^{2-}$  terminated  $\{0001\}$  surface and (c)  $\text{Ca}^{2+}$  terminated  $\{0001\}$  surface. The second plane in the top view has been omitted for clarity. (Ca = green, C = grey, O = red).

Stepped surfaces are usually present in natural and synthesized calcite crystals and experimental systems. Steps on the calcite cleavage face are common along the crystallographic directions defined by cleavage plane intersections. Because calcite has a rhombohedral lattice, two non-equivalent steps are produced by each of the cleavage planes that intersect at the surface. These steps differ in their local atomic arrangement and are named the acute and obtuse step by the angle they make with

the surface (Kristensen and Stipp, 2004). There are many surfaces that include these steps, but the surfaces on which the steps are closest together are the  $\{3\ 1\ \bar{4}\ 8\}$  and  $\{3\ \bar{1}\ \bar{2}\ 16\}$  surfaces, as illustrated in Figure 5.2, describing a plane with acute and obtuse steps, respectively. On the acute stepped  $\{3\ 1\ \bar{4}\ 8\}$  surface, the  $\text{CO}_3^{2-}$  groups on the edge overhang the plane below, forming an angle of  $80^\circ$  with the lower plane. On the obtuse stepped  $\{3\ \bar{1}\ \bar{2}\ 16\}$  surface, the  $\text{CO}_3^{2-}$  groups on the step edge lean backwards with respect to the below plane, forming an angle of  $105^\circ$  with the lower plane. Both  $\{3\ 1\ \bar{4}\ 8\}$  and  $\{3\ \bar{1}\ \bar{2}\ 16\}$  surfaces contain  $\{1\ 0\ \bar{1}\ 4\}$  terraces and monatomic steps. The side walls of the steps are also  $\{1\ 0\ \bar{1}\ 4\}$  planes and the step edges of the two stepped surfaces are identical to the two different edges of the calcite rhomb.

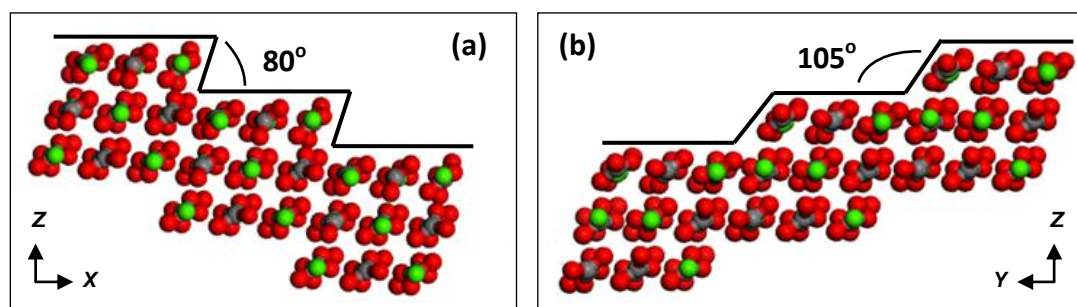


**Figure 5.2:** Side view of pure stepped surfaces, (a) acute  $\{3\ 1\ \bar{4}\ 8\}$  surface and (b) obtuse  $\{3\ \bar{1}\ \bar{2}\ 16\}$  surface. (Ca = green, C = grey, O = red).

As calcite is usually present in an aqueous environment, it is essential to include water in the simulations. Many experiments and computer simulations have indicated that water molecules organize into ordered layers in the mineral-water interface. For example, a classic molecular dynamics study by Kerist and Parker (2004) has found that there are three ordered layers of water on the calcite  $\{1\ 0\ \bar{1}\ 4\}$  surface. The existence of this arrangement is supported by experimental X-ray scattering data (Geissbühler *et al.*, 2004), which found two water layers on the calcite surface in

bulk water. This is expected to be a general effect at ionic surfaces. Previous studies of water adsorption at surfaces have shown that there is a clear difference between the water adsorbed at the mineral surface and bulk water, and only the adsorbed layering water molecules were shown to affect the structure and energy of the underlying surface. For these reasons, both monolayer and multi-layer water on the calcite surfaces were considered in this study.

At first, only a full monolayer of water molecules was added to the surface, which is defined as the maximum number of water molecules adsorbed at the surface in a single layer without formation of a second layer.  $\text{Ca}^{2+}$  sites at the top plane were selected as initial positions for adding the water molecules and the oxygen atoms in water molecules were placed at a distance of 2.0 Å above the  $\text{Ca}^{2+}$  sites. Surface calculations were carried out to determine the surface energies of the hydrated surfaces, which are listed in Table 5.2. It is clear that the surface energies of the hydrated surfaces are smaller than those of corresponding pure surfaces. It is evident that the adsorbed water molecules have a stabilizing effect on the surfaces.

**Table 5.2** Surface energies of hydrated calcite surfaces ( $\text{Jm}^{-2}$ )

surface	surface energy
{1 0 $\bar{1}$ 4}	0.16
{0001}- $\text{CO}_3^{2-}$	0.42
{0001}- $\text{Ca}^{2+}$	0.63
{3 1 $\bar{4}$ 8}	0.78
{3 $\bar{1}$ $\bar{2}$ 16}	0.60

Figure 5.3 shows a top view of the structures of the hydrated planar surfaces, where a very regular pattern of adsorbed water molecules presents on the planar

surfaces. The adsorbed water molecules lie flat on the  $\{1\ 0\ \bar{1}\ 4\}$  surface, which agrees with experimental and other computational findings on adsorption of water on calcite surfaces (Chang *et al.*, 1995; de Leeuw and Parker, 1997). Adsorption of water on the  $\{0001\}$  surface is more complicated. The water molecules show a clear tendency to cluster around the surface  $\text{CO}_3^{2-}$  groups (Figure 5.3b) or the surface  $\text{Ca}^{2+}$  atoms (Figure 5.3c) relaxing into the vacancies created by shifting half the  $\text{CO}_3^{2-}$  groups or  $\text{Ca}^{2+}$  ions to the bottom of the surface as described in the chapter 2.

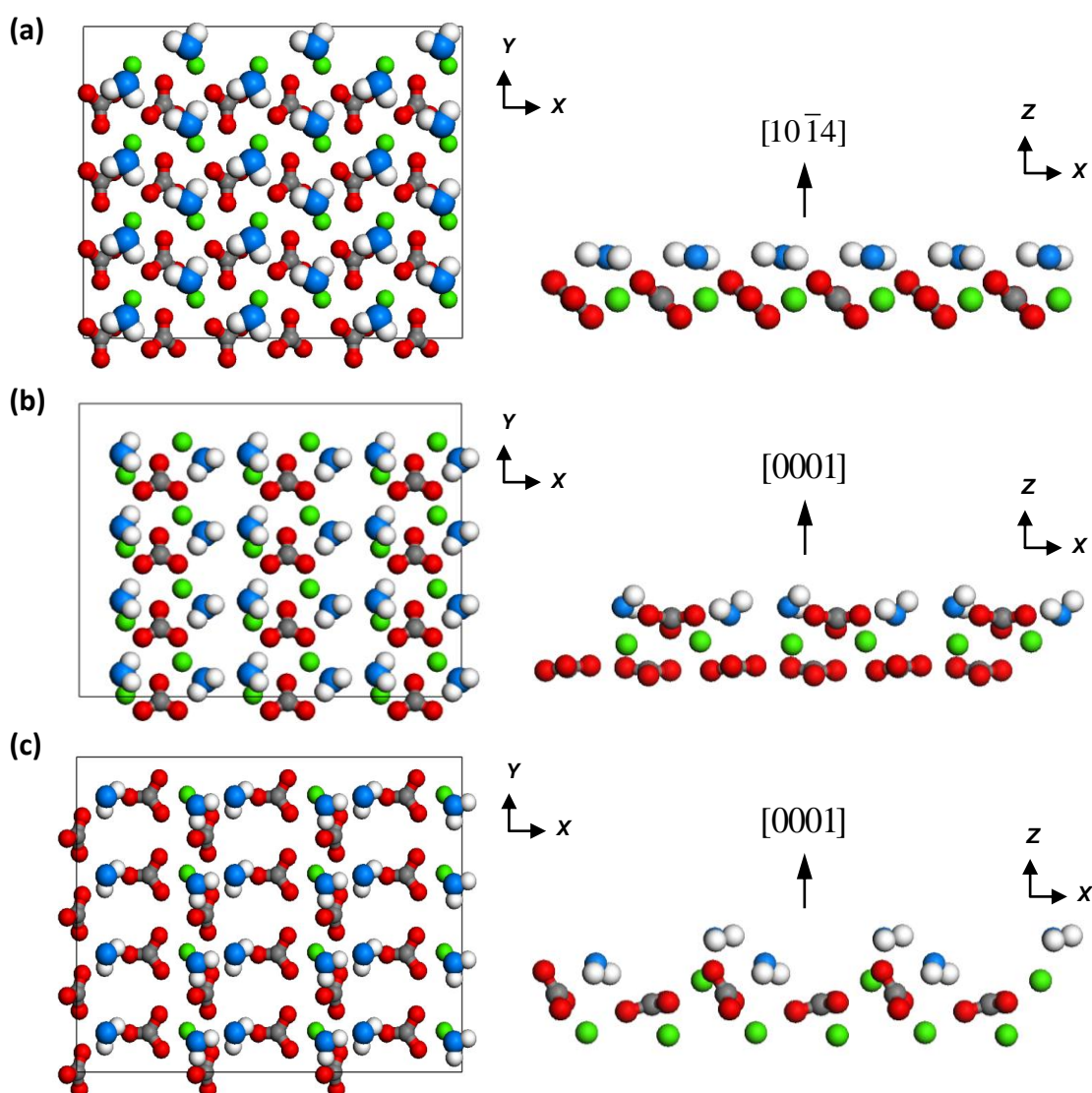


**Figure 5.3:** Top view and side view of hydrated planar surfaces with monolayer of water, (a)  $\{1\ 0\ \bar{1}\ 4\}$  surface, (b)  $\text{CO}_3^{2-}$  terminated  $\{0001\}$  surface and (c)  $\text{Ca}^{2+}$  terminated  $\{0001\}$  surface. (Ca = green, C = grey, O = red, H = white,  $\text{O}_{\text{water}}$  = blue).

In the cases of stepped surfaces, the presence of a step does not greatly affect the regular arrangement of water molecules that was in direct contact with the terraces. However, the arrangement of water molecules right next to the step was disrupted. At the acute step, the water molecules initially coordinated with  $\text{Ca}^{2+}$  at the step edge delocalize the possible adsorption sites, implying the water molecules are less strongly bound to the stepped surface than a planar surface. On the contrary, as  $\text{Ca}^{2+}$  at the step edge of the obtuse step creates new adsorption sites, the water molecules are much strongly bound to the obtuse step than the acute step (Figure 5.4).

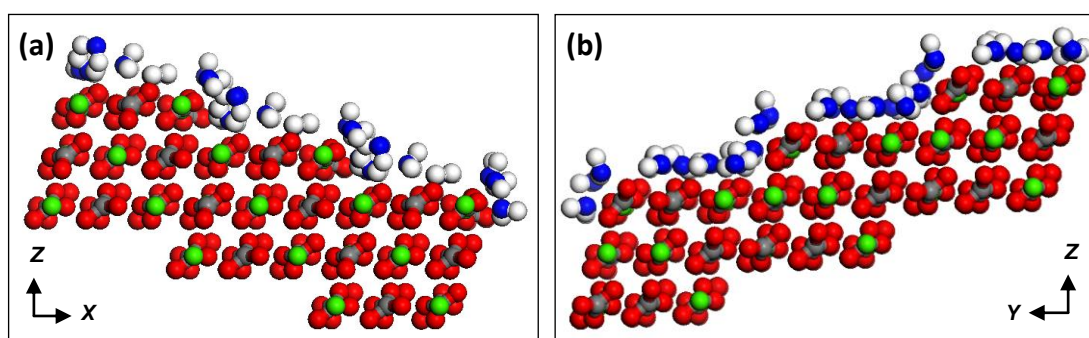


**Figure 5.4:** Side view of hydrated stepped surfaces with monolayer of water, (a) acute  $\{3\ 1\ \bar{4}\ 8\}$  surface and (b) obtuse  $\{3\ \bar{1}\ \bar{2}\ 16\}$  surface (Ca = green, C = grey, O = red, H = white,  $\text{O}_{\text{water}}$  = blue)

More layers of water were then introduced in a similar manner and each time an extra layer of water (24 molecules) was placed at a distance of  $2.0\ \text{\AA}$  above the top of existing hydrated surfaces. In total, four layers of water (96 molecules) were added onto each surface, which build about  $8\ \text{\AA}$  water layers above the pure surface. The calcite-water interfacial systems were then equilibrated by molecular dynamics simulations, using the DL\_POLY 2.20 code (Smith and Forester, 1996), where a combination of NVE and NVT ensembles were used in sequence at a temperature of 300 K. The Nosé-Hoover thermostat was set at 0.1 ps and the relaxation time of barostat was set at 0.5 ps in the calculations. The trajectories were generated using

the Verlet Leap-Frog algorithm using a time step of 0.2 fs. The simulation cell was equilibrated for 100 ps, after which data were collected for another 200 ps. The final hydrated structure was then used as the substrate for the adhesion of the calcite nanoparticle.

### 5.3 CaCO<sub>3</sub> nanoparticle

The CaCO<sub>3</sub> nanoparticle is constructed from the optimised bulk structure of calcite using the METADISE code as described in the methodology chapter. The morphology of the calcite particle is determined by the intersection of the cleavage planes, and surfaces with low surface energy lie on the outside of the polyhedron. The volume enclosed by this polyhedron is then filled with atoms based on periodic repeats of the lattice motif, thus generating an initial structure for a nanoparticle.

Due to the low surface energy ( $0.57 \text{ Jm}^{-2}$ ) of the  $\{1\ 0\ \bar{1}\ 4\}$  surface, the most stable calcite nanoparticle should consist of  $\{1\ 0\ \bar{1}\ 4\}$  surfaces. However, some experimental studies (Rajam and Mann, 1990; Pastero *et al.* 2004) have suggested that the morphology of calcite does not only consist of  $\{1\ 0\ \bar{1}\ 4\}$  surfaces, but also contains the  $\{0001\}$  surface, when  $\text{Li}^+$  is present in the aqueous solution. Therefore, three CaCO<sub>3</sub> nanoparticles with different morphologies were considered in this study, by using the surface energy of the  $\{1\ 0\ \bar{1}\ 4\}$ ,  $\{0001\}\text{-Ca}^{2+}$  and  $\{0001\}\text{-CO}_3^{2-}$ , respectively, as shown in Figure 5.5. In this thesis, nanoparticle<sub>104</sub>, nanoparticle<sub>001-Ca</sub> and nanoparticle<sub>001-CO3</sub> are used to label three CaCO<sub>3</sub> nanoparticles, consisting of  $\{10\bar{1}4\}$  surface,  $\{0001\}\text{-Ca}^{2+}$  surface and  $\{0001\}\text{-CO}_3^{2-}$  surface, respectively. The nanoparticle<sub>104</sub> is constructed as a 1.0 nm rhombohedra with  $\{1\ 0\ \bar{1}\ 4\}$  surfaces on the outside, which contains 18 CaCO<sub>3</sub> units. The nanoparticle<sub>001</sub> is constructed as a multi-prism with  $\{0001\}$  surface on both top and bottom of the prism, where both

$\text{Ca}^{2+}$  and  $\text{CO}_3^{2-}$  terminated  $\{0001\}$  surfaces are considered. The 1.0 nm nanoparticle<sub>001-Ca</sub> contains 38  $\text{CaCO}_3$  units, while the 1.2 nm nanoparticle<sub>001-CO3</sub> contains 61  $\text{CaCO}_3$  units.

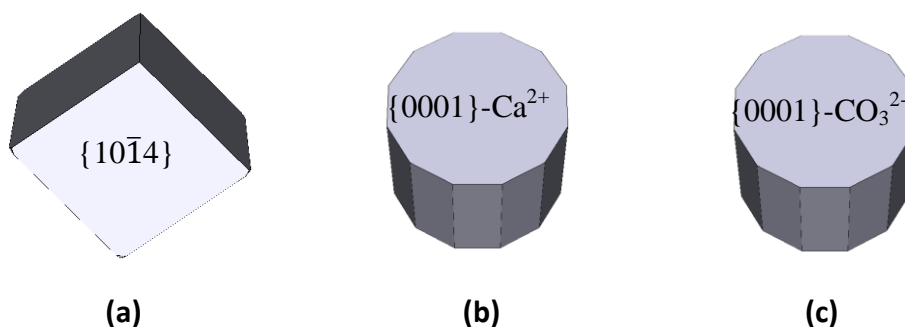


**Figure 5.5:** Morphology of  $\text{CaCO}_3$  nanoparticle, showing (a)  $\{1\ 0\ \bar{1}\ 4\}$  surface (b)  $\{0001\}\text{-Ca}^{2+}$  surface and (c)  $\{0001\}\text{-CO}_3^{2-}$  surface.

## 5.4 Adhesion energy of a nanoparticle on the surface

A nanoparticle-surface interfacial system consists of a calcite nanoparticle and a pure or hydrated calcite surface. To ensure a large number of interfacial configurations are sampled in the study, a comprehensive range of positions of the nanoparticle with respect to the calcite surface was examined, including a series of heights and orientations as well as lateral displacement of the nanoparticle. The vertical distance of the nanoparticle with respect to the surface has been investigated from 1 Å to 10 Å, and for each height, different orientations of the nanoparticle have been considered, where the angle of the rotation  $\theta$  ( $\theta$  is the rotation angle in  $x/y$  axes), was varied by  $30^\circ$  in turn. The initial orientation of the nanoparticle of  $\theta = 0^\circ$  is assumed, where the lattices of the nanoparticle and the pure surface are perfectly aligned. Figure 5.6 shows a calcite nanoparticle<sub>104</sub> with a rotation of  $\theta = 0^\circ$  and  $\theta = 60^\circ$  with respect to the  $\{1\ 0\ \bar{1}\ 4\}$  surface.

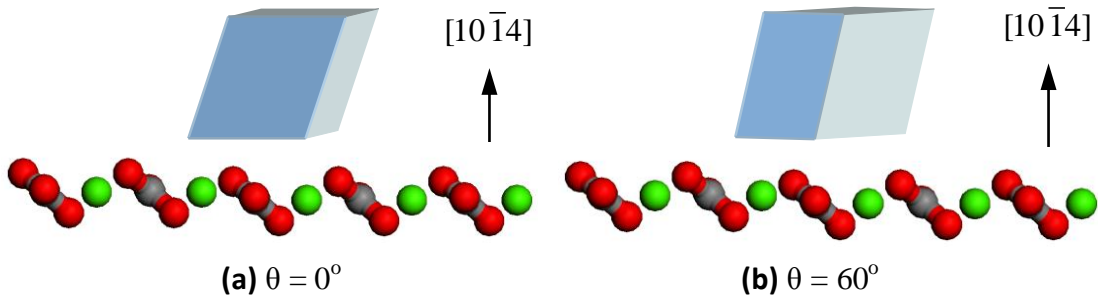


**Figure 5.6:** Examples of a calcite nanoparticle<sub>104</sub> on the top plane of planar  $\{1\ 0\ \bar{1}\ 4\}$  surface. (Ca = green, C = grey, O = red).

Prior to energy minimisation of the interfacial systems, the calcite nanoparticle is kept at a constant height above the surface, but moved systematically in two directions over the surfaces without relaxation of the surface or the nanoparticle. The interfacial energy for the unrelaxed system is calculated for a series of points on a grid. The grid was determined by the surface lattice vectors of the systems in two directions at intervals of  $0.5\ \text{\AA}$ . This scan supplies the information of interfacial energy at each point on the grid, hence identifying the lowest energy lateral displacement of the nanoparticle with respect to the surface in the unrelaxed system. The configuration with the lowest energy is then used as the starting point and a full geometry optimisation is performed to obtain the energy for the relaxed system. Newton-Raphson optimisation algorithm is used for the full geometry optimisation. During the geometry optimisation, both the nanoparticle and surfaces are completely unconstrained.

The adhesion energy per  $\text{CaCO}_3$  group in the bottom plane of the nanoparticle was calculated using the equation below:

$$U_{adhesion} = \frac{1}{n} [U_{interfacial} - (U_{surface} + U_{particle})] \quad (5.1)$$

where  $U_{interfacial}$  is the energy for the interfacial system,  $U_{surface}$  is the energy of calcite surface,  $U_{particle}$  is the energy of the nanoparticle and  $n$  is the number of  $\text{CaCO}_3$  units at the bottom of the nanoparticle. The adhesion energy for the hydrated system was calculated as following:

$$U_{adhesion} = \frac{1}{n} [U_{hy-interfacial} - (U_{hy-surface} + U_{particle})] \quad (5.2)$$

where  $U_{hy-interfacial}$  is the energy for the hydrated interfacial system and  $U_{hy-surface}$  is the energy of the hydrated surface.

## 5.5 Interaction between a nanoparticle<sub>104</sub> and calcite surface

In this part atomic simulation techniques have been employed to establish the key factors that affect the interaction between a calcite nanoparticle<sub>104</sub> and calcite surfaces, including both planar (e.g.  $\{1\ 0\ \bar{1}\ 4\}$  and  $\{0001\}$  surfaces) and stepped surfaces (e.g.  $\{3\ 1\ \bar{4}\ 8\}$  and  $\{3\ \bar{1}\ \bar{2}\ 16\}$  surfaces) in vacuum and aqueous environments. For each surface, firstly, scanning of the nanoparticle over the surface is carried out, taking into account a combination of different heights and orientations with respect to the surface. For each orientation, the interfacial system with the lowest energy from the scanning process is then used as starting configuration for a full geometry optimisation. The lowest unrelaxed and relaxed adhesion energies for the planar systems are presented in Table 5.3 and Table 5.4.

**Table 5.3** Unrelaxed adhesion energies of a calcite nanoparticle<sub>104</sub> on the calcite planar surfaces in vacuum and aqueous solution.

rotation	adhesion energies / kJ mol <sup>-1</sup>					
	{1 0 $\bar{1}$ 4}		{0001}-CO <sub>3</sub> <sup>2-</sup>		{0001}-Ca <sup>2+</sup>	
	pure	hydrated	pure	hydrated	pure	hydrated
$\theta=0^\circ$	-55.1	-13.7	-39.3	-15.1	-51.9	-9.6
$\theta=30^\circ$	-12.0	-5.0	-10.5	-6.4	-13.9	-3.9
$\theta=60^\circ$	-15.8	-7.9	-16.7	-9.8	-17.5	-6.0
$\theta=90^\circ$	-31.1	-7.8	-26.5	-17.5	-29.1	-7.2
$\theta=120^\circ$	-17.4	-8.4	-13.4	-11.5	-23.8	-5.8
$\theta=150^\circ$	-12.1	-6.0	-14.5	-9.1	-17.5	-5.5
$\theta=180^\circ$	-50.9	-13.1	-28.5	-18.2	-51.4	-8.0
$\theta=210^\circ$	-13.3	-5.0	-9.1	-5.6	-11.5	-4.7
$\theta=240^\circ$	-20.8	-6.3	-14.2	-11.2	-24.4	-6.2
$\theta=270^\circ$	-29.5	-6.9	-23.7	-15.8	-30.8	-6.4
$\theta=300^\circ$	-13.8	-6.2	-15.9	-14.1	-21.4	-6.0
$\theta=330^\circ$	-14.0	-7.2	-16.3	-6.8	-19.2	-4.7

**Table 5.4** Relaxed adhesion energies of a calcite nanoparticle<sub>104</sub> on the calcite planar surfaces in vacuum and aqueous solution.

rotation	adhesion energies / kJ mol <sup>-1</sup>					
	{1 0 $\bar{1}$ 4}		{0001}-CO <sub>3</sub> <sup>2-</sup>		{0001}-Ca <sup>2+</sup>	
	pure	hydrated	pure	hydrated	pure	hydrated
$\theta=0^\circ$	-137.0	-51.2	-186.4	-119.7	-168.3	-105.9
$\theta=30^\circ$	-119.8	-47.4	-159.4	-106.2	-152.4	-70.4
$\theta=60^\circ$	-121.9	-48.9	-151.3	-107.4	-139.2	-62.8
$\theta=90^\circ$	-134.8	-41.3	-156.8	-109.9	-151.0	-89.5
$\theta=120^\circ$	-123.4	-49.4	-168.0	-108.1	-156.4	-63.7
$\theta=150^\circ$	-117.6	-46.3	-162.1	-106.3	-147.4	-81.9
$\theta=180^\circ$	-133.4	-49.6	-181.1	-121.5	-167.6	-91.9
$\theta=210^\circ$	-120.8	-45.7	-158.7	-107.1	-155.8	-69.5
$\theta=240^\circ$	-119.9	-43.6	-154.1	-108.1	-142.3	-84.6
$\theta=270^\circ$	-135.3	-39.6	-160.5	-105.8	-140.3	-91.3
$\theta=300^\circ$	-125.5	-46.6	-152.1	-104.1	-164.1	-72.4
$\theta=330^\circ$	-127.4	-47.1	-163.2	-107.8	-150.1	-79.4

### 5.5.1 Nanoparticle<sub>104</sub> and pure {10 $\bar{1}$ 4} surface

Firstly the interaction between a calcite nanoparticle<sub>104</sub> and the pure calcite {10 $\bar{1}$ 4} surface was investigated. The variation of unrelaxed adhesion energies with height between the surface and the nanoparticle<sub>104</sub> for a various orientations is plotted in Figure 5.7. It is very clear from the figure that all the plots have a very similar curvature with an energy minimum at round 2.5 - 2.8 Å of the distance between the nanoparticle and the surface. The plots show that the unrelaxed adhesion energies are highly dependent on the rotation of the nanoparticle with respect to the surface. The 0° and 180° rotations lead to the energetically favourable interfacial configuration. The adhesion energy contours of the unrelaxed interfacial systems, as shown in Figure 5.8, reveal that the surface Ca<sup>2+</sup> sites form the low adhesion energy positions when the nanoparticle has a rotation of 0° whereas for a rotation of 180° the low adhesion energy sites are at the surface CO<sub>3</sub><sup>2-</sup> positions.

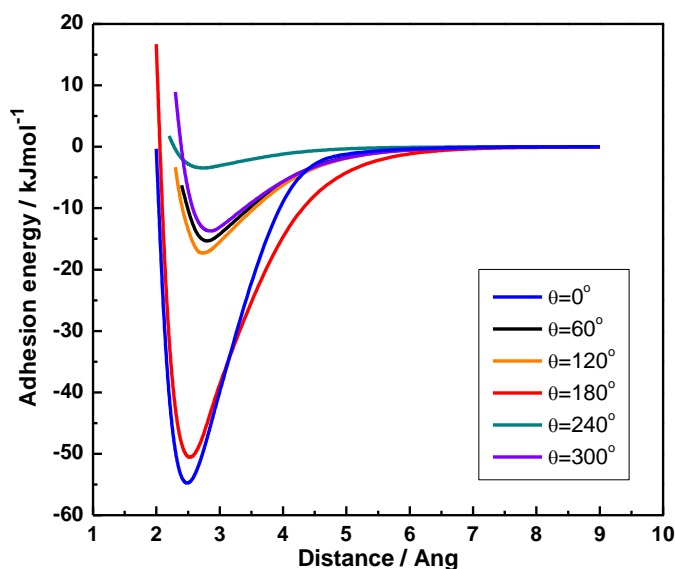


**Figure 5.7:** The variation of unrelaxed adhesion energies with distance between pure {1 0  $\bar{1}$  4} surface and a calcite nanoparticle<sub>104</sub> in vacuum. Results for some orientations have been omitted for clarity.

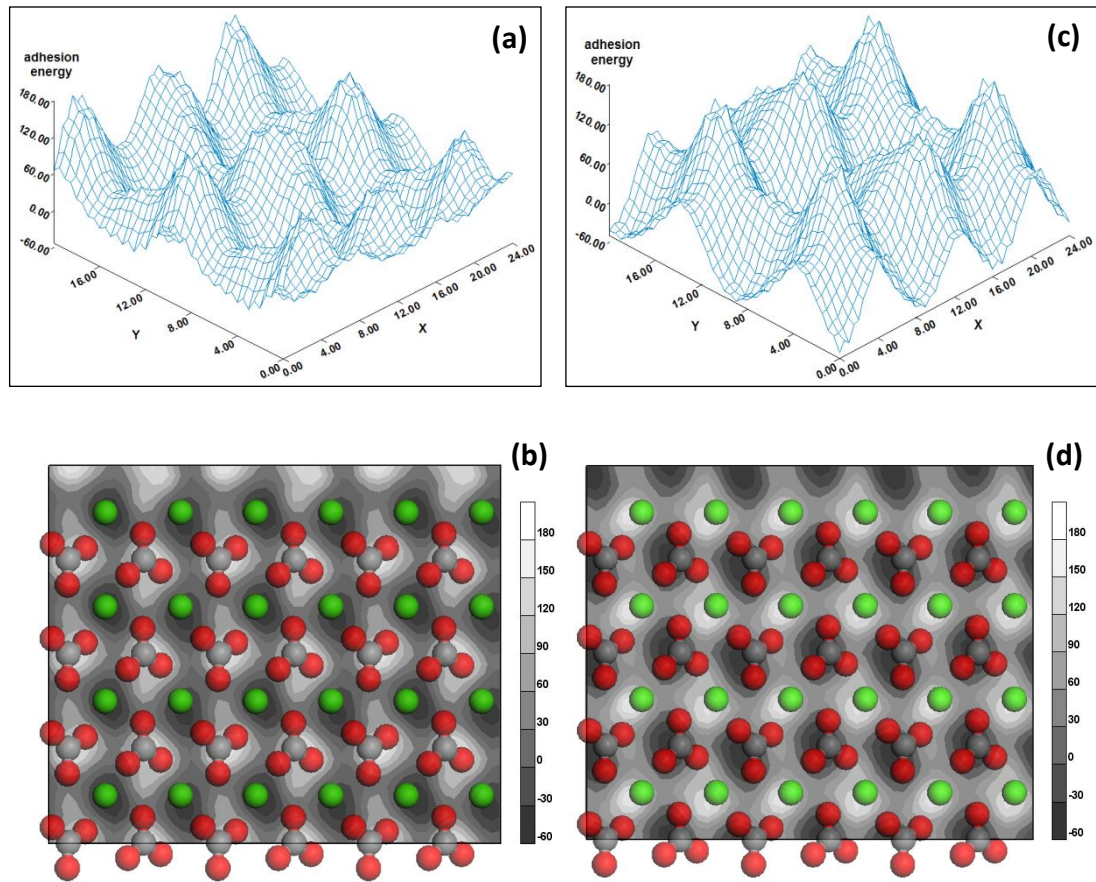


**Figure 5.8:** 3-D and 2-D adhesion energy contour of the nanoparticle<sub>104</sub> on the pure  $\{1\ 0\ \bar{1}\ 4\}$  surface with a rotation of (a) and (b)  $\theta = 0^\circ$ , (c) and (d)  $\theta = 180^\circ$ . (Ca = green, C = grey, O = red).

Further detailed structure analysis indicates that in both cases either a ‘row’ of  $\text{Ca}^{2+}$  ions of the nanoparticle<sub>104</sub> is aligned perfectly with a row of surface  $\text{CO}_3^{2-}$  groups or vice versa. The results agree well with those of Read and Shockley (1950) who used the dislocation model of grain boundaries, to show that the system energy sharply decreases when two adjacent crystals have their lattices perfectly aligned and this provides the driving force for the re-alignment of the crystallites within an aggregate.

While the adhesion energies of the relaxed systems (see Table 5.4) seem less orientation dependent, although the interfacial system with  $0^\circ$  rotation remains the

lowest energy configuration among all. The reason behind the relaxed energies are less dependent on the orientation may be due to the fact that during each structure optimisation, the nanoparticle rotates and re-align with respect to the surface to reach an energy minimum position. The final vertical distance between the nanoparticle and the surface is about 2.5 Å, which is only slightly larger than the standard Ca-O bond distance (2.4 Å).

### 5.5.2 Nanoparticle<sub>104</sub> and hydrated {10 $\bar{1}$ 4} surface

In order to study the influence of water on the interaction between the nanoparticle and surface, the {1 0  $\bar{1}$  4} surface is firstly hydrated by adding a monolayer of water molecules onto the surface, where the distance between the water molecules and pure surface is about 2.0 Å. Again, a comprehensive scanning and energy minimisation procedure is conducted.

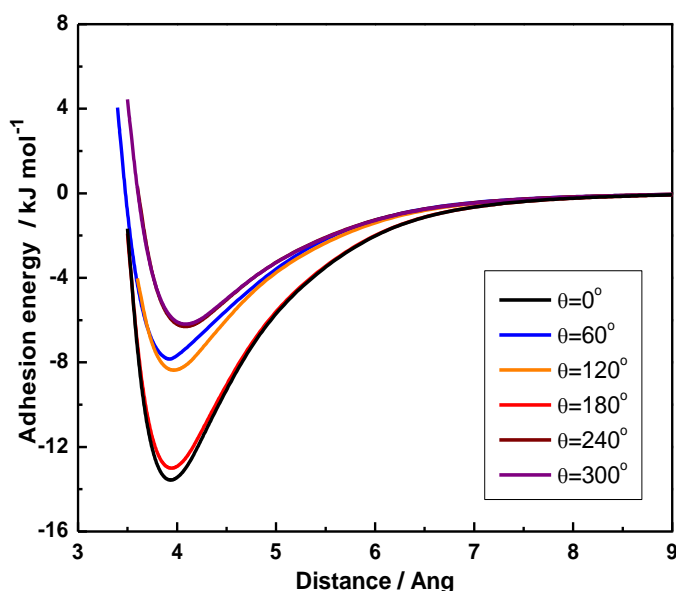


**Figure 5.9:** Adhesion energy as a function of the distance between the monolayer hydrated {1 0  $\bar{1}$  4} surface and a nanoparticle<sub>104</sub>. Results for some orientations have been omitted for clarity.

It is found that the general character of the plots of the energy vs. height is similar to those obtained in vacuum, but all the plots reach their lowest values when the nanoparticle is about 4.0 Å away from the surface regardless of the orientation of the nanoparticle (see Figure 5.9). This is different from the pure surface, where the location of the adhesion energy minimum varies somewhat with the orientation of the nanoparticle.

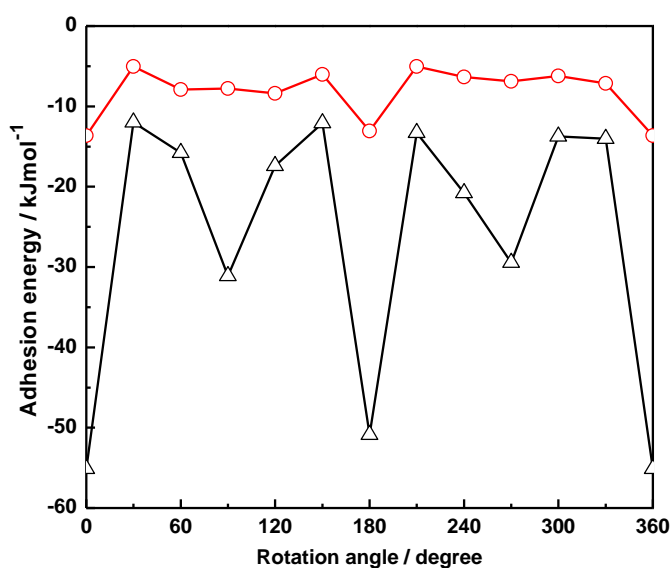


**Figure 5.10:** Adhesion energy as a function of the orientation of a nanoparticle<sub>104</sub> on pure (black triangle) and hydrated (red circle)  $\{1\ 0\ \bar{1}\ 4\}$  surface.

Although the adhesion energies of the unrelaxed hydrated systems are less dependent on the orientation compared to the pure  $\{1\ 0\ \bar{1}\ 4\}$  interfacial system, as shown in Figure 5.10, the 0° rotation still remains the energetically most favourable interfacial configuration. All these observations could be explained by the fact that the monolayer of water molecules has unified the surface structure, which makes the system less sensitive to the position of the nanoparticle. It is also notable that both unrelaxed and relaxed adhesion energies of the hydrated systems (see Table 5.3 and 5.4) are less negative than those of the corresponding pure systems. For example, in

the case of a rotation of  $0^\circ$ , the adhesion energy has lessened by more than 50% ( $85.8 \text{ kJmol}^{-1}$ ) compared to that of the corresponding pure system, indicating that the interfacial water layer reduces the interaction between the nanoparticle<sub>104</sub> and the surface.

Figure 5.11(a) has demonstrated that the energy surface of the monolayer hydrated  $\{10\bar{1}4\}$  interfacial system is much smoother than that of the pure surface at a rotation of  $0^\circ$ . Further analysis indicated that the location of the strong interaction positions has changed compared to the corresponding pure system, namely, the  $\text{CO}_3^{2-}$  sites become relatively low energy sites while  $\text{Ca}^{2+}$  sites interact more weakly no matter the rotations of the nanoparticle<sub>104</sub>, as it can be seen from Figure 5.11(b). The reason for such a change is probably due to the involvement of water molecules.

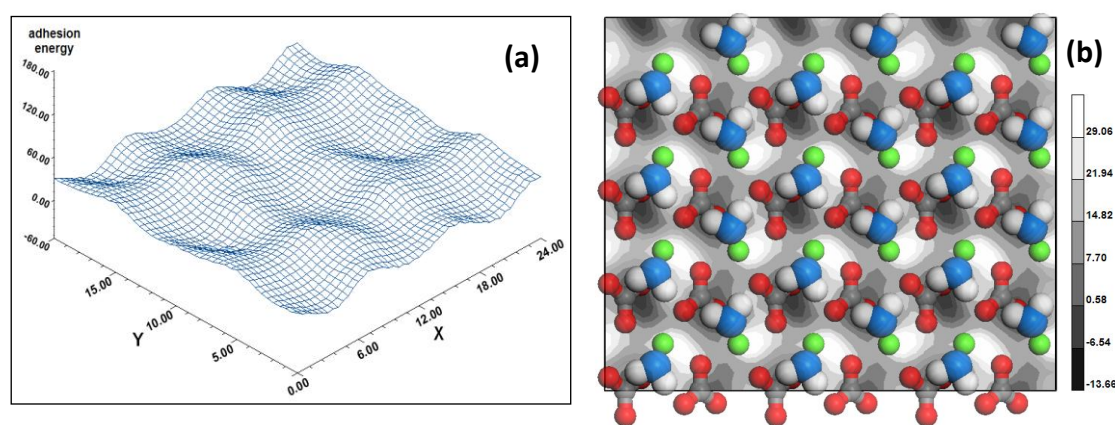


**Figure 5.11:** 3-D and 2-D adhesion energy contours of the nanoparticle<sub>104</sub> on the hydrated  $\{10\bar{1}4\}$  surface with a rotation of  $\theta = 0^\circ$ . (Ca = green, C = grey, H = white, O = red,  $\text{O}_{\text{water}}$  = blue).

Figure 5.12 showed that the monolayer of water molecules act like a ‘screen’, which prevents the surface  $\text{Ca}^{2+}$  ions to directly interact with the  $\text{CO}_3^{2-}$  groups of the nanoparticle, leading to significantly reduce the attractive interaction between the surface  $\text{Ca}^{2+}$  ions and  $\text{CO}_3^{2-}$  groups of the nanoparticle through the intercalated water

molecule's oxygen atom. However, the water layer only partially blocks the interaction way between surface  $\text{CO}_3^{2-}$  groups and the  $\text{Ca}^{2+}$  ions of the nanoparticle, which makes the water layer less impact on the interaction between surface  $\text{CO}_3^{2-}$  groups and the  $\text{Ca}^{2+}$  ions of the nanoparticle. As a result, the overall interaction pattern has altered.

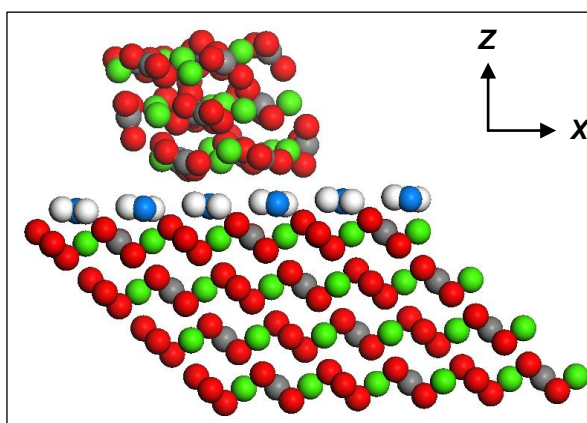


**Figure 5.12:** Side view of the unrelaxed interfacial system of the monolayer hydrated  $\{1\ 0\ \bar{1}\ 4\}$  surface/calcite nanoparticle<sub>104</sub> at a rotation of  $0^\circ$ . (Ca = green, C = grey, O = red, O<sub>water</sub> = blue, H = white).

Next, the interaction between the nanoparticle<sub>104</sub> and hydrated  $\{1\ 0\ \bar{1}\ 4\}$  surface with multilayer water was examined. A complete energy scanning procedure was carried out for double, triple and quadruple water layers, respectively, where the nanoparticle<sub>104</sub> is positioned at  $0^\circ$  rotation only. The adhesion energy surface for the system with double layers of water is smoother than that of the monolayer hydrated system. The energy surfaces for the hydrated system with triple and quadruple layers of water are rough and uneven, meaning the water molecules are starting to interact strongly with each other through hydrogen bonds.

The variation of adhesion energy of a nanoparticle<sub>104</sub> was then investigated, when it approaches the hydrated surface through multilayer water. Figure 5.13

displays the variation of adhesion energy with the distance between a nanoparticle<sub>104</sub> and the hydrated  $\{1\ 0\ \bar{1}\ 4\}$  surface with multilayer water. Four energy minimum positions  $P_1$ ,  $P_2$ ,  $P_3$  and  $P_4$  for each layer of water were determined. It can be seen from Figure 5.13 that the addition of water molecules onto the surfaces gradually reduces the adhesion energy.

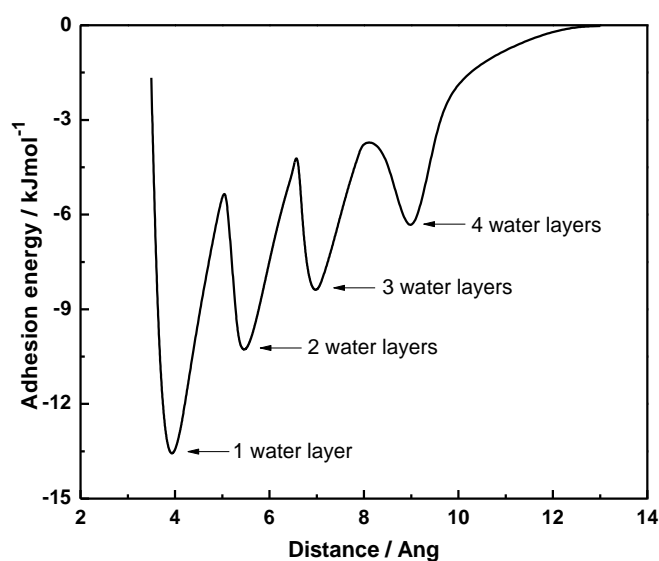


**Figure 5.13:** Adhesion energy as a function of the distance between the hydrated  $\{10\bar{1}4\}$  surface with multilayer water and the nanoparticle<sub>104</sub> at a rotation of  $0^\circ$ .

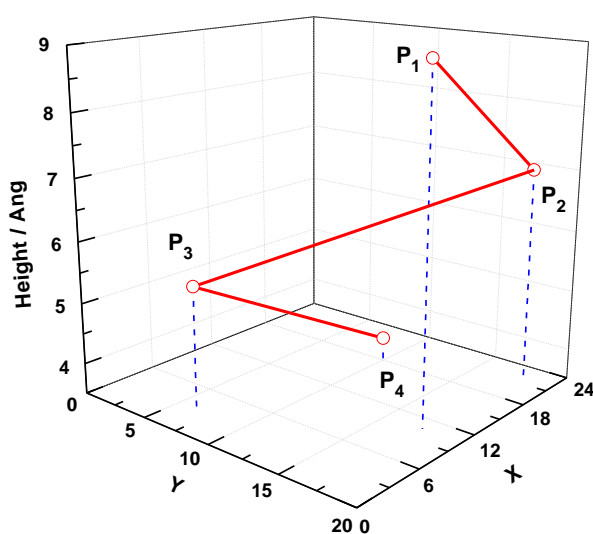


**Figure 5.14:** The twist pathway of a nanoparticle<sub>104</sub> through the multilayer water, where  $P_i$  ( $i = 1, 2, 3$  and  $4$ ) is the position of local energy minimum.

The calculated results also suggest when the nanoparticle<sub>104</sub> approaches the  $\{10\bar{1}4\}$  surface through the multiple water layers in a manner of a twist pathway rather than a straight perpendicular down pathway in order to follow a energetically favourable path, and to overcome a series of energy barriers through the water layers, as it is illustrated in Figure 5.14 (from P<sub>1</sub> to P<sub>4</sub>).

### 5.5.3 The effect of the size of a nanoparticle<sub>104</sub>

Having considered the role of the orientation of the nanoparticle on the adhesion energy, the effect of the size of a nanoparticle on the interactions was inspected, by considering a bigger calcite nanoparticle<sub>104</sub> with a diameter of 1.3 nm. There are 32 CaCO<sub>3</sub> units in this nanoparticle and 8 units in the bottom plane. Again the initial orientation of the nanoparticle<sub>104</sub> ( $\theta = 0^\circ$ ) is assumed in the position where the lattices of the nanoparticle<sub>104</sub> and the  $\{1\ 0\ \bar{1}\ 4\}$  surface are matching perfectly. Then a comprehensive scanning procedure on the planar  $\{1\ 0\ \bar{1}\ 4\}$  was carried out.

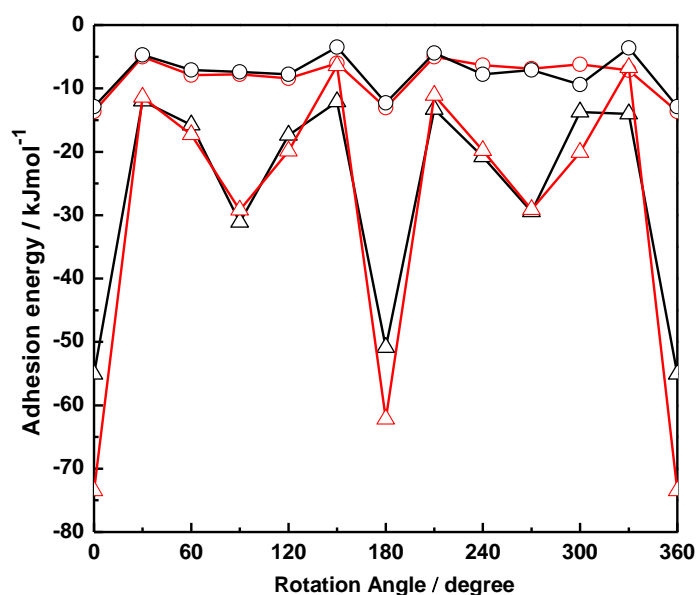


**Figure 5.15:** Unrelaxed adhesion energies as a function of the orientations of the nanoparticle<sub>104</sub> for the pure (triangle) and monolayer hydrated (circle)  $\{1\ 0\ \bar{1}\ 4\}$  interfacial systems, ( $d = 1.0$  nm: black line,  $d = 1.3$  nm: red line).

The adhesion energies for the systems with a nanoparticle<sub>104</sub> sized of 1.3 nm are displayed in Figure 5.15, comparing with those of the smaller nanoparticle<sub>104</sub> ( $d = 1.0$  nm). In the case of the bigger nanoparticle<sub>104</sub>, the adhesion energies for both pure and monolayer hydrated  $\{1\ 0\ \bar{1}\ 4\}$  interfacial systems are also dependent on the orientation of the nanoparticle, which is same as the case for the smaller nanoparticle<sub>104</sub>. The  $0^\circ$  and  $180^\circ$  rotations still lead to the energetically most favourable interfacial configurations.

Furthermore, the variation in the adhesion energies of the pure interfacial surface becomes larger when the size of the nanoparticle<sub>104</sub> increases. For example at a rotation of  $0^\circ$ , the adhesion energy decreases from  $-55.1\ \text{kJmol}^{-1}$  to  $-73.5\ \text{kJmol}^{-1}$ . The reason behind these differences may be due to the stability of bigger calcite nanoparticle<sub>104</sub>. The small nanoparticle<sub>104</sub> can become slightly disordered due to both rotation and translation of the under-coordinated  $\text{CO}_3^{2-}$  groups at the edge of the particle. As the nanoparticle size increased, the influence of the fully coordinated bulk ions begin to dominate and the long-range order in the particle increases (Cooke and Elliott, 2007), making the lattices of the nanoparticle<sub>104</sub> and calcite surface align much more perfectly. Although the consideration of a bigger nanoparticle<sub>104</sub> in the calculations leads to much stronger interaction between the nanoparticle<sub>104</sub> and pure surfaces in some cases, it does not contradict our findings for the smaller nanoparticle<sub>104</sub>, namely the adhesion energy is highly dependent on the orientation of the nanoparticle. Moreover, the size of the nanoparticle<sub>104</sub> does not have an apparent effect on the adhesion energy of the hydrated  $\{1\ 0\ \bar{1}\ 4\}$  interfacial system (Figure 5.15). Therefore, the nanoparticle<sub>104</sub> with a diameter of 1.0 nm has been used to further study its interaction with other calcite surfaces.

### 5.5.4 Nanoparticle<sub>104</sub> and pure {0001} surface

The next object is to inspect the interaction of the calcite nanoparticle<sub>104</sub> with the pure {0001} surface, which is less stable than the  $\{1\ 0\ \bar{1}\ 4\}$  surface (de Leeuw and Parker, 1998). Both  $\text{CO}_3^{2-}$  and  $\text{Ca}^{2+}$  terminated surfaces have been considered. It is found that the shape of the plots of the unrelaxed adhesion energy vs. the height of the nanoparticle<sub>104</sub> with respect to the surface (Figure 5.16) is similar to those obtained from the pure  $\{1\ 0\ \bar{1}\ 4\}$  system, but the locations of the adhesion energy minima have shifted towards the left to 1.5 - 1.9 Å in the case of the {0001}- $\text{CO}_3^{2-}$  system and 1.9 - 2.3 Å for the {0001}- $\text{Ca}^{2+}$  system. The change in the positions of the energy minima could be due to the unique feature of the surface structure of both  $\text{CO}_3^{2-}$  and  $\text{Ca}^{2+}$  terminated surfaces, namely the vacancies at the top of the surfaces, which allows the nanoparticle to position itself deeper into the surface rather than attach on the top of the surface.

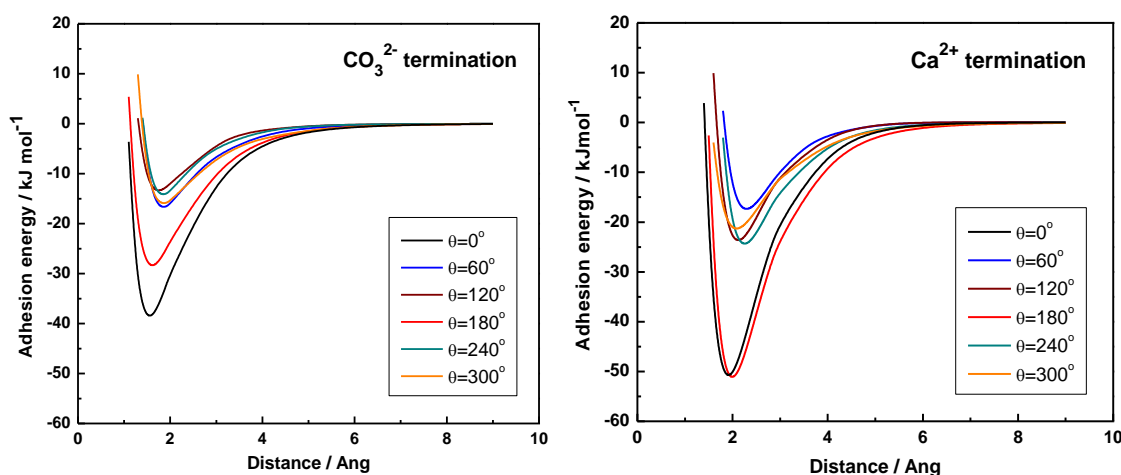


**Figure 5.16:** Adhesion energy as a function of the distance between the pure {0001} surface and a nanoparticle<sub>104</sub>. Results for some orientations have been omitted for clarity.

The unrelaxed adhesion energies for both {0001} interfacial systems with different rotations of the nanoparticle<sub>104</sub> towards the surfaces are plotted in Figure

5.17. Like the pure  $\{1\ 0\ \bar{1}\ 4\}$  interfacial system, the adhesion energies of the unrelaxed systems are highly dependent on the orientation of the nanoparticle<sub>104</sub>. It is notable that for the  $\{0001\}$ -Ca<sup>2+</sup> surface, both 0° and 180° rotation configurations lead to low energy configurations, although the configuration at 0° rotation is energetically more favourable. This phenomenon has also been observed in the pure  $\{1\ 0\ \bar{1}\ 4\}$  system. However, for the  $\{0001\}$ -CO<sub>3</sub><sup>2-</sup> surface, the energy difference between these two rotations is about 10.8 kJmol<sup>-1</sup>.

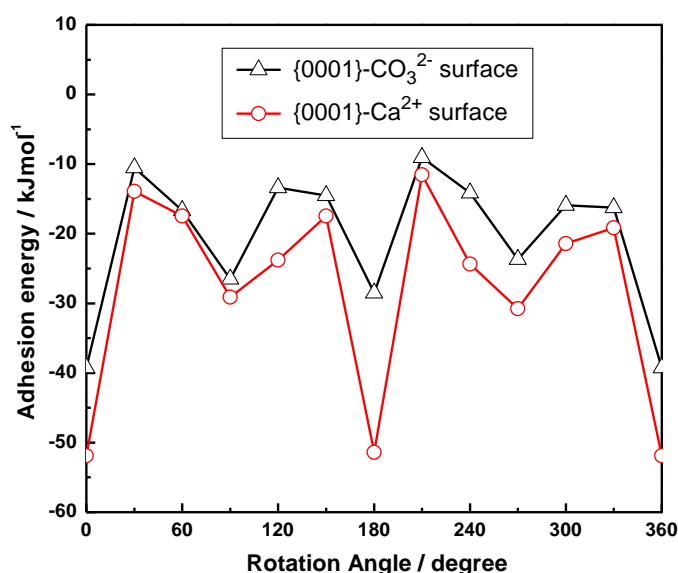


**Figure 5.17:** Adhesion energy as a function of the orientation of a nanoparticle<sub>104</sub> on pure  $\{0001\}$  surfaces.

The reason behind the distinct difference is probably due to the fact that both  $\{10\bar{1}4\}$  and  $\{0001\}$ -Ca<sup>2+</sup> surfaces have a similar surface atoms arrangement of CO<sub>3</sub><sup>2-</sup>-Ca<sup>2+</sup>-CO<sub>3</sub><sup>2-</sup>-Ca<sup>2+</sup>, while for the  $\{0001\}$ -CO<sub>3</sub><sup>2-</sup> surface, the arrangement has changed to CO<sub>3</sub><sup>2-</sup>-CO<sub>3</sub><sup>2-</sup>-CO<sub>3</sub><sup>2-</sup>-CO<sub>3</sub><sup>2-</sup>. In addition, detailed structure analysis indicated that in the case of  $\{0001\}$ -CO<sub>3</sub><sup>2-</sup> surface, when the nanoparticle<sub>104</sub> at a rotation of 180°, the distance between the CO<sub>3</sub><sup>2-</sup> groups at bottom plane of the nanoparticle<sub>104</sub> and those CO<sub>3</sub><sup>2-</sup> groups of the surface plane is smaller (2.84 Å)

compared to that of  $0^\circ$  rotation ( $3.04 \text{ \AA}$ ), which leads to a relatively more repulsive force between the nanoparticle<sub>104</sub> and the surface. The adhesion energy contours of the unrelaxed  $\{0001\}$  interfacial systems, displayed in Figure 5.18, show that the  $\text{Ca}^{2+}$  sites close to the surface form low energy pathway at a rotation of  $0^\circ$  in both cases.

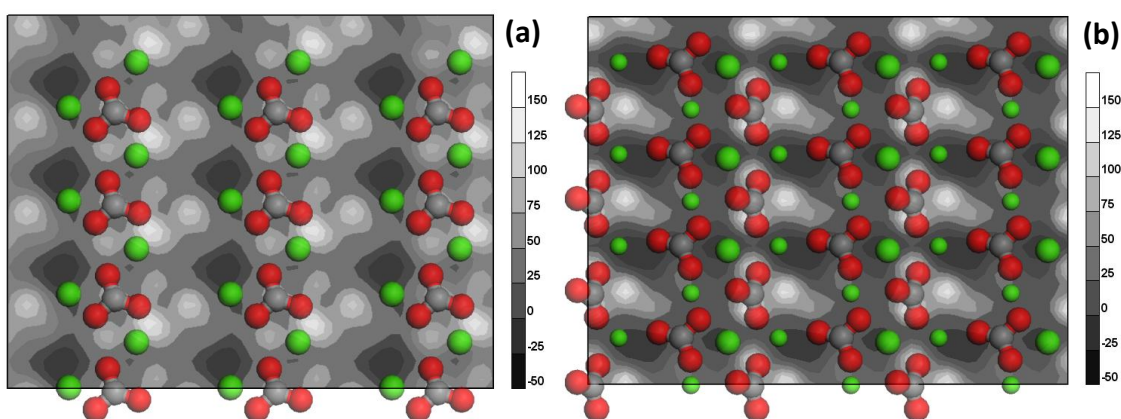


**Figure 5.18:** 2-D adhesion energy contour of the nanoparticle<sub>104</sub> on the pure  $\{0001\}$  surface with a rotation of  $\theta = 0^\circ$ , (a)  $\text{CO}_3^{2-}$  termination and (b)  $\text{Ca}^{2+}$  termination.

As shown in Table 5.4, the adhesion energies for the relaxed  $\{0001\}$  interfacial systems have slightly lower energies than those of the  $\{10\bar{1}4\}$  interfacial system. For almost all orientations studied, except  $300^\circ$ , the order of the relaxed adhesion energy of the pure systems is  $\{0001\}\text{-CO}_3^{2-}$  system  $<$   $\{0001\}\text{-Ca}^{2+}$  system  $<$   $\{10\bar{1}4\}$  system. Structure analysis suggests that this energy order may relate to the distance between the rows of  $\text{CO}_3^{2-}$  groups at the top plane of surfaces. As it is shown in Figure 5.19, the distance between adjacent  $\text{CO}_3^{2-}$  groups for these three systems is  $8.71 \text{ \AA}$  for the  $\{0001\}\text{-CO}_3^{2-}$  system,  $5.03 \text{ \AA}$  for the  $\{0001\}\text{-Ca}^{2+}$  system and  $4.07 \text{ \AA}$  for the  $\{10\bar{1}4\}$  system. The bigger gap at the  $\text{CO}_3^{2-}$  terminated  $\{0001\}$  surface allows the nanoparticle<sub>104</sub> to be more easily accommodated in the surface, which leads to an energetically more favourable configuration.

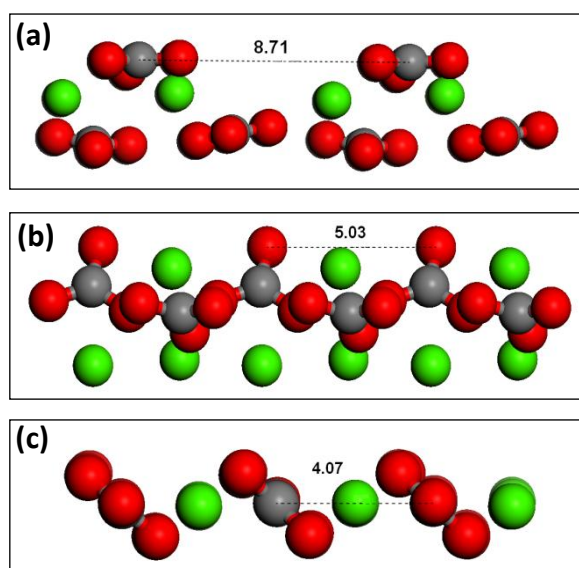


**Figure 5.19:** Side view of the top plane of (a)  $\{0001\}$ - $\text{CO}_3^{2-}$  surface, (b)  $\{0001\}$ - $\text{Ca}^{2+}$  surface and (c)  $\{1\ 0\ \bar{1}\ 4\}$  surface, (Ca = green, C = grey, O = red).

### 5.5.5 Nanoparticle<sub>104</sub> and hydrated $\{0001\}$ surface

The effect of hydration on the interaction of the  $\{0001\}$  interfacial systems was then studied. The results reveal that the main feature of the curves of the unrelaxed adhesion energy vs. the height of the nanoparticle<sub>104</sub> with respect to the surface of both hydrated  $\{0001\}$  systems has been kept but the positions of the energy minima have changed, moving away from the surface (see Figure 5.20 for details). In the case of the hydrated  $\{0001\}$ - $\text{Ca}^{2+}$  interfacial systems, the adhesion energy minima are at around  $3.9\ \text{\AA}$ , e.g. very similar to those in the hydrated  $\{1\ 0\ \bar{1}\ 4\}$  system. However, the adhesion energy minima for the hydrated  $\{0001\}$ - $\text{CO}_3^{2-}$  systems are located at approximately  $2.8\ \text{\AA}$ , which is smaller compared to those of  $\{0001\}$ - $\text{Ca}^{2+}$  and  $\{1\ 0\ \bar{1}\ 4\}$  systems. This could be attributed to the surface atom arrangement mentioned before. The calculated results also indicate that like the monolayer hydrated  $\{1\ 0\ \bar{1}\ 4\}$  system, the interaction between the nanoparticle<sub>104</sub> and the monolayer hydrated  $\{0001\}$  surfaces is weaker than those of the corresponding pure

systems (see Table 5.3 and Table 5.4), including both relaxed and unrelaxed systems. The strength of the interactions is relatively isotropic with the orientation of the nanoparticle, compared to the corresponding pure systems. The rotations of  $0^\circ$  and  $180^\circ$  still lead to the energetically favourable interfacial configurations.

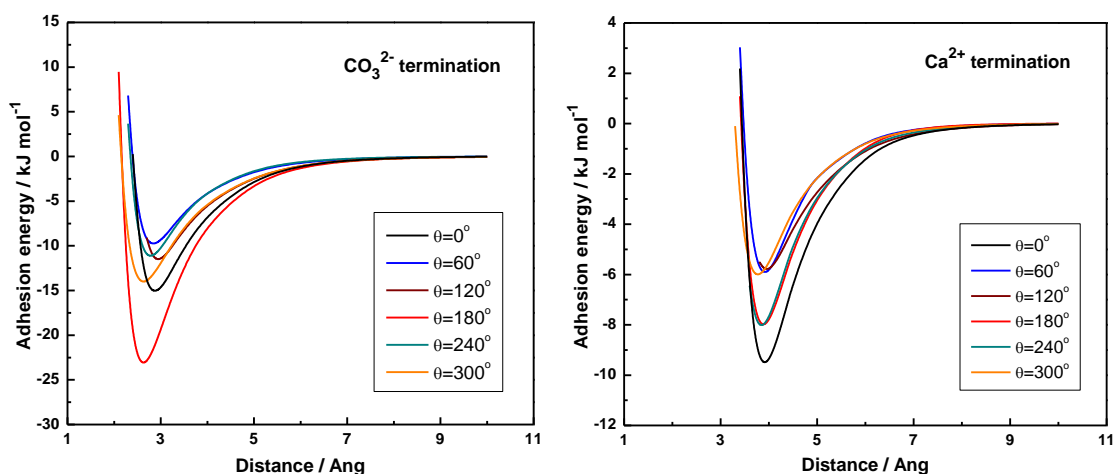


**Figure 5.20:** Adhesion energy as a function of the distance between the monolayer hydrated  $\{0001\}$  surface and a nanoparticle<sub>104</sub>. Results for some orientations have been omitted for clarity.

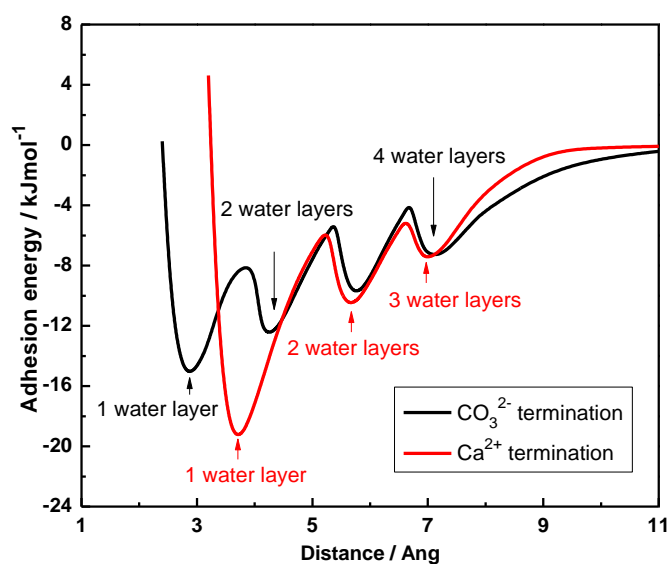


**Figure 5.21:** Adhesion energy as a function of the distance between the multilayer hydrated  $\{0001\}$  surface and the nanoparticle<sub>104</sub> at a rotation of  $0^\circ$ .

Like  $\{1\ 0\ \bar{1}\ 4\}$  system, the  $\{0001\}$  systems with multilayer water were also examined, where four layers of water molecules ( $4 \times 24$ ) have been sequentially added onto the surfaces layer by layer, where only the  $0^\circ$  rotation of nanoparticle<sub>104</sub> is considered. Figure 5.21 shows the variation of adhesion energy vs. the distance between the surface and nanoparticle<sub>104</sub> as the nanoparticle<sub>104</sub> approaches the  $\{0001\}$  surfaces through interfacial multiple water layers.

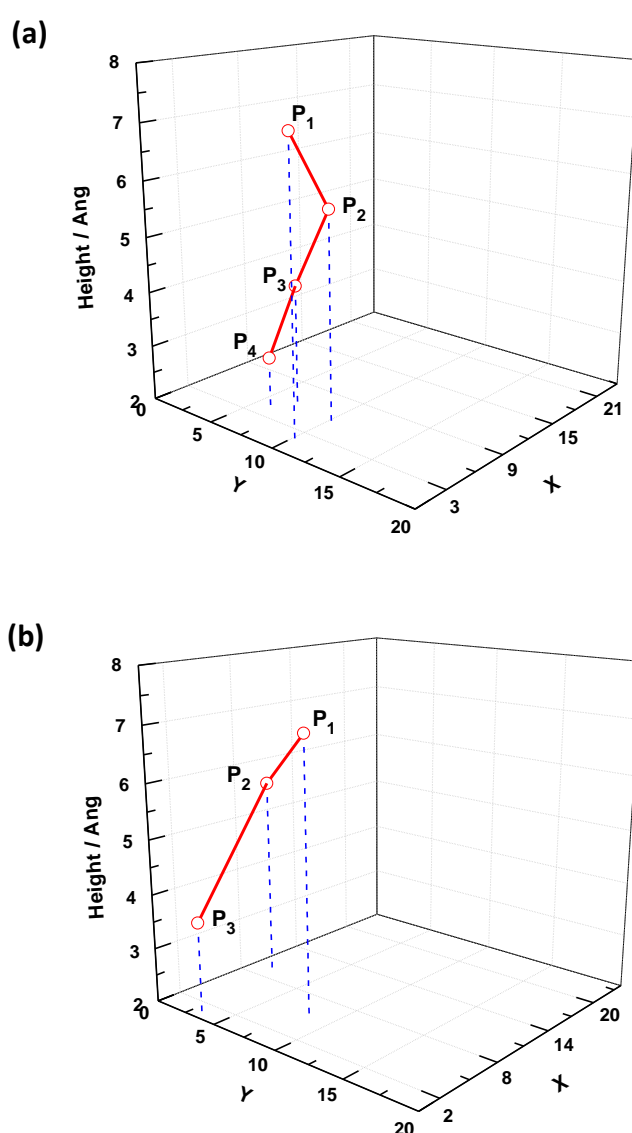


**Figure 5.22:** The twist pathway of a nanoparticle<sub>104</sub> through the multilayer water, where  $P_i$  is the position of local energy minimum, (a)  $\{0001\}$ -CO<sub>3</sub><sup>2-</sup> surface, from  $P_1$  to  $P_4$ ; (b)  $\{0001\}$ -Ca<sup>2+</sup> surface, from  $P_1$  to  $P_3$ .

The figure illustrates that there are energy barriers between the energy minima at different heights, and the adhesion energy gradually reduce with the increasing of water layers, as observed in the  $\{1\ 0\ \bar{1}\ 4\}$  interfacial system. However, there are only three energy minima for the  $\{0001\}$ - $\text{Ca}^{2+}$  system. This could be due to more  $\text{Ca}^{2+}$  atoms from sub-layers exposure to the surface (see surface structure of  $\{0001\}$ - $\text{Ca}^{2+}$  surface in Figure 5.1), which results to adsorb more water molecules to form the first layer than  $\text{CO}_3^{2-}$  terminated surface. The possible pathway of a nanoparticle<sub>104</sub> to approach the  $\{0001\}$  surface through interfacial multilayer water is showed in Figure 5.22.

### 5.5.6 Nanoparticle<sub>104</sub> and stepped surfaces

The interaction of a nanoparticle<sub>104</sub> with two stepped surfaces, namely  $\{3\ 1\ \bar{4}\ 8\}$  and  $\{3\ \bar{1}\ \bar{2}\ 16\}$  surfaces, have been considered in this part. As mentioned before, these surfaces consist of  $\{1\ 0\ \bar{1}\ 4\}$  planes. The study of the interaction between a nanoparticle<sub>104</sub> and the planar  $\{1\ 0\ \bar{1}\ 4\}$  surface has indicated that the most stable interfacial configuration occurs when the lattices of the nanoparticle<sub>104</sub> and planar  $\{10\bar{1}4\}$  surface are perfectly aligned. Therefore a nanoparticle<sub>104</sub> has been placed at a similar position, namely, a rotation of  $0^\circ$  with respect to the terraces of the stepped surfaces, which leads to the lattices of the nanoparticle aligned with those of the terraces, as shown in Figure 5.23. However, the nanoparticle is not necessarily aligned with the lattice of step wall in both stepped surfaces. A comprehensive scanning procedure was then conducted, where the nanoparticle<sub>104</sub> is allowed to move along the  $x$ -axis and  $y$ -axis (e.g. step wall) on the terraces, as well as different heights above the terraces. The lowest adhesion energies for both stepped surfaces together with those of the planar  $\{1\ 0\ \bar{1}\ 4\}$  system are recorded in Table 5.5.

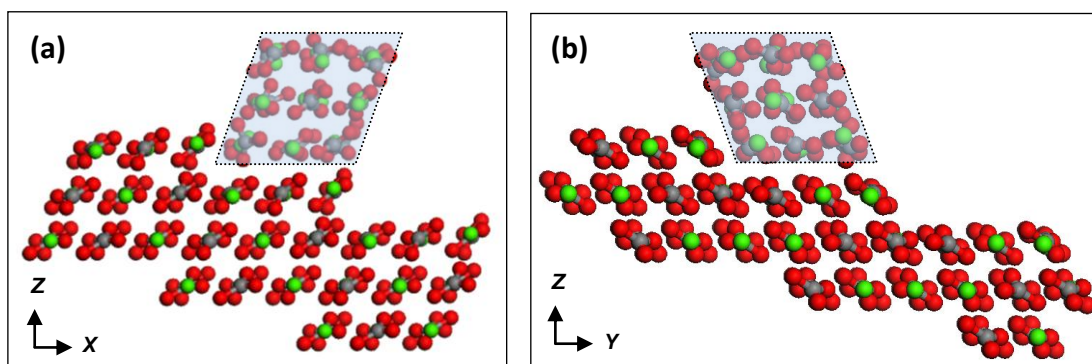


**Figure 5.23:** Side view of the unrelaxed interfacial systems of a nanoparticle<sub>104</sub> on the pure stepped surface, (a) acute stepped  $\{3\ 1\ \bar{4}\ 8\}$  surface and (b) obtuse stepped  $\{3\ \bar{1}\ \bar{2}\ 16\}$  surface, where the nanoparticle is at a rotation of  $0^\circ$  with respect to the terraces of the stepped surfaces (Ca = green, O = red, C = grey).

**Table 5.5:** The lowest unrelaxed adhesion energy of a nanoparticle<sub>104</sub> to the planar  $\{10\bar{1}4\}$  and stepped  $\{3\ 1\ \bar{4}\ 8\}$ ,  $\{3\ \bar{1}\ \bar{2}\ 16\}$  surfaces.

surface	adhesion energy ( $\text{kJmol}^{-1}$ )
pure $\{1\ 0\ \bar{1}\ 4\}$ surface	-55.1
pure $\{3\ 1\ \bar{4}\ 8\}$ surface	-59.6
pure $\{3\ \bar{1}\ \bar{2}\ 16\}$ surface	-57.6
hydrated $\{1\ 0\ \bar{1}\ 4\}$ surface	-13.7
hydrated $\{3\ 1\ \bar{4}\ 8\}$ surface	-11.8
hydrated $\{3\ \bar{1}\ \bar{2}\ 16\}$ surface	-13.2

The results shows that for the  $\{3\ 1\ \bar{4}\ 8\}$  interfacial system, the profile of adhesion energy along the step wall ( $y$ -axis) is very similar to that of the planar  $\{10\bar{1}4\}$  systems (Figure 5.24), which features periodic fluctuation. The difference in adhesion energies between two systems is fairly small ( $\sim 4.5\ \text{kJmol}^{-1}$ ). These evidences indicate that the step wall has very limited impact on the nanoparticle. The reasons for such a result may be two folds. Firstly, the step wall is shallow and

secondly, the lattice of the step wall is not perfectly aligned with that of the nanoparticle.

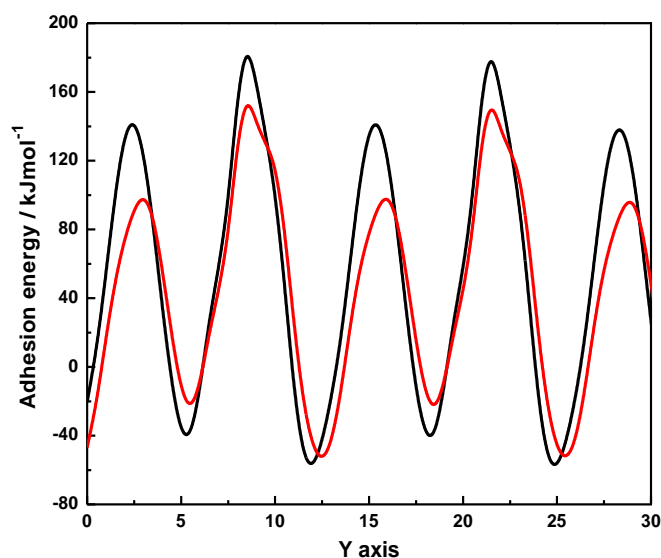


**Figure 5.24:** The variation of adhesion energy as the nanoparticle<sub>104</sub> moving along the step wall of pure  $\{3\ 1\ \bar{4}\ 8\}$  surface (black line) and planar  $\{1\ 0\ \bar{1}\ 4\}$  surfaces (red line).

Like the acute stepped  $\{3\ 1\ \bar{4}\ 8\}$  system, the obtuse stepped  $\{3\ \bar{1}\ \bar{2}\ 16\}$  system also has the periodic feature of its adhesion energy profile along the  $y$ -axis. The adhesion energy difference between the planar and the obtuse stepped systems is even smaller ( $\sim 2.5\ \text{kJmol}^{-1}$ ). The variation of adhesion energy with distance between the nanoparticle<sub>104</sub> and the terrace has a curvature with an energy minimum at  $2.3\ \text{\AA}$  for  $\{3\ 1\ \bar{4}\ 8\}$  system and  $2.5\ \text{\AA}$  for  $\{3\ \bar{1}\ \bar{2}\ 16\}$  systems, which is very similar to that of the planar  $\{1\ 0\ \bar{1}\ 4\}$  system ( $\sim 2.5\ \text{\AA}$ ). In addition, the shape of the curves is identical to that of planar system. As indicated in Table 5.5, the order of the adhesion energy for the pure systems studied here is  $\{1\ 0\ \bar{1}\ 4\} > \{3\ \bar{1}\ \bar{2}\ 16\} > \{3\ 1\ \bar{4}\ 8\}$ . In other words, under vacuum conditions, calcite nanoparticle aggregation would preferentially occur at acute stepped surface rather than obtuse stepped surface or planar surface.

In reality, aggregation process often takes place in aqueous solution rather than in vacuum. It is therefore essential to take the effect of water on the process into account. For this reason, the calculations have also been performed under the aqueous conditions, where the stepped  $\{3\ 1\ \bar{4}\ 8\}$  and  $\{3\ \bar{1}\ \bar{2}\ 16\}$  surfaces were covered by a monolayer of water molecules. A comprehensive scanning procedure was repeated on the hydrated stepped surfaces.

It is discovered that the most stable interfacial configuration occurs when the distance between the nanoparticle<sub>104</sub> and terrace is at 4.2 Å for both acute surface and obtuse surface, which is a little higher than that of the planar  $\{1\ 0\ \bar{1}\ 4\}$  system ( $\sim 4.0\text{Å}$ ). The variation of adhesion energies with the distance between the nanoparticle<sub>104</sub> and the terrace is plotted in Figure 5.25. It is clear from the figure that the plots have the same profile as that of hydrated planar surface (black line). The calculated adhesion energies for the hydrated stepped surfaces are less negative than those of the corresponding pure stepped surfaces.

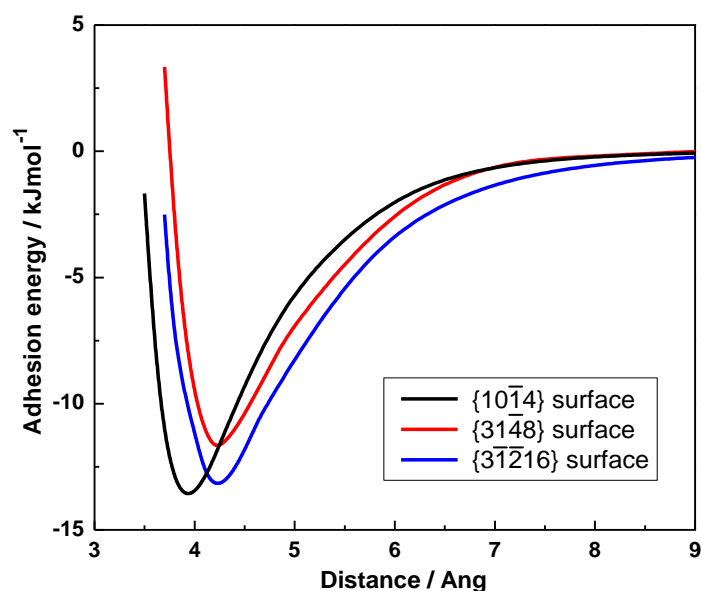


**Figure 5.25:** Adhesion energy as a function of the height between a nanoparticle<sub>104</sub> and the hydrated planar and stepped surfaces.

It is also very interesting to note that under aqueous condition, the order of the adhesion energies for three systems studied has altered to  $\{1\ 0\ \bar{1}\ 4\} < \{3\ \bar{1}\ \bar{2}\ 16\} < \{3\ 1\ \bar{4}\ 8\}$ , where the hydrated planar  $\{1\ 0\ \bar{1}\ 4\}$  surface becomes the most attractive to the nanoparticle<sub>104</sub> compared to the stepped surfaces. The main reason for such a change may be due to the fact that the water molecules are highly ordered and tightly bound to the planar surface in the  $\{1\ 0\ \bar{1}\ 4\}$  system, leading to a strong interaction between the nanoparticle<sub>104</sub> and the planar surface. The steps on the obtuse  $\{3\ \bar{1}\ \bar{2}\ 16\}$  surface creates new adsorption  $\text{Ca}^{2+}$  sites along the step edge, making the water molecules strongly bound to  $\text{Ca}^{2+}$  ions along the step edge; so the distribution of water molecules on the terraces of the obtuse stepped surface is similar to that of the  $\{1\ 0\ \bar{1}\ 4\}$  surface. However, the presence of the acute step on the  $\{3\ 1\ \bar{4}\ 8\}$  surface largely affects the distribution of water molecules, especially at the step edge, where water molecules are less ordered and a large number of the water molecules ‘stand up’ rather than ‘lie flat’, as shown in Figure 5.4a. This leads to the positively charged hydrogen atoms present on the top of acute stepped surface, making the interaction between nanoparticle<sub>104</sub> and the surface weaker. These results suggest the aggregation is most likely to take place between calcite nanoparticle<sub>104</sub> and planar surface rather than the stepped surface.

## 5.6 Interaction between a nanoparticle<sub>001</sub> and calcite surface

Apart from the calcite nanoparticle<sub>104</sub>, the interaction between the calcite surfaces and two calcite nanoparticles with  $\{0001\}$  surface on the outside were considered. The diameter of the nanoparticle<sub>001-Ca</sub> is 1.0 nm and there are 12  $\text{Ca}^{2+}$  atoms at the bottom, while the diameter of the nanoparticle<sub>001-CO<sub>3</sub></sub> is 1.2 nm and there are 12  $\text{CO}_3^{2-}$  groups at the bottom. The surface scanning method was used initially to determine the interaction between the calcite nanoparticle<sub>001</sub> and calcite planar

surfaces, e.g.  $\{1\ 0\ \bar{1}\ 4\}$  and  $\{0001\}$  surfaces in vacuum and aqueous environments. A combination of different heights and orientations with respect to the surface was taken into account, as the investigations have been done for the nanoparticle<sub>104</sub>. Since the nanoparticle<sub>001</sub> is not stable in the vacuum, the full geometry optimisation of the interfacial system was not performed in this case. The lowest unrelaxed adhesion energies of the planar surfaces with nanoparticle<sub>001</sub> are presented in Table 5.6 and Table 5.7.

**Table 5.6** Unrelaxed adhesion energies of a calcite nanoparticle<sub>001-Ca</sub> on the calcite planar surfaces in vacuum and aqueous solution.

rotation	adhesion energies / kJmol <sup>-1</sup>					
	$\{1\ 0\ \bar{1}\ 4\}$		$\{0001\}$ -CO <sub>3</sub> <sup>2-</sup>		$\{0001\}$ -Ca <sup>2+</sup>	
	pure	hydrated	pure	hydrated	pure	hydrated
0°	-33.4	-6.5	-42.2	-25.2	-27.8	-7.6
30°	-27.1	-4.6	-12.5	-11.0	-30.4	-0.2
60°	-33.4	-6.6	-42.4	-25.7	-29.9	-7.2
90°	-26.8	-4.5	-7.1	-10.0	-22.1	-0.6
120°	-33.3	-6.5	-42.3	-25.1	-27.5	-7.5
150°	-27.0	-4.6	-12.6	-11.0	-31.5	-0.4
180°	-33.2	-6.5	-42.4	-25.5	-29.9	-7.3
210°	-26.9	-4.5	-7.4	-10.0	-22.2	-0.5
240°	-33.2	-6.4	-42.3	-25.0	-27.8	-7.6
270°	-27.1	-4.6	-12.3	-11.0	-31.1	-0.4
300°	-33.3	-6.5	-42.5	-25.6	-30.1	-7.3
330°	-26.8	-4.5	-7.1	-10.0	-21.7	-0.5

**Table 5.7** Unrelaxed adhesion energies of a calcite nanoparticle<sub>001-CO<sub>3</sub></sub> on the calcite planar surfaces in vacuum and aqueous solution.

rotation	adhesion energies / kJmol <sup>-1</sup>					
	{1 0 $\bar{1}$ 4}		{0001}-CO <sub>3</sub> <sup>2-</sup>		{0001}-Ca <sup>2+</sup>	
	pure	hydrated	pure	hydrated	pure	hydrated
0°	-10.8	-8.1	-8.4	-7.5	-9.3	-6.4
30°	-5.6	-5.3	-4.2	-5.6	-6.4	-2.9
60°	-6.9	-8.5	-5.9	-8.4	-8.9	-5.4
90°	-6.0	-5.6	-4.9	-6.1	-6.6	-3.0
120°	-10.7	-8.0	-8.4	-7.4	-9.2	-6.2
150°	-5.5	-5.2	-4.2	-5.6	-6.3	-2.8
180°	-6.9	-8.5	-5.8	-8.4	-8.9	-5.4
210°	-6.0	-5.5	-4.9	-6.0	-6.5	-2.9
240°	-10.8	-8.1	-8.3	-7.5	-9.3	-6.3
270°	-5.4	-5.3	-4.2	-5.6	-6.3	-2.9
300°	-6.8	-8.5	-5.9	-8.4	-8.8	-5.3
330°	-6.1	-5.5	-4.7	-6.1	-6.6	-3.1

### 5.6.1 Nanoparticle<sub>001</sub> and pure {10 $\bar{1}$ 4} surface

At first the interaction between each of the two nanoparticles<sub>001</sub> and the pure {10 $\bar{1}$ 4} surface in vacuum was investigated. The variations of the unrelaxed adhesion energies with the height between the nanoparticle<sub>001</sub> and the planar surface for a various orientations are plotted in Figure 5.26. All the plots have similar curvatures with an adhesion energy minimum at 2.4 Å of the distance between the nanoparticle<sub>001-Ca</sub> and the {1 0  $\bar{1}$  4} surface, and around 2.6 - 2.8 Å in the case of the nanoparticle<sub>001-CO<sub>3</sub></sub>, which are comparable to the energy minima of the nanoparticle<sub>104</sub> (2.5 - 2.8 Å). Although the 0° rotation leads to the energetically most favourable interfacial configuration, the difference in adhesion energies of 0° and 30° rotations is only 6.3 kJmol<sup>-1</sup> for a nanoparticle<sub>001-Ca</sub> and 5.2 kJmol<sup>-1</sup> for a nanoparticle<sub>001-CO<sub>3</sub></sub>, which are much smaller than that of the nanoparticle<sub>104</sub>-{1 0  $\bar{1}$  4}

interfacial system ( $43.1 \text{ kJ mol}^{-1}$ ). Unlike the nanoparticle<sub>104</sub> interfacial system, the unrelaxed adhesion energies are less dependent on the orientation of the nanoparticle<sub>001</sub>.

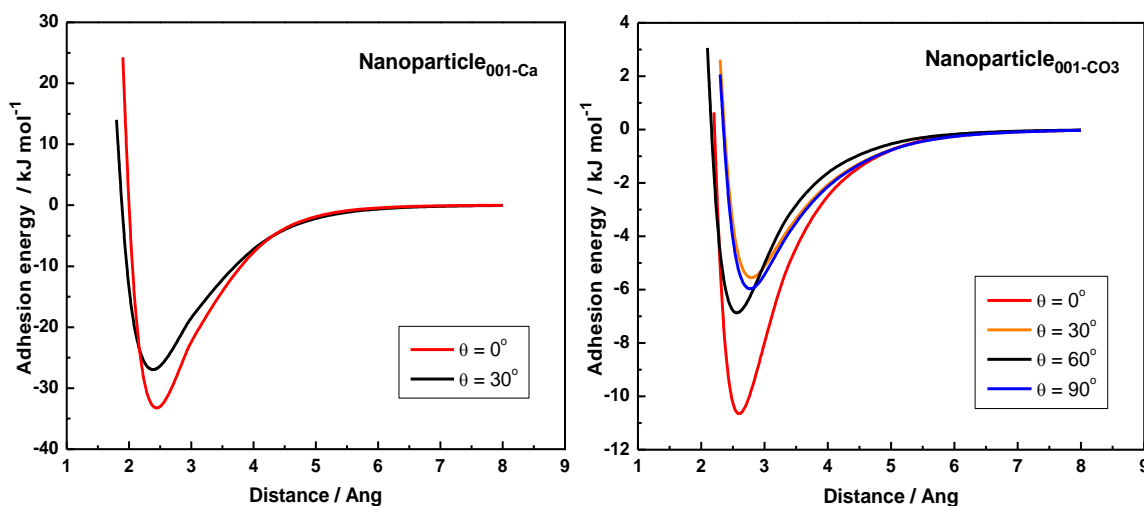


**Figure 5.26:** Adhesion energy as a function of the distance between the pure  $\{10\bar{1}4\}$  surface and a nanoparticle<sub>001</sub>. Results for some orientations have been omitted for clarity due to the periodic reiteration.

In general, the adhesion energy of a nanoparticle<sub>001-Ca</sub> on pure  $\{10\bar{1}4\}$  surface is more negative than that of a nanoparticle<sub>001-CO3</sub> for each orientation studied, meaning the positive charged nanoparticle is energetically more favourable to adhere to the pure  $\{10\bar{1}4\}$  surface than the negative charged nanoparticle. For the most stable interfacial configuration (a rotation of  $0^\circ$ ), the order of the adhesion energy of a nanoparticle on the pure  $\{10\bar{1}4\}$  surface is nanoparticle<sub>104</sub> < nanoparticle<sub>001-Ca</sub> < nanoparticle<sub>001-CO3</sub>. Further structure analysis suggests that this energy order may relate to the bottom structure of a nanoparticle, as displayed in Figure 5.27. For a nanoparticle<sub>104</sub>, both the rows of  $\text{Ca}^{2+}$  ions and  $\text{CO}_3^{2-}$  groups at the bottom of the nanoparticle<sub>104</sub> are aligned perfectly with the rows of  $\text{CO}_3^{2-}$  groups and  $\text{Ca}^{2+}$  ions of the  $\{10\bar{1}4\}$  surface. However, for a charged nanoparticle<sub>001</sub>, only the ‘row’ of  $\text{Ca}^{2+}$

ions or  $\text{CO}_3^{2-}$  groups of the nanoparticle<sub>001</sub> is aligned with the row of  $\text{CO}_3^{2-}$  groups or  $\text{Ca}^{2+}$  ions in the surface. Moreover, strong repulsive force occurs between the  $\text{CO}_3^{2-}$  groups of nanoparticle<sub>001- $\text{CO}_3$</sub>  and the  $\{1\ 0\ \bar{1}\ 4\}$  surface, which largely counteracts the attractive interaction. The periodic variation of the adhesion energy with the orientation of a nanoparticle<sub>001- $\text{CO}_3$</sub>  also demonstrates the effect of  $\text{CO}_3^{2-}$  groups in the nanoparticle<sub>001- $\text{CO}_3$</sub>  on the adhesion energy.

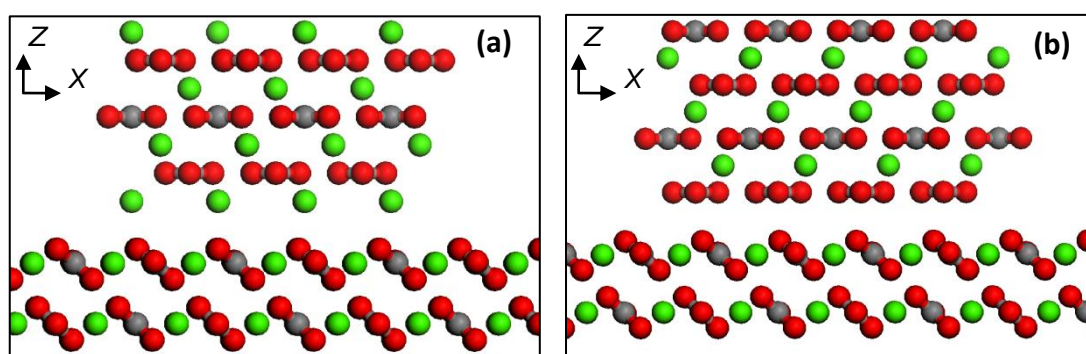


**Figure 5.27:** Side view of the most stable interfacial configurations of the pure  $\{10\ \bar{1}\ 4\}$  surface with a calcite nanoparticle<sub>001</sub>. (a) nanoparticle<sub>001-Ca</sub> and (b) nanoparticle<sub>001- $\text{CO}_3$</sub> , (Ca = green; C = grey; O = red).

### 5.6.2 Nanoparticle<sub>001</sub> and hydrated $\{10\ \bar{1}\ 4\}$ surface

Subsequently, the interactions between the nanoparticle<sub>001</sub> and the monolayer hydrated  $\{10\ \bar{1}\ 4\}$  surface was explored. Again a comprehensive scanning procedure was conducted. Figure 5.28 shows the plots of the adhesion energy vs. height from the hydrated surface. The general character of these plots is similar to those obtained in the case of the nanoparticle<sub>104</sub>. The plots of nanoparticle<sub>001-Ca</sub> reach the lowest values at 4.0 Å regardless of the orientations; whereas the plots of nanoparticle<sub>001- $\text{CO}_3$</sub>  have the energy minima at around 3.7 - 3.9 Å, which is a little smaller than those of the nanoparticle<sub>104</sub> (4.0 Å), due to the effect of hydrogen bonds formed between the  $\text{CO}_3^{2-}$  groups in the bottom of nanoparticle<sub>001- $\text{CO}_3$</sub>  and water molecules.

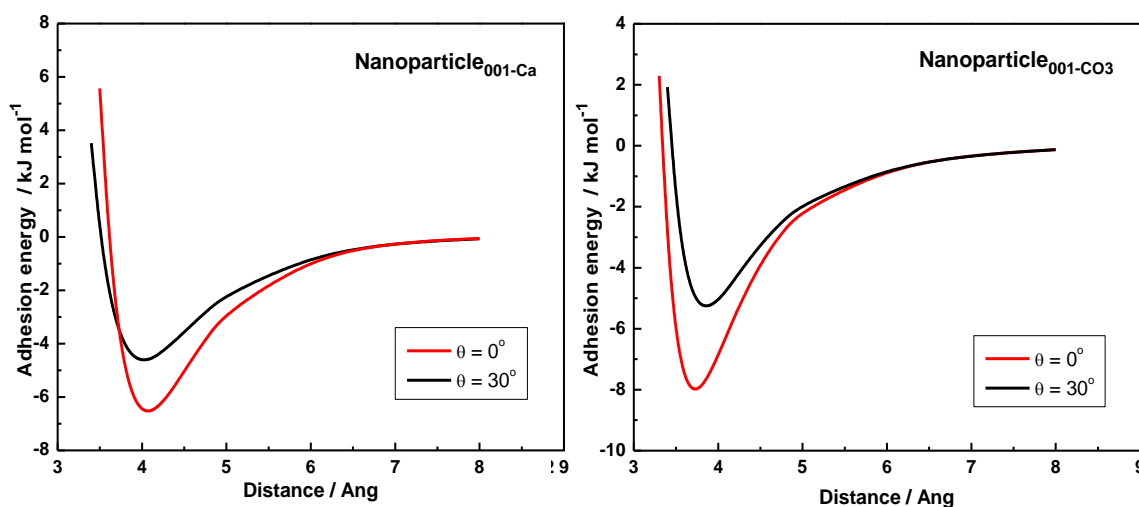


**Figure 5.28:** Adhesion energy as a function of the distance between the hydrated  $\{10\bar{1}4\}$  surface and nanoparticle<sub>001</sub>. Results for other orientations have been omitted for clarity.

Like the nanoparticle<sub>104</sub>, the adhesion energies of the nanoparticle<sub>001</sub> on the hydrated  $\{10\bar{1}4\}$  surfaces are less dependent on the orientation, for example, the energy difference between the  $30^\circ$  and  $60^\circ$  rotations is only  $2.0 \text{ kJmol}^{-1}$  for the nanoparticle<sub>001-Ca</sub> and  $3.2 \text{ kJmol}^{-1}$  for the nanoparticle<sub>001-CO3</sub>. All these findings can attribute to the fact that the monolayer water molecules have unified the surface structure, which makes the interfacial system less sensitive to the orientations of the nanoparticle.

It is also notable that the adhesion energy of the nanoparticle<sub>001-CO3</sub> at each rotation on the hydrated surface is more negative than that of the nanoparticle<sub>001-Ca</sub>, which is opposite to the energy order for the pure systems. The reason behind this contrary is probably due to the fact that the involvement of water molecules has not only weakened the interaction between the surface  $\text{Ca}^{2+}$  ions and  $\text{CO}_3^{2-}$  groups of the nanoparticle<sub>001-CO3</sub>, but also reduced the repulsive force between the  $\text{CO}_3^{2-}$  groups in both the surface and the nanoparticle<sub>001-CO3</sub>. Moreover, the hydrogen bonds formed between the oxygen in the  $\text{CO}_3^{2-}$  groups of nanoparticle<sub>001-CO3</sub> and hydrogen atoms of

water molecules enhance the interaction between the nanoparticle<sub>001-CO<sub>3</sub></sub> and hydrated surface, as it is illustrated in Figure 5.29.

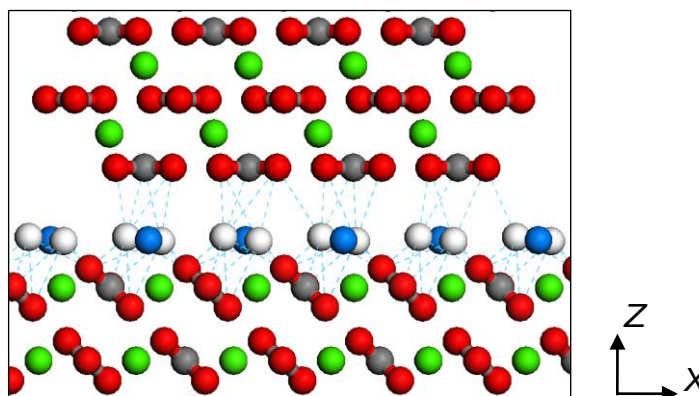


**Figure 5.29:** Side view of the most stable interfacial configuration of the hydrated  $\{10\bar{1}4\}$  surface with a nanoparticle<sub>001-CO<sub>3</sub></sub> (a  $0^\circ$  rotation), where the blue dashes lines show the hydrogen bonds, (Ca = green, C = grey, O = red, O<sub>water</sub> = blue, H = white).

### 5.6.3 Nanoparticle<sub>001</sub> and pure $\{0001\}$ surface

The interaction of the nanoparticle<sub>001</sub> with the pure  $\{0001\}$  surfaces in vacuum are discussed in this section, where both  $\text{CO}_3^{2-}$  and  $\text{Ca}^{2+}$  terminated  $\{0001\}$  surfaces have been considered. It is found that the shape of the plots of the unrelaxed adhesion energy vs. the height of the nanoparticle<sub>001</sub> with respect to the  $\{0001\}$  surface has been kept, as displayed in Figure 5.30. For the nanoparticle<sub>001-CO<sub>3</sub></sub>, the adhesion energy minima locate at around 2.3 - 2.6 Å on the pure  $\{0001\}$ -Ca<sup>2+</sup> surface and 2.4 - 2.7 Å on the pure  $\{0001\}$ -CO<sub>3</sub><sup>2-</sup> surface. However, for the nanoparticle<sub>001-Ca</sub>, the adhesion energy minima have shifted towards the left to 1.5 - 2.1 Å in the case of the  $\{0001\}$ -Ca<sup>2+</sup> surface, and 1.9 - 2.5 Å for the  $\{0001\}$ -CO<sub>3</sub><sup>2-</sup> surface. The change in the positions of the adhesion energy minima could be due to the surface structure of  $\{0001\}$  surfaces. For the nanoparticle<sub>001-CO<sub>3</sub></sub>, the strong repulsive force occurs between the  $\text{CO}_3^{2-}$  groups at the bottom plane of the

nanoparticle and  $\text{CO}_3^{2-}$  groups of the  $\{0001\}$  surface regardless of the orientation, which keeps the nanoparticle<sub>001-CO<sub>3</sub></sub> at a higher distance from the  $\{0001\}$  surface.

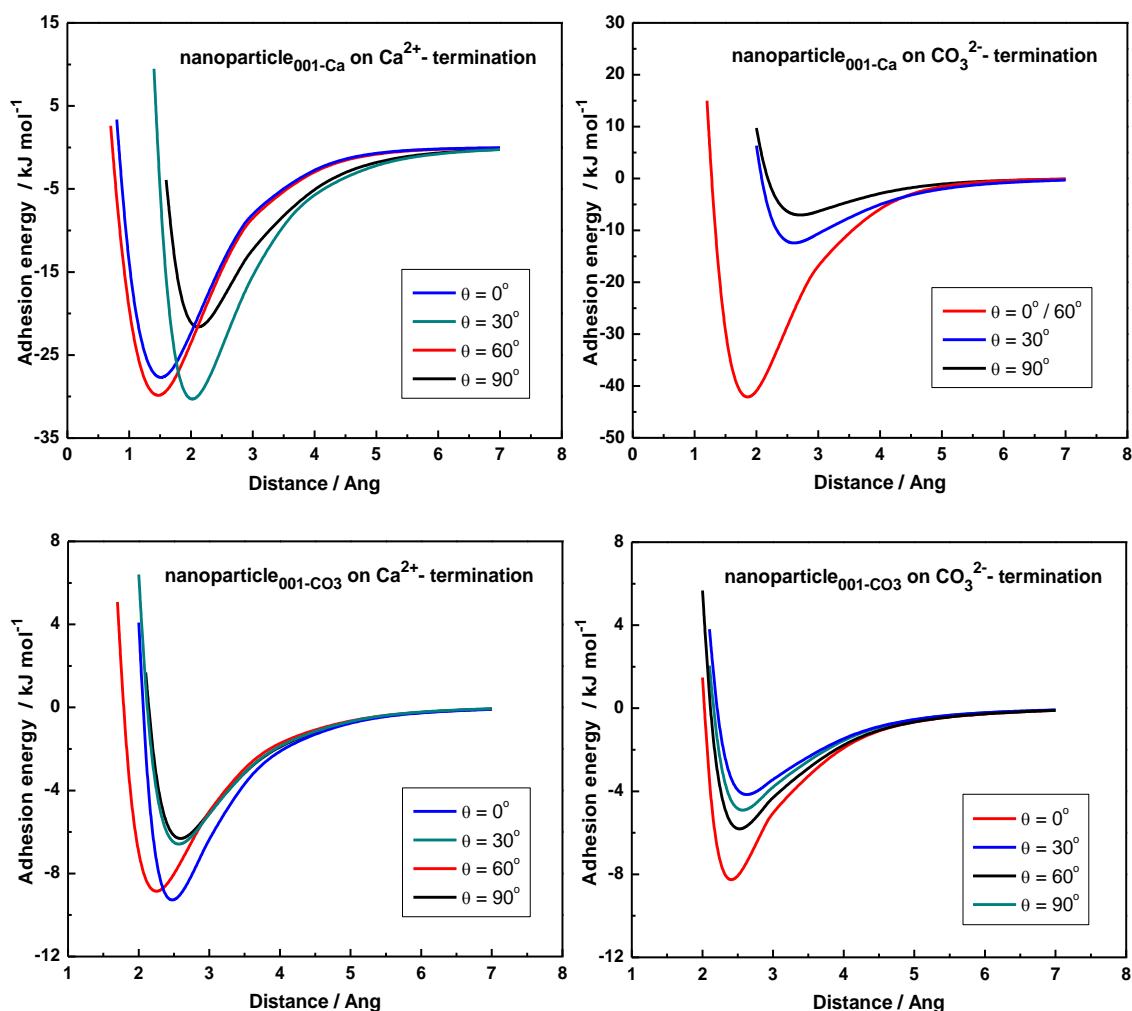


**Figure 5.30:** Adhesion energy as a function of the distance between a nanoparticle<sub>001</sub> and pure  $\{0001\}$  surface. Results for other orientations have been omitted for clarity.

Figure 5.31 displays two stable interfacial configurations of pure  $\{0001\}$  surface with a nanoparticle<sub>001-Ca</sub> at a rotation of  $60^\circ$ . For the  $\{0001\}$ - $\text{Ca}^{2+}$  surface, the “stand”  $\text{CO}_3^{2-}$  groups in the top plane of the surface point to the  $\text{Ca}^{2+}$  atoms in the nanoparticle. The distance between oxygen in the surface and  $\text{Ca}^{2+}$  ions in the nanoparticle is 2.34  $\text{\AA}$ , which results to a preponderant attractive force allowing the

nanoparticle<sub>001-Ca</sub> to be more easily accommodated to the {0001}-Ca<sup>2+</sup> surface. Similarly, for the {0001}-CO<sub>3</sub><sup>2-</sup> surface, the distance between oxygen in the surface and Ca<sup>2+</sup> ions in the nanoparticle is around 2.5 - 2.6 Å, which is only slightly larger than the standard Ca - O bond distance (2.4 Å), leading to an energetically favourable configuration.

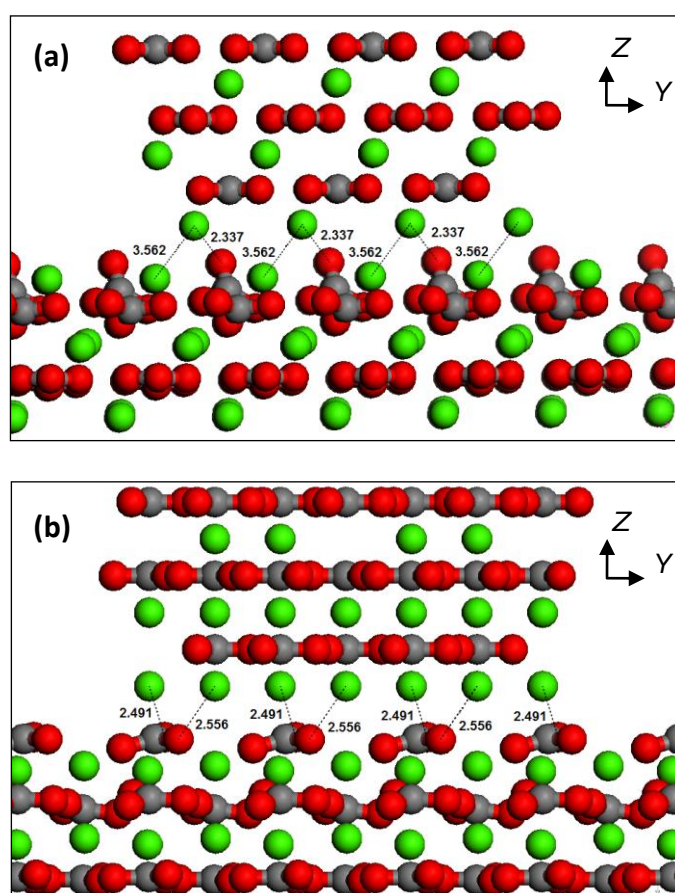


**Figure 5.31:** Side view of the most stable interfacial configurations of the pure {0001} surface with a nanoparticle<sub>001-Ca</sub>. (a) Ca<sup>2+</sup> termination and (b) CO<sub>3</sub><sup>2-</sup> termination, (Ca = green; C = grey; O = red).

The unrelaxed adhesion energies for both {0001} interfacial systems with different orientations of the nanoparticle<sub>001</sub> are illustrated in Figure 5.32. Like the cases of the nanoparticle<sub>001</sub> on the pure  $\{1\ 0\ \bar{1}\ 4\}$  surface, the adhesion energies of

the unrelaxed  $\{0001\}$  interfacial systems are less dependent on the orientation of the nanoparticle<sub>001</sub>, except for the nanoparticle<sub>001-Ca</sub> on the  $\{0001\}$ -CO<sub>3</sub><sup>2-</sup> surface, which forms an energetically favourable configuration when the nanoparticle<sub>001-Ca</sub> is at a rotation of  $n \times 60^\circ$  ( $n = 0, 1, \dots, 5$ ). This particular case is due to the strong attractive force between the nanoparticle<sub>001-Ca</sub> and  $\{0001\}$ -CO<sub>3</sub><sup>2-</sup> surface, which has been discussed before. For the nanoparticle<sub>001-CO3</sub>, the orientation of the CO<sub>3</sub><sup>2-</sup> groups at bottom plane of the nanoparticle<sub>001-CO3</sub> and top plane of the surface are more or less the same; therefore the repulsive force between the CO<sub>3</sub><sup>2-</sup> groups has been significantly increased regardless of the orientations. In summary, the positive charged nanoparticle<sub>001-Ca</sub> preferentially adheres to the  $\{0001\}$ -CO<sub>3</sub><sup>2-</sup> surface, while there is no preferential adhesion for the negative charged nanoparticle<sub>001-CO3</sub>.

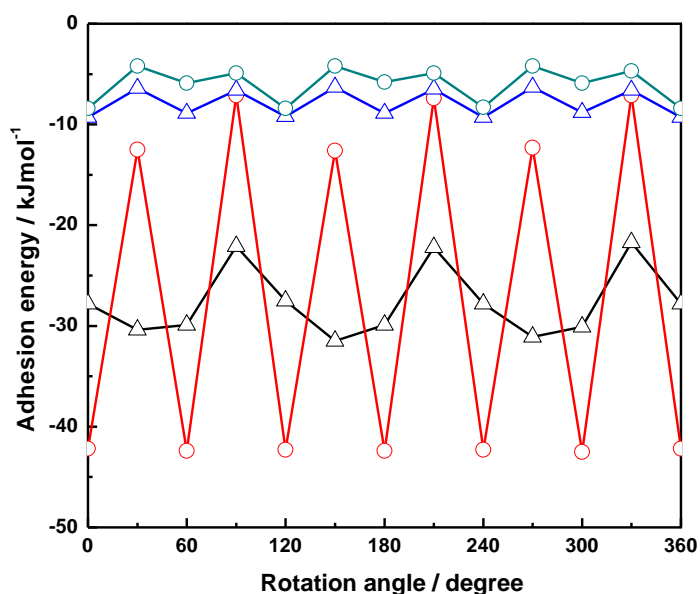


**Figure 5.32:** Adhesion energy as a function of the orientation of the nanoparticle<sub>001</sub> on pure  $\{0001\}$  surfaces. A nanoparticle<sub>001-Ca</sub> on the  $\{0001\}$ -CO<sub>3</sub><sup>2-</sup> surface (red line and circle) and  $\{0001\}$ -Ca<sup>2+</sup> surface (black line and triangle); a nanoparticle<sub>001-CO3</sub> on the  $\{0001\}$ -CO<sub>3</sub><sup>2-</sup> surface (green line and circle) and  $\{0001\}$ -Ca<sup>2+</sup> surface (blue line and triangle).

### 5.6.4 Nanoparticle<sub>001</sub> and hydrated {0001} surface

Finally the effect of hydration on the interactions of the {0001} interfacial systems was investigated. The calculations prove that the main feature of the curves of the unrelaxed adhesion energy vs. the height of the nanoparticle<sub>001</sub> with respect to the hydrated {0001} surface has been kept and the positions of the inflexion points have changed. In the case of the hydrated {0001}-Ca<sup>2+</sup> interfacial systems, the adhesion energy minima are at 4.1-5.0 Å for the nanoparticle<sub>001-Ca</sub> and 3.8 - 4.2 Å for the nanoparticle<sub>001-CO<sub>3</sub></sub>; while for the hydrated {0001}-CO<sub>3</sub><sup>2-</sup> systems, the adhesion energy minima have shifted to 2.5 - 3 Å for the nanoparticle<sub>001-Ca</sub> and 3 - 3.2 Å for the nanoparticle<sub>001-CO<sub>3</sub></sub>, which is the same to the case of nanoparticle<sub>104</sub> on the {0001} surface. This could be attributed to the surface atom arrangement mentioned early.

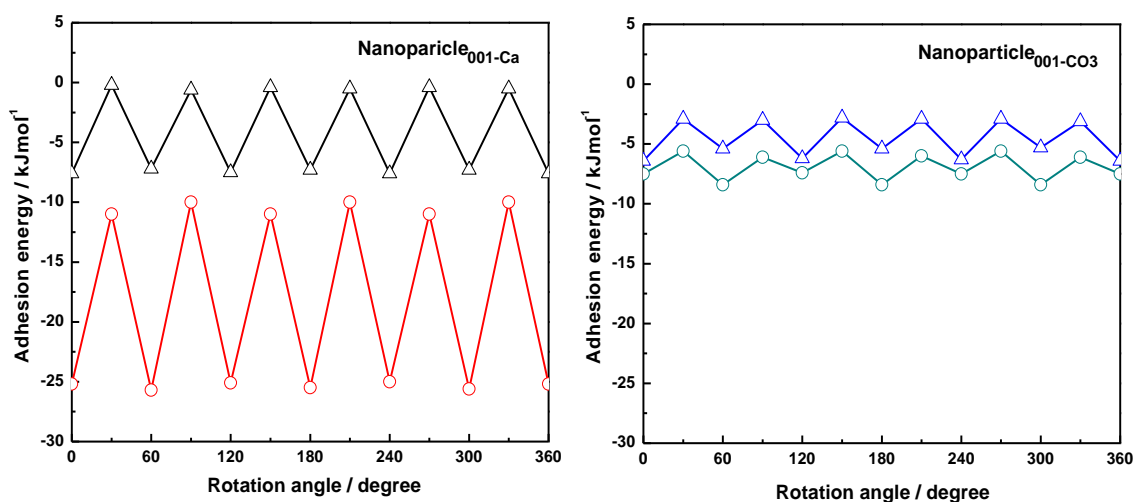


**Figure 5.33:** Adhesion energy as a function of the orientation of the nanoparticle<sub>001</sub> on hydrated {0001} surface: {0001}-CO<sub>3</sub><sup>2-</sup> surface (circle) and {0001}-Ca<sup>2+</sup> surface (triangle).

Figure 5.33 displays the variation of unrelaxed adhesion energies for the hydrated {0001} interfacial systems with different orientations of a nanoparticle<sub>001</sub>.

In general, the adhesion energies are approximately isotropic with the orientation of the nanoparticle<sub>001</sub>, which are similar to the pure {0001} interfacial system. Again, the only special case is the nanoparticle<sub>001-Ca</sub> on the hydrated {0001}-CO<sub>3</sub><sup>2-</sup> surface (red line), where a rotation of  $n \times 60^\circ$  ( $n=0, 1, \dots, 5$ ) leads to an energetically favourable interfacial configuration. Because the involvement of water molecules only partially blocks the interaction way between surface CO<sub>3</sub><sup>2-</sup> groups and the Ca<sup>2+</sup> ions of the nanoparticle<sub>001-Ca</sub>, which makes the water layer has less impact on the attractive force between oxygen in CO<sub>3</sub><sup>2-</sup> group and Ca<sup>2+</sup> ions of the nanoparticle<sub>001-Ca</sub>. As a result, the positive charged nanoparticle<sub>001-Ca</sub> energetically prefers to adhere to the {0001}-CO<sub>3</sub><sup>2-</sup> surface under aqueous conditions.

## 5.7 Chapter summary

In this chapter, atomistic simulations techniques have been applied to investigate the interaction of a calcite nanoparticle with the planar and stepped calcite surfaces in both vacuum and aqueous environment, where the size, orientation and structure of the nanoparticle have been considered.

Firstly, the size of a calcite nanoparticle has an apparent effect on the interaction between the nanoparticle and pure surfaces. A bigger size nanoparticle leads to stronger interaction in vacuum due to its increasing long-range order in the structure compared to a small size nanoparticle. However, this effect on the interaction between the nanoparticle and hydrated surface is negligible in the aqueous environment.

Secondly, for the nanoparticle<sub>104</sub> in vacuum, the interaction is highly dependent on the orientation of the nanoparticle<sub>104</sub> for both planar and stepped surfaces. The

most stable interface occurs when the lattices of the nanoparticle and the surface are perfectly aligned. It is energetically more favourable for the nanoparticle<sub>104</sub> to adhere to acute stepped  $\{3\ 1\ \bar{4}\ 8\}$  surface than planar  $\{1\ 0\ \bar{1}\ 4\}$  surface. Under aqueous conditions, the surfaces are stabilized but energy barriers occur as the nanoparticle<sub>104</sub> approaches the surface through the interfacial water layers. When the nanoparticle<sub>104</sub> approaches the hydrated surface through multiple water layers, the nanoparticle will move through a zigzag pathway rather than a direct perpendicular approach to overcome the energy barriers. Meanwhile hydration makes the interaction of the interfacial systems less sensitive to the orientation of the nanoparticle. Our results also suggest that the aggregation is most likely to occur at the planar surface rather than stepped surfaces in aqueous environment.

Finally, for the nanoparticle<sub>001</sub>, the adhesion energy is less dependent on the orientation of the nanoparticle<sub>001</sub> in both vacuum and aqueous environment, except for the positive charged nanoparticle<sub>001-Ca</sub> on the  $\{0001\}$ -CO<sub>3</sub><sup>2-</sup> surface. In general, the positive charged nanoparticle<sub>001-Ca</sub> preferentially adheres to the  $\{0001\}$ -CO<sub>3</sub><sup>2-</sup> surface, while there is no preferential adhesion on the planar surfaces for the negative charged nanoparticle<sub>001-CO<sub>3</sub></sub>.

# 6

## **The growth of calcium carbonate at tilt grain boundaries and stepped surfaces**

---

Surface defects such as steps and kinks are always present on the surfaces of natural and synthesized nanoparticles, and the tilt grain boundaries are easy to form between two colliding nanoparticles in aqueous environment. In this chapter atomistic simulation techniques have been employed to investigate the structure and stabilities of a range of tilt grain boundaries of calcite. Molecular dynamics simulations were used next to study the growth of a series of calcium carbonates units at the contact points of these tilt grain boundaries, which can then be used to assess the conditions required for the inter-growth of the crystal to occur. This study has given us the opportunity to further explore the growth mechanism of newly-formed joints during the aggregation process of nanoparticles.

## 6.1 Introduction

The crystallisation of calcite is one of the most important processes in the calcium carbonate industry in determining the size and morphologies of the solid products, which in turn affects their efficacy and applications. The calcite nanoparticles on the scale of ~100 nm have attracted increasing attention due to their widely applications, for example, as inorganic fillers in plastic, rubber, paper industries and as pigments in coating and painting industries (Patton, 1979; Schwuger, 1981; Zuiderduin *et al.*, 2003; Gilbert and Banfield, 2005). The dispersion of calcite nanoparticles is one of the important parameters from the viewpoint of technical applications and influences the properties of composite materials. As a filler material, the use of dispersive calcite nanoparticles may yield composite with perfect strength and smoothness (Chan *et al.*, 2002). For this reason, researchers are working overtime to chemically modify or otherwise force calcite nanoparticles not to aggregate or agglomerate.

When two nanoparticles collide in a suspension, hydrodynamic forces hold them together for a short time, before attempting to pull them apart. In a supersaturated solution, the nanoparticle will grow and new material will be deposited at the particle/particle interface. If the growth of the nanoparticle is fast and the hydrodynamic forces are weak, the nanoparticles will remain bound together to form an aggregate rather than being separated by the fluid shear forces (Collier *et al.*, 2000). Therefore, the investigation of the growth of new calcium carbonate at the particle/particle interface at the atomic level is essential to gain further understanding of the aggregation of calcite nanoparticles.

Although the perfect cleavage face  $\{1\ 0\ \bar{1}\ 4\}$  is the most stable surface of calcite and dominates the observed morphology, the natural and synthesized surfaces are rarely perfect or planar at the atomic scale. They always have defects such as steps and kinks. Indeed, calcite growth and dissolution are usually found to occur through steps and dislocations because of dangling bonds and local disorder (Putnis, 1992; Larsen *et al.*, 2010). When two calcite nanoparticles collide in solution, the different surfaces join together and form a grain boundary; the new  $\text{CaCO}_3$  units will then grow at these interfaces.

The grain boundary is the interface between two grains or crystallites in a polycrystalline material. They are the defects in the crystal structure and tend to decrease the electrical and thermal conductivity of the material. It is convenient to separate the grain boundaries by the extent of the mis-orientation between the two grains. A tilt grain boundary is that where the rotation axis is parallel to the boundary plane. An alternative is a twist grain boundary where the mis-orientation occurs around an axis that is perpendicular to the grain boundary planes.

In this chapter a number of symmetric tilt grain boundaries of calcite containing the acute and obtuse steps are modelled, which have been studied extensively both experimentally and theoretically (de Leeuw, 2002; Kristensen *et al.*, 2004; Stack and Grantham, 2010; Larsen *et al.*, 2010). The tilt grain boundaries are meant to act as models of two particles, after collision has occurred but before growth has had a chance to commence. The aim of this study is to investigate the structure and stability of these tilt grain boundaries of calcite. Also the growth of a series of  $\text{CaCO}_3$  units at different sites present on the steps in the tilt grain boundaries, to assess the conditions required for the growth of new  $\text{CaCO}_3$  material.

## 6.2 Methods

Atomistic simulation techniques are employed to model the geometries and energies of the tilt grain boundaries, which consist of large number of atoms. At first METADISE (Watson *et al.*, 1996) was used to create the stepped  $\{3\ 1\ \bar{4}\ 8\}$  and  $\{3\bar{1}\ \bar{2}\ 16\}$  surfaces, both of which contain  $\{1\ 0\ \bar{1}\ 4\}$  planes. The steps on the  $\{3\bar{1}\bar{4}\ 8\}$  surface are acute and the angle between the step wall and the terrace is  $80^\circ$  on the relaxed surface, whereas the steps on the  $\{3\ \bar{1}\ \bar{2}\ 16\}$  surface are obtuse with an angle of  $105^\circ$  between the step wall and the terrace. In order to form meaningful tilt grain boundaries, three different size stepped surfaces for each step direction have been modelled by gradually increasing the terrace area from  $620.9\ \text{\AA}^2$  to  $931.3\ \text{\AA}^2$  and  $1241.8\ \text{\AA}^2$  with the same step wall to terrace ratio.

The stepped surfaces were then used to generate the tilt grain boundaries through the following procedure. The grain boundary was created by mirroring two identical unrelaxed stepped surface blocks (3,456  $\text{CaCO}_3$  units) leaving a gap of  $2.0\ \text{\AA}$  between them. The resulting structure was then allowed to relax by MD simulations until the energy settled down. DL\_POLY 2.0 (Forester and Smith, 1995) was used for MD simulations of the grain boundaries. The equilibration of the pure system was achieved using NVE, NVT and NPT ensembles in sequence at 300 K for 150 ps with a time step of 0.2 fs. The final data collection simulations were run at NST for another 100 ps. The integration algorithms are based around the Verlet Leap-Frog scheme (Verlet, 1967) and the Nosé-Hoover algorithm (Nosé 1984; Hoover, 1985) is used for the thermostat. The parameter of the thermostat was set at 0.1 ps and the barostat relaxation time was set at 0.5 ps.

During MD simulations, the movable grain blocks tend to approach each other where there is a favourable interaction and the most stable grain boundary

configurations have been assumed to be those corresponding to energy minima. For ease the tilt grain boundary comprised of acute  $\{3\ 1\ \bar{4}\ 8\}$  surface is referred as A-grain boundary, while O-grain boundary is referred to the grain boundary comprised of obtuse  $\{3\ \bar{1}\ \bar{2}\ 16\}$  surface, represented schematically in Figure 6.1.

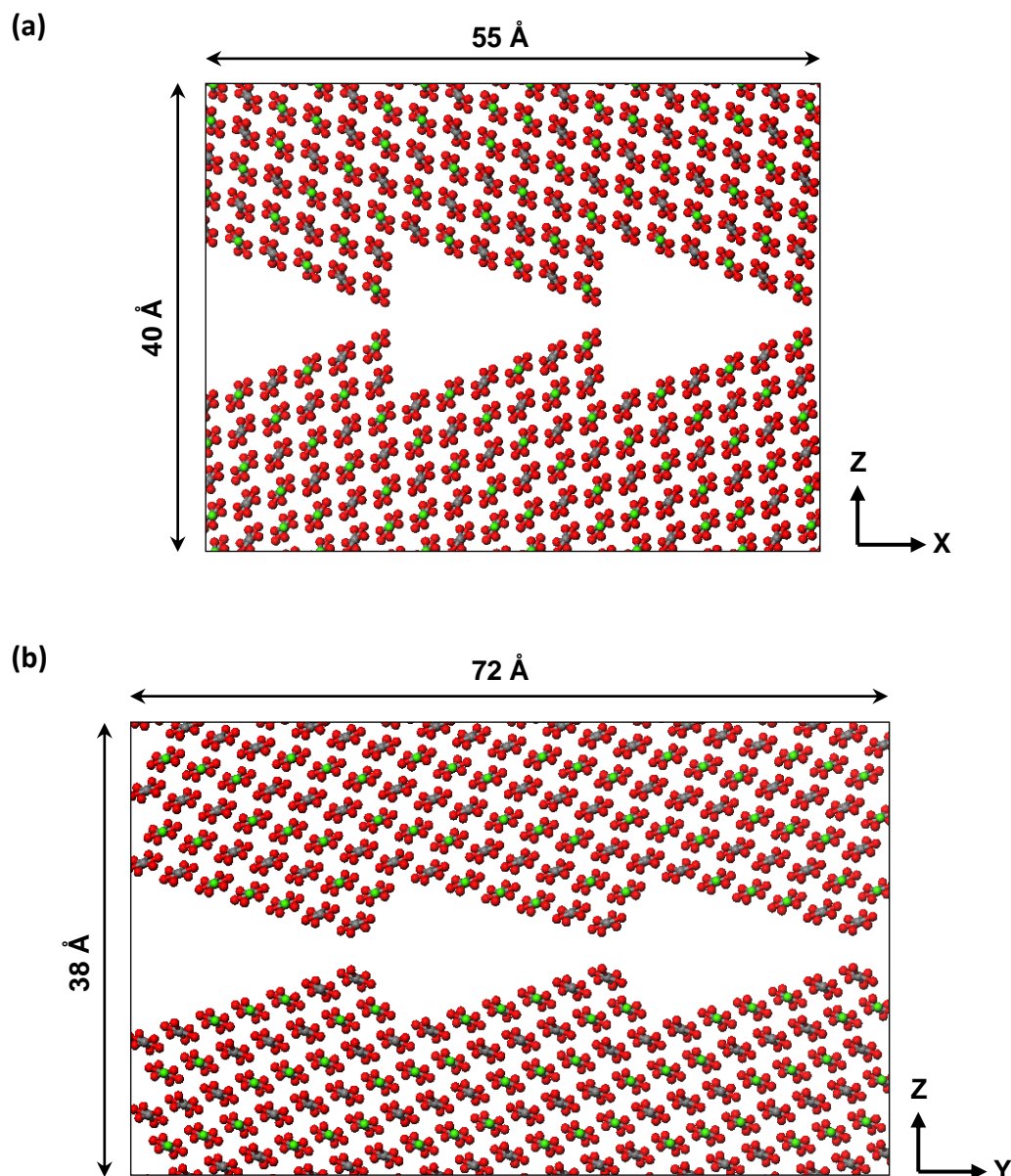


**Figure 6.1:** Side views of the unrelaxed calcite tilt grain boundaries: (a) A-grain boundary and (b) O-grain boundary. The surface area of each  $\{1\ 0\ \bar{1}\ 4\}$  terrace between the steps is  $620.9\ \text{\AA}^2$ . (Ca = green, C = gray, O = red).

To compare the relative stability of different grain boundaries, two energy contributions are considered here: the grain boundary energy  $\gamma_{grain}$  and the cleavage energy  $\gamma_{cleav}$ . The grain boundary energy is a measure of the thermodynamic stability of a grain boundary with respect to the bulk crystal. The cleavage energy is the energy required to cleave along the grain boundary to create two stepped surfaces and is a measure of the stability of the grain boundary with respect to the surfaces. These energies have been calculated for each grain boundary by using equations 6.1 and 6.2, respectively.

$$\gamma_{grain} = \frac{U_{grain} - U_{bulk}}{A}, \quad (6.1)$$

$$\gamma_{cleav} = \frac{2U_{surface} - U_{grain}}{A}. \quad (6.2)$$

where  $U_{grain}$  is the energy of the tilt grain boundary block,  $U_{bulk}$  is the energy of equal number of atoms in the bulk structure,  $U_{surface}$  is the energy of the stepped surface and  $A$  is the surface area.

For the hydrated grain boundaries, the boundary energies  $\gamma_{hydr}$  were calculated with respect to liquid water and bulk crystal:

$$\gamma_{hydr} = \frac{U_{hydr-grain} - (U_{bulk} + mU_{water})}{A} \quad (6.3)$$

where  $U_{hydr-grain}$  is the energy of the hydrated grain boundary block,  $U_{water}$  is the energy of a liquid water molecule and  $m$  is the number of water molecules. Then the hydration energy can be obtained by comparison of the hydrated with the pure grain boundaries and water molecules as follows:

$$U_{hydration} = \frac{1}{m} [U_{hydr-grain} - (U_{grain} + mU_{water})] \quad (6.4)$$

The growth of CaCO<sub>3</sub> unit in the grain boundary systems was also studied using MD simulations. For the addition of CaCO<sub>3</sub> unit at various sites of the grain boundaries in vacuum, the average growth energy per CaCO<sub>3</sub> unit,  $U_{growth}$ , was calculated according to the following equation:

$$U_{growth} = U'_{grain} - U_{unbound} = U'_{grain} - (U_{grain} + U_{CaCO_3}) \quad (6.5)$$

where  $U'_{grain}$  and  $U_{unbound}$  are the energies of the states with CaCO<sub>3</sub> unit incorporated and far from the stepped surface respectively. As the latter state is difficult to achieve in reasonably sized simulation cells, its energy can be expressed as the sum of the energy of the grain boundary and the average energy of an isolated CaCO<sub>3</sub> unit.

For the grain boundaries in aqueous solutions, the average growth energy per CaCO<sub>3</sub> unit  $U_{growth}$  was calculated using the following equation:

$$U_{growth} = U'_{hydr-grain} - (U_{hydr-grain} + U_{aqueous-CaCO_3}) \quad (6.6)$$

where  $U'_{hydr-grain}$  is the average energy of the grain boundary with the CaCO<sub>3</sub> unit incorporated under aqueous conditions, and  $U_{aqueous-CaCO_3}$  is the energy of the aqueous CaCO<sub>3</sub> unit.

### 6.3 Tilt grain boundaries of calcite

All the tilt grain boundaries form a series of open channels in the interfacial region with the acute or obtuse angles between the identical step walls and terraces preserved, for example, Figure 6.2 shows the quadrilateral channel voids formed in the interfacial region of tilt grain boundaries with a terrace area of 1241.8 Å<sup>2</sup>. For the A-grain boundary, the mirror step walls form an obtuse angle of 160° while the

terraces form an acute angle of  $40^\circ$ . For the O-grain boundary, these two angles are  $120^\circ$  and  $30^\circ$  respectively.

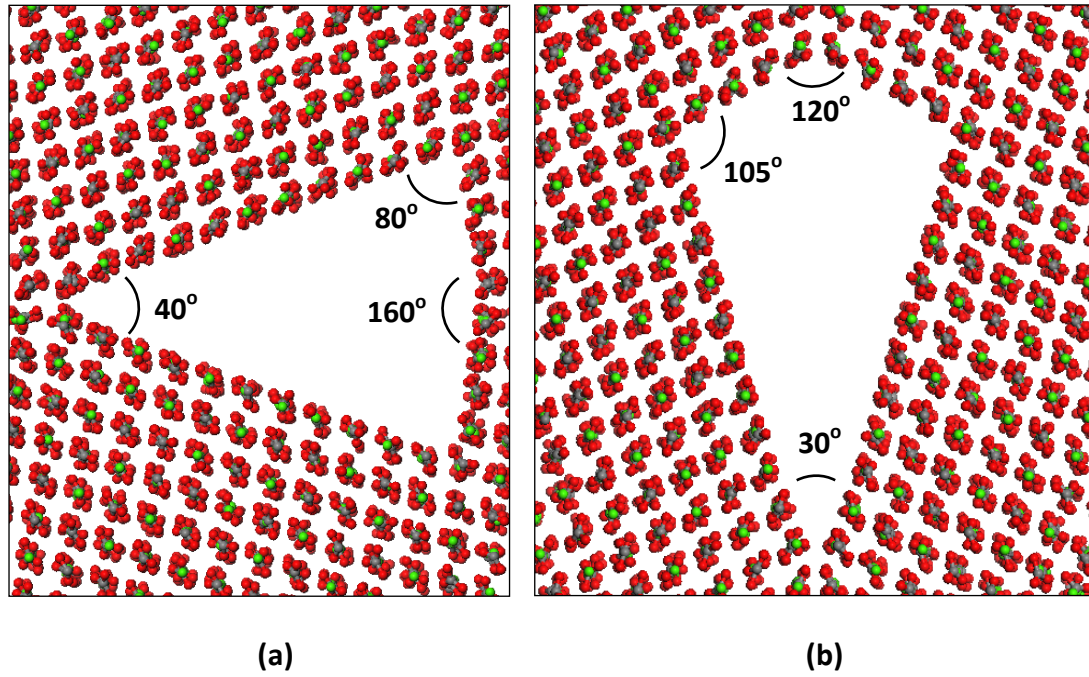


**Figure 6.2:** Side view of relaxed calcite grain boundaries: (a) A-grain boundary and (b) O-grain boundary. The surface area of the  $\{1\ 0\ \bar{1}\ 4\}$  terrace is  $1241.8\ \text{\AA}^2$ . (Ca = green, C = gray, O = red).

The boundary energies of the tilt grain boundaries created from the two stepped surfaces are listed in Table 6.1. For both grain boundaries, the grain boundary energies increase as the terrace area enlarges. The boundary energies of the small terrace ( $620.9\ \text{\AA}^2$ ) are the lowest for both grain boundaries, indicating that these grain boundaries are very stable. It is noteworthy that the boundary energies of the O-grain boundaries are lower than those of the A-grain boundaries with a comparable terrace area, which is consistent to the evidence from calculated stepped surface energy that the obtuse stepped  $\{3\ \bar{1}\ \bar{2}\ 16\}$  surface ( $0.72\ \text{Jm}^{-2}$ ) is more stable than the acute stepped  $\{3\ 1\ \bar{4}\ 8\}$  surface ( $0.88\ \text{Jm}^{-2}$ ).

The cleavage energy (Table 6.1) is a measure of the stability of the grain boundaries with respect to the stepped surfaces, where large cleavage energy indicates that the grain boundary is more stable with respect to the surfaces. The stable grain boundaries with the smallest terrace areas have the largest cleavage energies, which is due to the stability of the grain boundaries. As the obtuse stepped  $\{3 \bar{1} \bar{2} 16\}$  surface is more stable than the acute stepped  $\{3 1 \bar{4} 8\}$  surface, the O-grain boundary is clearly also more stable than the A-grain boundary, as already shown by the boundary energies.

**Table 6.1** Boundary and cleavage energies of the non-hydrated grain boundaries.

Terrace area / $\text{\AA}^2$	Boundary energy / $\text{Jm}^{-2}$	Cleavage energy / $\text{Jm}^{-2}$
A-grain boundary		
620.9	1.07	1.46
931.3	1.15	1.32
1241.8	1.31	0.84
O-grain boundary		
620.9	1.02	1.74
931.3	1.04	1.49
1241.8	1.11	1.39

The grain boundaries in aqueous liquid were then modelled. A number of water molecules were introduced in the open channels of the grain boundary by initially setting the water density at  $\rho = 1.0 \text{ gcm}^{-3}$ . The boundary and hydration energies of the hydrated grain boundaries are listed in Table 6.2. For all grain boundaries, the boundary energies follow the same trend as those of the non-hydrated grain boundaries, with boundary energies increasing as the terrace area increases. The hydrated grain boundaries are more stable compared to the non-hydrated grain

boundaries due to the stabilization by the water.

For all grain boundaries, the adsorption of water molecules in the open channels is exothermic (see Table 6.2). The grain boundaries with smaller terrace area have less negative hydration energies due to the stability of the non-hydrated boundaries, as the smaller channels in the interfacial region makes incorporation of water less easy. Furthermore, the hydration energies of the A-grain boundaries are more negative than those of the O-grain boundaries with comparable terrace areas. The acute angle of the channel in the O-grain boundary ( $30^\circ$ ) is smaller than that of the A-grain boundary ( $40^\circ$ ), making the water far away from the acute joining point. Figure 6.3 shows the structures of two hydrated grain boundaries with terrace area of  $1241.8 \text{ \AA}^2$  after 250 ps MD simulations. Hydration of the open channels of the large grain boundaries has little effect on the structure of the grain boundary regions. The figure also confirms that there is a high density water layer formed on the step wall and terrace.

**Table 6.2** Boundary and hydration energies of the hydrated grain boundaries.

Terrace area / $\text{\AA}^2$	Boundary energy / $\text{Jm}^{-2}$	Hydration energy / $\text{kJmol}^{-1}$
A-grain boundary		
620.9	0.56	-31.43
931.3	0.58	-35.18
1241.8	0.72	-40.65
O-grain boundary		
620.9	0.52	-30.32
931.3	0.56	-33.68
1241.8	0.60	-39.65

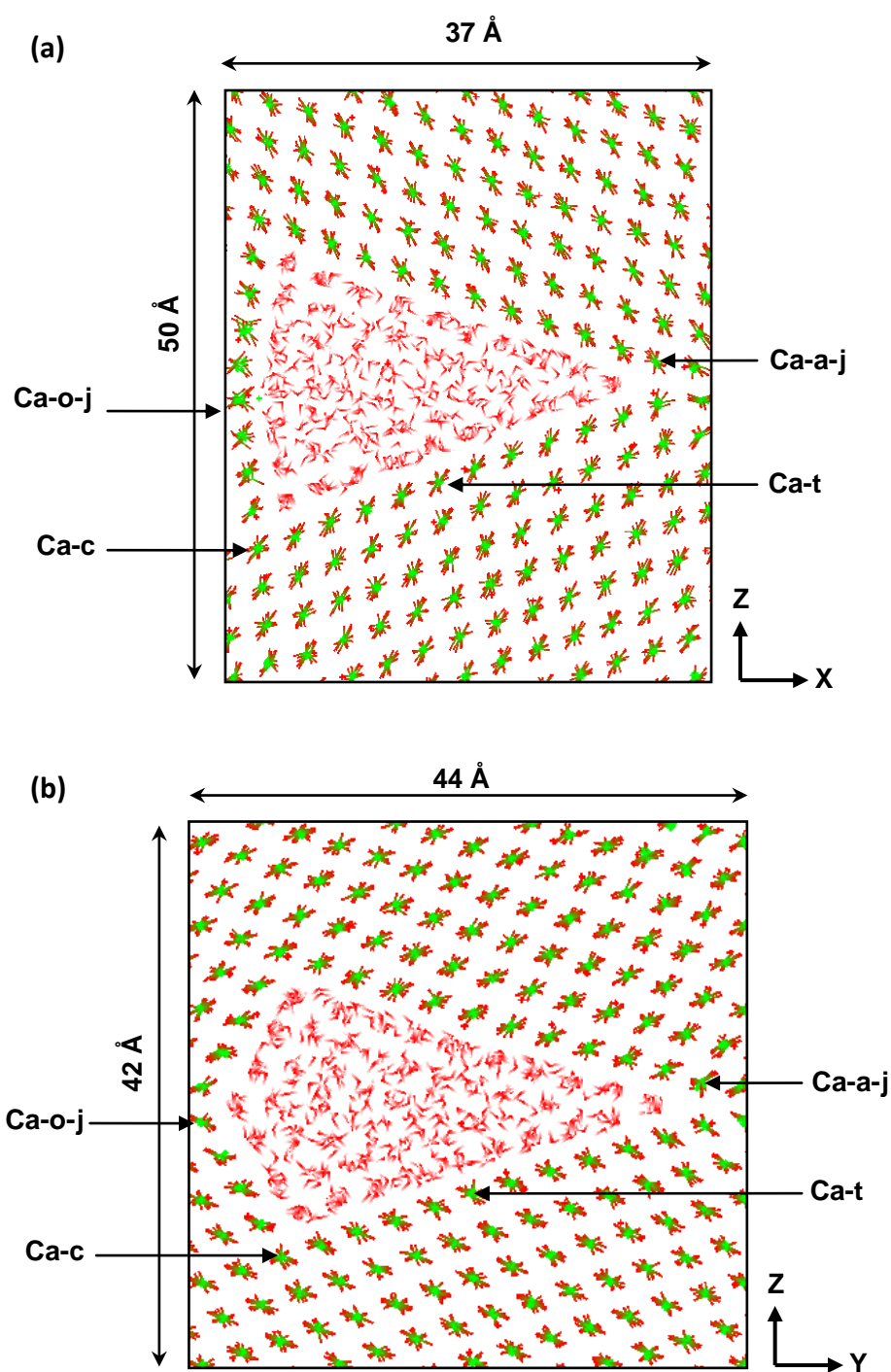


**Figure 6.3:** Snapshot of hydrated grain boundaries after 250 ps MD simulations, where four distinct Ca<sup>2+</sup> sites are labelled in the interfacial regions. The Ca<sup>2+</sup> in the acute step of the joints are labelled Ca<sub>a-j</sub>; the Ca<sup>2+</sup> in the obtuse step of the joints are labelled Ca<sub>o-j</sub>; the Ca<sup>2+</sup> at the step of original stepped surface are labelled Ca<sub>c</sub>, and Ca<sub>t</sub> stands for the Ca<sup>2+</sup> in the middle of the terraces. (a) A-grain boundary and (b) O-grain boundary. (Ca = green, O = red, C = grey, O<sub>water</sub> = red, H = white).

The structure of water around the  $\text{Ca}^{2+}$  ions at structurally different positions was extracted from the radial distribution functions (RDF), obtained from the MD simulations at 300 K, as average for 1000 configurations sampled over 100 ps of the production run. The results are shown in Figure 6.4 and Table 6.3.

**Table 6.3** Local environment of  $\text{Ca}^{2+}$  ions at structurally different positions in the hydrated grain boundaries. The distance listed here are from RDF results.

$\text{Ca}^{2+}$ positions	Ca-O <sub>water</sub> distance / Å	Ca-H <sub>water</sub> distance / Å
A-grain boundary		
$\text{Ca}^{2+}$ (o-j)	2.49	3.29
$\text{Ca}^{2+}$ (a-j)	4.20	3.39
$\text{Ca}^{2+}$ (c)	4.65	4.15
$\text{Ca}^{2+}$ (t)	2.39	3.19
O-grain boundary		
$\text{Ca}^{2+}$ (o-j)	2.49	3.29
$\text{Ca}^{2+}$ (a-j)	4.95	3.59
$\text{Ca}^{2+}$ (c)	4.05	3.39
$\text{Ca}^{2+}$ (t)	2.43	3.29

For the  $\text{Ca}^{2+}$  ions within the terrace of the grain boundaries ( $\text{Ca}_t$ ), which lack one coordinating  $\text{CO}_3^{2-}$  compared to the  $\text{Ca}^{2+}$  in the bulk, one water molecule is coordinated at an average distance of 2.39 Å in the A-grain boundary system and 2.43 Å in the O-grain boundary system. For the  $\text{Ca}^{2+}$  in the obtuse step of the joints ( $\text{Ca}_{o-j}$ ), which also lack one coordinating  $\text{CO}_3^{2-}$  compared to the bulk  $\text{Ca}^{2+}$ , one water molecule is coordinated at a distance of 2.49 Å in both two grain boundary systems. These  $\text{Ca}^{2+}$ -O<sub>water</sub> distances match closely the experimental determination for hydrated planar  $\{1\ 0\ \bar{1}\ 4\}$  surface (2.45 Å) from AFM (Ohnesorge and Binnig, 1993). This result is not surprising because a large expanse of the  $\{1\ 0\ \bar{1}\ 4\}$  plane is

exposed to the channel voids. However, for the  $\text{Ca}^{2+}$  in the acute step of the joints ( $\text{Ca}_{\text{a-j}}$ ), the narrow gap can only contain limited number of water molecules, as discussed before, making a longer  $\text{Ca}^{2+}$ - $\text{O}_{\text{water}}$  distance at 4.20 Å for the A-grain boundary system and 4.95 Å for the O-grain boundary system.

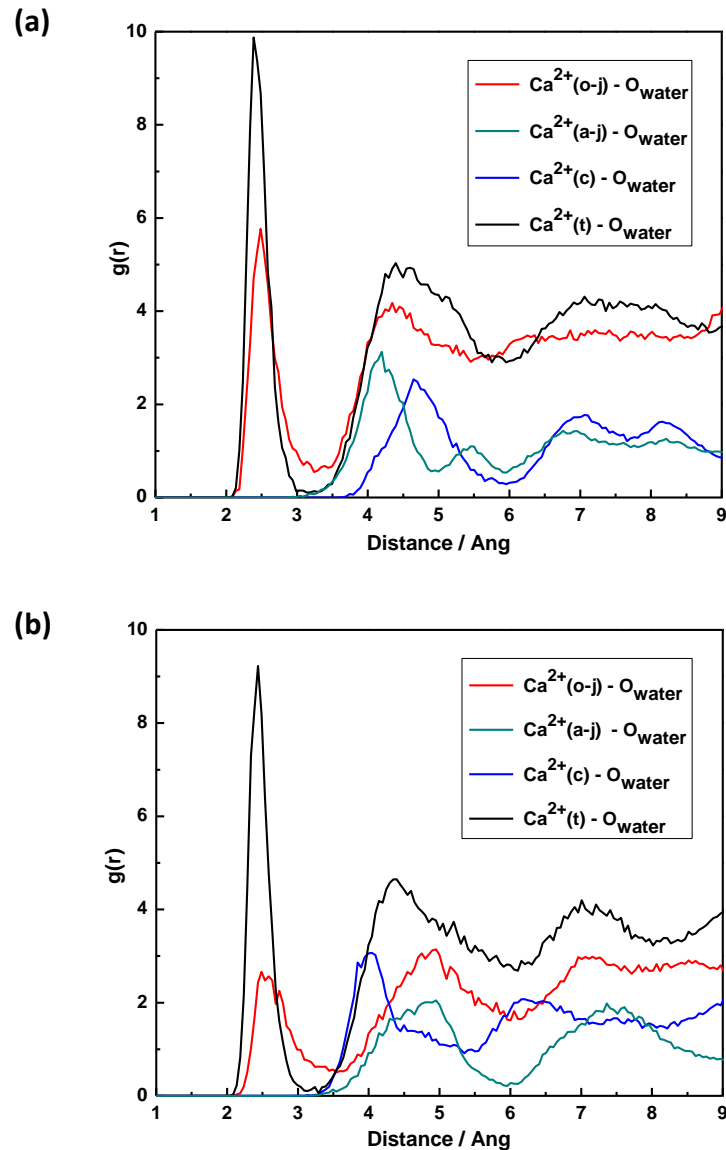


**Figure 6.4:** Radial distribution functions (RDF) for the local environment in the water at structurally different  $\text{Ca}^{2+}$  surface sites. (a) A-grain boundary and (b) O-grain boundary.

It is also clear from Figure 6.3 that there are highly ordered water molecules at the terraces of the grain boundaries. However, there is slightly disordered in the water distribution at the steps. This fluctuation in water distribution could be highly significant for the rate of  $\text{CaCO}_3$  growth and dissolutions, by slowing the transport of ions and molecules to the planar terraces. We will now focus on the growth of a series of  $\text{CaCO}_3$  units at the steps in the channel voids of the grain boundaries to assess the conditions required for the inter-growth of  $\text{CaCO}_3$  units.

## 6.4 Single $\text{CaCO}_3$ unit in aqueous environment

Theoretical investigations by Di Tommaso and de Leeuw (2008, 2009) have shown that, although the pairing of a  $\text{Ca}^{2+}$  ion with a  $\text{HCO}_3^-$  ion in solution is thermodynamically favourable, the subsequent addition of further  $\text{Ca}^{2+}$ ,  $\text{HCO}_3^-$  or  $\text{Ca}(\text{HCO}_3)_2$  units to the first  $\text{Ca}^{2+}$ - $\text{HCO}_3^-$  pair is endergonic. Bruneval *et al.* (2007), using a combination of MD and umbrella sampling method, also showed that the binding of  $\text{Ca}^{2+}$  to  $\text{CO}_3^{2-}$  in solution is strongly exothermic and there is no energy barrier to association of these two ions. Before considering the growth of  $\text{CaCO}_3$  units at the tilt grain boundaries of calcite in solution, the formation of single  $\text{CaCO}_3$  unit in aqueous environment has been examined using classic MD simulations.

The distance between the  $\text{Ca}^{2+}$  and the carbon of the  $\text{CO}_3^{2-}$  in the original system was set  $\sim 4.5$  Å, and classic MD simulations were performed using the NVT ensemble at 300 K without periodic boundary conditions. The energy of the  $\text{CaCO}_3$  group in vacuum was evaluated after equilibration. To obtain the energy of bulk liquid water, a box containing 256 water molecules was simulated at a temperature of 300 K. The equilibration of the water simulation cell was achieved by initially setting the experimental density at  $\rho = 1.0$   $\text{g cm}^{-3}$  and using NVE, NVT and NPT ensembles

in sequence. The final data collection simulations were run in NPT ensemble. The average energies of  $\text{CaCO}_3$  unit and liquid water at 300 K are listed in Table 6.4.

**Table 6.4** Average configurational energies for the  $\text{CaCO}_3$  unit in vacuum and water, and liquid water following simulations at 300 K for 0.2 ns.

	configurational energy / eV
$\text{CaCO}_3$ unit	-52.62
bulk liquid water	-9.54
aqueous $\text{CaCO}_3$ unit	-61.07

The average energy of the aqueous  $\text{CaCO}_3$  unit was calculated using a simulation box containing 251 water molecules plus the  $\text{CaCO}_3$  unit. The simulation box was equilibrated at NPT ensemble and 300 K for 30,000 time steps of 0.2 fs, after which data were collected for another 70,000 time steps. Then comparing the average energy of this simulation box with the energy of the 251 water molecules without the dissolved  $\text{CaCO}_3$  unit gave the energy of the hydrated pair.

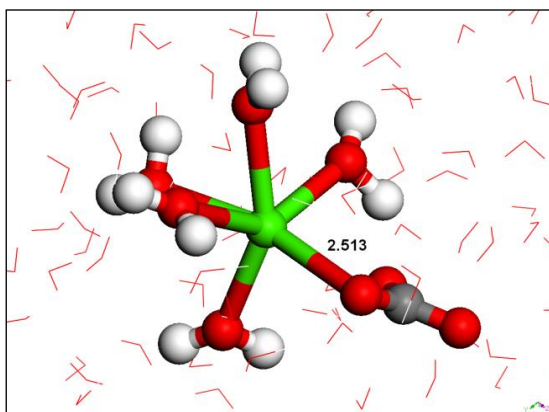


**Figure 6.5:** Representative snapshot from the MD simulations taken at 10 ps. (Ca = green; C = grey; O = red; H = white).

The configuration of the  $\text{CaCO}_3$  group in water after 10 ps is presented in Figure 6.5, which shows that the  $\text{CO}_3^{2-}$  group has replaced one water molecule in the first coordination shell to keep a coordination number of six. This structure agrees with the recent MD studies on the hydration structure of  $\text{CaCO}_3$  in water (Ikeda *et al.*, 2007; Di Tommaso and de Leeuw, 2008), which showed that the formation of the  $\text{CaCO}_3$  monomer would occur with an associate mechanism. The hydration structure of  $\text{Ca}^{2+}$  in water is highly variable as the 6-fold coordination is only marginally preferred over the next lowest minimum, a 7-fold pentagonal bipyramidal configurations. Figure 6.6 displays the RDFs of the  $\text{Ca-O}_{\text{carbonate}}$  and  $\text{Ca-O}_{\text{water}}$  pairs obtained from the MD simulations. For  $\text{Ca-O}_{\text{carbonate}}$ , the first peak is at 2.28 Å, which is 0.1 Å shorter than the average  $\text{Ca-O}_{\text{water}}$  distance. The results indicate that the most stable coordination model for the aqueous  $\text{CO}_3^{2-}$  is the monodentate configuration.

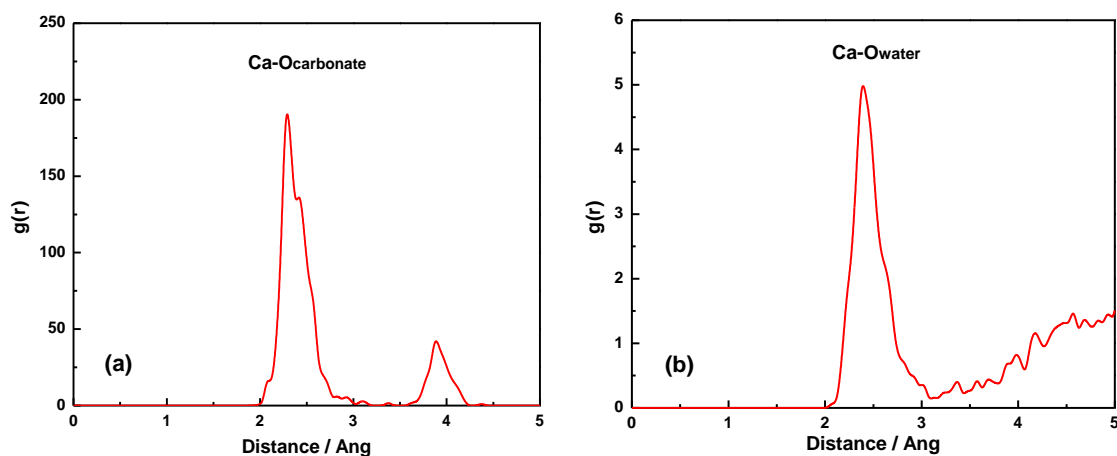


**Figure 6.6:** Radial distribution functions (RDF) of the  $\text{Ca}^{2+}\text{-O}_{\text{carbonate}}$  and  $\text{Ca}^{2+}\text{-O}_{\text{water}}$ .

## 6.5 The growth of $\text{CaCO}_3$ in pure grain boundary

Atomistic simulations have been employed successfully on many occasions to model the growth and dissolution of calcite by comparing the relative

thermodynamics of different mechanisms, surfaces or impurity inhibition. In this section, the MD simulations have been employed to investigate the growth of  $\text{CaCO}_3$  units in the tilt grain boundaries, which can then be used to assess the conditions required for the inter-growth between the nanoparticle aggregates. A recent computational study by Tribello *et al.* (2009) proposed the binding of  $\text{Ca}^{2+}$  to  $\text{CO}_3^{2-}$  is strongly exothermic and energetically more favourable than the binding of  $\text{Ca}^{2+}$  or  $\text{CO}_3^{2-}$  ion to  $\text{CaCO}_3$  unit. Therefore, only the subsequent addition of neutral  $\text{CaCO}_3$  units in the channel voids of the grain boundaries were modelled in this study. Moreover, only the large A-grain boundary and O-grain boundary (terrace area:  $1241.8 \text{ \AA}^2$ ) are considered here in order to ensure that the isolated  $\text{CaCO}_3$  unit is surrounded by a large number of water molecules without interaction with irrelevant  $\text{Ca}^{2+}$  or  $\text{CO}_3^{2-}$  ions in the grain boundary.

The growth of  $\text{CaCO}_3$  units in the channel voids of the non-hydrated grain boundaries were considered first, simulating the addition of successive  $\text{CaCO}_3$  units to different positions in the large grain boundaries and calculating the energy expended or released at each successive addition of a  $\text{CaCO}_3$  unit. Four different growing sites have been considered in this section. Figure 6.7 illustrates the initial structure of the large O-grain boundary with  $\text{CaCO}_3$  units at distinct positions, where Position-1 and Position-2 are at obtuse and acute step corner of the joints; Position-3 is close to the step corner of the original stepped surface, and Position-4 is above the middle of the planar terrace.

After addition of first  $\text{CaCO}_3$  unit at the Position-I ( $I = 1, 2, 3$  or  $4$ ), whereby both the grain boundary and the  $\text{CaCO}_3$  unit were allowed to relax to their new positions. The growth energies of  $\text{CaCO}_3$  units on the step or planar terrace were calculated using equation 6.5. Then successive  $\text{CaCO}_3$  units were added next to the adsorbed  $\text{CaCO}_3$  unit in sequence, as shown in Figure 6.8. The growth energies were

calculated again, namely the energies required or released per  $\text{CaCO}_3$  unit for each successive step.

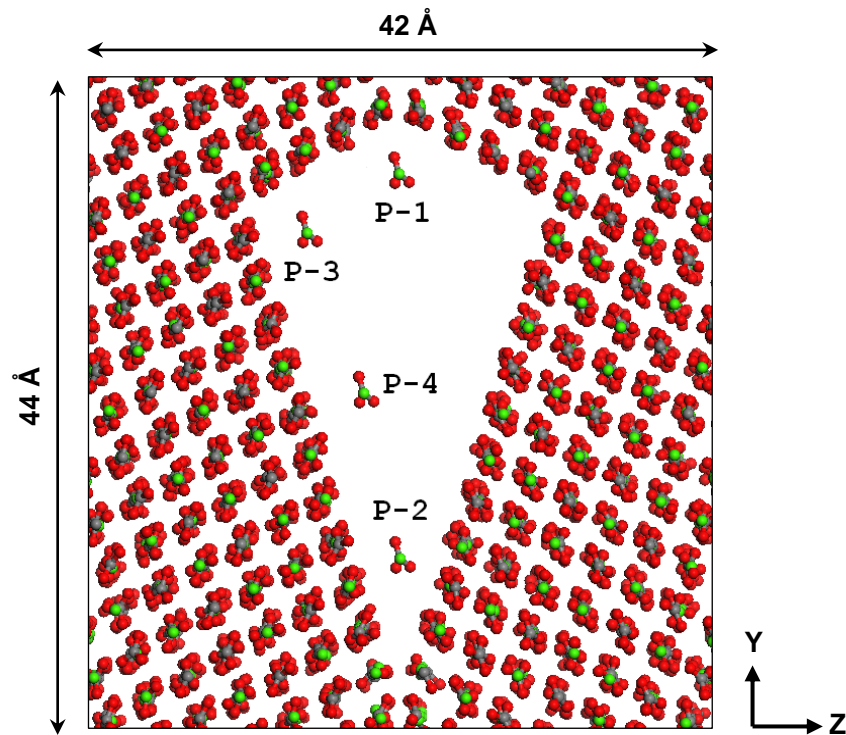


**Figure 6.7:** Initial structures of the O-grain boundary with single  $\text{CaCO}_3$  unit in vacuum. The  $\text{CaCO}_3$  unit was added at four different positions (P-I, I = 1, 2, 3 and 4) in the channel void, respectively.

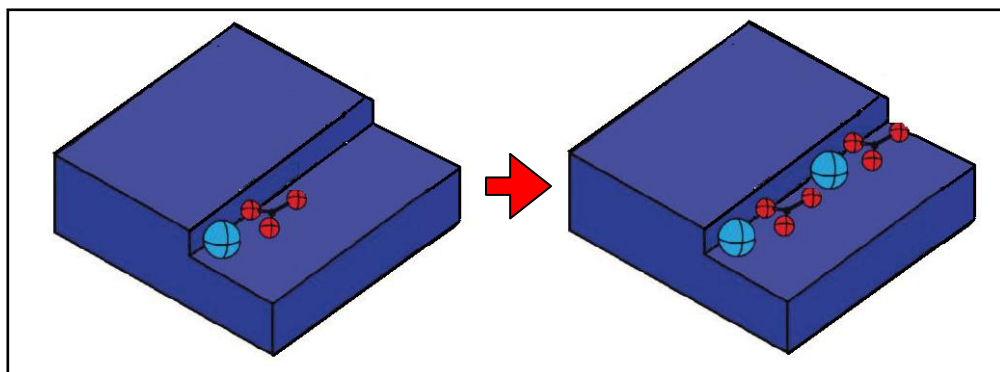


**Figure 6.8:** Schematic diagram of the incorporation of the first and second  $\text{CaCO}_3$  units along the step in the grain boundary. (Ca = green, C = black, O = red).

Table 6.5 lists the growth energies of successive addition of  $\text{CaCO}_3$  units at different positions in the grain boundary systems, either isolated or at kink sites next to existing  $\text{CaCO}_3$  units. In all cases, the consecutive growth of  $\text{CaCO}_3$  units in the grain boundaries is exothermic. Incorporation of  $\text{CaCO}_3$  units along the step is energetically more favourable than on the planar terrace as it is much more energetically expensive to create a “growth island” than a double kink on the surface (Mulline, 1992). The growth of a  $\text{CaCO}_3$  unit next to an existing unit was found to be much more energetically favourable as no new kinks were then introduced to the steps.

**Table 6.5** Growth energies of incorporation of  $\text{CaCO}_3$  units at various growth sites on the two non-hydrated grain boundaries ( $\text{kJmol}^{-1}$ ).

Positions	Angle	1 <sup>st</sup> $\text{CaCO}_3$	2 <sup>nd</sup> $\text{CaCO}_3$	3 <sup>rd</sup> $\text{CaCO}_3$	4 <sup>th</sup> $\text{CaCO}_3$
A-grain boundary					
P-1	160°	-310.5	-597.4	-682.4	-724.3
P-2	40°	-186.8	-724.3	-772.5	-792.3
P-3	80°	-219.1	-819.4	-821.0	-859.0
P-4	180°	-95.4	-579.6	-621.1	-638.1
O-grain boundary					
P-1	120°	-301.3	-652.3	-751.1	-772.9
P-2	30°	-137.1	-794.0	-824.3	-831.3
P-3	105°	-244.9	-782.3	-798.4	-802.5
P-4	180°	-90.3	-611.2	-635.9	-648.7

Comparing to the growth energies of  $\text{CaCO}_3$  units along the steps of the joints (Position-1 and Position-2) in A-grain boundaries and O-grain boundaries (Figure 6.9), it shows that introduction of the first  $\text{CaCO}_3$  unit at the obtuse step (Position-1) is much more energetically favourable than at the acute step (Position-2). When the second  $\text{CaCO}_3$  unit was introduced at the kink sites on each step, it is energetically

more favourable for further growth to occur at the acute step (Position-2) than the obtuse step (Position-1). This tendency retains from the growth next to a kink (2<sup>nd</sup> CaCO<sub>3</sub>) up to formation of a full step edge (4<sup>th</sup> CaCO<sub>3</sub>).

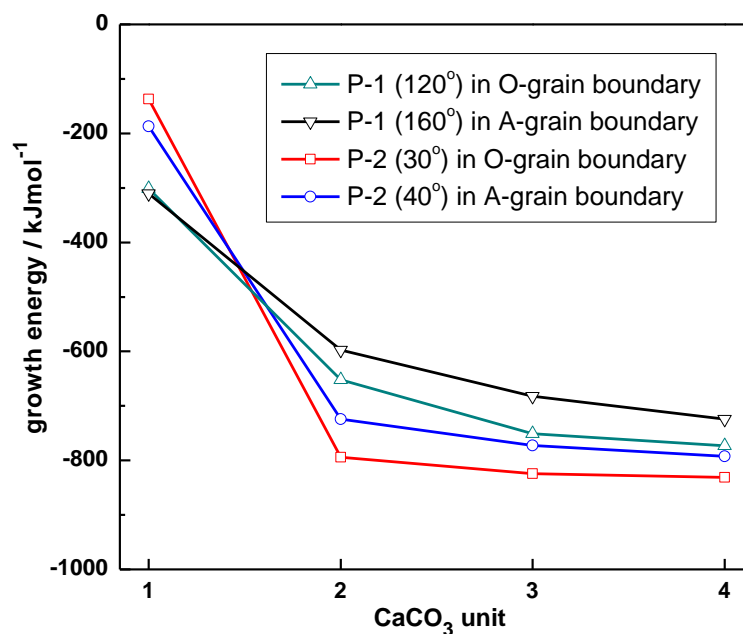


**Figure 6.9:** The growth energies of addition of successive CaCO<sub>3</sub> units at the steps of the joints (Position-1 and Position-2) in the A-grain boundary and O-grain boundary in vacuum.

Figure 6.10 compares the average growth energies per CaCO<sub>3</sub> unit released when growing a complete edge of CaCO<sub>3</sub> at various positions in the A-grain boundary and O-grain boundary. The growth of a complete row of CaCO<sub>3</sub> at the step is energetically more favourable compared to consecutive addition of CaCO<sub>3</sub> units on the planar terrace (Position-4). A comparison of the energies of growing a full CaCO<sub>3</sub> edge at the joints of the grain boundaries shows that larger energies are released for the incorporation of CaCO<sub>3</sub> at acute step (Position-2) than the obtuse step (Position-1) in the successive growth process. Therefore, under conditions simulating ultra-high vacuum, isolated CaCO<sub>3</sub> unit should initially grow at the obtuse step of the joints and

then prefer to grow at the acute step of the joints. However, the growth of  $\text{CaCO}_3$  in ultra high vacuum is not a sensible process and calcite aggregation and growth occur under aqueous conditions. It is therefore needed to consider the effects of water in this process.

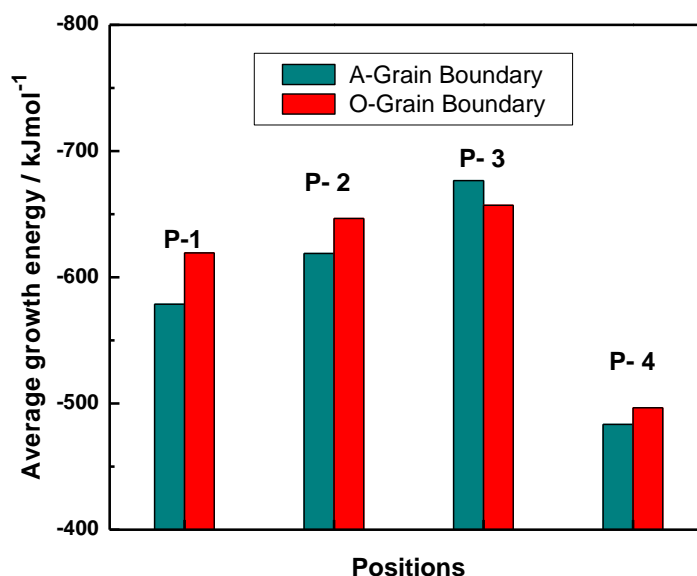


**Figure 6.10:** Bar charts of the average growth energies per  $\text{CaCO}_3$  unit released upon the growth of a full  $\text{CaCO}_3$  row in the A-grain boundary and O-grain boundary.

## 6.6 The growth of $\text{CaCO}_3$ in hydrated grain boundaries

Under aqueous conditions, the channel voids of the grain boundaries were filled with a number of water molecules to keep the water density at  $\rho = 1.0 \text{ gcm}^{-3}$  at 300 K. Again, four different positions have been investigated, the same as the cases of pure grain boundaries in vacuum. After addition of each  $\text{CaCO}_3$  unit and removal of relevant water molecules in the grain boundary system, a full MD simulation was then performed. The growth energy of  $\text{CaCO}_3$  units at isolated positions at three steps and planar terrace were calculated using equation 6.6, introducing kinks on each step, and also next to the adsorbed units, are listed in Table 6.6.

**Table 6.6** Growth energies of incorporation of CaCO<sub>3</sub> units at various growth sites in the hydrated A-grain boundary and O-grain boundary, as calculated by equation 6.6 (kJmol<sup>-1</sup>).

Positions	Angle	1 <sup>st</sup> CaCO <sub>3</sub>	2 <sup>nd</sup> CaCO <sub>3</sub>	3 <sup>rd</sup> CaCO <sub>3</sub>	4 <sup>th</sup> CaCO <sub>3</sub>
A-grain boundary					
P-1	160°	117.7	107.2	-76.9	-126.8
P-2	40°	233.5	84.6	-106.4	-192.3
P-3	80°	162.9	69.3	-95.9	-163.8
P-4	180°	277.4	168.7	30.7	-13.0
O-grain boundary					
P-1	120°	159.9	99.2	-70.4	-145.0
P-2	30°	230.8	48.8	-145.7	-208.6
P-3	105°	138.8	110.3	-13.8	-96.0
P-4	180°	282.9	226.6	75.1	-0.9

The results show that the additions of the first and second CaCO<sub>3</sub> units to all positions are endothermic and introduction of the first CaCO<sub>3</sub> unit at the acute step of the joints (Position-2) is much more energetically expensive than at the obtuse step of the joints (Position-1) in both A-grain boundary and O-grain boundary systems. For example, the difference in the growth energies between these two steps is 115.8 kJmol<sup>-1</sup> for the A-grain boundary system and 70.9 kJmol<sup>-1</sup> for the O-grain boundary system. However, once the activation energy barriers of incorporation of the first and second units have been overcome and the kinks have been created at the steps, it is energetically more favourable for further growth to occur at the acute step.

It is worthy to note that the average growth energies per CaCO<sub>3</sub> unit are positive when growing a complete row of CaCO<sub>3</sub> along the steps of the joints in grain boundary systems, except for Position-2 in the O-grain boundary system, where the average growth energy is -14.6 kJmol<sup>-1</sup>. These results contradict experimental findings of dissolution/growth processes of calcite, which spontaneously occur under

aqueous conditions (Gratz *et al.*, 1993; Stack and Grantham, 2010).

It is possible that the calculated growth energy is affected by the energy of the isolated aqueous CaCO<sub>3</sub> unit far from the grain boundary in equation 6.6. Therefore we have also calculated the average growth energy  $U_{growth}$  using the following equation:

$$U_{growth} = U'_{hydr-grain} - U_{hydr-grain-Ca} \quad (6.7)$$

where  $U'_{hydr-grain}$  is the average energy of the grain boundary with the CaCO<sub>3</sub> unit incorporated under aqueous conditions, and  $U_{hydr-grain-Ca}$  is the energy of the grain boundary with the single CaCO<sub>3</sub> unit in the centre of the channel voids.

**Table 6.7** Growth energies of incorporation of CaCO<sub>3</sub> units at various growth sites in the hydrated A-grain boundary and O-grain boundary, as calculated by equation 6.7 (kJmol<sup>-1</sup>).

Positions	Angle	1 <sup>st</sup> CaCO <sub>3</sub>	2 <sup>nd</sup> CaCO <sub>3</sub>	3 <sup>rd</sup> CaCO <sub>3</sub>	4 <sup>th</sup> CaCO <sub>3</sub>
A-grain boundary					
P-1	160°	-107.6	-118.1	-127.4	-140.3
P-2	40°	-48.0	-125.1	-146.5	-203.2
P-3	80°	-56.7	-130.3	-145.8	-194.3
P-4	180°	10.9	-17.6	-33.5	-50.7
O-grain boundary					
P-1	120°	-81.9	-122.6	-136.7	-150.5
P-2	30°	-22.8	-123.8	-165.3	-213.9
P-3	105°	-71.0	-89.6	-103.7	-112.3
P-4	180°	23.5	-2.4	-18.9	-43.6

The growth energies of consecutive CaCO<sub>3</sub> units in the hydrated grain boundary systems are listed in Table 6.7, calculated by equation 6.7. Now the results show that

initial additions of single  $\text{CaCO}_3$  units onto all positions are exothermic, except on the planar terraces (Position-4) in both hydrated grain boundaries. As we have discussed in the previous section, the adsorbed water molecules have a stabilizing effect on the grain boundaries. On the planar terrace the water molecules form an ordered layer, which is disturbed by the presence of steps, as shown in Figure 6.2. Therefore, the initial growth of  $\text{CaCO}_3$  unit could prefer to occur at the steps rather than at the terraces. However, once the activation energy barrier of incorporation of the initial  $\text{CaCO}_3$  unit has been overcome, it is exothermic to further grow on the terrace.

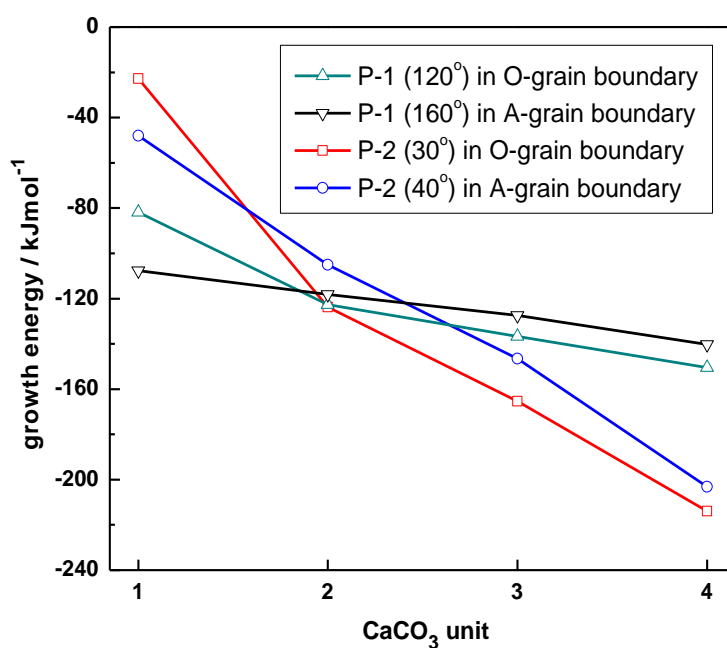


**Figure 6.11:** The energies of addition of successive  $\text{CaCO}_3$  units at the steps of the joints (Position-1 and Position-2) in the A-grain boundary and O-grain boundary under aqueous conditions.

The introduction of the first  $\text{CaCO}_3$  unit at the obtuse step (Position-1) is much more energetically favourable than at the acute step (Position-2), as displayed in Figure 6.11. For the A-grain boundary system, the growth energy of  $\text{CaCO}_3$  unit

incorporated at the obtuse step (Position-1,  $160^\circ$ ) is  $59.6 \text{ kJmol}^{-1}$  lower than that at the acute step (Position-2,  $40^\circ$ ), while the difference in growth energies between two steps is  $59.1 \text{ kJmol}^{-1}$  for the O-grain boundary system. After the incorporation of the first  $\text{CaCO}_3$  unit has created the kink at the step, it is energetically more favourable for further growth to occur at the acute step (Position-2). For example, the order of the energies of growing the 3rd and 4<sup>th</sup>  $\text{CaCO}_3$  units in the grain boundary systems is  $\text{P-2-O} < \text{P-2-A} < \text{P-1-O} < \text{P-1-A}$ , which is same as the order of step angles. The results demonstrate that the preferential growth of  $\text{CaCO}_3$  units at the grain boundaries is dependent on the angle of the steps.

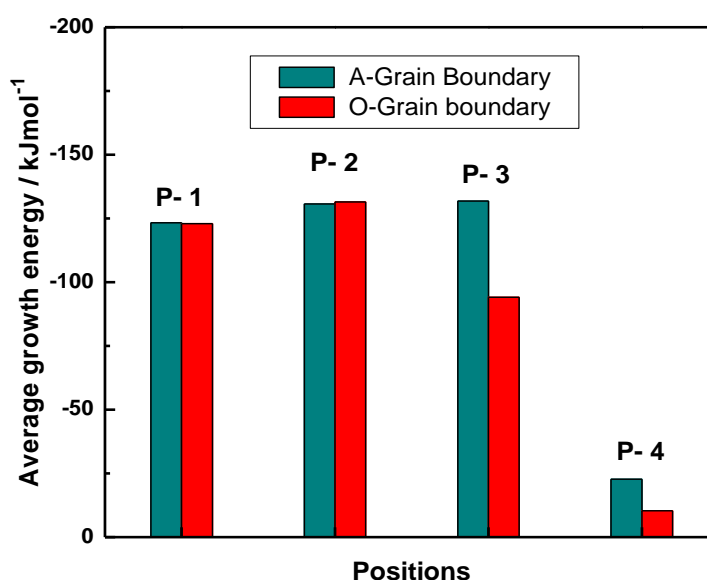


**Figure 6.12:** Bar charts of the average growth energies per  $\text{CaCO}_3$  unit released upon the growth of a full  $\text{CaCO}_3$  row at the hydrated A-grain boundary and O-grain boundary systems.

The average growth energies per  $\text{CaCO}_3$  unit released when growing a complete row of  $\text{CaCO}_3$  onto the steps and terraces in the A and O grain boundaries are illustrated in Figure 6.12. It is shown that the average growth energies of a  $\text{CaCO}_3$  unit at the acute step of the joints (Position-2) are slightly lower than at the obtuse

step of the joints (Position-1) during the successive growth process. Therefore when the two calcite nanoparticles collide and form a grain boundary in the aqueous solution, the growth velocities of the acute step should be higher than the obtuse step, once the initial growth unit has been deposited.

Early theoretical studies of calcite growth and dissolution at the stepped surfaces by de Leeuw and co-authors (1999, 2002) established that the activation energy required to create the first kink site at the acute edge is 1.5 times higher than that at the obtuse edge. Gratz *et al.* (1993) studied calcite growth at the two monomolecular steps by *in situ* AFM techniques and found an obtuse: acute ratio of growth velocities at the steps of 1.5 - 2.25 depending on the supersaturation. The ratio of activation enthalpies for the initial growth of acute: obtuse calculated in this study is 1.3 to 2.1, which agrees with previous computational and experimental research.

## 6.7 Chapter summary

In this chapter, atomistic simulation techniques have been employed to investigate the geometry and stabilities of a range of tilt grain boundaries formed from acute stepped  $\{3\ 1\ \bar{4}\ 8\}$  and obtuse stepped  $\{3\ \bar{1}\ \bar{2}\ 16\}$  surfaces of calcite. For both A-grain boundaries and O-grain boundaries, the boundary stability decreases as the terrace area increases. Furthermore, the O-grain boundary is more stable than the A-grain boundary in both vacuum and liquid water.

Molecular dynamic simulations were then performed to investigate the growth of a series of charge-neutral  $\text{CaCO}_3$  units at the large A-grain boundary and O-grain boundary, implying supersaturation conditions. Four different growing positions in vacuum and aqueous solution have been considered. The growth process modelled at

the non-hydrated grain boundaries is highly exothermic but unrealistic. Under aqueous conditions, the preferential growth of  $\text{CaCO}_3$  units is dependent on the angle of the steps formed in the channel voids of the grain boundaries. The initial incorporation of a  $\text{CaCO}_3$  unit is more preferential at the obtuse step of the joints in the grain boundary, but it is much more energetically favourable at the acute step of the joints when growing from a kink site. When the two calcite nanoparticles collide and form a grain boundary in the aqueous solution, the growth velocities of the acute step should be higher than the obtuse step, once the initial growth unit has been deposited on the steps.

# 7

## Conclusions and Future works

---

This chapter will summarise the findings of this computational study of calcium carbonate and draw conclusions about the incorporation of cationic impurities in calcite and the aggregation process of calcite nanoparticles, based on the results presented in this thesis. Moreover, some possible directions for the future research are presented.

## 7.1 Conclusions

A computer simulation study of calcium carbonate has been presented in this thesis, where the incorporation of divalent cationic impurities in calcite and the aggregation process of calcite nanoparticles have been included, using both molecular mechanics (MM) and molecular dynamics (MD) simulations based on interatomic potentials.

### 7.1.1 The incorporation of cationic impurities in calcite

Firstly, the mixing thermodynamics of calcite with a series of divalent cations ( $\text{Mg}^{2+}$ ,  $\text{Ni}^{2+}$ ,  $\text{Co}^{2+}$ ,  $\text{Zn}^{2+}$ ,  $\text{Fe}^{2+}$ ,  $\text{Mn}^{2+}$  and  $\text{Cd}^{2+}$ ) have been investigated by the atomistic simulation techniques, based on the calculation of all site occupancy configurations in  $2 \times 2 \times 1$  and  $3 \times 3 \times 1$  supercells of the calcite structure. The enthalpy of mixing, configurational entropy and free energy of mixing were then calculated to explore the mixing behaviour for a series of carbonate solid solutions.

The results show that the lowest energy configuration for each cationic impurity composition is always the one that maximises the homogeneity of the cations within (0001) layers but maximises the heterogeneity across layers. A full disorder is likely in  $(\text{Cd,Ca})\text{CO}_3$  solid solutions at equilibrium conditions. Although the fully disordered  $(\text{Mn,Ca})\text{CO}_3$  solid solutions has positive configurational enthalpies of mixing throughout the whole range of  $\text{Mn}^{2+}$  compositions, partial configurational ordering generally lead to better agreement with recent experiments. Our results indicate that the experimental “disordered”  $(\text{Mn,Ca})\text{CO}_3$  solid solutions, which are known to be favoured by kinetic factors, are actually not fully disordered, but contain a higher abundance of low-energy cation arrangement than that expected from a completely random distribution. For other divalent cations, i.e.  $\text{Fe}^{2+}$ ,  $\text{Zn}^{2+}$ ,  $\text{Co}^{2+}$ ,

$\text{Mg}^{2+}$  and  $\text{Ni}^{2+}$ , a great deal of cation ordering should be expected in the corresponding solid solutions at high temperature (e.g.  $\sim 1900$  K).

In particular, the structure and stability of the intermediate compositions ( $\text{Mn}/\text{Ca} = 1$ ) were investigated by a random sampling method. The most stable configuration corresponds to the ordered dolomite-type structure. The ordered kutnahorite ( $\text{Mn}_{0.5}\text{Ca}_{0.5}\text{CO}_3$ ) is metastable and becomes less stable than the fully disordered 50:50 solid solution at  $\sim 850$  K and this disordering temperature decreases to a value in better agreement with experiment (695 K), if a transition to a partially ordered structure is considered.

The calculations have also revealed that the solubility of the cationic impurities in calcite is largely related to the cationic coordination distance with oxygen, and the solubility of the smaller cations in calcite is higher than that of  $\text{Ca}^{2+}$  in the other end-member carbonates due to less elastic strain in the lattice. For the binary carbonate solid solutions,  $\text{CdCO}_3$  and  $\text{CaCO}_3$  can form continuous stable solid solution in the whole range of  $\text{Cd}^{2+}$  compositions at moderate temperatures. A miscibility gap at  $\text{Mn}^{2+}$  composition  $0.12 < x < 0.92$  has been found in the  $\text{Mn}_x\text{Ca}_{1-x}\text{CO}_3$  system. A higher abundance of cationic ordering are present in the  $(\text{Fe},\text{Ca})\text{CO}_3$ ,  $(\text{Co},\text{Ca})\text{CO}_3$ ,  $(\text{Zn},\text{Ca})\text{CO}_3$ ,  $(\text{Mg},\text{Ca})\text{CO}_3$  and  $(\text{Ni},\text{Ca})\text{CO}_3$  systems, and the solubility of these cations in calcite is extraordinarily limited below 1000 K, which are in good agreement with available experimental measurements.

### **7.1.2 The adhesion of calcite nanoparticles on calcite surfaces**

The aggregation process of calcite nanoparticles has then been investigated by atomistic simulations techniques. The adhesion of a calcite nanoparticle on some major calcite surfaces has been studied in both vacuum and aqueous environment,

where the effects of size, orientation and structure of calcite nanoparticle on the interaction between a nanoparticle and a surface have been investigated, respectively.

The results show that the size of a calcite nanoparticle has an apparent effect on the interaction between the nanoparticle and surfaces in vacuum, but this influence has not been found in the aqueous environment. For a nanoparticle<sub>104</sub> in vacuum, the interaction is highly dependent on the orientation of the nanoparticle for both planar  $\{1\ 0\ \bar{1}\ 4\}$  and stepped surfaces (e.g.  $\{3\ 1\ \bar{4}\ 8\}$  and  $\{3\ \bar{1}\ \bar{2}\ 16\}$ ). The most stable interface occurs when the lattices of the nanoparticle and the surface are perfectly aligned. The aggregation would preferentially occur at the acute stepped  $\{3\ 1\ \bar{4}\ 8\}$  surface rather than the planar  $\{1\ 0\ \bar{1}\ 4\}$  surface. While in the aqueous environment, the hydration makes the adhesion energy of the systems less sensitive to the orientation of the nanoparticle. Meanwhile energy barriers occur as the nanoparticle approaches the surface through the interfacial multiple water layers. When a nanoparticle approaches the hydrated surface through multiple water layers, it will move through a zigzag pathway rather than a straight perpendicular way to overcome these energy barriers. It is energetically more favourable for the nanoparticle to adhere to the planar  $\{1\ 0\ \bar{1}\ 4\}$  surface than the stepped surface in aqueous environment, although the difference in adhesion energies is negligible.

The study has also been extended to consider a nanoparticle with different structure, namely the nanoparticle<sub>001</sub> in this thesis. The interaction between the nanoparticle<sub>001</sub> and calcite surfaces is less dependent on the orientation of the nanoparticle in both vacuum and aqueous environment, except for the positive charged nanoparticle<sub>001</sub> on the  $\text{CO}_3^{2-}$  terminated  $\{0001\}$  surface. Generally, the positive charged nanoparticle<sub>001</sub> preferentially adheres to the  $\text{CO}_3^{2-}$  terminated  $\{0001\}$  surface, while there is no preferential adhesion on the planar surfaces for the negative charged nanoparticle<sub>001</sub>.

### 7.1.3 The growth of calcium carbonate in tilt grain boundaries

Finally, atomistic simulation techniques were employed to investigate the geometry and stabilities of a range of tilt grain boundaries, which are meant to act as models of two calcite nanoparticles, after collision has occurred but before growth has had a chance to commence. The stability of the tilt grain boundary decreases as the terrace area increases. The grain boundary generating by obtuse stepped surface, is more stable than the grain boundary generating by acute stepped surface in both vacuum and aqueous environment, which is consistent to the evidence from calculated surface energy of stepped surface.

Molecular dynamic (MD) simulations were then used to investigate the growth of a series of charge-neutral  $\text{CaCO}_3$  units at different positions in the grain boundary. It is observed that the growth process modelled in the grain boundary in vacuum is highly exothermic but unrealistic. Under aqueous conditions, the preferential growth of  $\text{CaCO}_3$  units is dependent on the angle of the steps formed in the channel voids of the grain boundary. The initial incorporation of a  $\text{CaCO}_3$  unit is preferential at the obtuse step of the joints in the grain boundary, while it is much more energetically favourable at the acute step of the joints when growing from a kink site. Our results suggest that when the two calcite nanoparticles collide and form a grain boundary in the aqueous solution, the ratio of activation enthalpies for the initial growth of a  $\text{CaCO}_3$  unit at acute step to obtuse step is 1.3 to 2.1. Furthermore, the growth velocities of the acute step should be higher than the obtuse step, once the initial growth unit has been deposited on the steps, which agrees with experimental findings and other theoretical studies.

## 7.2 Future works

Having investigated the incorporation of cationic impurities in calcite and the aggregation process of calcite nanoparticles, this computational study of calcium carbonate is only a start in its expansive and diversity fields and there are still much more work to be done to gain a further understanding of this fantastic material.

One of the possible directions for the future research is to investigate the incorporation of double various cationic impurities in calcite and predict the mixing thermodynamics of tertiary carbonate solid solutions, for example, the (Co,Zn,Ca)CO<sub>3</sub> system. However, the set of potential parameters should be improved to give a good description of both structural and strain effects in this mixed system before considering the substitution of Co<sup>2+</sup> and Zn<sup>2+</sup> in calcite. Furthermore, some divalent cations with ionic radius larger than Ca<sup>2+</sup> usually prefer to substitute in aragonite structure, i.e. Sr<sup>2+</sup>, Pb<sup>2+</sup> and Ba<sup>2+</sup>. It is interesting to employ the same method to investigate the aragonite-type solid solutions and compare the mixing behaviors of these divalent cations in both calcite and aragonite.

For the aggregation of calcite nanoparticles, another future work should involve the investigation of the interaction between a nanoparticle and calcite surfaces in order to further investigate more complicated systems in terms of particle size and aqueous conditions. It should also include developing and applying free energy-based molecular dynamic simulations to study the variation of free energy during the aggregation and growth process of calcite nanoparticles, where the entropy of water molecules should be considered in the system.

Furthermore, impurities in a crystallization process have been found to have vast effects on the morphology of the resulting crystal, with both possible beneficial and

detrimental effects for the resultant product. Modelling of growth rates and how the presence of impurities affects the morphology of the crystal will be another interesting research direction. Under the premise of the accurate potential parameters for cationic impurities, it is possible to study the effect of these impurities on the growth of calcium carbonate using molecular dynamics simulations, which could give us the opportunity to discover the impurity inhibition mechanism under complicated conditions.

## Bibliographic

---

Allen M. P. and Tildesley D. J. (1988) *Computer simulation of liquids*. Oxford University Press, Oxford, UK.

Alloway B. J. (1995) *Heavy Metals in Soils*. Chapman and Hall, Glasgow, UK, 2<sup>nd</sup> edition.

Andrews D. H. (1930) The relation between the Raman spectra and the structure of organic molecules. *Physical Review* **36**: 544-554.

Austen K. F., Wright K., Slater B. and Gale J. D. (2005) The interaction of dolomite surfaces with metal impurities: a computer simulation study. *Physical Chemistry and Chemical Physics* **7**: 4150-4156.

BCCF (The British Calcium Carbonates Federation) (2007) Calcium carbonate: modern day applications, <http://www.calcium-carbonate.org.uk/index.asp>.

Belcher A. M., Wu X. H., Christensen R. J., Hansma P. K., Stucky G. D. and Morse D. E. (1996) Control of crystal phase switching and orientation by soluble mollusk shell proteins. *Nature* **381**: 56-58.

Benny S., Grau-Crespo R. and de Leeuw N. H. (2009) A theoretical investigation of alpha-Fe<sub>2</sub>O<sub>3</sub>-Cr<sub>2</sub>O<sub>3</sub> solid solutions. *Physical Chemistry and Chemical Physics* **11**: 808-815.

Berner R. A. (1975) The role of magnesium in the crystal growth of calcite and aragonite from seawater. *Geochimica et Cosmochimica Acta* **39**: 489-504.

Bertaut F. (1958) Physique du cristal - le terme électrostatique de l'énergie de surface. *Comptes Rendus Chimie* **246**: 3447.

Beruto D. and Giordani M. (1993) Calcite and aragonite formation from aqueous calcium hydrogen carbonate solutions: effect of induced electromagnetic field on the activity of  $\text{CaCO}_3$  nuclei precursors, *Journal of the Chemistry Society, Faraday Transaction* **89**: 2457-2461.

Bramley A. S., Hounslow M. J. and Ryall R. L. (1997) Aggregation during precipitation from solution: kinetics for calcium oxalate monohydrated. *Chemical Engineering Science* **52**: 747-757.

Bruneval F., Donadio D. and Parrinello M. (2007) Molecular dynamics study of the solvation of calcium carbonate in water. *Journal of Physical Chemistry B* **111**: 12219-12227.

Born M., Huang K. (1954) *Dynamic theory of crystal lattices*, Oxford University Press, Oxford, UK.

Buckingham A. (1938) The Classical Equation of State of Gaseous Helium, Neon and Argon, Proceedings of the Royal Society of London. Series A, *Mathematical and Physical Sciences* **168**: 264-283.

Carpenter M. A. (1980) Mechanisms of exsolution in sodic pyroxenes. *Contributions to Mineralogy and Petrology* **71**: 289-300.

Catlow C. R. A. and Macrodt W. C. (1982) *Computer Simulation of Solids*. Springer Verlag, Berlin, Germany.

Capobianco C. and Navrotsky A. (1987) Solid solution thermodynamics in  $\text{CaCO}_3$ - $\text{MnCO}_3$ . *American Mineralogist* **72**: 312-318.

Chan C. M., Wu J. S., Li J. X. and Cheung Y. K. (2002) Polypropylene/calcium carbonate nano composites. *Polymer* **43(10)**: 2981-2992.

Chang F. R. C., Skipper N. T. and Sposito G. (1995) Computer simulation of interlayer molecular structure in sodium montmorillonite hydrates. *Langmuir* **11**: 2734-2741.

Chang L. L. Y., Howie R. A. and Zussman J. (1996) *Rock-forming Minerals*, 2<sup>nd</sup> edition, Vol. 5, Non-silicates, 108-135.

Chiarello R. P., Sturchio N. C., Grace J. D., Geissbuhler P., Sorensen L. B., Likwan Cheng L. and Xu S. (1997) Otavite-calcite solid solution formation at the calcite water interface studied *in situ* by synchrotron X-ray scattering. *Geochimica et Cosmochimica Acta* **61(7)**: 1467-1474.

Colfen H. (2003) Precipitation of carbonates: recent progress in controlled production of complex shapes. *Current Opinion in Colloid & Interface Science* **8**: 23-31.

Collier A. P., Hetherington C. J. D. and Hounslow M. J. (2000) Alignment mechanisms between particles in crystalline aggregates. *Journal of Crystal Growth* **208**: 513-519.

Cooke D. J. and Elliott J. A. (2007) Atomistic simulations of calcite nanoparticles and their interaction with water. *The Journal of Chemical Physics* **127**: 104706.

Cygan R. T., Wright K., Fidler D. K., Gale J. D. and Slater B. (2002) Atomistic models of carbonate minerals: bulk and surface structures, defects, and diffusion. *Molecular Simulation* **28**: 475-495.

Davidson P. M. (1994) Ternary iron, magnesium, calcium carbonates: A thermodynamic model for dolomite as an ordered derivative of calcite-structure solutions. *American Mineralogist* **79**: 332-339.

Davis J. A., Fuller C. C. and Cook A. D. (1987) A model for trace element sorption processes at the calcite surface: Adsorption of Cd<sup>2+</sup> and subsequent solid-solution formation. *Geochimica et Cosmochimica Acta* **51**: 1477-1490.

Davis K. J., Dove P. M. and de Yoreo J. J. (2000) The role of Mg<sup>2+</sup> as an impurity on calcite growth. *Science* **290**: 1134-1137.

Davis P. K. and Navrotsky A. (1983) Quantitative correlations of deviations from ideality in binary and pseudobinary solid solutions. *Journal of Solid State Chemistry*

**46:** 1-22.

Deer W. A., Howie R. A. and Zussmann J. (1992) *Introduction to the Rock-forming Minerals*. Longman Group UK Limited, Harlow, UK, 2<sup>nd</sup> edition.

Didymus J. M., Mann S., Sanderson N. P., Oliver P., Heywood B. R. and Aso-Samper E. J. (1993) Modelling biomineralization: studies on the morphology of synthetic calcite. Springer Verlag, Tokyo, 267-271.

Di Tommaso D. and de Leeuw N. H. (2008) The onset of calcium carbonate nucleation: A density functional theory molecular dynamics and hybrid microsolvation continuum study. *Journal of Physical Chemistry B* **112**: 6965-6975.

Di Tommaso D. and de Leeuw N. H. (2009) Theoretical study of the dimerization of calcium carbonate in aqueous solution under natural water conditions. *Geochimica et Cosmochimica Acta* **73**: 5394-5405.

Dick B. G. and Overhauser A. W. (1958) Theory of the dielectric constants of alkali halide crystals. *Physical Review* **112**: 90-103.

de Leeuw N. H. and Parker S. C. (1997) Atomistic simulation of the effect of molecular adsorption of water on the surface structure and energies of calcite surfaces. *Journal of the Chemical Society Faraday Transactions* **93**: 467-475.

de Leeuw N. H. and Parker S. C. (1998) Surface structure and morphology of calcium carbonate polymorphs calcite, aragonite, and vaterite: an atomistic approach. *Journal of Physical Chemistry B* **102**: 2914-2922.

de Leeuw N. H., Parker S. C. and Harding J. H. (1999) Molecular dynamics simulation of crystal dissolution from calcite steps. *Physical Review B* **60**: 13792-13799.

de Leeuw N. H. and Parker S. C. (2000) Modeling absorption and segregation of magnesium and cadmium ions to calcite surfaces: Introducing MgCO<sub>3</sub> and CdCO<sub>3</sub> potential models. *Journal of Chemical Physics* **112**: 4326-4333.

de Leeuw N. H. (2002) Molecular dynamics simulation of the growth inhibiting effect of  $\text{Fe}^{2+}$ ,  $\text{Mg}^{2+}$ ,  $\text{Cd}^{2+}$  and  $\text{Sr}^{2+}$  on calcite crystal growth. *Journal of Physical Chemistry B* **106**: 5241-5249.

de Leeuw N. H. and Cooper T. G. (2003) A computer modeling study of the inhibiting effect of organic adsorbates on calcite crystal growth. *Crystal Growth and Design* **4**: 123-133.

Domingo C., Garcia-Carmona J., Loste E., Fanovich A., Fraile J. and Gomez-Morales J. (2004) Control of calcium carbonate morphology by precipitation in compressed and supercritical carbon dioxide media. *Journal of Crystal Growth* **271**: 268-273.

Du Z. and de Leeuw N. H. (2006) Molecular Dynamics simulations of hydration, dissolution and nucleation processes at the  $\alpha$ -quartz (0001) surface in liquid water. *Dalton Transactions* **22**: 2623-2634.

El-Korashy S. A. (2003) Studies on divalent ion uptake of transition metal cations by calcite through crystallization and cation exchange process. *Journal of Materials Science* **38**: 1709-1719.

Ewald P. (1921) Die Berechnung optischer und elektrostatischer Gitterpotentiale. *Annals Physics* **369**: 253-287.

Fenter P., Geissbühler P., DiMasi E., Srajer G., Sorensen L. B. and Sturchio N. C., (2000) Surface speciation of calcite observed *in situ* by high resolution x-ray reflectivity. *Geochimica et Cosmochimica Acta* **64(7)**: 1221-1228.

Fisler D. K., Gale J. D. and Cygan R. T. (2000) A shell model for the simulation of rhombohedral carbonate minerals and their point defects. *American Mineralogist* **85**: 217-224.

Freeman C. L., Harding J. H. and Duffy D. M. (2008) Simulations of calcite crystallization on self-assembled monolayers. *Langmuir* **24**: 9607-9615.

Freij S. J., Godelitsas A. and Putnis A. (2005) Crystal growth and dissolution

processes at the calcite water interface in the presence of zinc ions. *Journal of Crystal Growth* **273**: 535-545.

Frye R. (1981) *Calcite Group in Encyclopedia of Mineralogy*. Hutchinson Ross Publishing Company, Stroudsborg, Pennsylvania, USA.

Gabriely I., Leu J. P. and Barzel U. S. (2008) Clinical problem-solving, back to basics. *New England Journal of Medicine* **358**: 1952-1956.

Gale J. D. (1997) GULP: A computer program for the symmetry-adapted simulation of solids. *Journal of the Chemical Society, Faraday Transactions* **93**: 629-637.

Gale J. D. and Rohl A. L. (2003) The general utility lattice program. *Molecular Simulation* **29**: 291-341.

Gamsjaeger H., Koenigsberger E. and Preis W. (2000) Lippmann diagrams: Theory and application to carbonate systems. *Aquatic Geochemistry* **6**: 119-132.

Garcia-Sanchez A. and Alvarez-Ayuso E. (2002) Sorption of Zn, Cd and Cr on calcite. Application to purification of industrial wastewaters. *Minerals Engineering* **15**: 539-547.

Gebauer D., Völkel A. and Cölfen H. (2008) Stable pre-nucleation calcium carbonate clusters, *Science*, **322**: 1819-1822.

Geissbühler P., Fenter P., DiMasi E., Srajer G., Sorenson L. B. and Sturchio N. C., (2004) Three-dimensional structure of the calcite-water interface by surface X-ray scattering. *Surface Science* **573**: 191-203.

Ghose S. K., Waychunas G. A. and Trainor T. P. (2010) Hydrated goethite ( $\alpha$ -FeOOH) (100) interface structure: Ordered water and surface functional groups. *Geochimica et Cosmochimica Acta* **74**: 1943-1953.

Gilbert B. and Banfield J. (2005) Chapter 6: Molecular-scale processes involving nanoparticulate minerals in biogeochemical systems. *Reviews in Mineralogy and Geochemistry* **59**: 109-156.

Goldsmith J. R. and Graf D. L. (1957) The system CaO-MnO-CO<sub>2</sub>: solid solution and decomposition relations. *Geochimica et Cosmochimica Acta* **11**: 310-334.

Goldsmith J. R. and Heard H. C. (1961) Subsolidus Phase Relations in the System CaCO<sub>3</sub>-MgCO<sub>3</sub>. *The Journal of Geology* **69**: 45-74.

Goldsmith J. R. and Northrop D. A. (1965) Subsolidus phase relations in the systems CaCO<sub>3</sub>-MgCO<sub>3</sub>-CoCO<sub>3</sub> and CaCO<sub>3</sub>-MgCO<sub>3</sub>-NiCO<sub>3</sub>. *The Journal of Geology* **73**: 817-829.

Gratz A. J., Hillner P. E. and Hansma P. K. (1993) Step dynamics and spiral growth on calcite. *Geochimica et Cosmochimica Acta* **57**: 491-495.

Grau-crespo R., Hamad S., Catlow C. R. A. and de Leeuw N. H. (2007) Symmetry-adapted configurational modelling of fractional site occupancy in solids. *Journal of Physics: Condensed Matter* **19**: 256201-256217.

Gutjahr A., Dabringhaus H. and Lacmann R. (1996) Studies of the growth and dissolution kinetics of the CaCO<sub>3</sub> polymorphs calcite and aragonite II. The influence of divalent cation additives on the growth and dissolution rates. *Journal of Crystal Growth* **158**: 310-315.

Harding J. H. (1990) Computer simulation of defects in ionic solid. *Reports on Progress in Physics* **53**: 1403.

Hillner P. E., Manne S.; Hansma P. K. and Gratz A. J. (1993) Atomic force microscope: a new tool for imaging crystal growth processes. *Faraday Discussions* **95**:191-197.

Hoch A. R., Reddy M. M. and Aiken G. R. (2000) Calcite crystal growth inhibition by humic substnaces with emphasis on hydrophobic acids from the Florida Everglades. *Geochimica et Cosmochimica Acta* **65(1)**: 61-72.

Hochella M. F., Jr. Eggleston C. M., Elings V. B., Parks G. A., Brown G. E., Jr. Kjoller K. K. and Wu C. M. (1989) Mineralogy in two dimensions: Scanning tunneling microscopy of semiconducting minerals with implications for geochemical

reactivity. *American Mineralogist* **74**: 1233-1246.

Hockney R. W. (1970) *The potential calculation and some applications*. Vol. **9**. Academic Press, New York.

Hoover W. G. (1985) Canonical dynamics: equilibrium phase-space distributions. *Physical Review A* **31**: 1695-1697.

Ikeda T., Boero M. and Terakura K. (2007) Hydration properties of magnesium and calcium ions from constrained first principles molecular dynamics. *Journal of Chemical Physics* **127**:74503.

IMA-NA (The Industrial Minerals Association - North America) (2011) Introduction to calcium carbonate. <http://www.ima-na.org/calcium-carbonate>.

Järup L. (2003) Hazards of heavy metal contamination. *British Medical Bulletin* **68(1)**: 167-182.

Jensen F. (2007) *Introduction to Computational Chemistry*, John Wiley & Sons Ltd, Chichester, West Sussex, UK, 2<sup>nd</sup> edition.

Jorgensen W. L., Chandrasekhar J., Madura J. D., Impey R. W. and Klein M. L. (1983) Comparison of simple potential functions for simulating liquid water. *Journal of Chemical Physics* **79**: 926-935.

Katsikopoulos P., Fernandez-Gonzalez A. and Prieto M. (2009) Precipitation and mixing properties of the “disordered” (Mn,Ca)CO<sub>3</sub> solid solution. *Geochimica et Cosmochimica Acta* **73**: 6147-6161.

Kerisit S. and Parker S. C. (2004) Free energy of adsorption of water and calcium on the {10 $\bar{1}$ 4} calcite surface. *Chemical Communications* **1**: 52-54.

Kerisit S. and Parker S.C. (2004) Free energy of adsorption of water and metal ions on the {10 $\bar{1}$ 4} Calcite Surface. *Journal of the American Chemical Society* **126**: 10152-10161.

Kerisit S., Cooke D. J., Spagnoli D. and Parker S. C. (2005) Molecular dynamics simulations of the interactions between water and inorganic solids. *Journal of Materials Chemistry* **15**: 1454-1462.

Koparde V. N. and Cummings P. T. (2005) Molecular dynamics simulation of titanium dioxide nanoparticle sintering. *Journal of Physical Chemistry B* **109**: 24280-24287.

Kristensen R. and Stipp S. L. S. (2004) Modeling steps and kinks on the surface of calcite. *Journal of Chemical Physics* **121**: 8511-8523.

Kuriyavar S. I., Vetrivel R., Hegde S. G., Ramaswamy A. V., Chakrabarty D. and Mahapatra S. (2000) Insights into the formation of hydroxyl ions in calcium carbonate: temperature dependent FTIR and molecular modelling studies. *Journal of Materials Chemistry*, **10**: 1835-1840.

Lardge J. S. (2009) Investigation of the interaction of water with the calcite  $\{10\bar{1}4\}$  surface using ab-initio simulation. PhD thesis, University College London.

Larsen K., Bechgaard K. and Stipp S. L. S. (2010) Modelling spiral growth at dislocations and determination of critical step lengths from pyramid geometries on calcite  $\{10\bar{1}4\}$  surfaces. *Geochimica et Cosmochimica Acta* **74**: 558-567.

Lebron I. and Suarez D. L. (1998) Modeling calcite precipitation as affected by PCO<sub>2</sub> and organic ligands at 25°C. *Mineralogical Magazine* **62A**: 864-865.

Lennard-Jones, J. E. (1924). On the Determination of Molecular Fields, *Proceedings of the Royal Society A* **106**: 463-477.

Liang Y., Baer D. R., McCoy J. M., Amonette J. E. and Lafemina J. P. (1996) Dissolution kinetics at the calcite-water interface. *Geochimica et Cosmochimica Acta* **60**: 4883-4887.

Liang Y. and Baer D. R. (1997) Anisotropic dissolution at the CaCO<sub>3</sub>  $\{10\bar{1}4\}$ -water interface. *Surface Science* **373**:275-287.

Liang Y., Lea A. S., Baer D. R. and Engelhard M. H. (1996) Structure of the cleaved  $\text{CaCO}_3$  {10 $\bar{1}$ 4} surface in an aqueous environment. *Surface Science* **351**: 172-182.

Lieberman H. A., Lachman L. and Schwartz B. J. (1990) *Pharmaceutical Dosage Forms: Tablets*. Dekker, New York, USA.

Liew T. L., Barrick J. P. and Hounslow M. J. (2003) A micro mechanical model for the rate of aggregation during precipitation from solution. *Chemical Engineering & Technology* **26**: 282-285.

Lippmann F. (1980) Phase diagrams depicting aqueous solubility of binary mineral systems. *Neues Jahrbuch für Mineralogie* **139**: 1-25.

Mandell G. K., Rock P. A., Fink W. H. and Casey W. H. (1999) Lattice energies of calcite structure metal carbonates III. Theoretical excess energies for solid solutions (Ca, M)CO<sub>3</sub> [M=Cd, Mn, or Fe]. *Journal of Physics and Chemistry of Solids* **60**: 651-661.

Meldrum F. C. (2003) Calcium carbonate in biomineralisation and biomimetic chemistry. *International Materials Review* **48**: 187-224.

Mitchell P. J. and Fincham D. (1993) Shell model simulations by adiabatic dynamics. *Journal of Physics: Condensed Matter* **5**: 1031-1038.

Morse J. W. and Mackenzie F. T. (1990) *Geochemistry of Sedimentary Carbonates*. Elsevier, Amsterdam, the Netherlands.

Morse P. M. (1929) Diatomic molecules according to the wave mechanics. II. Vibrational levels. *Physical Review* **34**: 57-64.

Mulline J. W. (1992) *Crystallization*. Butterworth-Heinmann Oxford, UK.

Murphy S. (2009) Atomistic simulation of defects and diffusion in oxides. PhD thesis, Imperial College.

Nriagu J. O. (1980) *Cadmium in the Environment, Part-I, Ecological Cycling*.

Wiley-Interscience.

Nriagu J. O. (1981) *Cadmium in the Environment, Part-II, Health Effects*. Wiley-Interscience.

Ohnesorge F. and Binnig G. (1993) True atomic resolution by atomic force microscopy through repulsive and attractive forces. *Science* **260**: 1451-1456.

Oliver P. M., Parker S. C. and Mackrodt W. C. (1993) Computer simulation of the morphology of NiO. *Modelling and Simulation of Material Science and Engineering* **1**: 755-760.

Park N., Kim M., Langford S. C. and Dickinson J. T. (1996) Atomic layer wear of single-crystal calcite in aqueous solution using scanning force microscopy. *Journal of Applied Physics* **80**: 2680-2686.

Pastero L., Costa E., Bruno M., Rubbo M., Sgualdino G. and Aquilano D. (2004) Morphology of calcite (CaCO<sub>3</sub>) crystals growing from aqueous solutions in the presence of Li<sup>+</sup> ions. Surface behavior of the {0001} form. *Crystal Growth and Design* **4**: 485-490.

Patton T. C. (1979) *Paint Flow and Pigment Dispersion*. Wiley Press, New York, 2<sup>nd</sup> edition.

Pavese A., Catti M., Parker S. C. and Wall A. (1996) Modelling of the thermal dependence of structural and elastic properties of calcite, CaCO<sub>3</sub>. *Physics and Chemistry of Minerals* **23**: 89-93.

Pertlik F. (1986) Structure of hydrothermally synthesized cobalt carbonate and nickel carbonate. *Acta Crystallographica C* **42**: 4-5.

Pouget E. M., Bomans P. H. H., Goos J. A. C. M., Frederik P. M., de With G. and Sommerdijk N. A. J. M. (2009) The Initial Stages of Template-Controlled CaCO<sub>3</sub> Formation Revealed by Cryo-TEM, *Science* **323**: 1455-1458.

Prieto M., Culbillas P. and Fernandez-Gonzalez A. (2003) Uptake of dissolved by

biogenic and abiogenic aragonite: a comparison with sorption onto calcite. *Geochimica et Cosmochimica Acta* **67**: 3859-3869.

Putnis A. (1992) *Introduction to Mineral Science*. Cambridge University Press, Cambridge. UK.

Rajam S. and Mann S. (1990) Selective stabilization of the (001) face of calcite in the presence of lithium. *Journal of Chemical Society, Chemical Communications* **24**: 1789-1791.

Reeder R. J. (1983) Crystal chemistry of the rhombohedral carbonates. *Reviews in Mineralogy and Geochemistry* **11**: 1-47.

Reeder R. J. (1996) Interaction of divalent cobalt, zinc, cadmium, and barium with the calcite surface during layer growth. *Geochimica et Cosmochimica Acta* **60**: 1543-1552.

Read W. T. and Shockley W. (1950) Dislocation models of crystal grain boundaries. *Physical Review* **78**: 275-289.

Rick S. W. (2004) A reoptimization of the five-site water potential (TIP5P) for use with Ewald sums. *Journal of Chemical Physics* **120**: 6085-6093.

Rieger, J., Frechen, T., Cox, G., Heckmann, W., Schmidt, C. and Thieme, J. (2007) Precursor structures in the crystallization/precipitation processes of CaCO<sub>3</sub> and control of particle formation by polyelectrolytes. *Faraday Discuss.* **136**: 265-277.

Rocha-Marisa. C. G., Silva A. H. M. F. T., Coutinho-Fernanda M. B. and Silva Ana Lúcia N. (2005) Study of composites based on polypropylene and calcium carbonate by experimental design. *Polymer Testing* **24**: 1049-1053.

Rock P. A., Casey W. H., McBeach M. K. and Walling E. M. (1994) A new method for determining Gibbs energies of formation of metal-carbonate solid solutions: 1. The Ca<sub>x</sub>Cd<sub>1-x</sub>CO<sub>3</sub>(s) system at 298K and 1bar. *Geochimica et Cosmochimica Acta* **58**: 4281-4291.

Romanek C. S., Grossman E. L. and Morse J. W. (1992) Carbon isotopic fractionation in synthetic aragonite and calcite: Effects of temperature and precipitation rate. *Geochimica et Cosmochimica Acta* **56**: 419-430.

Ruiz-Hernandez S. E., Grau-Crespo R., Ruiz-Salvador A. R. and de Leeuw N. H., (2010) Thermodynamistry of strontium incorporation in aragonite from atomistic simulations. *Geochimica et Cosmochimica Acta* **74**, 1320-1328.

Sadus R. J. (2002) *Molecular Theory of Fluids: Theory, Algorithms and Object-Oriented*, Elsevier Science Press. 231.

Schwuger M. J. (1981) *Anionic Surfactants, Surfactants Science Series*. Vol. **11**, Marcel Dekker, New York, USA.

Shannon R. D. (1976) Revised effective ionic radii and systematic studies of interatomic distances in halides and chalcogenides. *Acta Crystallographica A* **32**, 751-767.

Smith W. and Forester T. R. (1996) DL\_POLY: A general-purpose parallel molecular dynamics simulation package. *Journal of Molecular Graphics* **14**: 136-141.

Söhnel O. and Mullin J.W. (1982) Precipitation of calcium carbonate. *Journal of Crystal Growth* **60**: 239-250.

Spagnoli D., Allen J. P. and Parker S. C. (2011) The structure and dynamics of hydrated and hydroxylated magnesium oxide nanoparticles. *Langmuir* **27**: 1821-1829.

Spagnoli D., Banfield J. F. and Parker S. C. (2008) Free energy change of aggregation of nanoparticles. *Journal of Physical Chemistry C* **112**: 14731-14736.

Spagnoli D., Kerist S. and Parker S. C. (2006) Atomistic simulation of the free energies of dissolution of ions from flat and stepped calcite surfaces. *Journal of Crystal Growth* **294**: 103-110.

Stack A. G. and Grantham M. C. (2010) Growth rate of calcite steps as a function of

aqueous calcium to carbonate ratio: Independent attachment and detachment of calcium and carbonate ions. *Crystal Growth and Design* **10**: 1409-1413.

Stipp S. L. S., Eggleston C. M. and Nielsen B. S. (1994) Calcite surface structure observed at microtopographic and molecular scales with atomic force microscopy (AFM). *Geochimica et Cosmochimica Acta* **58**:3023-3033.

Stipp S. L. S. and Hochella M. F. (1991) Structure and bonding environments at the calcite surface as observed with X-ray photoelectron spectroscopy and low energy electron diffraction. *Geochimica et Cosmochimica Acta* **55**: 1723-1736.

Stipp S. L. S., Hochella M. F., Parks G. A. and Leckie J. O. (1992) Cd<sup>2+</sup> uptake by calcite, solid state diffusion, and the formation of solid-solution; Interface process observed with near surface sensitive techniques. *Geochimica et Cosmochimica Acta* **56**: 1941-1954.

Stipp S. L. S., Parks G. A., Nordstrom D. K. and Leckie J. O. (1993) Solubility product constant and thermodynamic properties for synthetic otavite, CdCO<sub>3</sub>(s), and aqueous association constants for the Cd(II)-CO<sub>2</sub>-H<sub>2</sub>O System. *Geochimica et Cosmochimica Acta* **57**: 2699-2713.

Stipp S. L. S., Konnerup-Madsen J., Franzreb K., Kulik A. and Mathieu H. J. (1998) Spontaneous movement of ions through calcite at standard temperature and pressure. *Nature* **396**:356-359.

Tasker P. W. (1979) The stability of ionic crystal surfaces. *Journal of Physics C: Solid State Physics* **12**: 4977-4983.

Tesoriero A. J. and Pankow J. F. (1995) Solid solution partitioning of Sr<sup>2+</sup>, Ba<sup>2+</sup> and Cd<sup>2+</sup> to calcite. *Geochimica et Cosmochimica Acta* **60**: 1053-1063.

Todorov I. T., Allan N. L., Lavrentiev M. Y., Freeman C. L., Mohn C. E. and Purton J. A. (2004) Simulation of mineral solid solutions at zero and high pressure using lattice statics, lattice dynamics and Monte Carlo methods. *Journal of Physics: Condensed Matter* **16**: 2751.

Tohda H., Tsuchiya Y., Kobayashi T., Kishiro H. and Yanagisawa T. (1994) The Crystalline Structure of Pancreatic Calculi. *Journal of Electron Microscopy* **43**: 57-61.

Tribello G. A., Bruneval F., Liew C. and Parrinello M. (2009) A molecular dynamics study of the early stages of calcium carbonate growth. *Journal of Physical Chemistry B* **113**: 11680-11687.

Verlet L. (1967) Computer "Experiments" on classical fluids. I. Thermodynamical properties of Lennard-Jones molecules. *Physical Review* **159**: 98-103.

Vinograd V. L., Sluiter M. H. F. and Winkler B. (2009) Subsolidus phase relations in the  $\text{CaCO}_3\text{-MgCO}_3$  system predicted from the excess enthalpies of supercell structures with single and double defects. *Physical Review B* **79**: 104201-104209.

Vinograd V. L., Paulsen N., Winkler B. and van der Walle A. (2010) Thermodynamics of mixing in the ternary rhombohedral carbonated solid solution  $(\text{Ca}_x\text{Mg}_y, \text{Mn}_{1-x-y})\text{CO}_3$  from atomistic simulations. *CALPHAD: Computer coupling of phase diagrams and thermochemistry* **34**: 113-119.

Vinograd V. L., Winkler B., Putnis A., Gale J. D. and Sluiter M. H. F. (2006) Static lattice energy calculations of mixing and ordering enthalpy in binary carbonate solid solutions. *Chemical Geology* **225**: 304-313.

Watson G. W., Kelsey E. T., de Leeuw N. H., Harris D. J. and Parker S. C. (1996) Atomistic simulation of dislocations, surfaces and interfaces in MgO. *Journal of Chemical Society, Faraday Transactions* **92**: 433-438.

White D. N. J. (1997) A computationally efficient alternative to the Buckingham potential for molecular mechanics calculations. *Journal of Computer-Aided Molecular Design* **11**: 517-521.

Wolf S. E., Leiterer J., Kappl M., Emmerling F. and Tremel W. (2008) Early homogenous amorphous precursor stages of calcium carbonate and subsequent crystal growth in levitated droplets. *Journal of American Chemical Society*. **130**:

12342-12347.

Wulff G. (1901) Zur Frage der Geschwindigkeit des Wachstums und der Auflösung der Krystallflagen. *Zeitschrift für Kristallographie* **34**: 449.

Zachara J. M., Cowan C. E. and Resch C. T. (1991) Sorption of divalent metals on calcite. *Geochimica et Cosmochimica Acta* **55**: 1549-1562.

Zachara J. M., Kittrick J. A. and Harsh J. B. (1988) The mechanism of  $Zn^{2+}$  adsorption on calcite. *Geochimica et Cosmochimica Acta* **52**: 2281-2291.

Zhang J. and Reeder R. J. (1999) Comparative compressibilities of calcite-structure carbonates: deviation from empirical relations. *American Mineralogist* **84**: 861-870.

Zhang H. and Banfield J. F. (2004) Aggregation, coarsening, and phase transformation in ZnS nanoparticles studied by molecular dynamics simulations. *Nano Letter* **4(4)**: 713-718.

Zuiderduin W. C. J., Westzaan C., Huetink J. and Gaymans R. J. (2003) Toughening of polypropylene with calcium carbonate particles, *Polymer* **44**: 261-275.